Atmospheric Controls on Mineral Dust Emission from Southern African Source Areas and Their Representation in Numerical Models



Matthew Clements

Hertford College

University of Oxford

A thesis submitted for the degree of

Doctor of Philosophy

Trinity Term 2022

Table of Contents

Acknowledgments (1)

Abstract (2)

Chapter 1: Introduction (4)

1.1) Overview of Thesis (4)

1.1.1) Background Summary (4)

1.1.2) Key Questions and Research Objectives (6)

1.1.3) Thesis Structure (7)

1.2) Dust in the Climate System (9)

1.2.1) Overview (9)

1.2.2) Climate Impacts (9)

1.2.2.1) Dust-Radiation-Cloud Interactions (9)

1.2.2.2) Dust and Biogeochemical Cycles (10)

1.2.3) Global Dust Source Areas (11)

1.2.4) Dust in Climate Models (12)

1.3) Atmospheric Controls on Dust Emission (15)

1.3.1) Overview (15)

1.3.2) Mesoscale Processes (16)

1.3.2.1) Nocturnal Low-Level Jets (16)

1.3.2.2) Cold Pool Outflows (21)

1.3.3) Synoptic Scale (23)

1.4) Southern African Climate and Dust Source Areas (24)

1.4.1) Climate of Southern Africa (24)

1.4.1.1) Climatic Setting and Variability (24)

1.4.1.2) Thermal and Topographic Airflows (27)

1.4.1.3) Climate Change (28)

1.4.2) Southern African Dust Source Areas (28)

1.4.2.1) Overview (28)

1.4.2.2) The Etosha Pan (30)

1.4.2.3) The Makgadikgadi Pans (31)

1.4.2.4) Other Source Areas (32)

Chapter 2: Data and Methods (33)

2.1) In Situ Observational Data (33)

2.1.1) Summary of Data Sources (33)

2.1.2) Strengths, Limitations and Applications in Other Dust Source Areas (35)

2.2) Satellite Imagery (38)

2.2.1) Summary of Data Sources (38)

2.2.2) Strengths, Limitations and Applications in Other Dust Source Areas (39)

2.3) Reanalysis and Gridded Precipitation Data (41)

2.3.1) Summary of Data Sources (41)

2.3.2) Application in Thesis Research (42)

2.4) Model Data (45)

2.4.1) Summary of Data Sources (45)

2.4.2) Model Selection (45)

2.4.3) Evaluation Against Observations and Reanalysis Data (46)

Chapter 3: Atmospheric Controls on Mineral Dust Emission From the Etosha Pan, Namibia: Observations From the CLARIFY-2016 Field Campaign

Chapter 4: Summer Dust Emissions From the Etosha Pan, Namibia: The Role of the Namib Anabatic-Sea Breeze System

Chapter 5: An Analysis of Dust Emission Mechanisms in CMIP6 Models and Their Influence on Simulated Uplift Across Southern Africa

Chapter 6: Discussion & Conclusions (48)

6.1) Discussion of Results (48)

6.1.1 Spatial Distribution and Temporal Variability in Dust Emissions (48)

6.1.1.1 Spatial Distribution (48)

6.1.1.2 Temporal Variability (49)

6.1.2) Meteorology of Southern African Dust Source Areas (51)

6.1.2.1) Mesoscale Atmospheric Processes (51)

6.1.2.2) Forcing Mechanisms (53)

6.1.3) Atmospheric Controls on Dust Emission (55)

6.1.3.1) Surface Winds (55)

6.1.3.2) Mesoscale Atmospheric Processes (56)

6.1.3.3) Synoptic Forcing (58)

6.2) Future Dust Research in Southern Africa (60)

6.2.1 Temporal Extent of Meteorological Observations (60)

6.2.1.1) Interannual Variability in NLLJ (60)

6.2.1.2) Relationship Between Anabatic-Sea Breeze and Convection (60)

6.2.1.3) Drivers of Dust Uplift in Austral Spring (61)

6.2.2 Spatial Coverage of Meteorological Observations (62)

6.2.2.1) Spatial Extent of NLLJ (62)

6.2.2.2) Drivers of Dust Uplift from Other Source Areas (63)

6.2.3) Modelling Work (63)

6.2.3.1) Convection Permitting Simulations (63)

6.2.3.2) Response of Mesoscale Processes to Future Climate Change (64)

6.3) Summary of Main Findings (66)

References

Data Sources

Appendix A: Statement of co-authorship

Acknowledgements

I would like to thank the tutors, instructors, and all other staff on the NERC DTP programme and in the School of Geography and the Environment for the advice and technical expertise they have provided during my DPhil studies.

I would like to thank Shane Kötting and his team at the Etosha National Park for their invaluable support in the field, without which the data collection that underpinned part of this thesis would not have been possible.

Finally, I would like to thank my supervisors Professor Richard Washington and Dr Sebastian Engelstaedter for the invaluable guidance and support they have provided during my DPhil studies and the writing of this thesis.

Abstract

Mineral aerosol (dust) is a critical component of the earth system, affecting climate processes and biogeochemical cycles; accurate simulation of dust in coupled models is therefore essential, so as to avoid uncertainties in the representation of current and future climate. Evaluation of dust in climate models shows biases in simulated emissions and concentrations, with models failing to capture the observed wind speed distribution in dust source areas. A number of atmospheric processes have been identified as critical to the uplift of dust from Saharan source areas, with their misrepresentation in models a likely source of the bias in the simulated surface wind speed distribution. Very little work has been conducted in southern Africa; this is despite the identification of major source areas using remotely sensed data. The research conducted as part of this thesis therefore aims to identify the atmospheric processes driving dust emissions from southern Africa source areas, and evaluate their representation in numerical models.

High-resolution, in situ meteorological observations have been collected at the Etosha Pan, the most prominent dust source area in southern Africa. This data, used in conjunction with atmospheric reanalyses, has been used to characterise the meteorology of the source area across the two main dust seasons. Utilising a suite of satellite products, emissions from the pan (and southern Africa more generally) have been tracked across a range of temporal scales, which in turn has permitted an assessment of the atmospheric processes driving uplift. The in situ, reanalysis and satellite data also provide a constraint on model fields, and have been used to evaluate the representation of dust processes across southern Africa in the latest phase of coupled models.

Two mesoscale atmospheric processes have been shown to be especially important to dust emissions across southern Africa; namely, a nocturnal low-level jet (NLLJ) during austral winter, and an integrated anabatic-sea breeze during austral summer. NLLJ's are important emission mechanisms in North African source areas, however this is the first time the jet at Etosha has been linked to dust uplift. Thermally and topographically induced regional airflows have been observed along the west coast of southern Africa during austral summer, however this is the first time the sea breeze system has been shown to affect Etosha's meteorology and hence dust emissions. The representation of these mechanisms in coupled models is mixed, and together with the treatment of land surface properties, helps to explain the inability of the models to capture the spatial distribution in uplift across southern Africa.

Chapter 1: Introduction

1.1) Overview of Thesis

1.1.1) Background Summary

Mineral aerosol (dust) is a critical component of the earth system, affecting radiative transfer and cloud microphysical properties whilst resident in the atmosphere (Andreae & Rosenfeld, 2008; Haywood & Boucher, 2000), and providing important micronutrients to marine and terrestrial ecosystems upon deposition (Jickells et al., 2005; Swap et al., 1996). For this reason, it is essential that the dust cycle is accurately incorporated in numerical models, so as to avoid large uncertainties in the representation of current and future climate (Boucher et al., 2003). Evaluation of coupled models shows that there are biases in the quantity and spatial distribution of dust concentrations (Evan et al., 2014; Wu et al., 2020); a likely source of this bias is the treatment of the emission process in the models, with recent studies highlighting a lack of low-frequency, high wind speed events that have been observed to drive uplift in dust source areas (Evan, 2018; Roberts et al., 2017). This in part is due to the misrepresentation of key atmospheric processes responsible for generating dust-emitting winds (Allen & Washington, 2014; Heinold et al., 2013), and so improving understanding of these mechanisms, and refining their representation in numerical models is an important research task.

The majority of work investigating the controls on dust emission has been conducted in the Sahara, with recent field campaigns such as the Bodélé Dust Experiment (BodEx) (Todd et al., 2007), Fennec (Washington et al., 2012) and the African Monsoon Multidisciplinary Analysis (AMMA) (Lebel et al., 2011)

delivering meteorological data from source areas. Atmospheric processes operating across a range of spatial scales have been identified as fundamental to dust uplift, from microscale dust devils and dry convective plumes to the West African monsoon circulation and synoptic disturbances (Knippertz & Todd, 2012). Two mesoscale processes have been shown to be of particular importance to Saharan dust emissions; namely, the mixing-down of momentum from nocturnal low-level jets (NLLJ's), and downdrafts from moist convection (cold pool outflows (CPOs)) (Allen et al., 2013; Knippertz & Todd, 2012). Data delivered by the BodEx and Fennec field campaigns have provided an observational constraint on modelled winds, however the representation of the aforementioned mesoscale processes in coupled models and reanalyses is poor, and is a likely source of the bias in simulated surface winds and dust emissions (Allen & Washington, 2014; Heinold et al., 2013). State-of-the-art simulations that explicitly resolve convection have improved the match between model output and observations (Heinold et al., 2013), however more work is required to fully determine the effect of grid spacing, temporal resolution and physical parameterisations on model performance.

Relatively little attention has been given to investigating the controls on dust emission from southern Africa, despite the identification of major source areas utilising remotely sensed data (Prospero et al., 2002; Washington et al., 2003). These sources include the Etosha and Makgadikgadi Pans, the southern Kalahari Basin, and a collection of ephemeral river valleys and smaller pans along the Namib coast (Vickery et al., 2013). Previous studies have determined some of the hydrological and surface controls on the erodibility of these source areas (Bryant, 2003), however the atmospheric processes driving dust

emission across the subcontinent remain uncertain. Recent field campaigns in southern Africa include Dust Observations for Models (DO4Models) and CLoud-Aerosol-Radiation Interactions and Forcing: Year 2016 (CLARIFY-2016), which have for the first time provided high-resolution, in situ meteorological observations for some of the subcontinents major dust source areas; this data will permit an analysis of the atmospheric processes driving dust uplift, whilst also providing the means to test the performance of coupled models and reanalyses outside of a Saharan context. In so doing, the research conducted as part of this thesis will contribute to refining the representation of dust in coupled models, the primary tools for climate prediction, in a region that is highly sensitive to environmental change and variability.

1.1.2) Key Questions and Research Objectives

Given the importance of southern Africa as a dust source region, and the need to improve understanding of the atmospheric processes that drive uplift, as well as refine their representation in coupled models, this thesis will aim to address three key questions by achieving seven research objectives, utilising a range of in situ, satellite, reanalysis and model data. The key questions (1-3) and research objectives (a-g) are as follows:

1. *What are the spatial and temporal characteristics of dust emissions across southern Africa, and how are they represented in numerical models?*

    a. Characterise the spatial distribution of dust emissions across southern Africa and evaluate their representation in coupled models.

b. Characterise the variability in southern African dust emissions across a range of different timescales.

2. *What are the characteristic features of the meteorology of southern African dust source areas, and how are they represented in numerical models?*

    c. Characterise the key meteorological processes operating across southern Africa's dust source areas and identify the controls on their variability.

    d. Evaluate the representation of the key meteorological processes in reanalyses and coupled models, and assess the influence of resolution and physical parametrisations on model skill.

3. *What features of the meteorology identified in key question 2 are responsible for driving dust emissions from southern African source areas, and how are these processes represented in coupled models?*

    e. Identify the atmospheric processes from key question 2 that contribute to the uplift of dust from southern African source areas.

    f. Evaluate the representation of the dust-emitting processes in coupled models, and assess the influence of resolution and physical parametrisations on model skill.

    g. Assess how the representation of the dust-emitting processes helps to account for the spatial distribution of emissions in coupled models described in key question 1.

1.1.3) Thesis Structure

The thesis is structured as follows: In the remainder of chapter 1, an overview of the current state of knowledge regarding dust research is given, with sections summarising the key literature on; dust-climate interactions, global dust source areas, modelling the dust cycle, atmospheric controls on dust uplift and dust research in southern Africa. In chapter 2, the in situ, satellite, reanalysis and model data that has been used in the research is described, along with the methods employed to analyse the data and address the key questions. The three research papers that have been submitted are presented in chapters 3, 4 and 5 and detail the main results of the thesis. A discussion of the results and a summary of the main conclusions of the thesis are given in chapter 6, along with ideas for future work originating from the findings of the research conducted as part of the thesis.

1.2) Dust in the Climate System

1.2.1) Overview

Aerosols are an important constituent of the earth system and account for large uncertainties in state-of-the-art modelling of the planetary energy budget and biogeochemical cycles (Boucher et al., 2013; Haywood & Boucher, 2000; Jickells et al., 2005). Mineral aerosol, or dust, defined as 'soil-derived material from arid regions' (Schütz & Sebert, 1987), contributes to the total atmospheric aerosol burden and optical thickness (Kaufman et al., 2002; Textor et al., 2006), although its concentrations fluctuate wildly in time and space (Ginoux et al., 2012; Prospero et al., 2002). Estimates of annual dust emissions range from 1000-4000 $Tgyr^{-1}$ (Boucher et al., 2013), with major source areas situated across tropical and subtropical latitudes, especially in the deserts of the Northern Hemisphere (Prospero et al., 2002; Washington et al., 2003). In recent decades, these remote source areas have been instrumented as part of extensive field campaigns (Haustein et al., 2015; Washington et al., 2006; Washington et al., 2012), which together with advances in remote sensing techniques (Kaufman et al., 2002; Schepanski et al., 2007), have helped to progress dust research.

1.2.2) Climate Impacts

1.2.2.1) Dust-Radiation-Cloud Interactions

One of the means by which dust impacts on climate is through its interaction with radiation; this includes direct (scattering and absorption of both solar and terrestrial wavelengths) and indirect (alteration of cloud properties by acting as condensation nuclei) effects (Andreae & Rosenfeld, 2008; Tegen et al., 1996),

which makes it difficult to determine the overall radiative forcing due to the presence of dust in the atmosphere (Haywood & Boucher, 2000). For example, Tegen et al. (1996) estimates the global net radiative forcing at the surface to be -0.96Wm^{-2}, with a maximum perturbation (-25Wm^{-2}) recorded adjacent to the major northern source areas over the Arabian Sea, whilst Miller and Tegen (1998) and Hansen et al. (1998) estimate a much smaller negative forcing, reporting values of -0.06Wm^{-2} and -0.12Wm^{-2} respectively. Modelling studies of the direct effect predict a range of net forcing values, including both positive (Liao & Seinfeld, 1998; Tegen et al., 1996) and negative perturbations (Miller & Tegen, 1998), although these estimates are sensitive to dust properties such as particle size distribution and mineral composition, as well as the albedo of the underlying surface (Haywood & Boucher, 2000; Miller et al., 2014). Given the relatively large size of dust particles, their ability to act as a condensation nuclei is diminished compared to other aerosol species (Andreae & Rosenfeld, 2008), however observations suggest that dust emitted from the Sahara can seed thin, low-altitude clouds over the west coast of North Africa (Mahowald & Kiehl, 2003), and may also inhibit precipitation, potentially exacerbating the effects of drought in the Sahel (Rosenfeld et al., 2001).

1.2.2.2) Dust and Biogeochemical Cycles

Dust also impacts on climate through its interaction with global biogeochemical cycles (Jickells et al., 2005), acting as a source of essential nutrients such as iron and phosphorous, and hence fertilising remote terrestrial and marine ecosystems once deposited (Dansie et al., 2017; Swap et al., 1996). Iron delivery to the oceans is an especially important climatological process, and has been used to explain variability in atmospheric CO_2 concentrations on

glacial-interglacial timescales (Martin, 1990); iron uptake by marine organisms increases the rate of nitrogen fixation and therefore primary productivity (Jickells et al., 2005; Mahowald et al., 2010), ultimately resulting in a drawdown of carbon which is then sequestered in the deep ocean (Martin, 1990). In the present-day climate, dust fertilisation has been observed in ecosystems that are distant from major source areas, with for example dust from the Sahara providing nutrients to the far North Atlantic (Prospero, 1996) and Amazon Basin (Koren et al., 2006; Swap et al., 1992).

1.2.3) Global Dust Source Areas

In situ observations of emission from dust source areas are scarce, and where available are limited in their temporal extent (Haustein et al., 2015; Wiggs et al., 2022). The spatial distribution and temporal variability of dust emissions has therefore been inferred from dust concentration data (Dubovik et al., 2002; Prospero et al., 2002) or model simulations (Ginoux et al., 2012; Tegen & Fung, 1994), with recent advances in remote sensing techniques and dust detection algorithms making it possible to track individual plumes (Brindley et al., 2012; Murray et al., 2016). These studies have shown a concentration of major dust source areas in the global subtropics (Ginoux et al., 2012; Prospero et al., 2002; Washington et al., 2003), coincident with a belt of large-scale atmospheric subsidence and hence aridity at the surface. In particular, the northern subtropics are home to some of the most prominent source areas, with a dust belt stretching from the western Sahara to the Arabian Peninsula and southwest Asia (Prospero et al., 2002; Washington et al., 2003).

Within the global subtropics, the location of dust source areas is tightly coupled to topography, with uplift (from herein, uplift is used synonymously with emission to refer to the entrainment and transport of dust from source areas) observed from topographic lows and adjacent to mountainous regions (Ginoux et al., 2012; Prospero et al., 2002; Washington et al., 2003). The association with topographic lows is a consequence of the role of hydrology in supplying erodible sediment; indeed, many source areas are either ephemeral lakes or the remnants of paleolakes which have been inundated in recent geologic history (Mahowald et al., 2003; Prospero et al., 2002; Washington et al., 2006). For example, the Bodélé Depression, the most prominent global source area (Washington et al., 2003), was once Mega-Lake Chad, with diatomite sediment deposited when the lake was inundated during the early Holocene (Washington et al., 2006, 2009). The association between dust source areas and highlands is again due to hydrology and the tendency of these regions to receive large amounts of runoff (and hence particulate matter) (Prospero et al., 2002), and also the enhancement of dust-emitting atmospheric processes by topographic features (see chapter 1.3) (Caton Harrison et al., 2019; Todd et al., 2008).

1.2.4) Dust in Climate Models

Given the processes described in chapter 1.2.2, it is essential that the dust cycle, which begins with the uplift of material from source areas, is accurately incorporated in models, so as to avoid errors in the simulation of current and future climate (Boucher et al., 2013). The treatment of dust depends on the type of model; aerosol-chemistry and dust models calculate emissions and transport offline, driven by atmospheric fields derived from climate simulations or reanalysis data (Mann et al., 2010), whereas dust distributions are calculated

online in coupled and earth-system models, with emission and transport driven by the resolved wind fields (Textor et al., 2006). Simulation of the emission process is parameterised, and is sensitive to the surface wind speed as well as properties of the land surface (e.g., vegetation cover, soil moisture, bare soil fraction) which vary according to the dust scheme employed (Kok et al., 2012; Marticorena & Bergametti, 1995; Tegen et al., 2002). Recent testing of common dust schemes has shown them to overestimate fluxes by an order of magnitude, with surface crusting, a process not included in parameterisations but common in dryland environments inhibiting observed uplift (Haustein et al., 2015; Nield et al., 2016). The relationship between the saltation flux and vertical dust flux is described in dust schemes by the vertical-to-horizontal flux ratio (α), however is another parameter that is complicated by direct entrainment of sediment (i.e., vertical flux in the absence of saltation flux), a frequent process when uplift is triggered by dry convective plumes (Haustein et al., 2015; Shao et al., 2011). The vertical emission flux is also sensitive to the size distribution of soil particles, however there is very little field data describing the dust flux at different size ranges, and so the parameterisation of the dust size distribution in models (sorting particles into different size bins) is another parameter potentially limiting the skill of emission schemes (Haustein et al., 2015; Zhang & Li, 2014).

Evaluation of models that participated in the fifth phase of the Coupled Model Intercomparison Project (CMIP5) has shown their representation of dust to be poor, with for example Evan et al. (2014) finding a low bias in simulated dust concentrations over the Sahara and Wu et al. (2020) reporting large inter-model differences in simulated emissions. Evan et al. (2018) suggests that the source

of these biases is not the emission schemes, but instead the misrepresentation of surface winds in dust source areas. Indeed, Roberts et al. (2017) show that ERA-Interim (ERA-I), which shares many commonalities with coarse-resolution coupled models, miss the tail of low-frequency, high wind speed events that drive uplift in the Sahara, with daily correlations between observed and analysed winds higher than three-hourly correlations, indicating that the representation of sub-daily processes (e.g., NLLJ's, CPOs (see chapter 1.3)) needs refining in models. Initial analysis of the dust cycle in the latest phase of the CMIP experiments (CMIP6) has shown that there is still a large spread in simulated dust emissions and concentrations (Zhao et al., 2022), with more work required to determine the cause of this inter-model variability.

1.3) Atmospheric Controls on Dust Emission

1.3.1) Overview

The entrainment and subsequent transport of dust in the atmosphere occurs when the erosivity (capacity of the wind to mobilise sediment) exceeds the erodibility of the underlying surface (Kok et al., 2012; Wiggs, 2011). Erodibility can be quantitatively represented by a threshold wind velocity, and is affected by factors such as particle grain size, surface crusting (Nield et al., 2016), slope angle (Hardisty & Whitehouse, 1988), moisture content (Bauer et al., 2009) and vegetation cover (Wiggs, 2011). For dust-sized sediment, the process of saltation, whereby lifted particles splash new surface particles into the wind field (Kok et al., 2012), is a more common method of sediment transport than direct entrainment, and has been observed in a number of dust source areas (Wiggs et al., 2011).

The meteorological processes responsible for generating surface winds that surpass local emission thresholds operate across a range of spatial scales (Knippertz & Todd, 2012; Kok et al., 2012). As the world's primary dust source region (Prospero et al., 2002; Washington et al., 2003), North Africa has been the focus of much of the work detailing the atmospheric drivers of uplift (Allen et al., 2013; Marsham et al., 2013; Schepanski et al., 2009). Two mesoscale processes have been identified as especially important contributors to Saharan dust emissions; namely, nocturnal low-level jets (NLLJ's) and cold pool outflows. These processes have been estimated to account for 80% of dust-emitting winds in the summertime central Sahara (Marsham et al., 2013), and

are the dominant uplift mechanism in other North African source areas (Marsham et al., 2008; Todd et al., 2008).

The current state of knowledge regarding these emission mechanisms comes largely from work conducted in a Saharan context (Schepanski et al., 2007, 2009; Todd et al., 2008; Washington et al., 2006), however some studies have considered dust emissions from other global source areas. For example, Ge et al. (2016) use reanalysis data to characterise a NLLJ over the Taklimakan Desert, and show that it is the mix-down of momentum from the jet core that produces an enhancement of aerosol optical depth, consistent with work in the Sahara (Allen & Washington, 2014; Knippertz & Todd, 2012). Of the major Southern Hemisphere sources, the Lake Eyre basin in central Australia has received arguably the most attention, with for example Baddock et al. (2015) highlighting the importance of frontal systems in driving emission. Given the inability of models to capture salient features of the Saharan dust climatology (Evan et al., 2014; Roberts et al., 2017), more work is required to investigate dust-emitting mechanisms, and test model fidelity in other geographical regions.

The following sections give a more detailed overview of these two key processes, as well as discussing their relationship with the synoptic circulation.

1.3.2) Mesoscale Processes

1.3.2.1) Nocturnal Low-Level Jets

Background and Definition

Nocturnal low-level jets (NLLJ's) are lower-tropospheric (below 2km) maxima in the vertical profile of horizontal winds that develop during the evening and

early morning hours (Bonner, 1968; Wexler, 1961). They have been observed in a number of geographic regions (Rife et al., 2010; Stensrud, 1996), and have been identified as a key uplift mechanism in several major dust source areas including the Bodélé Depression (Washington & Todd, 2005; Washington et al., 2006), the central Sahara (Allen et al., 2013; Schepanski et al., 2009) and the Taklimakan Desert (Ge et al., 2016). As well as this, NLLJ's play a critical role in the transport of atmospheric water vapour (Acosta & Huber, 2017; Spavins-Hicks et al., 2021), help to initiate convection and thunderstorm activity (Bonner, 1968), and also affect the stability of nocturnal boundary layers through shear-induced turbulence and mixing (Banta et al., 2002; Mahrt, 1999).

Whilst there is no unifying definition of NLLJ's, previous studies have often employed similar methods in an attempt to identify the process in observations and model simulations. These methods utilise characteristic features of the NLLJ, for instance the height of the wind speed maximum (referred to as the jet core), the wind speed in the jet core and the above and below-core wind shear (Banta et al., 2002; Bonner, 1968). The choice of thresholds for the above characteristics can have a profound effect on the classification of NLLJ's; for example, Allen and Washington (2014) found that application of the Fiedler et al. (2013) identification criteria, designed for detecting NLLJ's in ERA-I reanalysis data, would miss 60% of the NLLJ's driving dust emission in their observations from the central Sahara. Similarly, Banta et al. (2002) found Bonner's (1968) criterion of an above-core wind speed decrease (to the next minimum) of $6ms^{-1}$ too severe, and lead them to discount profiles which had been identified as NLLJ's on visual inspection.

Forcing Mechanisms

Several theories have been presented to account for the formation of NLLJ's; these include inertial oscillations, shallow baroclinicity and orographic effects (Stensrud, 1996). The former of these theories was first proposed by Blackadar (1957), and is most frequently invoked to explain the development of NLLJ's in cloud-free, desert environments, where there is a large diurnal cycle in surface energy balance and hence boundary layer turbulence (Heinold et al., 2015).

During the day, strong solar heating produces a large energy surplus at the surface which is almost entirely dissipated through sensible heating of the atmosphere and subsequent turbulent mixing (dissipation through latent heating is negligible due to the lack of soil moisture). This turbulence provides a frictional constraint on airflow and retards wind speeds within the boundary layer (Knippertz & Todd, 2012; Stensrud, 1996). After sunset, strong radiative cooling of the surface stabilises the lower atmosphere, and the reduction in turbulent mixing removes the frictional constraint on overlying air, with the flow at the top of the stable layer effectively becoming 'decoupled' from the surface (Blackadar, 1957; Knippertz & Todd, 2012). The perturbed geotriptic balance produces an acceleration of the flow as the wind vector undergoes an anticlockwise (in the Southern Hemisphere) inertial oscillation (Heinold et al., 2015; Shapiro & Fedorovich, 2010).

More recent work has advanced Blackadar's theory to include the effects of nocturnal turbulence and friction within the boundary layer (Thorpe & Guymer, 1977; Van de Wiel et al., 2010) and orography (Shapiro & Fedorovich, 2009). Indeed, orographic features have been shown to play an important role in observational studies of NLLJ's, either by inducing baroclinic zones through uneven surface heating (Caton-Harrison et al., 2021; Fiedler et al., 2013), or by

channelling and accelerating the NLLJ flow (Todd et al., 2008; Washington & Todd, 2005).

Influence on Dust Emissions

Dust emissions attributed to NLLJ's show a distinct diurnal cycle, with uplift concentrated in the hours between midmorning and midday (Allen et al., 2013; Schepanski et al., 2009). After sunrise, and with the onset of surface heating and the associated increase in turbulent mixing, the stable layer that developed during the nocturnal period is eroded, and momentum is mixed down from the NLLJ core to the surface (Fiedler et al., 2013; Knippertz & Todd, 2012). This produces an acceleration of the surface wind speeds which will drive uplift should they exceed the local emission threshold (Allen & Washington, 2014; Kok et al., 2012). In the Bodélé, where a NLLJ has been shown to be the primary emission mechanism (Washington & Todd, 2005; Todd et al., 2008), up to 85% of uplift events are triggered between 0600 and 0900 (Schepanski et al., 2009), whilst Allen et al. (2013) report a period of increased surface wind speeds between 0600 and 1200 in the central Sahara, coincident with elevated dust loadings.

Subtropical latitudes (which host the majority of major dust source areas (Prospero et al., 2002; Washington et al., 2003)) provide the optimal setting for abrupt NLLJ breakdown, with the timing of maximum core wind speeds coincident with sunrise (Knippertz & Todd, 2012). Latitude is a key determinant of the period of the inertial oscillation, as;

$$P = \frac{2\pi}{f}$$

and;

$$f = 2\Omega \sin \varphi$$

where P is the period of the oscillation, f is the Coriolis parameter, Ω is the angular velocity of earth's rotation and φ is latitude. At a latitude of 20°, this gives an oscillation period of ≈35 hours (Heinold et al., 2015), and so for a decoupled period of 12 hours, around one-third of an oscillation is completed. According to Blackadar's theory, NLLJ flow enhancement peaks between one-quarter and one-half of an oscillation (Fiedler et al., 2013); this results in high core wind speeds towards the end of the decoupled period (sunrise), and hence maximum momentum mixed down to the surface.

Representation in Numerical Models

The representation of NLLJ's in coarse-resolution models and reanalyses is poor, and likely contributes to the observed model biases in surface wind speed distributions and dust emission (Evan et al., 2014; Roberts et al., 2017). Regional climate models perform better however, with the increased horizontal and vertical grid resolution permitting improved simulation of key NLLJ features (Acosta & Huber, 2017; Allen & Washington, 2014; Todd et al., 2008). For instance, Allen and Washington (2014) find that the strength of NLLJ's embedded in the north-easterly Harmattan flow in the central Sahara are underestimated by 4ms^{-1} in ERA-I compared to only 0.2ms^{-1} in the Met Office Africa Limited Area Model, whilst Todd et al. (2008) show that the representation of the Bodélé NLLJ close to topographic features improves with increasing model resolution. It is also important that the temporal output of model and reanalysis data is sufficiently high, given the diurnal cycle of surface

wind speed and dust uplift associated with source areas where NLLJ's are the primary emission mechanism (Fiedler et al., 2013; Schepanski et al., 2009).

1.3.2.2) Cold Pool Outflows

Background

Cold pool outflows are downdrafts from moist convective storms, and can raise substantial amounts of dust when the gusts at the leading edge of the outflow reach the surface (Allen et al., 2013; Knippertz & Todd, 2012). Cold pools are termed 'haboobs' when they result in dust emission (Caton Harrison et al., 2019), and are capable of producing 'moving walls of dust' (Knippertz & Todd, 2012) given that they operate over spatial scales of hundreds of kilometres. They form where evaporation or sublimation of precipitation in the sub-cloud layer adiabatically cools the surrounding air, which then sinks to the surface and spreads out as a density current (Figure 3) (Allen et al., 2013; Caton Harrison et al., 2019). They are important features of North African climate, not only contributing to dust emissions but also ventilating the Saharan heat low and hence influencing the West African Monsoon (WAM) circulation (Garcia-Carreras et al., 2013; Marsham et al., 2013).

Influence on Dust Emissions

Attributing dust activity to cold pools is difficult given the issues associated with identifying plumes underneath convective cloud (Knippertz & Todd, 2012; Marsham et al., 2011), however estimates suggest that up to half of emissions from the summertime Sahara are driven by outflow events (Heinold et al., 2013; Marsham et al., 2013). This prominence is invariably linked to the WAM circulation, with cold pools frequently spawned from mesoscale convective

systems that are embedded in the moist inflow (Marsham et al., 2013; Schepanski et al., 2009). Cold pools are also observed in mountainous regions, where orographic effects enhance moist convection (Caton Harrison et al., 2019; Emmel et al., 2010); dust uplift from the foothills of the Atlas Mountains has for example been linked to outflow events, where density currents are further strengthened by downslope acceleration (Knippertz et al., 2007). Like NLLJ's, uplift associated with cold pool outflows shows a clear diurnal cycle, with emission concentrated in the afternoon and evening hours when moist convective activity is at a maximum (Marsham et al., 2008; Schepanski et al., 2009).

Representation in Numerical Models

Given that moist convection is parameterized in coarse-resolution climate models and reanalyses, cold pools pose a considerable problem, with the parent system and outflow event often poorly represented (Garcia-Carreras et al., 2013; Marsham et al., 2011). Simulations run on high-resolution grids, with the convection parameterization turned off (so-called 'convection-permitting' simulations), have however improved model performance in terms of representing cold pools, and as such have refined the distribution of modelled winds across the Sahara (Heinold et al., 2013; Marsham et al., 2011). For example, runs of the Met Office Unified Model with explicit convection simulated increased emission due to cold pools (computed using an offline dust model) on convectively active days, correcting a low bias in runs with parameterized convection (Heinold et al., 2013). The inability of coarse-resolution models and reanalyses to resolve sub-daily processes such as cold pool outflows likely

contributes to the observed bias in surface winds and dust emission described in section 1.4 (Evan et al., 2014; Roberts et al., 2017).

1.3.3) Synoptic Scale

Dust emission from numerous source areas has been shown to be synoptically modulated, with changes in the broad-scale circulation regulating the efficacy of the mesoscale processes described in the previous sections (Fiedler et al., 2013; Washington & Todd, 2005; Washington et al., 2003). This is especially true for NLLJ's that are generated by frictional decoupling, but are further enhanced by strong horizontal pressure gradients (Knippertz & Todd, 2012). For example, ridging of the Libyan High accounts for variability in dust emissions from the Bodélé Depression by increasing the strength of the north-easterly flow within which NLLJ's are embedded (Todd et al., 2008; Washington & Todd, 2005), whilst the north-westward expansion of the Saharan heat low relative to the Azores High during boreal summer increases the frequency of NLLJ's embedded in the Atlantic inflow over West Africa (Fiedler et al., 2013; Knippertz & Todd, 2012). Dust emissions from North Africa driven by outflow events also show variability on synoptic timescales, with convective cold pools displaying a tendency to form to the east of African easterly waves and upstream of the western Sahara dust hotspot (Knippertz & Todd, 2010).

1.4) Southern African Climate and Dust Source Areas

1.4.1) Climate of Southern Africa

1.4.1.1) Climatic Setting and Variability

Given the large hydrological influence on uplift, dust emissions from southern Africa's major source areas are sensitive to the annual cycle of wetting and drying across the subcontinent (see section 1.4.2) (Bryant, 2003; Mahowald et al., 2003). This section therefore considers the broadscale climatic setting of southern Africa, including the major controls on precipitation and the dominant modes of variability which have the potential to modulate dust emissions on seasonal and interannual timescales.

Southern Africa, broadly defined as the land mass south of the equator, is affected by both tropical and temperate features of the general circulation, whilst the unique topography of the subcontinent and adjacent ocean currents give rise to stark zonal gradients in temperature and precipitation (Reason, 2017). The seasonal cycle in precipitation across southern Africa can be largely accounted for by the meridional shifts in the Intertropical Convergence Zone (ITCZ), which reaches its most southerly latitude (≈18°S) over the east of the subcontinent during austral summer (Nicholson & Grist; 2003; Reason, 2017), and the transition of the Angola Low from a dry to moist convecting system around December (Howard & Washington, 2018; Munday & Washington, 2017). The majority of the subcontinent therefore receives all of its precipitation during a summer wet season (October – March), however its distribution is not zonally uniform, with the observed east-west decrease in mean totals helping to explain the concentration of dust source areas in the arid southwest of the

subcontinent (Vickery et al., 2013; Prospero et al., 2002; Washington et al., 2003). The exceptions to this summer precipitation regime are regions influenced by frontal systems during the winter season owing to the equatorward shift in the temperate westerlies, and so include the far southwest of southern Africa (winter dominant regime) and the south coast (all season regime) (Reason, 2017). The annual cycle in precipitation is bimodal in eastern Tanzania and Kenya, which receive rainfall during April as the ITCZ migrates northwards across the eastern half of the subcontinent (Reason, 2017).

The seasonal migration of the ITCZ is accompanied by the movement of two subtropical high-pressure cells that sit adjacent to southern Africa; the South Atlantic Anticyclone (SAA) and the South Indian Anticyclone (SIA). The difference between their mean summer and winter positions is ≈5° latitude (further equatorward in winter), whilst the seasonal meridional shifts in the position of the SIA (≈24° - 30° further west in winter) are much greater than those of the SAA (≈7° - 13° further west in winter) (Reason, 2017; Tyson & Preston-Whyte, 2000). The meridional position of the SAA also undergoes variability on interannual timescales (Venegas et al., 1997).

The dominant mode of interannual climate variability across southern Africa is the El Nino/Southern Oscillation (ENSO), which is manifest as deviations in regional sea surface temperatures (SSTs) and in the strength of the Indian Ocean Walker circulation (Lindesay, 1986; 1988, Reason, 2017). During the negative phase of the oscillation (El Nino), anomalous subsidence over the subcontinent suppresses tropical convection, and is associated with below average precipitation across southern Africa (Lindesay, 1988; Blamey et al., 2018). The relationship between southern Africa precipitation and ENSO is

modulated to a degree by the strength of the Angola low, which demonstrates variability independently of ENSO (Howard & Washington, 2018; Lyon & Mason, 2007), although for individual El Nino events, this modulating effect can be weak in comparison to the perturbations to Indian Ocean SSTs (Driver et al., 2019; Reason and Jagadheesha 2005). The influence of ENSO on southern Africa precipitation is also modulated by other features of the regional circulation, with for example a strengthening of the Botswana High during the 2015/2016 El Nino event exacerbating the intensity of drought conditions over the subcontinent (Blamey et al., 2018).

Another important mode of variability is the Benguela Nino, which is manifest as deviations in SSTs near the Angola-Benguela Front (ABF) located at ≈15°S - 17°S along the Angolan coast (Reason, 2017). The ABF separates the warm waters of the Angola current and the cool upwelled waters of the BUS (Colberg & Reason, 2006; Reason, 2017), and during Benguela Ninos, is displaced to the south, with positive SST anomalies along the southern Angola/northern Namibia coastline shifting the area of tropical convection further south and west (Florenchie et al., 2004; Rouault, 2012). The SST anomalies are therefore associated with enhanced precipitation over the adjacent land areas from February – April, when SSTs (28°C) peak in the annual cycle, as was the case in 2011 when floods in Namibia and Angola displaced several hundred thousand people (Reason & Smart, 2015; Rouault et al., 2003).

Precipitation across southern Africa is also sensitive to variability in SSTs in the southwest Indian Ocean, given that this is the major source of moisture influx to the subcontinent (Randriamahefasoa and Reason, 2017; Reason, 2017), and so the Indian Ocean Dipole (IOD) and the South Indian Ocean dipole

(SIOD) (Manatsa et al., 2008; Reason, 2002) represent important modes of climate variability. When above average temperatures associated with the SIOD are observed along the east coast of southern Africa, low-level easterly moisture transport into the subcontinent is enhanced, resulting in increased convective uplift and rainfall, a process that was responsible for the extreme wet years recorded in 1974 and 1976 (Reason, 2002; Washington & Preston, 2006). Although moisture flux from the South Atlantic Ocean is less significant than that from the South Indian Ocean (Randriamahefasoa and Reason, 2017; Reason, 2017), a dipole mode also exists in the South Atlantic Ocean (SAOD) (Nnamchi et al., 2011), whilst the South Atlantic midlatitude mode, manifest as variability in the position and strength of the SAA, can produce changes in the position of the ITCZ along with the strength of the Angola Low (Vigaud et al., 2009).

1.4.1.2) Thermal and Topographic Airflows

Regional thermal and topographic airflows have been observed along the east and west coasts of southern Africa, and in some instances, may completely dominate the diurnal and seasonal cycle of boundary layer winds (Goldreich & Tyson, 1988; Lindesay & Tyson, 1990; Tyson, 1967). Topographically induced airflows (plain-mountain/mountain-plains winds) tend to be best developed in the east given the more extreme relief of the KwaZulu Natal coastline and the weaker synoptic winds, whereas sea breezes tend to be best developed in the west, with the strong thermal contrast between the interior plateau and the cool waters of the BUS (Lindesay & Tyson, 1990; Tyson, 1967). Topographic airflows have also been observed at Etosha, where cool air drainage from higher ground to the south during the nocturnal period produces southerlies,

which replace the daytime easterlies/north-easterlies associated with the synoptic circulation (Preston-Whyte et al., 1994). During austral summer, an integration of the onshore anabatic and sea-breeze circulations along the west coast, and the inland propagation of this system through the evening hours has been shown to prevent the easterly movement of tropical lows across the Atlantic coast, and helps to account for the climatological position of the Angola Low (Howard & Washington, 2018).

1.4.1.3) Climate Change

Southern Africa is one of many regions that has experienced the effects of anthropogenic climate change over the last century, with an average warming of ≈1°C since 1901 (Boucher et al., 2013; Reason, 2017). Further change is predicted through the 21st century, with the CMIP6 models simulating increasing temperatures and reductions in precipitation under weak, moderate and strong forcing scenarios (Almazroui et al., 2020), a consequence of the expansion of the tropical Hadley cell and the poleward displacement of the subtropical anticyclones (Reason, 2017). Given the first order control imposed by the broad-scale atmospheric circulation on the distribution of dust source areas (see chapter 1.2.3) (Prospero et al., 2003; Washington et al., 2002), these predictions have important consequences with regards to future changes in dust emissions from southern Africa.

1.4.2) Southern African Dust Source Areas

1.4.2.1) Overview

Previous remote sensing studies have identified a number of dust source areas in southern Africa (Prospero et al., 2002; Vickery et al., 2013; Washington et

al., 2003), and whilst not as prominent as those in the Sahara, annual emissions from the subcontinent (2,300 Mg) make up ≈5% of the global total (Formenti et al., 2019; Ginoux et al., 2012). These source areas are concentrated in the arid southwest of southern Africa (Engelstaedter & Washington, 2007), with two large salt pan complexes, Etosha and Makgadikgadi, producing the highest dust loadings (mean AI values of 1.1 and 0.8 respectively) (Washington et al., 2003). Emissions from the subcontinent peak towards the end of the dry season (August – October) (Prospero et al., 2002; Vickery et al., 2013), although dust activity has also been reported at Etosha during the austral summer months (Bryant, 2003; Ginoux et al., 2012).

The transport of dust (and other aerosol species) across the subcontinent is dominated by the anticyclonic circulation that presides over the interior of southern Africa; initial westward transport towards the Atlantic coast is followed by recirculation south and east so that the plume exits over the Indian Ocean close to Durban (Tyson & Preston-Whyte, 2000; Tyson et al., 1996). Tyson et al. (1996) estimates that annual mass flux to the Atlantic Ocean totals $29x10^6$ tonnes compared to $45x10^6$ tonnes transported to the Indian Ocean, whilst 60 $x10^6$ tonnes doesn't exit the landmass and is deposited over the subcontinent. Easterly waves can result in increased transport towards the west coast, with long-range transport events towards the tropical South Atlantic recorded given suitable synoptic conditions (Swap et al., 1996; Tyson et al., 1996).

These characteristic transport pathways mean that dust from the subcontinent's source areas contribute to the high aerosol loadings observed across southern Africa; for example, Formenti et al. (2019) report a dust event at Etosha in September 2017 where the plume was transported west towards the Atlantic

coast, and an AOD reading of ~0.2 - 0.3 was subsequently recorded in a layer directly above the semipermanent cloud deck. Tesfaye et al. (2015) use a regional climate model to estimate the direct and semi-direct effects of dust over the west and south of South Africa, with the overall net radiative forcing reported to be negative at the surface owing to the dominant short-wave influence of resident dust, along with increases in cloud cover and liquid water path. Dust from the subcontinents source areas also has the potential to fertilise the productive waters of the adjacent BUS given that the sediment is rich in important micronutrients such as iron and nitrogen (Bhattachan et al., 2015; Dansie et al., 2017).

1.4.2.2) The Etosha Pan

The Etosha Pan is a large salt pan in northern Namibia (18.75°S, 16.25°W) covering an area of ≈5000-6000 km^2 (Bryant, 2003) and serves as the basin to a catchment that stretches to the southern Angolan highlands, with inflow through a network of ephemeral channels (locally known as oshanas) (Preston-Whyte et al., 1994). Palaeoclimatic studies show evidence of perennial lake conditions at Etosha, with aridity and subsequent desiccation of the lake during the Pleistocene giving rise to the pan surface observed today (Hipondoka et al., 2006). Present-day wetting of the pan occurs during austral spring and summer, when the Intertropical Convergence Zone (ITCZ) moves south and the Angola Low transitions from a dry to moist convecting system (Howard & Washington, 2018; Munday & Washington, 2017; Reason, 2017). These sporadic inundation events deliver sediment to the pans which is readily deflated upon drying (Bryant, 2003; Mahowald et al., 2003).

Whilst previous work at Etosha has detailed some of the surface controls on uplift from the pan surface (Bryant, 2003; Nield et al., 2016), very little is known about the atmospheric drivers of dust emission, with a dearth of meteorological data for the source area. Murray et al. (2016) use ERA-I reanalysis data to show a statistically significant relationship between emission at Etosha and surface wind gust metrics, however the processes responsible for generating the surface gusts were not investigated. In one of the only observational studies of the meteorology of the pan, Zunckel et al. (1996) identify a persistent NLLJ during September and October, a process that has been shown to drive uplift in other dust source areas. Using tethersonde soundings, the authors found a NLLJ profile on every morning of the observation period at a height of between 50-200m, coincident with the top of an inversion layer (Larom et al., 1997; Zunckel et al., 1996); the influence of the NLLJ on dust uplift from the pan surface was not investigated however.

1.4.2.3) The Makgadikgadi Pans

The Makgadikgadi Pans are a collection of salt pans that form the remnants of paleolake Makgadikgadi, which at one point in the past covered an area 120,000km^2, and was the second largest pluvial lake in Africa (Washington et al., 2003). Today, the Ntwetwe and Sua Pans are the largest complexes, and are fed by the Boteti River to the west, and the Okavango River to the north, with inundation events during austral summer providing sediment for deflation in the dry season (Prospero et al., 2002; Vickery et al., 2013). As is the case with Etosha, more is known about the surface controls on emission (Eckardt et al., 2008; Nield et al., 2015), although dust activity has again been shown to correlate well with high wind speed events (Murray et al., 2016). Meteorological

observations from Sua Pan have been used to test the validity of various dust emission schemes (Haustein et al., 2015), however more work is required to determine the mesoscale processes that drive uplift at Makgadikgadi.

1.4.2.4) Other Source Areas

Numerous dust source areas have been identified along the Namib coastline, including ephemeral river valleys, smaller pans and a mine (Eckardt & Kuring, 2005; Vickery et al., 2013); whilst less intense than Etosha and Makgadikgadi, dust from these sources is richer in nutrients (Dansie et al., 2017), and given their proximity to the productive waters of the Benguela upwelling system, are of potentially great importance to marine biogeochemistry. In terms of dust plume frequency, the ephemeral river valleys are the most emissive source type (Vickery et al., 2013), with the Kuiseb identified as the dustiest river in southern Africa (von Holdt & Eckardt, 2018). Rising in the Khomas Hochland, the Kuiseb runs from east to west towards the coast, with intermittent flow events between January and April delivering sediment that is primed for uplift in the following winter months (Vickery & Eckardt, 2013; von Holdt & Eckardt, 2018). Dust activity is associated with easterly berg winds (Dansie et al., 2017; Vickery et al., 2013) that are enhanced by topographic channelling through the incised river canyon (Vickery & Eckardt, 2013).

Chapter 2: Data and Methods

In this chapter, the data sources utilised in the research conducted as part of the thesis are described, including the in situ meteorological observations, satellite imagery, reanalysis datasets and model output. A summary of the strengths and limitations of each of the data sources is provided, and the methods employed to achieve each of the research objectives outlined in chapter 1 are detailed.

2.1) In Situ Observational Data

2.1.1) Summary of Data Sources

High-resolution in situ meteorological observations are presented for the Etosha Pan, the most prominent source area in southern Africa (see chapter 1.4) (Washington et al., 2003). The data was collected at the Okaukuejo field site (−19.18, 15.92) (Figure 1), situated on the southwestern perimeter of the pan, as part of the CLoud-Aerosol-Radiation Interactions and Forcing: Year 2016 (CLARIFY-2016) ground-based deployment. The CLARIFY-2016 project aimed to improve understanding of the climate of southeast Atlantic region, especially with regards to the processes linking aerosol species and the semipermanent cloud deck over the west coast of southern Africa. Given the predominance of Etosha in terms of generating dust loadings across the subcontinent, the research conducted as part of this thesis will contribute to the broader aims of the CLARIFY-2016 project by quantifying the temporal (diurnal, seasonal, interannual) variability in uplift from the pan, as well as highlighting the meteorological processes operating across a range of scales that drive emissions.

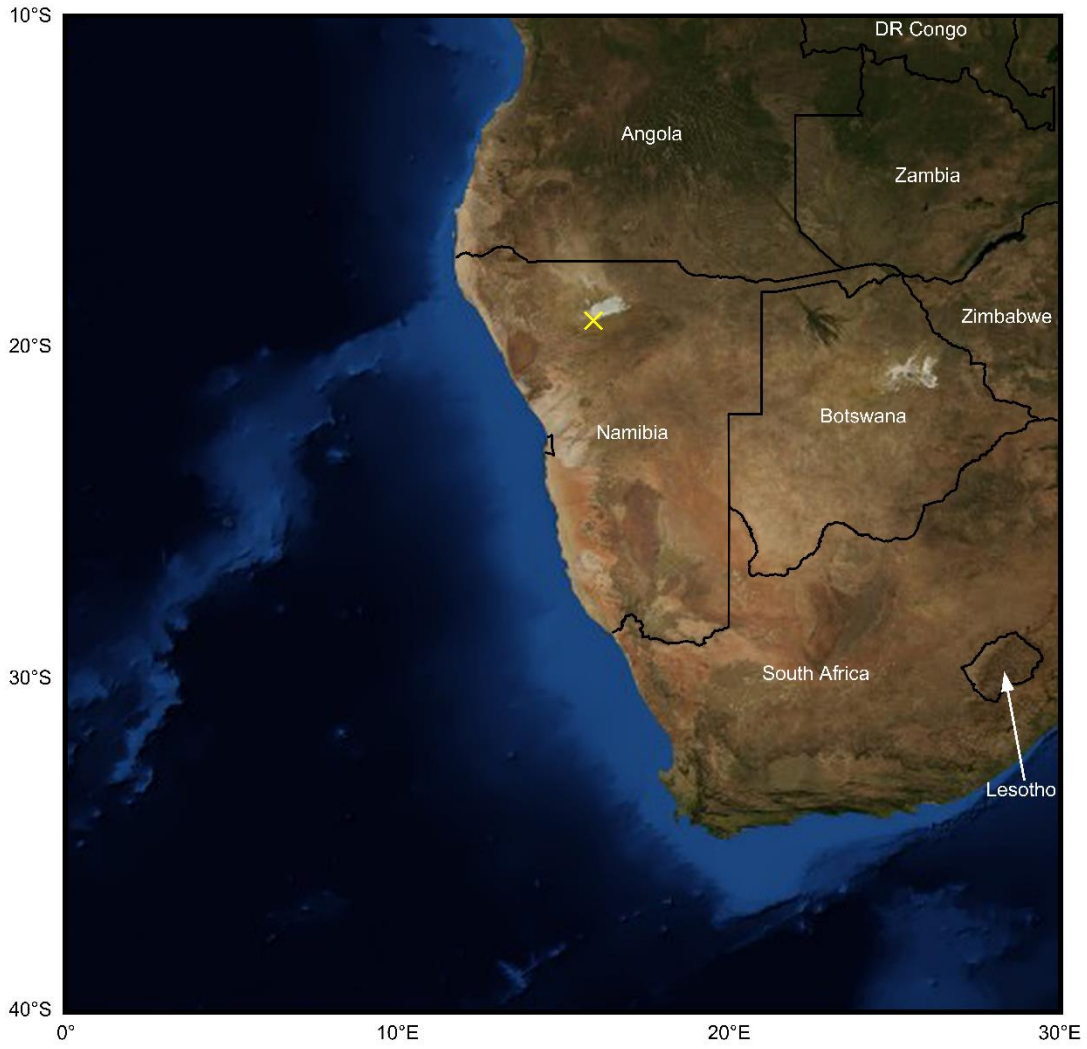


Figure 1 *- NASA Blue Marble image of southern Africa showing the location of the Okaukuejo field site (−19.18, 15.92 (yellow cross)) relative to the Etosha Pan.*

The field site was instrumented with a HALO Photonics Doppler lidar and a Davis automatic weather station (AWS), and data collection took place from 13th August 2016 – 25th September 2016. Coincident with the end of the dry season, August and September are two of the most active months in terms of dust activity at Etosha (Prospero et al., 2002; Vickery et al., 2013; Washington et al., 2003), and so as well as capturing the low-level and boundary layer winds during this season (research objective c), the data collected has enabled a

detailed analysis of the atmospheric processes driving emission from the pan (research objective e), and provide an observational constraint on model fields (research objectives d,f).

The lidar records vertical velocity, aerosol backscatter, wind speed and wind direction whilst the AWS takes wind speed, wind direction, and temperature measurements. The lidar uses the Doppler frequency shift of laser pulses scattered by moving aerosols in the atmosphere to measure the radial velocity (wind speed in the direction of the emitted beam) (Park et al., 2018; Sroga et al., 1980). A velocity-azimuth display (VAD) technique is then applied to retrieve wind components from a radial velocity distribution, obtained from a conical scan at fixed elevation angle (Browning & Wexler, 1968; Park et al., 2018). Aerosol backscatter measurements are made using an inversion technique (Fernald et al., 1972). The vertical resolution of the lidar is 3 m, with the lowest measurement taken at 30 m above the instrument, and the height of the highest measurement variable, depending on attenuation of the beam signal. Attenuation typically occurs at heights between 1 and 2 km, therefore permitting a thorough analysis of the boundary layer at Etosha. The error in the wind speed measurements is <0.2 m s^{-1}. Vertical velocity and aerosol backscatter measurements were taken every minute, whilst VAD scans for wind speed and direction were taken every 15 minutes. The AWS was located 50 m north of the lidar and mounted at a height of 3 m; this height was chosen so that the Davis was stationed above long grasses (z_0 level) found at the field site, below which the windspeed was effectively zero. Readings for wind speed, wind direction and temperature were taken every 10 minutes by the AWS.

2.1.2) Strengths, Limitations and Applications in Other Dust Source Areas

The observations taken by the lidar and AWS represent significant advances on previous attempts to characterise the meteorology of southern Africa's dust source areas, with previous work relying on reanalysis data or nearby weather stations (Bryant et al., 2007; Murray et al., 2016). One of the few studies to have utilised in situ observations was conducted as part of the Southern African Fire-Atmosphere Research Initiative (SAFARI), in which tethersonde soundings provided measurements of wind speed, wind direction and wet/dry bulb temperature through the lower boundary layer at Okaukuejo during September and October 1992 (Larom et al., 1997; Zunckel et al., 1996). A limitation of the instrumentation employed was the inability of the helium balloon to penetrate through the high wind speeds found in the nocturnal boundary layer at Etosha associated with the NLLJ (see chapter 1), and so the depth of the jet core and height of the inversion layer were likely underestimated (Zunckel et al., 1996). The greater range of the lidar beam will resolve the full structure of the NLLJ and inversion layer, whilst the increased frequency of readings (tethersonde soundings were made hourly (Zunckel et al., 1996)) will allow a precise determination of the diurnal cycle in low-level winds. LLJs have been identified in other parts of southern Africa, for example in the Limpopo and Zambezi River valleys, and their role in atmospheric water vapour transport has been analysed (Barimalala et al., 2021; Spavins-Hicks et al., 2021). These studies utilised reanalysis or regional climate model data however, and so the lidar readings presented here are some of the only direct observations of LLJs in southern Africa, and so provide a novel contribution to the regional climate science literature.

The instrumentation deployed at Etosha has been previously utilised in other dust source areas (Allen et al., 2013; Marsham et al., 2013), and has been shown to be appropriate for measuring boundary layer and surface winds in similar dryland environments. For example, lidar data has been used to quantify the characteristics of NLLJ's in the central Sahara, and has also been used in conjunction with other data sources (e.g., satellite imagery) to attribute dust activity to specific atmospheric processes (Allen & Washington, 2014; Allen et al., 2013; Marsham et al., 2013). Allen and Washington (2014) use the aerosol backscatter measurements taken by the lidar to help detect dust events in the central Sahara; given the position of the field site on the southwest perimeter of the Etosha Pan however, the ability of the lidar to detect dust activity is highly sensitive to the direction of transport of the plume. Whilst the predominant direction of transport of dust emitted from the pan is towards the southwest, some plumes are transported directly westward, and so do not track over the field site and would not be detected by the lidar. Indeed, Wiggs et al. (2022) note that the lidar (also deployed at Okaukuejo in 2015) missed 50% of dust events, with those not detected tracking to the north of the lidar, and so in this study, dust detection is achieved using only satellite data.

2.2) Satellite Imagery

2.2.1) Summary of Data Sources

In order to determine the atmospheric controls on dust uplift (research objective e), it is necessary to monitor dust emissions from southern Africa's major source areas across a range of temporal scales. This has been achieved using a number of satellite products which are described below.

An RGB dust composite, derived from data collected by the Spinning Enhanced Visible and Infrared Imager (SEVIRI) instrument on board the Meteosat-10 Second Generation (MSG-10) geostationary satellite has been used to detect dust plumes at the Etosha Pan. The RGB composite uses SEVIRI IR8.7, IR10.8, and IR12.0 channels, with the Brightness Temperature Difference (BTD) between airborne particles and the surface giving dust plumes a magenta hue (Ashpole & Washington, 2012; Schepanski et al., 2007). The imagery is available at a nadir resolution of 4 km and at a frequency of 15 minutes, making it possible to track the movement of individual dust plumes (Schepanski et al., 2007; Vickery et al., 2013). The temporal resolution is a clear strength of the SEVIRI instrument, with Hennen et al. (2019) finding a 50% reduction in the number of dust events detected when using the same data at hourly intervals. Detection of dust is complicated by the presence of water vapour and cloud in the atmosphere, and is also sensitive to the height of the dust plume and the characteristics of the underlying surface (Ashpole & Washington, 2012; Brindley et al., 2012).

Visible imagery from the Moderate Resolution Imaging Spectroradiometer (MODIS) on board NASA's polar orbiting Terra and Aqua satellites is also used

to detect dust plumes at the Etosha Pan. MODIS takes readings in 36 spectral bands from visible to infrared wavelengths, with an orbit period of 100 minutes for the Terra and Aqua platforms. MODIS imagery is available at a nadir resolution of 0.25 km, with Terra and Aqua overpass times of ≈08:30 and ≈13:30 UTC respectively (Vickery et al., 2013).

Aerosol Index (AI) data from the Total Ozone Mapping Spectrometer (TOMS) instrument on board the NASA Nimbus 7 polar-orbiting satellite is also used to monitor dust activity across southern Africa. The TOMS instrument takes measurements in six ultraviolet (UV) wavelengths, with the initial objective to track changes in the Earth's ozone (McPeters et al., 1996), however it has also been used to infer the presence of UV absorbing aerosols (such as dust) in the atmosphere (Prospero et al., 2002; Washington et al., 2003). AI data is given in non-dimensional units with absorbing aerosols returning positive values, and for dust, the magnitude of the AI signal reflects the optical depth of the aerosol (Bryant, 2003; Herman et al., 1997). The frequency of the TOMS output is daily, and it has been projected onto a latitude-longitude grid of resolution 1.0° x 1.25°. The major advantage UV remote sensing has over visible and infrared (IR) wavelengths is its low reflectivity over land surfaces (including Deserts), making for efficient detection of airborne dust particles (Torres et al., 2002).

2.2.2) Strengths, Limitations and Applications in Other Dust Source Areas

Given the relative strengths of each of the satellite products, they are used for different purposes so as to fully address the research objectives outlined in chapter 1. In order to quantify the diurnal cycle of dust emissions at Etosha (research objective b), it is necessary to use satellite data available at sub-daily

timescales (i.e., SEVIRI and MODIS). These datasets also permit the identification of individual dust events that can be traced back to their source area using the 15-minute SEVIRI imagery, hence giving a precise time and location of emission. This multisensor approach is similar to that used by Vickery et al. (2013) to compile a dust source inventory for southern Africa. The RBG dust composite has also been used in isolation to detect dust activity across the Sahara (Caton Harrison et al., 2019) and southern Africa (Murray et al., 2016), with the high temporal resolution of the imagery allowing quantification of the diurnal cycle of emissions, and attribution of uplift to specific atmospheric processes based on the time of source activation (Schepanski et al., 2009).

Characterising the spatial distribution of dust emissions (research objective a), and monitoring variability over longer timescales (e.g., interannual) (research objective b) requires a satellite product that captures broader scale trends in uplift (as opposed to individual events), and so for this purpose, TOMS AI data has been used. TOMS data has been utilised in a number of different studies that have compiled climatologies of global and regional dust source areas (Prospero et al., 2002; Washington et al., 2003), whilst it has also been used to characterise the annual cycle in dust emissions (Engelstaedter & Washington, 2007) as well as interannual to decadal variability in uplift (Bryant et al., 2003). A limitation of the TOMS data is that it does not exclusively detect dust in the atmosphere, but also other UV absorbing aerosols such as smoke from biomass burning, and so some preliminary understanding of likely dust/biomass sources is a prerequisite for interpreting the AI values.

2.3) Reanalysis and Gridded Precipitation Data

2.3.1) Summary of Data Sources

ERA-Interim (ERA-I) and ERA5 reanalysis data from the European Centre for Medium-Range Weather Forecasts (ECMWF) are utilised to address a number of the research objectives outlined in chapter 1. ERA-I covers the period 1979–present, with analysis fields output at six hourly intervals, at a spatial resolution of ≈79 km, and 60 model levels in the vertical, whilst ERA5 data covers the period 1950–present, with analysis fields output at hourly intervals, at a spatial resolution of ≈31 km, and 137 model levels in the vertical. ERA5 benefits from over a decade of research and development since the release of ERA-I, with an increase in horizontal resolution, an improved data assimilation methodology and refined parameterisation schemes (Hersbach et al., 2020). Upgrades to model parameterisations include the adoption of the 'McRad' radiation scheme (Morcrette et al., 2008), improvements to the original precipitation and convective schemes (Bechtold et al., 2014), as well as advances in the treatment of subgrid turbulent mixing and orographic drag effects (Hersbach et al., 2020). ERA5 also features a new land surface scheme (HTESSEL), which, through the adoption of satellite derived vegetation datasets, has improved the representation of variables such as temperature and humidity at the surface (Boussetta et al., 2013; Hersbach et al., 2020). For a detailed discussion of the ERA-I and ERA5 reanalyses, including data assimilation systems, model setup, and an overview of performance, see Dee et al. (2011) and Hersbach et al. (2020) respectively.

Precipitation data from the Climate Hazards Group InfraRed Precipitation with Station data (CHIRPS) version 2.0 is also used in the research. CHIRPS utilises satellite derived rainfall estimates in conjunction with station gauge data to produce a daily gridded precipitation dataset from 1981 to near-present with a 0.05° x 0.05° horizontal resolution (Funk et al., 2015). In southern Africa, gauge data is provided by the Southern African Science Service Centre for Climate Change and Adaptive Land Management (SASSCAL) (Funk et al., 2015). For a full discussion of the CHIRPS dataset, see Funk et al. (2015).

A merged precipitation dataset was preferred over in-situ observations for the analysis of the wetting and drying regime across southern Africa due to the dearth of rain gauge stations across the subcontinent (Funk et al., 2015), as well as the need to monitor precipitation across the entirety of the Etosha and Makgadikgadi catchments, which span areas well to the north and northwest of their respective pan surfaces. The CHIRPS dataset covers the period for which the TOMS AI data was evaluated (1980 – 1992), whilst it has been shown to outperform other satellite rainfall products in its representation of African rainfall (Dinku et al., 2018), and produce the lowest bias in southern African rainfall (1.4%) when compared to the Tropical Applications of Meteorology Using Satellite dataset (TAMSAT) (16%) and the Global Satellite Mapping of Precipitation dataset (GSMaP) (15%) (Macharia et al., 2022).

2.3.2) Application in Thesis Research

ERA5 data is used to characterise some of the meteorological processes operating across southern Africa's source areas and the controls on their variability (research objective c), and also identify which of those processes

contribute to dust emissions (research objective e). Parameters extracted from the ERA5 dataset for analysis include u and v components of wind (10m and model level), temperature (2m, model and pressure level), specific humidity (model level), top net thermal radiation and divergence (model level). Wind speed was calculated as the square root of the sum of the squared u and v components at each grid point ($ws = \sqrt{u^2 + v^2}$), outgoing longwave radiation (OLR) was calculated as the negative of top net thermal radiation, divided by the averaging period (3600s), whilst potential temperature was calculated from the Poisson equation ($\theta = T(P_0/P)^k$), where T is air temperature, P_0 is a reference pressure of 1,000 hPa, P is the atmospheric pressure and k is the Poisson constant. Where atmospheric data is presented for Etosha in the ressearch, the grid point closest to the centre of the pan (-18.75,16.25) is used. This data is also used to evaluate the representation of certain processes in the coupled models.

ERA5 and ERA-I reanalyses are also evaluated against the in situ observational data collected at Etosha (research objectives f and g). This was to assess the influence of resolution and parameterisations on the skill of the reanalyses, given the contrast in the model setups described in chapter in 2.3.1, but more so to evaluate the performance of ERA5, given its use in climate research as a driver of offline dust models (Hennen et al., 2022).

As has been described in chapters 1.2 and 1.4, dust emission is not only a function of surface wind speed, but also surface characteristics, with inundation of source areas suppressing uplift (Bryant, 2003; Mahowald et al., 2003). CHIRPS data was used in the analysis of longer-term variability in dust

emissions (research objective b) to investigate the relative influence of meteorology and hydrology in modulating interannual dust fluctuations.

2.4) Model Data

2.4.1) Summary of Data Sources

Model output from the CMIP6 historical simulations (1850 – 2014) has been extracted from the Centre for Environmental Data Analysis (CEDA) archive, and evaluated against some of the in situ, satellite and reanalysis datasets described above. The historical simulations evolve out of spin-up control runs that have reached equilibrium with pre-industrial greenhouse gas concentrations, and are subsequently forced by natural (e.g., volcanic eruptions) and human (e.g., CO_2 concentration) factors (Eyring et al., 2016).

Model	Variant-ID (if applicable)	Lon/Lat Grid	Levels in <1500m	Reference
HadGEM3-GC31-MM	r1i1p1f3	432x324	14	Ridley et al. (2019)
HadGEM3-GC31-LL	r1i1p1f3	192x144	14	Ridley et al. (2019)
MPI-ESM-1-2-HAM	r1i1p1f1	192x96	6	Neubauer et al. (2019)
MIROC-ES2L	r1i1p1f2	128x64	10	Hajima et al. (2019)
MIROC6	r1i1p1f1	256x128	11	Tatebe et al. (2018)
CanESM5	r1i1p2f1	128x64	12	Swart et al. (2019)
MRI-ESM2-0	r1i1p1f1	320x160	12	Yukimoto et al. (2019)
CNRM-ESM2-1	r1i1p1f2	256x128	15	Seferian et al. (2018)
ERA5	n/a	1440x720	24	Hersbach et al. (2020)
ERA-I	n/a	512x256	12	Dee et al. (2011)

Table 1 – *Summary of the CMIP6 models and reanalysis datasets used in the thesis research.*

2.4.2) Model Selection

Given the research objectives of the thesis (d, f, g) include evaluation of dust emissions in the models, as well as an assessment of their ability to capture

dust-emitting mechanisms (e.g., NLLJ's), the criteria for model selection was as follows:

1) Monthly dust emission data available at the time of writing.
2) 6-hourly u, v, and temperature model level data available at the time of writing.
3) 3-hourly u, v, and temperature surface data available at the time of writing.

The models that met the above criteria are detailed in Table 1, along with the ensemble variant-id, the spatial resolution and the number of model levels for each of the simulations.

2.4.3) Evaluation Against Observations and Reanalysis Data

Variables extracted from the CMIP6 models for analysis include u and v components of wind (surface, model level), temperature (surface, model level), total column soil moisture and geopotential height (850hPa). Wind speed was calculated as the square root of the sum of the squared u and v components at each grid point ($ws = \sqrt{u^2 + v^2}$). For the model levels, which are given as hybrid height coordinates (terrain following in the lower troposphere), data was converted to pressure levels following the equation;

$$p = a*p0 + b*ps$$

where a and b are vertical coordinate formula terms, p0 is a reference pressure level (typically 1000hPa or 1013hPa), and ps is the surface pressure. Pressure level data was then converted to geometric altitude using the hypsometric equation, permitting a comparison with the observational data obtained by the

lidar. Where atmospheric data is presented for Etosha, the grid point closest to the Okaukuejo field site in each of the models is used.

Chapter 3: Atmospheric Controls on Mineral Dust Emission From the Etosha Pan, Namibia: Observations From the CLARIFY-2016 Field Campaign

This chapter details the results of the first research paper presented as part of the thesis. The paper makes use of the high-quality observational data collected at Etosha (as described in Chapter 2) to characterise the low-level circulation and surface winds during the winter season. Used in conjunction with satellite imagery and reanalysis data, the in-situ observations also make it possible to attribute dust activity to specific atmospheric processes operating across a range of spatial scales. Finally, the observations are used to evaluate the representation of key atmospheric processes (with regards to dust emission) in two reanalysis datasets of varying resolution. This paper is the first to try and identify dust-emitting mechanisms at Etosha and is therefore a logical starting place for the thesis research.

Check for updates

JGR Atmospheres

RESEARCH ARTICLE
10.1029/2021JD034746

Atmospheric Controls on Mineral Dust Emission From the Etosha Pan, Namibia: Observations From the CLARIFY-2016 Field Campaign

Matthew Clements[1] and **Richard Washington**[1]

[1]Climate Research Lab, Oxford University Centre for the Environment, Oxford, UK

Key Points:

- Dust emission from one of the Southern Hemisphere's largest sources of dust is driven by the mixing-down of momentum from a low-level jet
- Lidar observations from the winter of 2016 show that a jet is present on >90% of mornings, with core wind speeds peaking between 06:00 and 08:00
- Low-level jet strength is modulated by ridging of the South Atlantic Anticyclone which enhances the pressure gradient across southern Africa

Correspondence to:
M. Clements,
matthew.clements@ouce.ox.ac.uk

Citation:
Clements, M., & Washington, R. (2021). Atmospheric controls on mineral dust emission from the Etosha Pan, Namibia: Observations from the CLARIFY-2016 field campaign. *Journal of Geophysical Research: Atmospheres*, *126*, e2021JD034746. https://doi.org/10.1029/2021JD034746

Received 9 FEB 2021
Accepted 23 JUN 2021

© 2021. The Authors.
This is an open access article under the terms of the Creative Commons Attribution License, which permits use, distribution and reproduction in any medium, provided the original work is properly cited.

Abstract This paper presents meteorological observations from the Etosha Pan, an ephemeral lake bed in northern Namibia that is a major source of mineral dust. The pan was instrumented during August and September 2016 as part of the CLoud-Aerosol-Radiation Interactions and Forcing: Year 2016 (CLARIFY-2016) field campaign, with a Doppler lidar and Davis weather station providing detailed measurements of the boundary layer and surface winds at Etosha. A low-level jet (LLJ) is observed on >90% of mornings during the observation period, with mean core wind speeds of ≈12 m s^{-1} recorded between 06:00 and 08:00. The LLJ is eroded with the onset of surface heating, and momentum is mixed-down from the core, producing peak surface winds between 09:00 and 11:00. This process is responsible for driving dust emission from the pan, with all six dust events recorded during the observation period triggered in the hours following LLJ breakdown. Wind speeds in the core of the LLJ are significantly stronger on dust days compared to non-dust days, hence producing stronger morning surface winds. Dust emission is synoptically modulated, with ridging of the South Atlantic Anticyclone (SAA) enhancing the pressure gradient across southern Africa and driving a stronger easterly flow at Etosha. Key features of the LLJ are represented well in ERA5, however ERA-Interim underestimates core wind speeds by >2 m s^{-1} at 00:00 and by >3 m s^{-1} at 06:00. Both reanalyses struggle to capture the timing of LLJ onset and breakdown, with the LLJ too quick to develop during the evening transition, and too quick to erode through the morning hours.

1. Introduction

Mineral dust is a critical component of the earth system, affecting climate through its interaction with radiation and clouds (Haywood & Boucher, 2000; Mahowald & Kiehl, 2003), and biogeochemical cycles through its ability to fertilize terrestrial and marine ecosystems (Jickells et al., 2005; Koren et al., 2006; Mahowald et al., 2005; Wagener et al., 2008). It is therefore essential that the dust cycle, which begins with the uplift of material from source areas, is accurately incorporated in models, so as to avoid errors in the simulation of current and future climate (Boucher et al., 2013). Dust emission is a function of momentum transfer from the atmosphere to the surface (Kok et al., 2012; Marticorena & Bergametti, 1995; Tegen et al., 2002), however models and reanalyses fail to adequately capture the high wind speed events responsible for uplift (Evan, 2018; Roberts et al., 2017), and so miss key features of the global dust climatology (Evan et al., 2014).

Observations from the Sahara, the world's primary dust source (Prospero et al., 2002; Washington et al., 2003), have demonstrated the efficacy of a number of meteorological processes in generating peak surface winds; these include the mixing-down of momentum from nocturnal low-level jets (LLJ's) (Allen & Washington, 2014; Fiedler et al., 2013; Schepanski et al., 2009; Washington & Todd, 2005), cold pool outflows (Allen et al., 2013; Caton Harrison et al., 2019; Marsham et al., 2008, 2013), and intense dry convection (Jemmett-Smith et al., 2015; Knippertz & Todd, 2012). The representation of these processes in models and reanalyses is poor however (Acosta & Huber, 2017; Allen & Washington, 2014; Marsham et al., 2011) and likely contributes to the observed model biases in surface winds and dust emission (Evan, 2018; Evan et al., 2014; Roberts et al., 2017). Understanding the mechanisms that produce dust-emitting winds, and refining their representation in models and reanalyses is therefore a critical step in improving the simulation of the emission process.

Relatively little attention has been given to dust emission from southern Africa, despite the identification of major source areas across the arid southwest of the subcontinent (Prospero et al., 2002; Vickery

21698996, 2021, 14, Downloaded from https://agupubs.onlinelibrary.wiley.com/doi/10.1029/2021JD034746 by Test, Wiley Online Library on [08/03/2023]. See the Terms and Conditions (https://onlinelibrary.wiley.com/terms-and-conditions) on Wiley Online Library for rules of use; OA articles are governed by the applicable Creative Commons License

21698996, 2021, 14, Downloaded from https://agupubs.onlinelibrary.wiley.com/doi/10.1029/2021JD034746 by Test, Wiley Online Library on [08/03/2023]. See the Terms and Conditions (https://onlinelibrary.wiley.com/terms-and-conditions) on Wiley Online Library for rules of use; OA articles are governed by the applicable Creative Commons License

et al., 2013; Washington et al., 2003), and annual emissions totaling 2,300 Mg (≈5% of the global total) (Formenti et al., 2019; Ginoux et al., 2012). These source areas include the Etosha and Makgadikgadi Pans, ephemeral lake beds located in northern Namibia and northeastern Botswana respectively. Aerosol Index (AI) data from the Total Ozone Mapping Spectrometer (TOMS) shows Etosha (Mean AI >1.1) as one of the most prominent dust source areas in the Southern Hemisphere, with emissions comparable to those from the Lake Eyre Basin in Australia (AI >1.1) and greater than those from the Makgadikgadi (AI >0.8) (Washington et al., 2003). Dust activity at Etosha shows a clear annual cycle (Vickery et al., 2013); periodic inundation events during the wet season (October–April) as well as the presence of surface crusts (Nield et al., 2016) inhibit uplift; however sediment is available for deflation during the dry season (May–September) (Bryant, 2003). Dust emitted from Etosha is generally transported toward the west–southwest (Garstang et al., 1996; Swap et al., 1996), hence contributing to the considerable aerosol loadings observed over the west coast of southern Africa, a problematic region for climate models (Formenti et al., 2019), and providing important micronutrients to the Benguela upwelling system (Bhattachan et al., 2015; Dansie et al., 2017).

Previous remote sensing work has determined the factors controlling the erodibility of the pan surface (Bryant, 2003; Mahowald et al., 2003), however the meteorological drivers of dust emission at Etosha have not been assessed. Murray et al. (2016) use ERA-Interim (ERA-I) data to show the association between surface gustiness and dust activity at Etosha, although the mechanisms responsible for producing strong wind gusts were not established. Zunckel et al. (1996) identified a LLJ in the nocturnal boundary layer at Etosha during the dry season, however its role in generating dust was not investigated. According to the Blackadar (1957) theory of frictional decoupling and inertial oscillations, conditions for LLJ formation are favorable at Etosha during austral winter; the absence of cloud permits considerable radiative losses during the night, with a temperature inversion developing in the lowest ≈500 m of the atmosphere (Larom et al., 1997; Zunckel et al., 1996). Owing to the nocturnal reduction in eddy viscosity, air aloft is freed of frictional effects, and the perturbed geotriptic balance produces an oscillation of the wind vector and acceleration of the flow (Shapiro & Fedorovich, 2010; van de Wiel et al., 2010).

In other source areas, dust emission is tied to the breakdown of the LLJ structure, and the subsequent enhancement of the surface circulation. After sunrise, turbulence within the boundary layer erodes the jet profile, and momentum is mixed-down from the core to the surface, producing a peak in surface winds between midmorning and midday (Allen & Washington, 2014; Knippertz & Todd, 2012; Washington et al., 2006). Emission associated with LLJ's therefore shows a clear diurnal cycle, a finding that has been used to attribute dust activity to specific mechanisms across the Sahara (Allen et al., 2013; Schepanski et al., 2009). As well as the magnitude of the LLJ (quantified using numerous different methods in previous studies, usually involving some measure of maximum core wind speed, with some more advanced metrics also including above and below-core wind shear; Fiedler et al., 2013), its pace of development through the nocturnal period has important consequences with regards to dust emission. LLJ's that are close to their peak around sunrise, when the structure begins to breakdown, are more effective in generating strong surface winds (Heinold et al., 2015).

On a synoptic scale, dust emission from southern African sources is regulated by ridging of the South Atlantic Anticyclone (SAA); the movement of mass associated with west-to-east traveling eddies tightens the pressure gradient across the subcontinent, and enhances the background easterly flow (Washington et al., 2003). Synoptic modulation of dust activity has been observed in other source areas, with for example ridging of the Libyan High accounting for variability in emission from the Bodélé Depression in the Sahara (Washington & Todd, 2005; Washington et al., 2009). The relationship between southern Africa's synoptic circulation and the meteorological processes operating at Etosha has not yet been investigated however, and so the influence of SAA ridging events on emission from the pan is not completely understood.

Given the importance of Etosha as a dust source area, and the requirement to understand and model the atmospheric processes driving emission, this paper aims to address the following key questions: (i) What are the observed characteristics of the boundary layer winds at Etosha during austral winter? (ii) What are the atmospheric controls on dust emission from Etosha? (iii) How well is the observed wind climatology at Etosha represented in ERA-I and ERA5 reanalysis data? The structure of the paper is as follows: Section 2 describes the location of the field site and how it was instrumented, as well as documenting the satellite and reanalysis data used. Results are presented in Sections 3, 4, and 5, with each of the key questions addressed

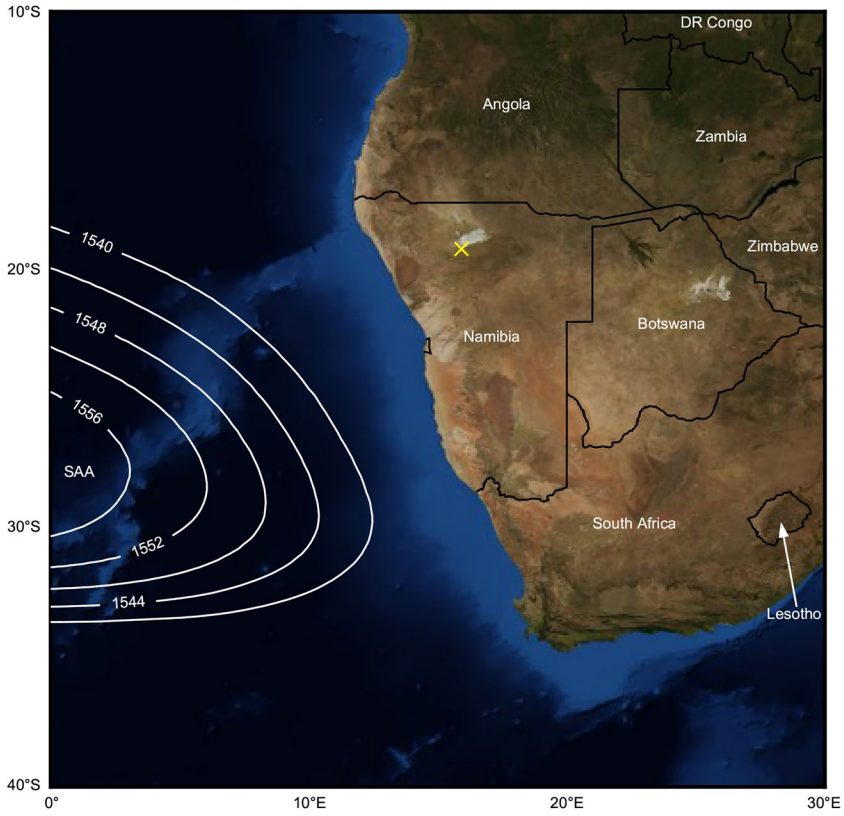


Figure 1. NASA Blue Marble image of southern Africa showing the location of the Okaukuejo field site (−19.18, 15.92 (yellow cross)) relative to the Etosha Pan. The mean position of the SAA during August and September 2016 is shown by the 850 hPa geopotential heights (white contours), with heights given in meters.

in turn. A discussion of the results is presented in Section 6, along with a summary of the papers main findings.

2. Data and Methods

2.1. Physical Setting, Field Site, and Instrumentation

At an average altitude of ≈1,080 m above sea level (asl) (Zunckel et al., 1996) and covering an area of ≈4,800 km^2 (Prospero et al., 2002), the Etosha Pan is an extensive, flat salt pan situated in the semi-arid north of Namibia (Figure 1). It sits in a structural basin, bordered to the south and west by an arc of higher terrain, and to the north and east by an expanse of gently rising terrain (Preston-Whyte et al., 1994; Zunckel et al., 1996). The pan drains an area to the north, stretching to the southern Angolan highlands, and is fed by a network of ephemeral channels (locally known as oshanas), with shallow inundation events occurring during the wet season (Bryant, 2003; Preston-Whyte et al., 1994). Rainfall in the catchment is largely confined to the austral summer months, when the equatorial trough moves south, and the Angola Low shows characteristics of a tropical low, associated with moist convection (Howard & Washington, 2018; Munday & Washington, 2017; Reason, 2017). Interannual variability of rainfall is high, with sea-surface temperatures in the southeast Atlantic (Reason & Smart, 2015) and western Indian Ocean (Landman & Mason, 1999) regulating the flux of moisture into southern Africa. During austral winter, outflow from the northern monsoons produces strong subsidence over southern Africa (Reason, 2017), giving stable, dry conditions at Etosha.

Data collection took place at the Okaukuejo field site (−19.18, 15.92), situated on the southwestern perimeter of the pan (Figure 1) and ≈1,102 m asl (Preston-Whyte et al., 1994). The field site was instrumented with a HALO Photonics Doppler lidar and a Davis weather station, and the observation period ran from August

21698996, 2021, 14, Downloaded from https://agupubs.onlinelibrary.wiley.com/doi/10.1029/2021JD034746 by Test, Wiley Online Library on [08/03/2023]. See the Terms and Conditions (https://onlinelibrary.wiley.com/terms-and-conditions) on Wiley Online Library for rules of use; OA articles are governed by the applicable Creative Commons License

21698996, 2021, 14, Downloaded from https://agupubs.onlinelibrary.wiley.com/doi/10.1029/2021JD034746 by Test, Wiley Online Library on [08/03/2023]. See the Terms and Conditions (https://onlinelibrary.wiley.com/terms-and-conditions) on Wiley Online Library for rules of use; OA articles are governed by the applicable Creative Commons License

13 2016 to September 25 2016. Coinciding with the end of the dry season, August and September are two of the most active months in terms of dust activity at Etosha (Vickery et al., 2013), and so the data collected has enabled a detailed analysis of the processes driving emission from the pan. August and September 2016 featured above average pressure over much of the subtropical South Atlantic and the interior of southern Africa. Mean surface easterly flow was around 2.5 m s^{-1} weaker than usual over northern Namibia. Also consistent with the stronger anticyclonic conditions, mean temperatures were around 0.5°C warmer than normal and subsidence at 500 hPa slightly stronger. Instrumentation of the Okaukuejo field site took place as part of the CLoud-Aerosol-Radiation Interactions and Forcing: Year 2016 (CLARIFY-2016) ground-based deployment. No rainfall was recorded during the observation period.

Vertical velocity, aerosol backscatter, wind speed and wind direction were recorded by the lidar during the observation period. The lidar uses the Doppler frequency shift of laser pulses scattered by moving aerosols in the atmosphere to measure the radial velocity (wind speed in the direction of the emitted beam) (Park et al., 2018; Sroga et al., 1980). A velocity-azimuth display (VAD) technique is then applied to retrieve wind components from a radial velocity distribution, obtained from a conical scan at fixed elevation angle (Browning & Wexler, 1968; Park et al., 2018). Aerosol backscatter measurements are made using an inversion technique (Fernald et al., 1972). The vertical resolution of the lidar is 3 m, with the lowest measurement taken at 30 m above the instrument, and the height of the highest measurement variable, depending on attenuation of the beam signal. Attenuation typically occurred at heights between 1 and 2 km, therefore permitting a thorough analysis of the boundary layer at Etosha. The error in the wind speed measurements is <0.2 m s^{-1}. Vertical velocity and aerosol backscatter measurements were taken every minute, whilst VAD scans for wind speed and direction were taken every 15 min. The lidar collected data from August 14 to September 25, although due to technical difficulties, no data was collected from 11 to September 13.

The Davis weather station was located 50 m north of the lidar and mounted at a height of 3 m and recorded wind speed, wind direction, and temperature measurements every 10 min. This height was chosen so that the Davis was stationed above long grasses (z_0 level) found at the field site, below which the windspeed was effectively zero. From hereinafter, measurements from the Davis are referred to as surface observations. The Davis collected data from August 13 to September 22, although due to technical difficulties, no data was collected from 1 to September 4.

2.2. Satellite Imagery and Dust Detection

In order to address key question 2, it was necessary to monitor dust activity at Etosha during the observation period. This was achieved using a multisensor approach similar to Vickery et al. (2013), with dust plumes identified by examining visible imagery from the Moderate Resolution Imaging Spectroradiometer (MODIS) on board NASA's polar orbiting Terra and Aqua satellites, and an RGB dust composite, derived from data collected by the Spinning Enhanced Visible and Infrared Imager (SEVIRI) instrument on board the Meteosat-10 Second Generation (MSG-10) geostationary satellite. The RGB composite uses SEVIRI IR8.7, IR10.8, and IR12.0 channels, with the Brightness Temperature Difference (BTD) between airborne particles and the surface giving dust plumes a magenta hue (Ashpole & Washington, 2012; Schepanski et al., 2007). MODIS imagery is available at a nadir resolution of 0.25 km, with Terra and Aqua overpass times of ≈08:30 and ≈13:30 UTC respectively (Vickery et al., 2013). SEVIRI imagery is available at a nadir resolution of 4 km and 15 min intervals, making it possible to track the movement of individual dust plumes (Schepanski et al., 2007; Vickery et al., 2013). Plumes were identified by manual inspection of the satellite products, and subsequently traced back to their source area using the SEVIRI dust composite. The high temporal resolution of the SEVIRI data also made it possible to estimate the time of emission for each dust event.

2.3. Reanalysis Data

ERA-I and ERA5 reanalysis data from the European Center for Medium-Range Weather Forecasts (ECMWF) are evaluated in Section 5. For a detailed discussion of the ERA-I and ERA5 reanalyses, including data assimilation systems, model setup, and an overview of performance, see Dee et al. (2011) and Hersbach et al. (2020) respectively. ERA-I covers the period 1979–present, with analysis fields output at six hourly

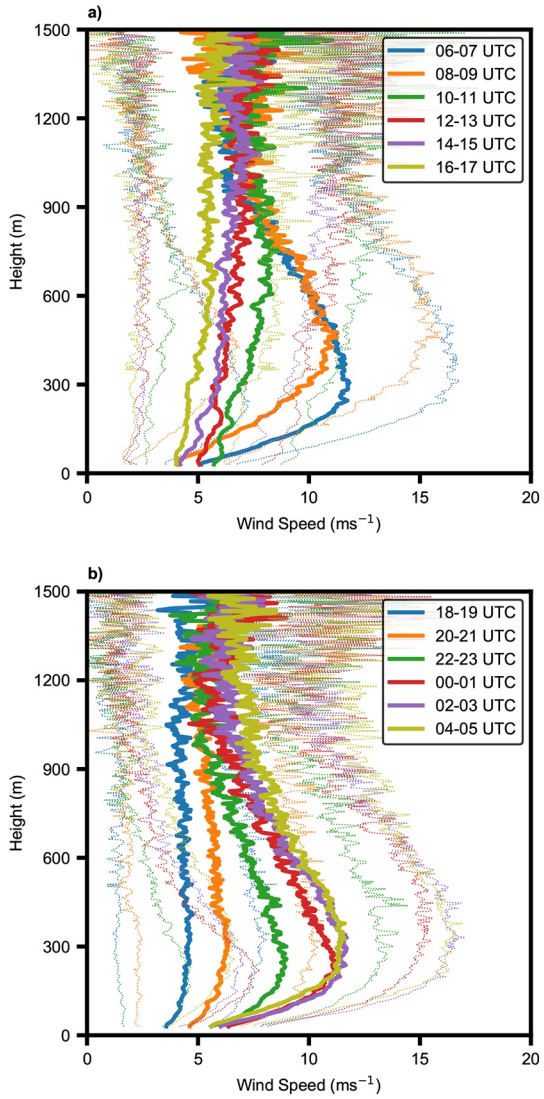


Figure 2. Mean wind speed-height profiles for the 2016 observation period (August 13 to September 25), for (a) daytime and (b) nocturnal hours. Each profile corresponds to the four readings taken by the lidar within the specified hourly interval. One standard deviation above and below the mean are plotted as thinner, dashed lines.

intervals, at a spatial resolution of ≈79 km, and 60 model levels in the vertical. ERA5 covers the period 1950–present, with analysis fields output at hourly intervals, at a spatial resolution of ≈31 km, and 137 model levels in the vertical.

In order to address key question 3, it was necessary to compare ERA-I and ERA5 data with observations from Etosha. This was achieved by taking the closest grid point to the Okaukuejo field site in each reanalysis product; for ERA-I this corresponded to latitude/longitude coordinates of (−19.5, 15.75), and for ERA5 this corresponded to coordinates of (−19.25, 16). Times for which there is data missing from the observations at Etosha are also excluded from calculations performed on ERA-I and ERA5 data, so as to preserve the integrity of any comparison.

3. Diurnal Cycle of Winds at Etosha

The following sections address key question 1: What are the observed characteristics of the boundary layer winds at Etosha during austral winter?

3.1. 2016 Climatology

3.1.1. Wind Structure and Variability

Mean wind speed data from the lidar during the observation period shows a diurnal cycling of winds at Etosha, with a distinct LLJ structure observed in the nocturnal and morning profiles (Figure 2). The jet begins to develop in the hours after sunset (16:44 UTC on August 15) and can first be identified in the 22:00–23:00 profile (Figure 2b) as a core of enhanced wind speeds located ≈300 m above the surface. Vertical shear is generated upon formation of the jet structure, with wind speeds decreasing above and below the height of the core. The jet strengthens through the nocturnal period and peaks in the hours immediately after sunrise (05:16 UTC on August 15), registering mean core wind speeds in excess of 12 m s^{-1} (Figure 2a; Table 1). The height of the core remains fixed between 200 and 400 m during the night, but begins to increase from 07:00 to 08:00 as the jet structure is eroded upwards from the surface, with a corresponding drop in core wind speed. No jet structure is evident by 10:00–11:00, as the profiles begin to show a more uniform increase of wind speed with height.

Whilst a LLJ structure is evident in some of the nocturnal and morning hourly means at Etosha, there is considerable day-to-day variability in the magnitude and shape of the observed wind speed profiles. Figure 3a shows variability in the 05:00–06:00 hourly profile, a time at which the jet is well developed, with a mean core wind speed of 11.61 m s^{-1}. Wind speeds in excess of 20 m s^{-1} were recorded on 15% of LLJ mornings (e.g., 21.94 m s^{-1} on August 25), while there is no obvious jet structure in the hourly profile on three days of the observation period. The height of the core tends to increase as the strength of the jet increases, as is shown by the elevated (lowered) maximum in the profile denoting one standard deviation above (below) the mean in Figure 3b. Variability in jet characteristics is not limited to the 05:00–06:00 profile, with other hourly intervals displaying similar departures from the mean (Figure 2).

3.1.2. Surface Winds

Surface winds at Etosha also follow a clear diurnal cycle, with Davis station data showing a bidaily peak in mean wind speed (Figure 4a). Maximum surface winds are observed between 09:00 and 11:00, as wind speeds increase in the hours following sunrise. Variability in surface winds is also greatest during this

21698996, 2021, 14, Downloaded from https://agupubs.onlinelibrary.wiley.com/doi/10.1029/2021JD034746 by Test, Wiley Online Library on [08/03/2023]. See the Terms and Conditions (https://onlinelibrary.wiley.com/terms-and-conditions) on Wiley Online Library for rules of use; OA articles are governed by the applicable Creative Commons License

Table 1
2016 Observation Period Mean Wind Statistics

Hour (UTC)	Core wind speed (m s^{-1})	Core height (m)	Surface wind speed (m s^{-1})
21:00–22:00	7.85	276	3.19
22:00–23:00	8.99	258	3.46
23:00–00:00	10.24	249	3.33
00:00–01:00	11.20	219	3.13
01:00–02:00	11.44	216	3.11
02:00–03:00	11.70	330	2.86
03:00–04:00	11.68	288	2.61
04:00–05:00	11.61	378	2.31
05:00–06:00	11.61	315	2.35
06:00–07:00	11.82	306	2.91
07:00–08:00	12.33	363	4.27
08:00–09:00	11.27	477	5.24

Note. Core wind speed and height values refer to the mean wind speed-height profiles from the lidar, some of which are shown in Figure 2. Mean surface wind speed values correspond to the six readings taken by the Davis station within the specified hourly interval.

period, with wind speeds in excess of 10 m s^{-1} recorded on individual days of the observation period (e.g., 11.6 m s^{-1} on August 23). After waning through the afternoon and evening, a strengthening of the surface winds is recorded in the hours following sunset, as wind speeds increase from a minimum at 17:00–18:00 to a secondary peak before midnight. Variability in the surface winds is high during the late afternoon-evening period, where the coefficient of variation (σ/μ) approaches one for some hourly intervals.

3.1.3. Surface Heating and Convection

The observed sequence of surface heating, convection and boundary layer development at Etosha follows the diurnal cycle expected of a cloud free, semi-arid environment during winter. With the onset of surface heating after sunrise (Figure 4b), dry convection is triggered within the boundary layer (Figure 5b), resulting in the vertical mixing of aerosols and increased loadings through the lowest ≈1,000 m of the atmosphere (Figure 5c). The standard deviation of vertical velocity is used to illustrate dry convective activity, as eddies of opposite direction tend to negate each other in the composite mean (Figure 5a). Surface temperatures rise to a maximum during the early afternoon (33.5°C at 13:00–14:00) and remain above 30°C until 16:00–17:00. After sunset, and with the reduction in surface heating, dry convection within the boundary layer subsides; this is manifest as a thin layer of the atmosphere where vertical velocity drops to zero at a height of ≈500 m (Figure 5a) which is the likely location of an inversion layer. The reduction in turbulence and vertical mixing is illustrated by the clearer stratification of aerosol loadings during the nocturnal period, with a window of cleaner air (loadings $<3 \times 10^{-7}$ m^{-1} sr^{-1}) emerging at ≈1,000 m (Figure 5c).

3.2. Mechanisms of the LLJ

3.2.1. LLJ Formation

The diurnal cycle of surface heating and associated turbulence plays an important role in the evolution of the LLJ at Etosha, with the timing of jet development and breakdown coinciding with sunset and sunrise respectively. During the evening transition, frictional effects within the boundary layer subside due to the reduction in dry convective activity (Figure 5b), producing an acceleration of the flow in a layer which effectively becomes decoupled from the surface (Figure 5d). This process has been observed in other dryland environments, especially over flat or gently sloping terrain, and is frequently invoked to explain LLJ's that develop through the nocturnal period (Fiedler et al., 2013; Heinold et al., 2015; Washington et al., 2006). The decoupling produces a rotation of the ageostrophic component around the geostrophic component, and the wind vector undergoes an anticlockwise (in the Southern Hemisphere) inertial oscillation. At Etosha, this can be seen as a change in wind direction through the lowest ≈500 m of the atmosphere, from predominantly northeasterlies during the daytime, to southeasterlies–easterlies during the nocturnal period (Figure 5e). Hodographs of u-v wind components (Figure 6) show an abrupt shift at ≈18:00–19:00, with the nocturnal hours tracing an anticlockwise circular rotation of the wind vector until LLJ breakdown; this is especially prominent at 150 and 300 m, heights adjacent to that of the jet core.

3.2.2. LLJ Evolution

After decoupling, the evolution of the LLJ through the nocturnal hours is paced by the inertial oscillation, with the period (P) determined by the Coriolis parameter (f), which in turn is a function of geographic latitude, so that;

$$P = 2\pi / f \quad (1)$$

$$f = 2\Omega \sin \phi \quad (2)$$

21698996, 2021, 14, Downloaded from https://agupubs.onlinelibrary.wiley.com/doi/10.1029/2021JD034746 by Test, Wiley Online Library on [08/03/2023]. See the Terms and Conditions (https://onlinelibrary.wiley.com/terms-and-conditions) on Wiley Online Library for rules of use; OA articles are governed by the applicable Creative Commons License

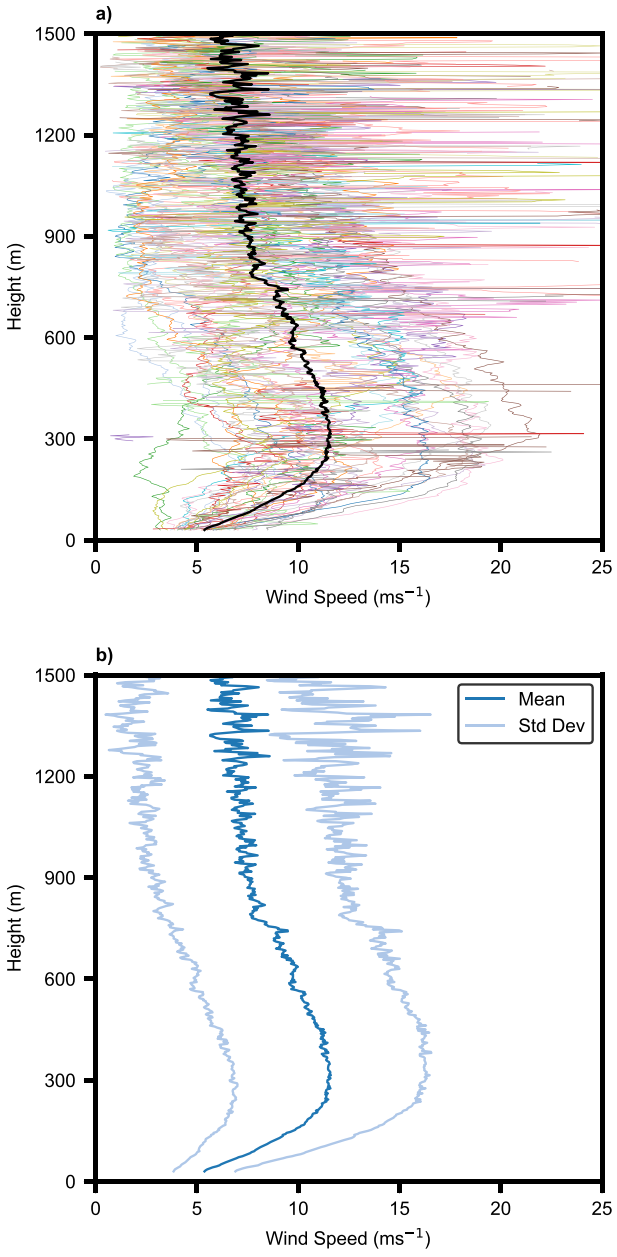


Figure 3. (a) 05:00–06:00 wind speed-height profiles for each day of the 2016 observation period (August 13 to September 25), from the lidar. The mean profile is given by the thicker black line. (b) Mean and standard deviation for the 05:00–06:00 interval.

where Ω is the angular velocity of earth's rotation (7.29×10^{-5} rad s^{-1}) and ϕ is latitude. At Etosha ($\phi = -19.2$), f is equal to -4.8×10^{-5} s^{-1}; this gives an oscillation period of ≈36 h, and so for a decoupled interval of ≈12 h (16:44–05:16 on 15 August), around one-third of the oscillation is completed. According to theory, maximum flow enhancement occurs between one-quarter and one-half of the oscillation period, when the ageostrophic component is aligned with the geostrophic component; this equates to wind speeds peaking between 02:00 (9 h after initial decoupling) and 11:00 (18 h after initial decoupling), although the jet will typically have been eroded by 11:00, given that only one-third of an oscillation is completed. This theory is consistent with the observed LLJ evolution at Etosha, where a strong jet structure is established by 02:00 (core wind speeds 95% of maximum), and core wind speeds peak ≈14 h after initial decoupling (Figure 2; Table 1). Hodographs show the wind vector tracing between one-quarter and one-half the segment of a circle during the nocturnal hours (Figure 6), in accordance with the proportion of the oscillation completed.

3.2.3. LLJ Breakdown

The breakdown of the LLJ structure is driven by surface heating in the hours after sunrise; as surface temperatures rise from 0500-0600 onwards (Figure 4b), dry convection is re-established within the boundary layer (Figure 5b), and the stable vertical stratification associated with the nocturnal period is removed. A frictional constraint on the previously decoupled atmospheric layers is restored, with the jet core eroded upwards until a LLJ structure is no longer discernible in the hourly profiles (Figure 2a). This breakdown is captured well by the hodographs presented in Figure 6, which show a sharp break from the smooth nocturnal rotation at ≈0700–0800, as the wind vector returns to a position representing a diminished northeasterly flow. Critically, the LLJ is at its strongest in the hours around sunrise, resulting in an abrupt breakdown that is illustrated by the considerable drop off between the 08:00–09:00 and 10:00–11:00 profiles (Figure 2a).

3.3. LLJ and Surface Winds

Changes in the surface winds at Etosha are preceded by critical stages in the evolution of the LLJ (i.e., formation and breakdown), suggesting a relationship between upper and lower-level winds. The rise in surface wind speed after sunset (Figure 4a) is likely a result of turbulence induced by the considerable vertical wind shear associated with jet development, with below-core shear values in excess of 15 m s^{-1} being recorded on individual days of the observation period. This would also explain the variable nature of surface winds during the evening transition, a period during which the decoupling process takes place and the jet begins to form. The peak in surface winds during the morning hours is driven by surface heating and the subsequent breakdown of the jet, as can be seen by the ≈1 h lag between increasing surface temperature and wind speed (Figure 4). As the jet profile is eroded upwards, momentum is mixed-down from the core to the surface, generating the observed rise in wind speed from 06:00 to 07:00 onwards (Figure 4a). The increased variability in surface winds during this period is also linked to the LLJ, given the irregularity of jet profiles recorded immediately prior to breakdown (Figure 3a). The strength of the jet, and hence momentum available to mix-down to the surface is in part influenced by changes in the synoptic circulation, and in particular the ridging of the SAA; the relationship between synoptics, LLJ strength and surface winds is discussed further in Section 4.3.2.

21698996, 2021, 14, Downloaded from https://agupubs.onlinelibrary.wiley.com/doi/10.1029/2021JD034746 by Test, Wiley Online Library on [08/03/2023]. See the Terms and Conditions (https://onlinelibrary.wiley.com/terms-and-conditions) on Wiley Online Library for rules of use; OA articles are governed by the applicable Creative Commons License

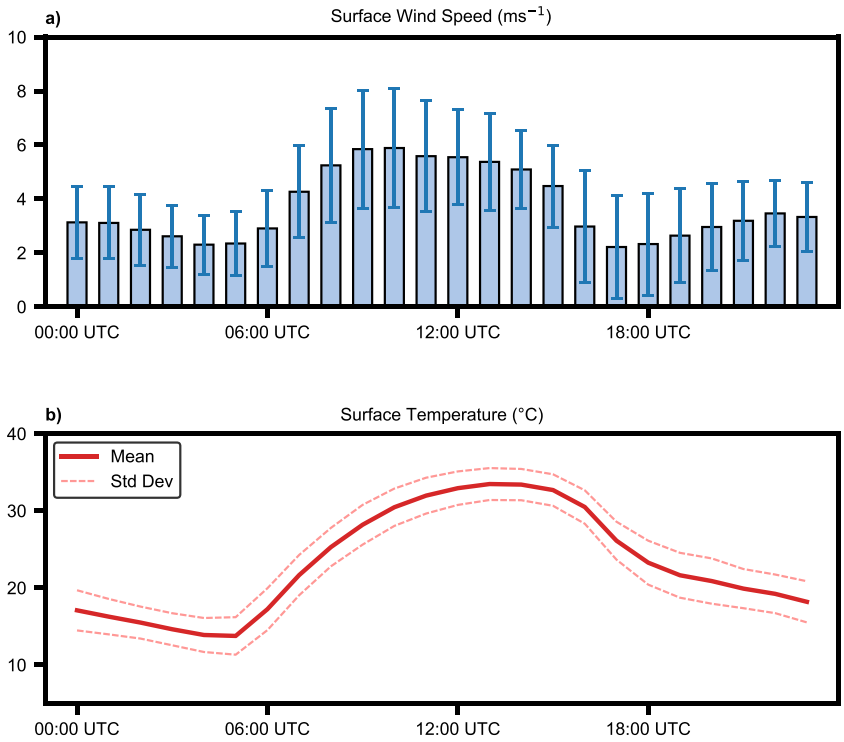


Figure 4. Mean and standard deviation of (a) surface wind speed and (b) surface temperature for the 2016 observation period (August 13 to September 25). Data is plotted hourly, with each value corresponding to the six readings taken by the Davis station within the given interval. 12:00 therefore represents the average of the readings taken between 12:00 and 13:00.

4. Dust Emission at Etosha

The following sections address key question 2: What are the atmospheric controls on dust emission from Etosha?

4.1. Observed Dust Events

4.1.1. Dust Emission and Transport

From the August 13 to the September 25, Etosha was the source of six dust plumes that were identified and tracked on satellite imagery (details of the method used to detect dust activity at Etosha can be found in Section 2.2). This number is consistent with the frequency of emission outlined by Vickery et al. (2013), who identified seven plumes originating from Etosha during August and September, averaged across a four year period. Dust activity was triggered exclusively in the morning hours, with the time of first emission for all six plumes falling between 09:00 and 11:00 (Table 2). Following emission, the six plumes were transported toward the west - southwest, characteristic of the predominant northeasterly-easterly flow at Etosha. An example of this can be seen in Figure 7, which shows the dust event on the 25 August; dust (magenta in color) becomes visible after emission in the 09:00 imagery, with the plume transported toward the south-west through the subsequent hours.

4.1.2. Dust and Non-Dust Classifications

Mornings on which plumes were identified at Etosha are shown in Table 2, along with a non-dust classification consisting of mornings on which no emission took place. Non-dust days are characterized by the absence of a plume in the satellite imagery; a randomised sample of six of these days were selected so as to ensure a similar number of observations in the dust and non-dust classifications. Dust and non-dust composites have been constructed from these two classifications and are referenced in the following sections.

21698996, 2021, 14, Downloaded from https://agupubs.onlinelibrary.wiley.com/doi/10.1029/2021JD034746 by Test, Wiley Online Library on [08/03/2023]. See the Terms and Conditions (https://onlinelibrary.wiley.com/terms-and-conditions) on Wiley Online Library for rules of use; OA articles are governed by the applicable Creative Commons License

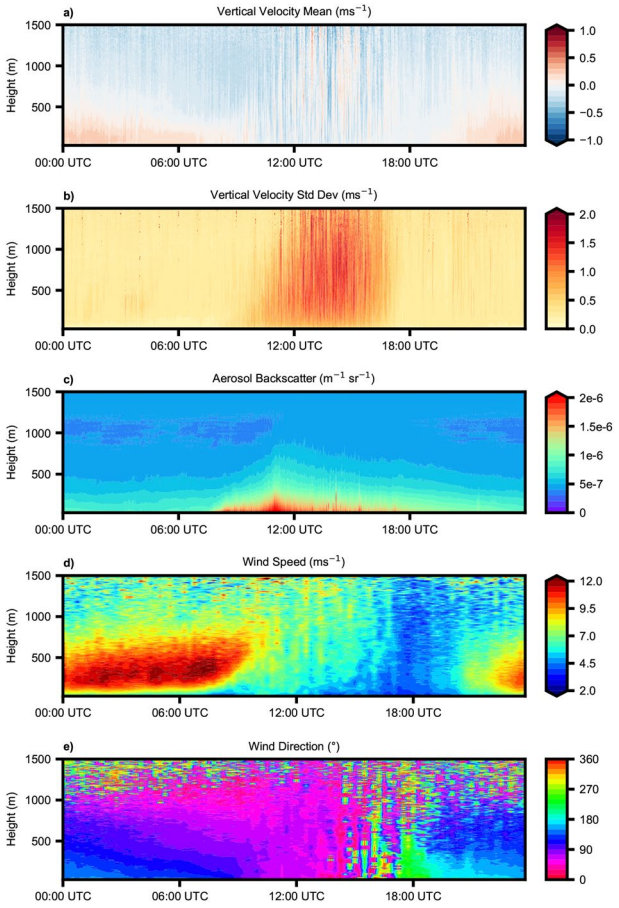


Figure 5. Mean time-height cross sections of (a) vertical velocity, (c) aerosol backscatter, (d) wind speed, and (e) wind direction for the 2016 observation period (August 13 to September 25). (b) Standard deviation time-height cross section of vertical velocity for the 2016 observation period. All measurements are from the lidar.

Data from 12:00 to 00:00 (i.e., afternoon and evening hours) are taken from the day prior to emission, whereas data from 00:00 to 12:00 (i.e., morning hours) are taken from the day of the observed emission. For example, for the dust event on the August 23, data from 12:00 to 00:00 on the August 22 (day prior to emission) and 00:00–12:00 on the August 23 (day of emission) are used to construct the dust composite. This is to capture the full evolution of the circulations observed on mornings when dust emission occurred at Etosha.

4.2. Surface Winds on Dust and Non-Dust Days

Dust and non-dust composites of surface wind speed and temperature from Davis station data are shown in Figure 8. Surface temperature follows the diurnal cycle described in Section 3.1 on both dust and non-dust days (Figure 8b), with values falling to a minimum at 05:00–06:00, and then increasing with the onset of surface heating after sunrise. Wind speed also follows the diurnal cycle described in Section 3.1 (Figure 8a), however there are considerable differences in the strength of the surface winds on dust and non-dust days. Through the nocturnal period, a strengthening of the surface winds is recorded in both composites, although wind speeds on non-dust days are in excess of those on dust days. This is reversed as soon as wind speeds begin to increase after sunrise, with the morning peak in surface winds greater on dust days. Unpaired, one-tailed *t*-tests were conducted on the data displayed in Figure 8a for the hours after 06:00–07:00 (Table 3); the difference between dust and non-dust surface wind speed becomes significant ($\alpha = 0.05$) at 07:00–08:00, and remains significant ($\alpha = 0.05$, $\alpha = 0.01$) until 11:00–12:00. This is consistent with the timing of dust emission at Etosha, with peak surface wind speeds on dust days (10:00–11:00) coinciding with the observed window of dust activation (09:00–11:00) outlined in Section 4.1.

4.3. Influences on Dust Emission at Etosha

Given that dust emission is primarily driven by the surface circulation, it is necessary to consider what influences variability in surface wind speed at Etosha. In the following sections, two of the main influences on surface winds are analyzed, namely, day-to-day variability in the LLJ and changes in the synoptic situation.

4.3.1. Day-to-Day Variability in the LLJ

4.3.1.1. LLJ on Dust and Non-Dust Days

Dust and non-dust composites of hourly wind speed are shown in Figure 9, with clear differences evident between the two sets of profiles. Unpaired, one-tailed *t*-tests were conducted on the dust and non-dust core wind speeds to assess the significance of the difference in the composites (Table 4). The core of each profile was identified as the maximum wind speed beneath 600 m. The LLJ is stronger on dust days, with core wind speeds in excess of 15 m s^{-1} recorded between 22:00 and 23:00 and the time of jet breakdown (Figure 9a); on non-dust days, core wind speeds only surpass 10 m s^{-1} for one hourly interval (Table 4). Significant differences were found between the dust and non-dust core wind speeds at $\alpha = 0.05$ and $\alpha = 0.01$ for all of the hourly profiles between 21:00 to 22:00 and 08:00–09:00.

Enhanced wind speeds persist through a greater depth of the atmosphere on dust days, with for example wind speeds in excess of 15 m s^{-1} recorded in a layer ≈300 m deep in the 02:00–03:00 profile (Figure 9a). The combined effect of higher wind speeds and a deeper core produces a more energetic LLJ structure on dust days, increasing momentum available to mix-down to the surface as the jet dissipates. The breakdown of the

21698996, 2021, 14, Downloaded from https://agupubs.onlinelibrary.wiley.com/doi/10.1029/2021JD034746 by Test, Wiley Online Library on [08/03/2023]. See the Terms and Conditions (https://onlinelibrary.wiley.com/terms-and-conditions) on Wiley Online Library for rules of use; OA articles are governed by the applicable Creative Commons License

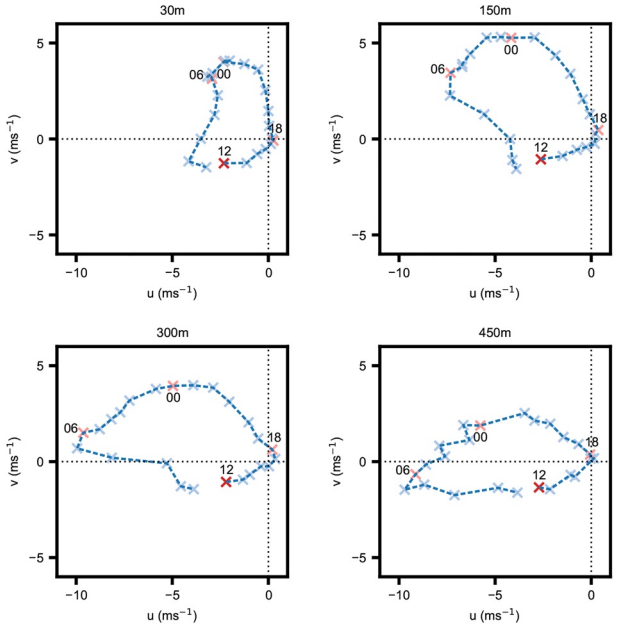


Figure 6. Hodographs of mean u-v wind components for the 2016 observation period (August 13 to September 25), from the lidar. Each cross represents an hourly average wind vector, corresponding to the four readings taken by the lidar in the given interval, beginning with 12:00–13:00 UTC (dark red). The crosses representing wind vectors at 18:00–19:00, 00:00–01:00, and 06:00–07:00 are given in light red.

Table 2
Dust and Non-Dust Classifications

Date	Time of dust activation (UTC)	Direction of dust transport
	Dust	
August 23	09:00	WSW
August 24	10:00	SW
August 25	09:00	SW
August 27	10:00	SW
August 28	09:15	WSW
September 18	09:30	SW
	Non-Dust	
August 16	N/A	N/A
August 20	N/A	N/A
August 31	N/A	N/A
September 6	N/A	N/A
September 17	N/A	N/A
September 22	N/A	N/A

Note. Time of dust activation and direction of transport were estimated from RGB composite imagery (see Section 2.2 for more details). Time of dust activation refers to the time of first dust emission. The direction refers to the compass point in which the plume was transported. The non-dust classification is constructed from days on which no emission took place (see Section 4.1.2 for more details).

LLJ is also more abrupt on dust days; the jet is eroded quickly between 06:00–07:00 and 08:00–09:00 (Figure 9a), whereas the difference between these two profiles is not as substantial on non-dust days (Figure 9b).

Dust, non-dust and difference composites of vertical velocity, aerosol backscatter and wind speed are displayed in Figure 10. The significant difference in the magnitude of the jet between dust and non-dust days is captured well by the wind speed cross section (Figure 10l), whilst the spike in aerosol loadings from ≈08:00 onwards (Figure 10i) is consistent with the timing of emission detected on satellite imagery and the observed peak in surface winds. The non-dust composite shows increased vertical movement through the nocturnal period (Figures 10e and 10f), with a weaker vertical stratification (Figure 10h) compared to the dust composite (Figure 10g). This helps to explain the weaker LLJ on non-dust days, as turbulence increases friction within the boundary layer and potentially disrupts the decoupling process integral to jet formation and development.

4.3.1.2. LLJ Detection and Strength Index

In order to further investigate jet variability and its effect on surface winds at Etosha, a LLJ detection scheme has been developed, along with an index of LLJ strength. The detection scheme is used to identify individual days of the observation period on which a LLJ is present, based on the 05:00–06:00 profiles displayed in Figure 3. This hourly interval was chosen as the jet is well developed in the mean (Table 1), but close to breakdown, a critical process with regards to dust emission. 05:00–06:00 was favored over 06:00–08:00 (the interval of peak core wind speeds (Table 1), as the latter interval occurs after sunrise, and on some days the jet has already started to breakdown. LLJ's were detected according to the following criteria:

1. The jet core was identified as the maximum wind speed below 600 m (so as to avoid elevated wind speed maxima not associated with LLJ development). Profiles with core wind speeds <8 m s^{-1} were not considered as LLJ's.
2. Below-core wind shear was calculated by subtracting the lowest wind speed measurement (typically taken at 30 m) from the core wind speed. This value was then standardised to give wind shear/30 m, permitting comparisons between profiles with cores at different heights. Profiles with negative below-core wind shear (i.e., wind speeds decrease from the surface up) were not considered as LLJ's.
3. Above-core wind shear was calculated by subtracting the core wind speed from the wind speed measurement 300 m above the height of the core. Profiles with positive above-core wind shear (i.e., wind speeds increase above the jet core) were not considered as LLJ's.

The LLJ index is similar to that employed by Allen and Washington (2014), and is used to quantify the strength of individual jet events. The index was calculated by summing wind speed above a specified threshold through the lowest kilometer of the atmosphere for the hourly profiles between 00:00 and 09:00, so that;

$$LLJi = \sum_{h=1}^{n} \int_{z1}^{z2} f_h(z)dz \quad (3)$$

21698996, 2021, 14, Downloaded from https://agupubs.onlinelibrary.wiley.com/doi/10.1029/2021JD034746 by Test, Wiley Online Library on [08/03/2023]. See the Terms and Conditions (https://onlinelibrary.wiley.com/terms-and-conditions) on Wiley Online Library for rules of use; OA articles are governed by the applicable Creative Commons License

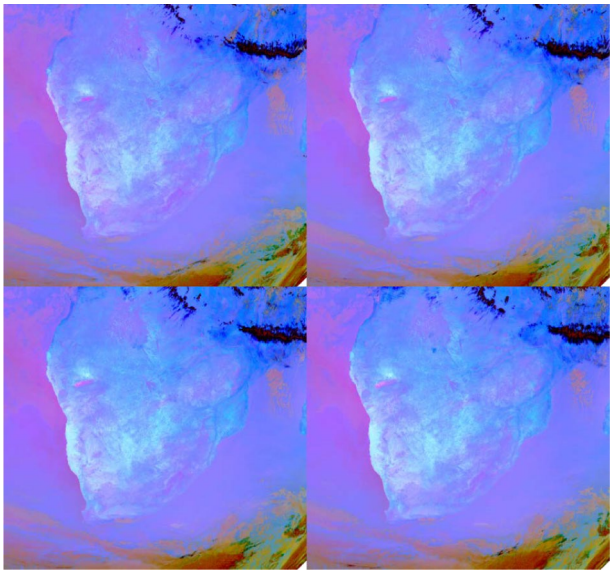


Figure 7. RGB composite imagery for 09:00 (top left), 10:00 (top right), 11:00 (bottom left), and 12:00 (bottom right) on August 25. A dust plume (magenta in color) can be seen traveling away from Etosha toward the southwest. The dust composites are derived from MSG-SEVIRI IR channel data.

where n equals 9 (number of hourly profiles between 00:00 and 09:00), $z1$ equals 30 m, $z2$ equals 999 m, and $f_h(z)$ is the wind speed profile above 8 m s^{-1} (this threshold was chosen to correspond with the LLJ detection scheme).

05:00–06:00 hourly profile statistics are displayed in Table 5, with each day of the observation period grouped according to the LLJ detection scheme and observed dust emission at Etosha. Within each group, individual days are ranked by their index of LLJ strength. LLJ's were identified on all but three days of the observation period, emphasizing that the jet is a pervasive feature of the nocturnal boundary layer at Etosha during winter. Of the six LLJ's resulting in dust emission, five were ranked in the top 10 strongest jets based on their LLJ index, and all six registered 05:00–06:00 core wind speeds in excess of 17 m s^{-1}. There were, however, strong jets that did not coincide with dust activity, with for example no plume observed on the August 30, despite the third strongest jet being recorded on that day.

The process linking the LLJ with dust emission is the mixing-down of momentum from the jet core, with a subsequent intensification of the morning surface winds, which are ultimately responsible for driving uplift at Etosha. The relationship between LLJ strength and surface wind speed is examined in Figure 11, where the LLJ index is plotted against average 09:00–11:00 wind speed for individual days of the observation period. The 09:00–11:00 interval was chosen as this is when surface winds peak in the mean at Etosha (Figure 4a). In general, there is a positive correlation between LLJ strength and morning surface winds (Figure 11b),

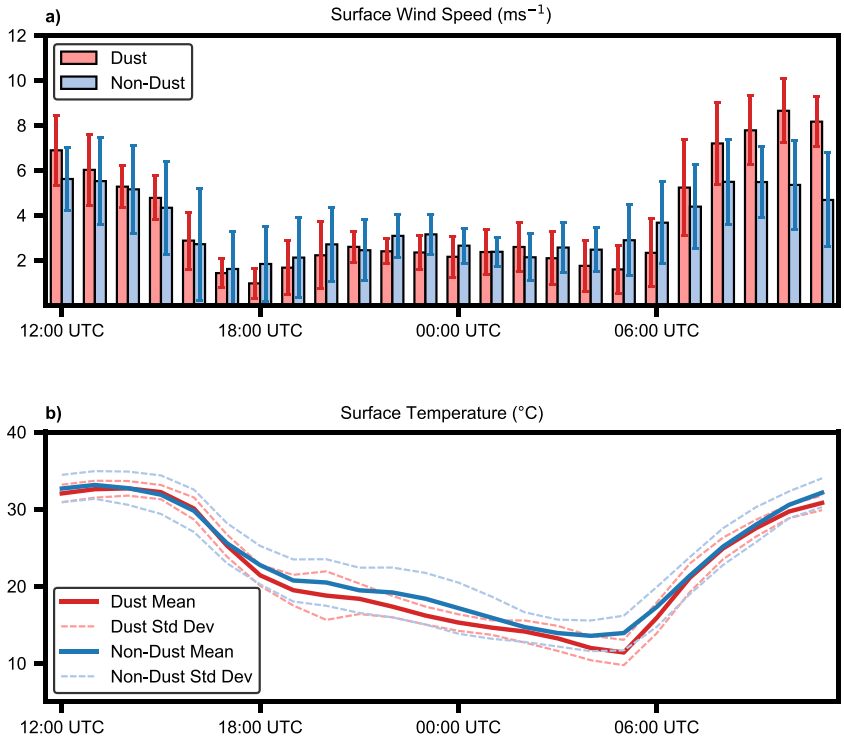


Figure 8. Mean and standard deviation of (a) surface wind speed and (b) surface temperature for dust and non-dust days from the Davis station. Data is plotted hourly, with each value corresponding to the six readings taken by the Davis station within the given interval. 12:00 therefore represents the average of the readings taken between 12:00 and 13:00.

21698996, 2021, 14, Downloaded from https://agupubs.onlinelibrary.wiley.com/doi/10.1029/2021JD034746 by Test, Wiley Online Library on [08/03/2023]. See the Terms and Conditions (https://onlinelibrary.wiley.com/terms-and-conditions) on Wiley Online Library for rules of use; OA articles are governed by the applicable Creative Commons License

Table 3
Results of T-Test Calculations Performed on Dust and Non-Dust Hourly Mean Surface Wind Speeds

Time (UTC)	WS (m s^{-1}) dust	WS (m s^{-1}) non-dust	*t*-stat	*p*-value	*t*-crit ($\alpha = 0.05$)	*t*-crit ($\alpha = 0.01$)
06:00–07:00	2.33	3.67	−3.41	5.56×10^{-4}	1.67	2.38
07:00–08:00	5.23	4.38	1.80	3.80×10^{-2}	1.67	2.38
08:00–09:00	7.19	5.49	3.89	1.13×10^{-4}	1.67	2.38
09:00–10:00	7.78	5.48	6.29	1.18×10^{-8}	1.67	2.38
10:00–11:00	8.65	5.35	8.13	1.06×10^{-11}	1.67	2.39
11:00–12:00	8.16	4.68	8.31	7.32×10^{-11}	1.68	2.41

Note. Results are for unpaired, one-tailed *t*-tests assuming unequal variances. The hours selected are for the period after sunrise during which surface wind speeds increase at Etosha (see Figure 8). Mean surface wind speeds were calculated from Davis station data.

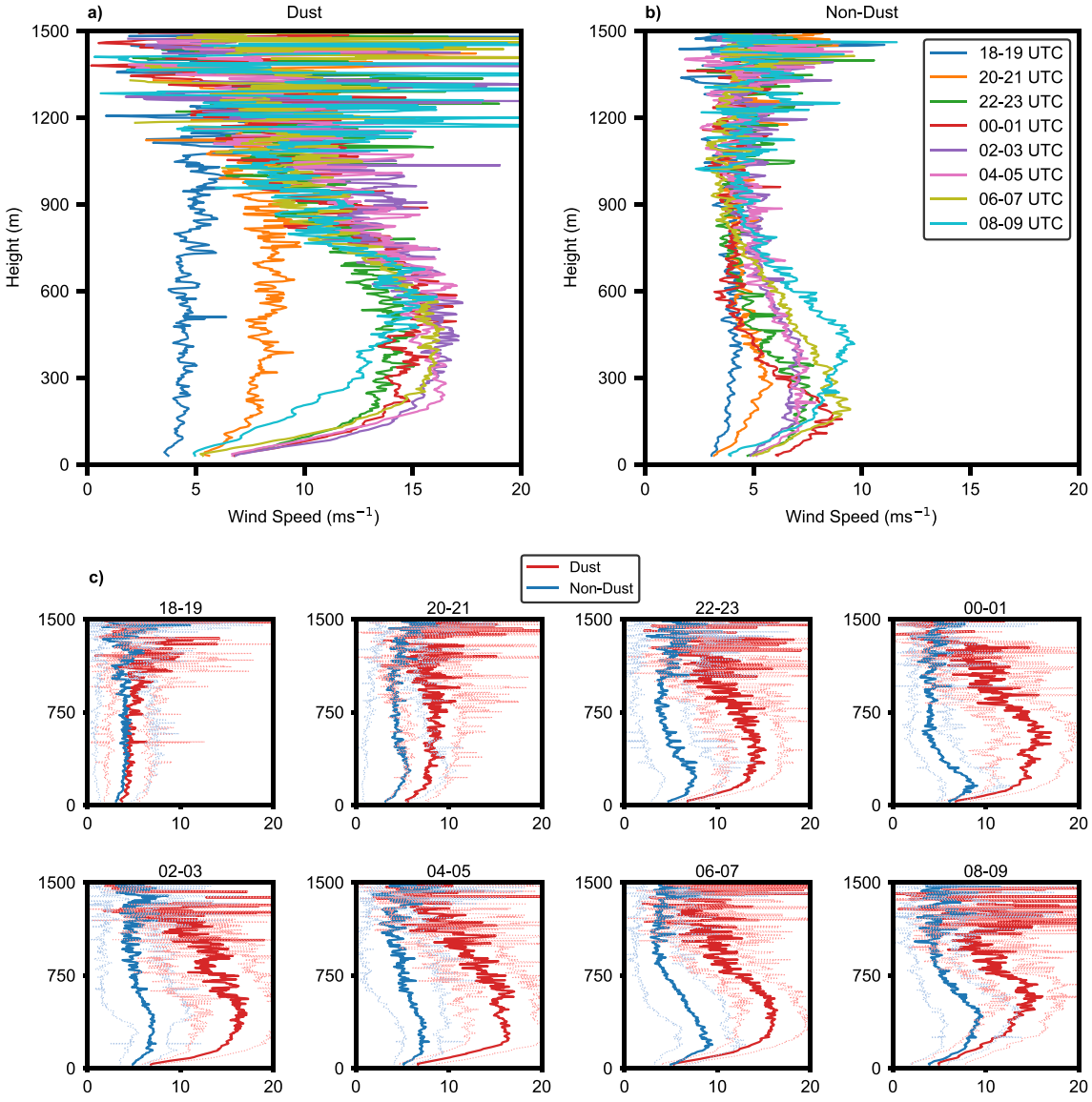


Figure 9. Mean wind speed-height profiles for (a) dust and (b) non-dust days for selected hours, from the lidar. (c) Dust (red) and non-dust (blue) profiles for individual hourly intervals, with one standard deviation above and below the mean plotted as thinner, dashed lines.

21698996, 2021, 14, Downloaded from https://agupubs.onlinelibrary.wiley.com/doi/10.1029/2021JD034746 by Test, Wiley Online Library on [08/03/2023]. See the Terms and Conditions (https://onlinelibrary.wiley.com/terms-and-conditions) on Wiley Online Library for rules of use; OA articles are governed by the applicable Creative Commons License

21698996, 2021, 14, Downloaded from https://agupubs.onlinelibrary.wiley.com/doi/10.1029/2021JD034746 by Test, Wiley Online Library on [08/03/2023]. See the Terms and Conditions (https://onlinelibrary.wiley.com/terms-and-conditions) on Wiley Online Library for rules of use; OA articles are governed by the applicable Creative Commons License

Table 4
Results of T-Test Calculations Performed on Dust and Non-Dust Hourly Mean LLJ Core Wind Speeds

Time (UTC)	WS (m s^{-1}) dust	WS (m s^{-1}) non-dust	*t*-stat	*p*-value	*t*-crit ($\alpha = 0.05$)	*t*-crit ($\alpha = 0.01$)
21:00–22:00	12.44	7.47	3.44	6.73×10^{-4}	1.68	2.42
22:00–23:00	15.20	7.77	4.51	3.47×10^{-5}	1.69	2.44
23:00–00:00	15.28	7.91	7.14	8.05×10^{-9}	1.69	2.43
00:00–01:00	17.02	9.08	6.40	1.30×10^{-7}	1.69	2.44
01:00–02:00	16.79	9.24	4.83	1.88×10^{-5}	1.70	2.46
02:00–03:00	17.29	7.35	7.90	7.62×10^{-10}	1.69	2.43
03:00–04:00	17.98	6.75	12.29	1.49×10^{-14}	1.69	2.44
04:00–05:00	16.98	7.87	8.45	2.84×10^{-10}	1.69	2.44
05:00–06:00	16.26	7.67	8.07	2.65×10^{-10}	1.68	2.42
06:00–07:00	16.44	9.46	6.58	2.87×10^{-8}	1.68	2.42
07:00–08:00	17.94	10.55	7.00	3.08×10^{-8}	1.69	2.45
08:00–09:00	16.11	9.65	4.43	5.50×10^{-5}	1.70	2.45

Note. Results are for unpaired, one-tailed *t*-tests assuming unequal variances. The hours selected are for the period during which the LLJ is well developed at Etosha (see Figure 9). Tests were conducted on the core wind speeds of the dust and non-dust profiles, identified as the maximum wind speed beneath 600m.

with wind speed increasing as the LLJ index increases. This is evidenced by the period 23 August to 30 August, when the strongest morning surface winds of the observation period coincided with the most active phase of the LLJ, and five dust events were observed (Figure 11a). There were however a number of mornings on which relatively weak jets produced strong surface winds (Figure 11b), indicating that variability in the LLJ is not the only influence on surface wind speed.

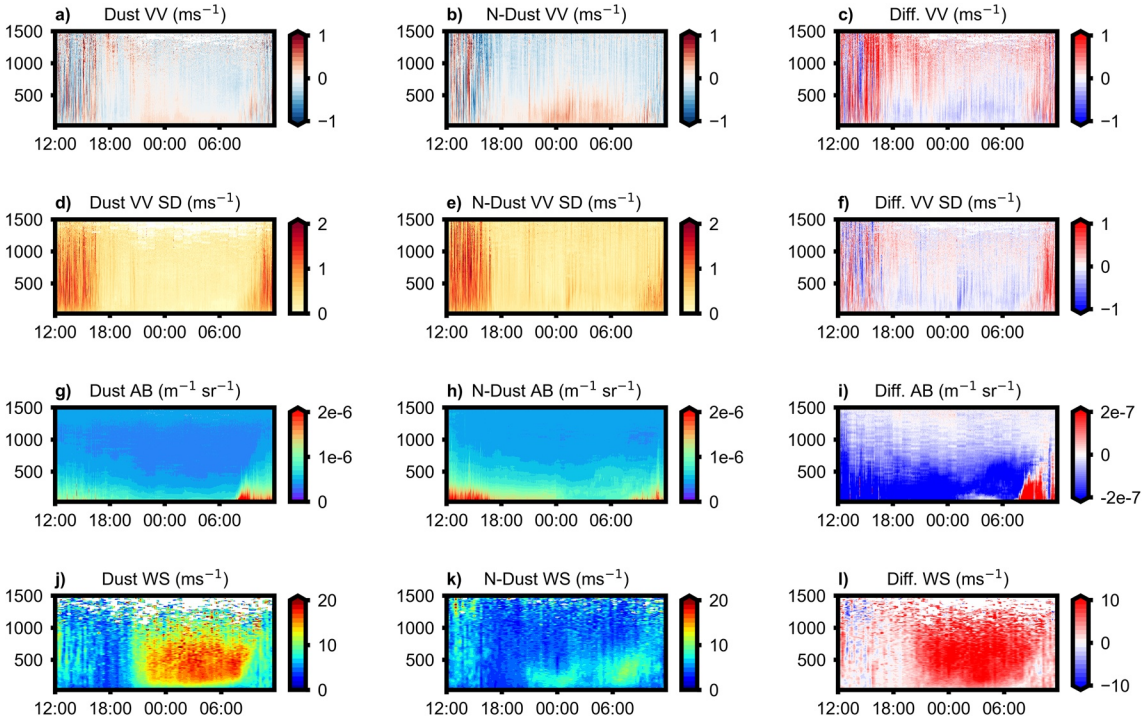


Figure 10. Mean time-height cross sections of (a–c) vertical velocity, (g–i) aerosol backscatter and (j–l) wind speed for (a, g, and j) dust, (b, h, and k) non-dust, and (c, i, and l) difference composites. (d–f) Standard deviation time-height cross sections of vertical velocity for (d) dust, (e) non-dust, and (f) difference composites. The difference composites were calculated by subtracting the non-dust composites from the dust composites. All measurements are from the lidar.

Table 5
Day-to-Day Variability in 05:00–06:00 Wind Speed Profiles

Date	Core WS ($m\ s^{-1}$)	Core height (m)	Above-core shear ($m\ s^{-1}$)	Below-core shear ($m\ s^{-1}$/30 m)	LLJ?	LLJi ($m^2\ s^{-1}$)	Dust
			Not LLJ's				
September 6	7.93	291	−3.33	0.49	N	N/A	N
August 19	8.88	588	1.85	0.31	N	N/A	N
August 17	9.87	600	2.81	0.19	N	N/A	N
			LLJ's w/o dust emission				
	>8 $m\ s^{-1}$		<−1.3 $m\ s^{-1}$	>0.3 $m\ s^{-1}$/30 m			
August 21	10.25	150	−5.70	1.26	Y	603	N
August 20	8.94	159	−4.26	0.84	Y	675	N
September 10	19.41	411	−11.16	1.10	Y	863	N
August 16	8.79	129	−4.55	0.87	Y	997	N
September 17	15.20	492	–[a]	0.68	Y	1,026	N
August 15	11.30	117	−3.73	1.89	Y	1,402	N
September 1	10.31	345	−3.72	0.40	Y	1,561	N
September 7	12.66	213	−6.63	1.17	Y	1,788	N
September 25	9.45	237	−3.34	0.74	Y	2,262	N
September 8	14.53	450	−6.95	0.76	Y	2,388	N
September 22	11.64	351	−5.98	0.69	Y	2,707	N
September 16	13.90	240	–[a]	1.32	Y	2,882	N
September 9	13.82	333	−2.47	0.97	Y	3,160	N
September 23	22.50	261	–[a]	2.15	Y	3,303	N
September 15	24.10	315	–[a]	2.26	Y	3,344	N
September 24	13.56	384	−10.22	0.75	Y	3,672	N
September 20	13.94	249	−6.80	1.27	Y	3,927	N
August 22	14.17	216	−6.78	1.16	Y	4,538	N
August 31	15.53	474	−5.87	0.81	Y	4,716	N
September 2	15.95	432	−3.95	0.87	Y	5,280	N
September 21	11.94	255	−3.10	0.84	Y	5,478	N
September 19	29.32	462	−13.56[b]	1.63	Y	6,212	N
August 18	18.37	444	−7.18	0.99	Y	10,648	N
August 26	18.91	276	−8.26	1.58	Y	11,574	N
September 4	16.50	183	−1.32	2.16	Y	12,305	N
September 3	15.77	387	−4.56	0.77	Y	12,370	N
August 29	19.06	300	−4.52	1.17	Y	17,465	N
August 30	19.51	342	−4.01	1.22	Y	18,024	N
			LLJ's w/dust emission				
	>17 $m\ s^{-1}$		<-2 $m\ s^{-1}$	>0.4 $m\ s^{-1}$/30 m			
September 18	17.07	600	−10.65	0.49	Y	5,122	Y
August 23	17.80	543	−7.96	0.78	Y	11,254	Y
August 27	18.60	564	−4.92	0.77	Y	12,545	Y
August 24	19.23	222	−3.74	2.33	Y	13,382	Y

21698996, 2021, 14, Downloaded from https://agupubs.onlinelibrary.wiley.com/doi/10.1029/2021JD034746 by Test, Wiley Online Library on [08/03/2023]. See the Terms and Conditions (https://onlinelibrary.wiley.com/terms-and-conditions) on Wiley Online Library for rules of use; OA articles are governed by the applicable Creative Commons License

21698996, 2021, 14, Downloaded from https://agupubs.onlinelibrary.wiley.com/doi/10.1029/2021JD034746 by Test, Wiley Online Library on [08/03/2023]. See the Terms and Conditions (https://onlinelibrary.wiley.com/terms-and-conditions) on Wiley Online Library for rules of use; OA articles are governed by the applicable Creative Commons License

Table 5
Continued

Date	Core WS ($m\ s^{-1}$)	Core height (m)	Above-core shear ($m\ s^{-1}$)	Below-core shear ($m\ s^{-1}$/30 m)	LLJ?	LLJi ($m^2\ s^{-1}$)	Dust
August 28	20.11	237	−2.09	1.89	Y	19,521	Y
August 25	21.94	312	−3.69	1.61	Y	20,815	Y

Note. The LLJ core was identified as the maximum wind speed below 600 m. For a description of shear calculations, the LLJ detection scheme, and the LLJ index see Section 4.3.1.2.

[a]Not possible to calculate above-core shear due to attenuation of the lidar signal. [b]Above-core shear calculated at a height of 297 m.

4.3.2. Synoptic Circulation

Synoptic modulation of emission has been observed for dust source regions in the Northern Hemisphere, including those where LLJ's are the primary emission mechanism (Washington & Todd, 2005; Washington et al., 2006); changes in the configuration of the high pressure cells that dominate southern Africa's winter climate could therefore have important consequences with regards to dust activity at Etosha. Figure 12 shows dust, non-dust and difference composites of 06:00 850 hPa geopotential height, wind speed and wind direction from ERA5, with clear distinctions visible in the synoptic situation between dust and non-dust days. In contrast to the non-dust composite (Figure 12b) which shows a relatively slack geopotential gradient across southern Africa, the pressure gradient is enhanced across the subcontinent in the dust composite (Figure 12a), helping to drive a stronger easterly–northeasterly flow at Etosha. The synoptic situation in Figure 12b is much closer to the climatological average, with the SAA and South Indian Anticyclone (SIA) discernible in the geopotential contours. In Figure 12a, the synoptics are a consequence of the ridging of the SAA, with a west-to-east movement of mass tightening the height contours across the subcontinent. The enhanced pressure gradient across southern Africa increases momentum available to the LLJ and subsequently mixed-down to the surface, producing stronger winds for dust emission at Etosha.

4.4. Case Study: Dust Emission on August 25

Figures 13 and 14 document the atmospheric processes contributing to the observed dust event at Etosha on the August 25. On the evening of the August 24, a LLJ structure develops from 20:00 to 21:00 onwards (Figure 13a) and strengthens through the nocturnal hours to give core wind speeds in excess of 20 $m\ s^{-1}$ by 02:00–03:00 (Figures 13b and 14a). With the onset of surface heating and dry convective activity within the boundary layer (Figure 13c), the jet structure gets eroded (Figure 13e); the abruptness of this process is captured by the substantial difference between the 06:00–07:00 and 08:00–09:00 profiles (Figure 13b). This results in a mix-down of momentum from the jet core, enhancing a surface circulation which is already strong at Etosha due to the ridging of the SAA (Figure 14c). The emission is driven by an increase in the surface wind speed to almost 10 $m\ s^{-1}$ (Figure 13d), with the dust plume transported toward the southwest (Figure 7) in the prevailing northeasterly flow (Figure 14b). The plume was initially detected at 09:00 in satellite imagery, and is consistent with the spike in aerosol loadings captured by the lidar (Figure 13d).

4.5. Etosha LLJ in ERA-I and ERA5 Reanalysis Data

The following section addresses key question 3: How well is the observed wind climatology at Etosha represented in ERA-I and ERA5 reanalysis data?

Figure 15 shows hourly wind speed profiles from the lidar, ERA5 and ERA-I, averaged across the 2016 observation period. An overview of the reanalysis data sets is given in Section 2.3, along with details of the grid point used for comparison with observational data at Etosha. Whereas ERA5 data is available hourly, ERA-I is available six hourly, making comparisons with observations possible at 00:00, 06:00, 12:00, and 18:00 only. In Figure 16, wind speed-height cross sections are shown for the lidar and ERA5 (again averaged across the 2016 observation period). Figure 16b shows hourly averaged lidar data, so that a comparison with ERA5 is

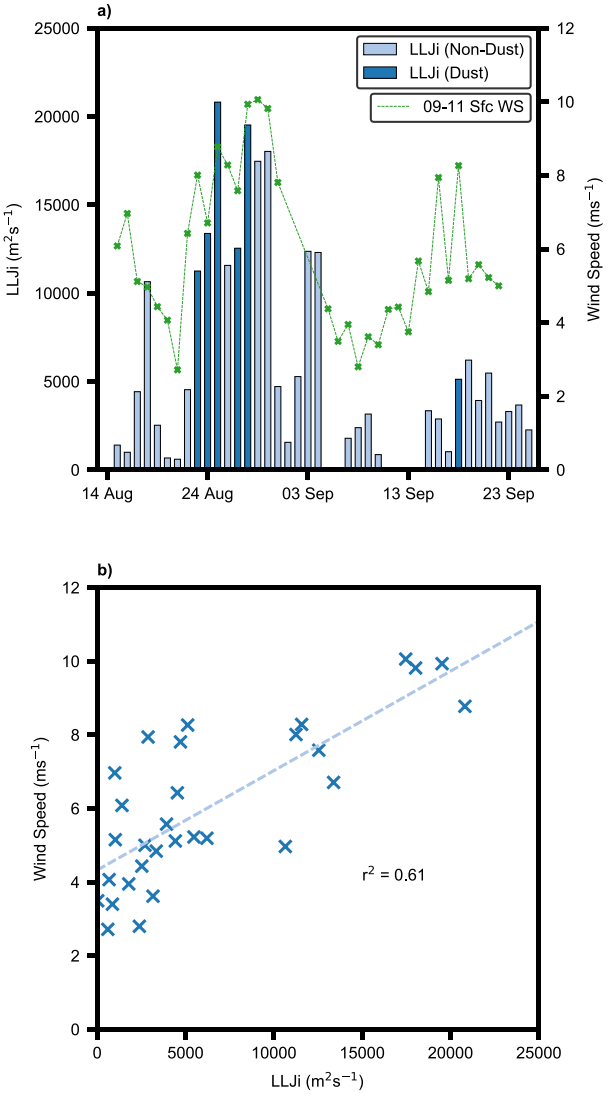


Figure 11. (a) Timeseries of LLJ index (bars) and 09:00–11:00 surface wind speed (line) plotted for the 2016 observation period (August 13 to September 25), and (b) 09:00–11:00 surface wind speed plotted against the LLJ index with a regression line fitted. The 09:00–11:00 period was chosen as this is when surface winds peak in the mean at Etosha (Figure 4a).

possible. In general, the representation of the LLJ at Etosha in ERA5 is good, with some of the key characteristics of the jet picked up through the hourly profiles (Figures 15 and 16c). The magnitude of the jet is represented well through the nocturnal period (00:00–04:00), and the height of the core is consistent with the observed profiles. The jet develops too quickly through the evening transition in ERA5 however (18:00–22:00), and is too quick to erode during the morning hours (06:00–08:00). ERA-I is less successful in its representation of the LLJ; jet development is again premature at 18:00, and the magnitude of the jet is underestimated by >2 m s^{-1} at 00:00 and by >3 m s^{-1} at 06:00.

The varying skill of the reanalyses in representing the LLJ at Etosha is likely the result of differences in the horizontal/vertical grid and temporal resolution, as well as the improvement in subgrid parameterization schemes from ERA-I to ERA5 (Hersbach et al., 2020). ERA5 has 24 model levels in the lowest 1,500 m, compared to ERA-I which has 12; the ability to resolve a meteorological process which has been shown to be limited in vertical extent to the lowest ≈1,000 m of the atmosphere is therefore greater in ERA5. The finer horizontal grid spacing (0.25° × 0.25° compared to 0.75° × 0.75°) also improves the skill of ERA5 relative to ERA-I, given that the LLJ is a response to local changes in surface heating and boundary layer structure. The difficulty both datasets experience in representing the temporal evolution of the LLJ is also unsurprising, given that critical stages in jet development are tied to the diurnal cycle and particularly precise periods of time around sunset and sunrise. The observed breakdown of the jet has been shown to be especially abrupt in some instances, with large differences between consecutive hourly profiles; datasets with temporal resolutions on the order of hours are therefore hard-pressed to track such processes. The inability of models to accurately reproduce the breakdown of the NLLJ has been linked to difficulties in simulating the growth of the daytime boundary layer (Garcia-Carreras et al., 2015; Roberts et al., 2017); this has likely improved from ERA-I to ERA5 with refinement of the subgrid turbulent mixing scheme (Hersbach et al., 2020).

5. Discussion and Conclusion

This paper has presented meteorological observations from the Etosha Pan, a major dust source that has received relatively little attention compared to dust source areas in the Northern Hemisphere. The observations have been used to identify the atmospheric processes operating at Etosha, including those significant to the uplift of dust from the pan surface, and have provided a constraint on relevant model fields. Three key questions were posed in the introduction: (i) What are the observed characteristics of the boundary layer winds at Etosha during austral winter? (ii) What are the atmospheric controls on dust emission from Etosha? (iii) How well is the observed wind climatology at Etosha represented in ERA-I and ERA5 reanalysis data? The results presented in Sections 3–5 will now be discussed, and the main conclusions summarized, addressing each of these questions in turn.

A LLJ has been shown to be a persistent feature of the nocturnal boundary layer at Etosha during austral winter (key question 1), with a jet structure identified on all but three days of the observation period (Table 5). The LLJ strengthens through the nocturnal hours, peaking around sunrise (Figure 2; Table 1), with core wind speeds in excess of 20 m s^{-1} recorded on individual days of the observation period. Jet profiles are limited to the lowest kilometer of the atmosphere, with the core of the LLJ anchored between 200 and 400 m until the structure begins to breakdown (Figure 2; Table 1). The detection of a LLJ is consistent with the findings of Zunckel et al. (1996), who identified jet profiles at Etosha using tethersonde soundings,

21698996, 2021, 14, Downloaded from https://agupubs.onlinelibrary.wiley.com/doi/10.1029/2021JD034746 by Test, Wiley Online Library on [08/03/2023]. See the Terms and Conditions (https://onlinelibrary.wiley.com/terms-and-conditions) on Wiley Online Library for rules of use; OA articles are governed by the applicable Creative Commons License

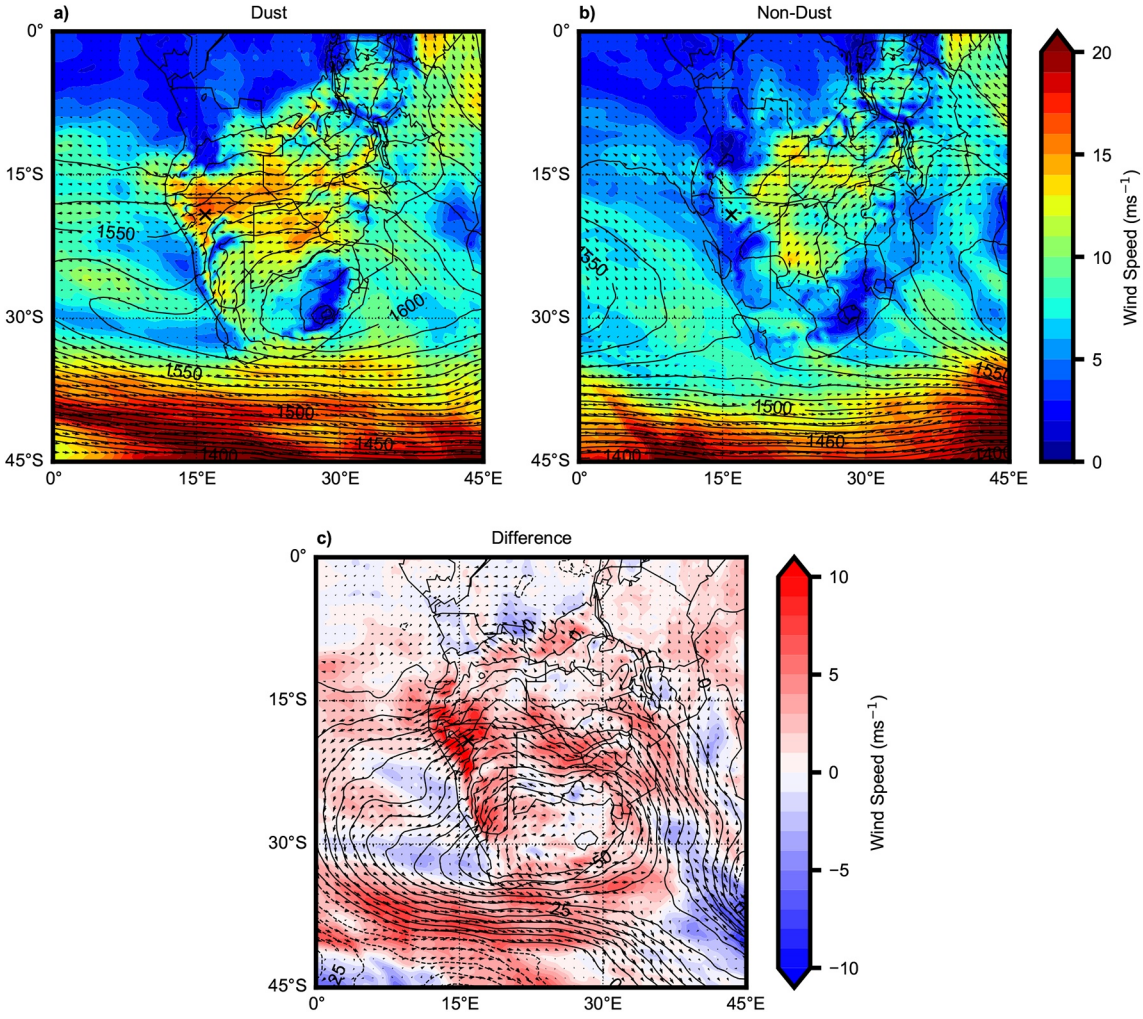


Figure 12. Mean 06:00 850 hPa geopotential height and wind speed/direction for (a) dust, (b) non-dust, and (c) difference composites. The difference composite is calculated by subtracting the non-dust composite from the dust composite. Geopotentials are given by the black lines, with heights shown in meters. Wind vectors are plotted at a resolution of 1° × 1°. All data from ERA5.

although the height of the core (50–200 m) and wind speeds (>11 m s^{-1}) reported differ from the results presented here. This is likely due to the tethersonde soundings not capturing the full vertical extent of the LLJ, with the authors acknowledging the difficulties experienced collecting balloon data in the windy conditions associated with the jet (Zunckel et al., 1996). Mean core wind speeds at Etosha (≈12 m s^{-1}) fall in the range observed for diurnally varying LLJ's in other geographic regions (Rife et al., 2010), and are comparable to jets in other dust source areas; for example, speeds of ≈12 m s^{-1} have been reported for LLJ's in the Bodélé Depression (Todd et al., 2008), and the central Sahara (Allen & Washington, 2014).

The evolution of the LLJ at Etosha is largely consistent with the Blackadar (1957) theory of frictional decoupling and inertial oscillations, with jet formation and breakdown coinciding with sunset and sunrise respectively. Decoupling takes place with the loss of surface heating and reduction in eddy viscosity during the evening transition (Figure 5b), and the flow accelerates in a layer close to the top of a temperature inversion/stable layer (Figures 5a and 5d). Given the near absence of cloud at Etosha during austral winter, inversions are a frequent nocturnal occurrence (Zunckel et al., 1996); by acting as a cap on vertical movement, they help to explain the persistence of the inertial jet recorded throughout the observation period. The oscillation can be seen as an anti-clockwise rotation of the wind vector after sunset (Figure 6), although the southerly component of the nocturnal winds may also be the result of cold air drainage from the higher ground to the south of Etosha (Preston-Whyte et al., 1994). Etosha's latitude ($\phi = -19.2$) means that ≈one-

21698996, 2021, 14, Downloaded from https://agupubs.onlinelibrary.wiley.com/doi/10.1029/2021JD034746 by Test, Wiley Online Library on [08/03/2023]. See the Terms and Conditions (https://onlinelibrary.wiley.com/terms-and-conditions) on Wiley Online Library for rules of use; OA articles are governed by the applicable Creative Commons License

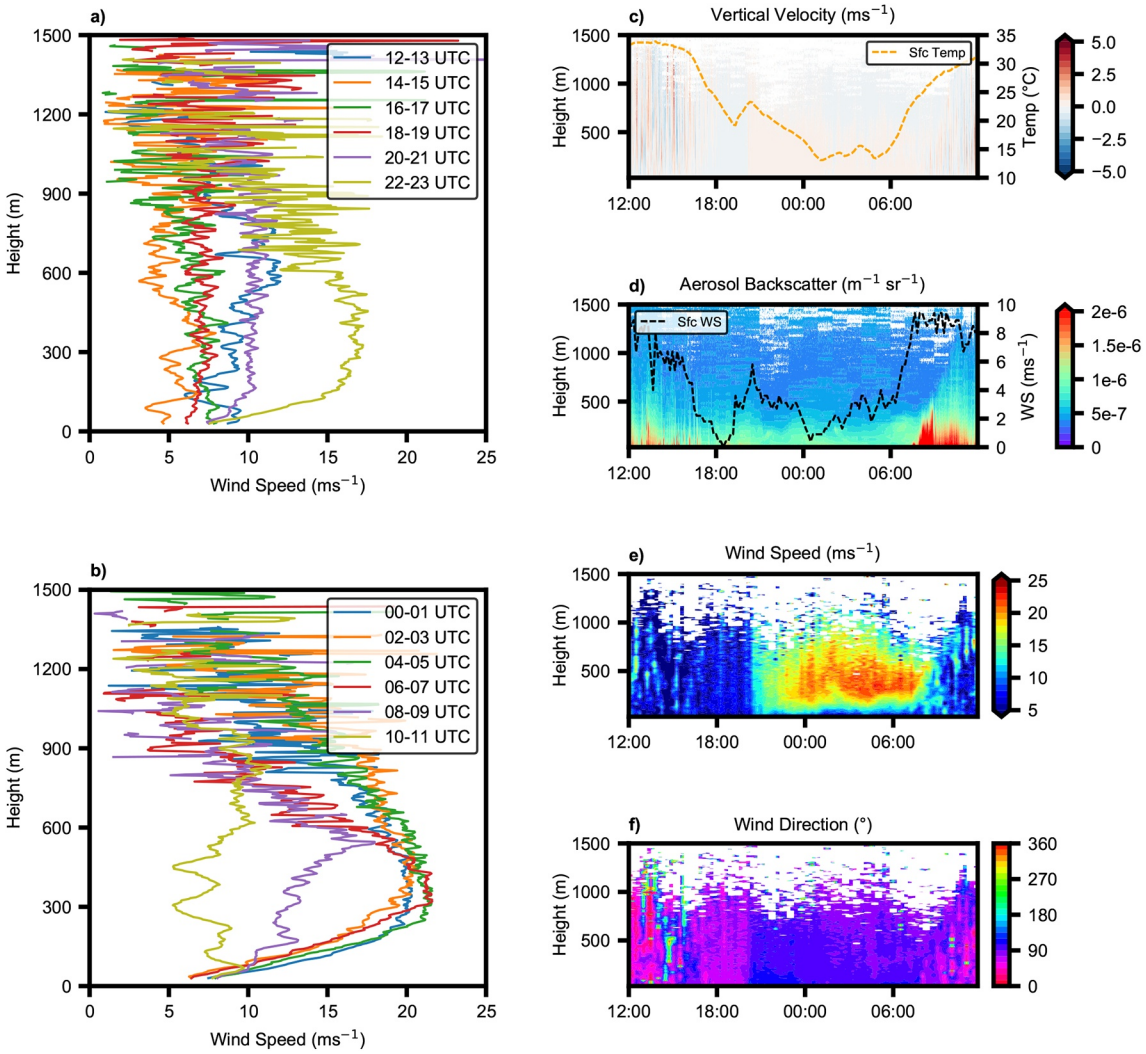


Figure 13. Hourly wind speed profiles for (a) the evening of August 24 and (b) morning of August 25 from the lidar. (c) Vertical velocity, (d) aerosol backscatter, (e) wind speed and (f) wind direction time-height cross sections for the period 12:00 August 24 to 12:00 August 25 (UTC), from the lidar. Surface temperature (orange line) data from the Davis station is plotted with the vertical velocity cross section. Surface wind speed (black line) data from the Davis station is plotted with the aerosol backscatter cross section.

third of an oscillation is completed, producing peak core wind speeds between 06:00 and 08:00 (Figure 2; Table 1); this is consistent with the idealized simulations performed by Heinold et al. (2015), who suggest that a latitude of 20° is optimal for generating peak core wind speeds at around the time of jet breakdown. The LLJ at Etosha shows a slightly later peak than the jet identified at Bordj-Badji Mokhtar (between 03:00 and 05:00) (Allen & Washington, 2014), which sits at a higher latitude ($\phi = 21.4$) to Etosha in the Northern Hemisphere, consistent with longer oscillation periods and slower jet development with decreasing latitude.

The timing of dust uplift at Etosha, along with the absence of moist convection (precluding cold pools as an emission mechanism), point to the LLJ as the primary driver of dust emission from the pan surface (key question 2). With the onset of surface heating, dry convection within the boundary layer erodes the jet structure (Figures 5b and 5d), and momentum is mixed-down from the core, generating peak surface winds between midmorning and midday (Figure 4). More energetic LLJ's are observed on dust days compared to non-dust days (Figure 9; Table 4), increasing momentum mixed-down from the jet core, and producing a greater enhancement of the surface winds (Figure 8; Table 3). As noted previously, peak core wind speeds at Etosha coincide with the hours around sunrise (Figure 2; Table 1), meaning the breakdown of the jet is abrupt, particularly on dust days (Figure 9). On non-dust days, greater nocturnal turbulence

21698996, 2021, 14, Downloaded from https://agupubs.onlinelibrary.wiley.com/doi/10.1029/2021JD034746 by Test, Wiley Online Library on [08/03/2023]. See the Terms and Conditions (https://onlinelibrary.wiley.com/terms-and-conditions) on Wiley Online Library for rules of use; OA articles are governed by the applicable Creative Commons License

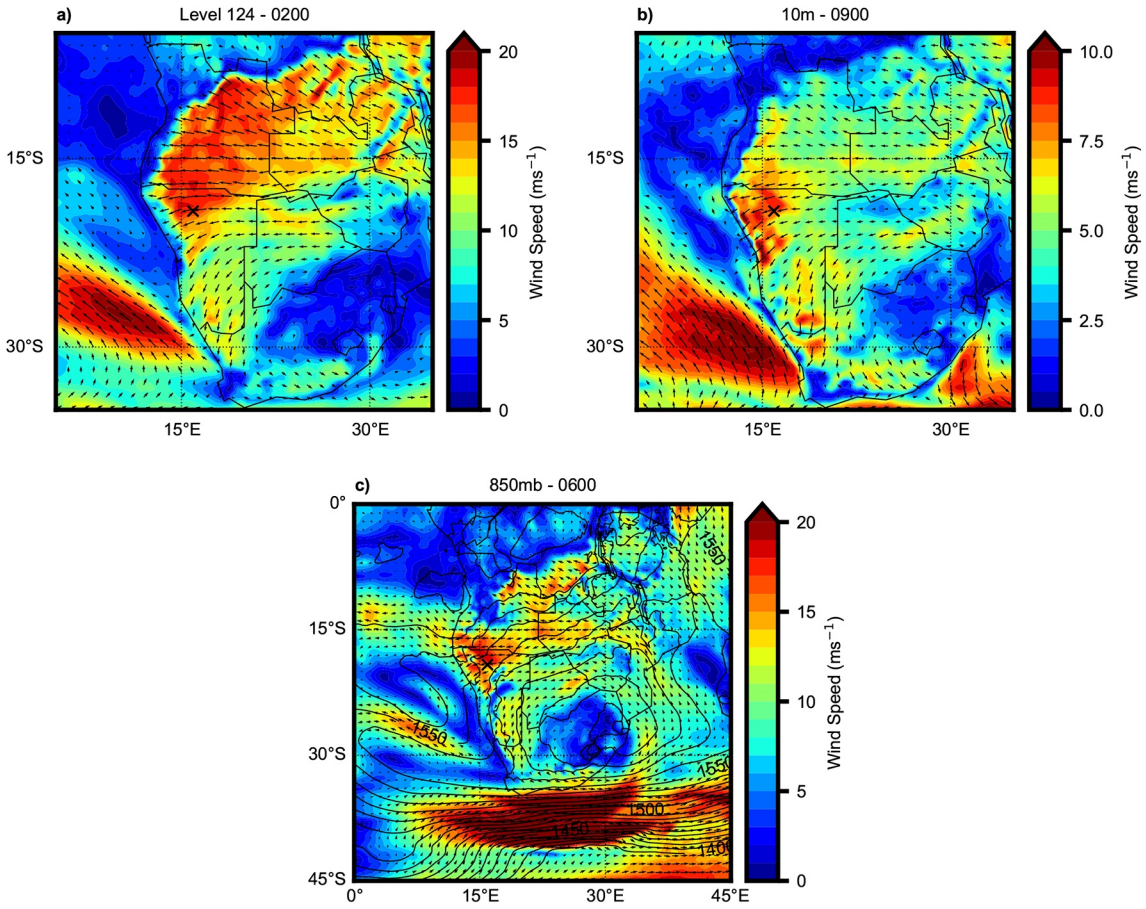


Figure 14. (a) Wind speed/direction for model level 124 (≈500 m) at 02:00 and (b) for 10 m at 09:00 on August 25. (c) 850 hPa geopotential height and wind speed/direction for 06:00 on 25 August. Geopotentials are given by the black lines, with heights shown in meters. Wind vectors are plotted at a resolution of 1° × 1°. All data from ERA5.

likely disturbs the decoupling process (Figure 10e), resulting in an earlier and less abrupt breakdown of the jet (Heinold et al., 2015). Momentum mixed-down from nocturnal jets has been identified as the primary emission mechanism in other dust source areas (Fiedler et al., 2013; Schepanski et al., 2009; Washington & Todd, 2005), and so the results presented here reinforce the importance of LLJ's to global dust emissions.

Uplift at Etosha is modulated by changes in the synoptic circulation, with dust activity recorded during the observation period coincident with a ridging of the SAA, and a subsequent increase in the pressure gradient across southern Africa (Figure 12). This is consistent with the findings of Washington et al. (2003), who suggest that dust emissions across the subcontinent are driven by an enhanced easterly flow resulting from a movement of mass across southern Africa, associated with west-to-east traveling eddies. This is evidenced by the cluster of dust activity between August 23 and 28, when the synoptic flow at Etosha was strengthened for a number of days whilst a transient system tracked across the subcontinent (Figure 14). Synoptic modulation of emission has been identified in other dust source areas, including those where LLJ's are the primary driver of uplift; ridging of the Libyan high accounts for variability in emissions from the Bodélé Depression (Washington & Todd, 2005; Washington et al., 2009), whilst the northwestward expansion of the Saharan heat low relative to the Azores High during boreal summer increases the frequency of LLJ's embedded in the Atlantic inflow over West Africa (Fiedler et al., 2013).

ERA5 is more successful than ERA-I in capturing key features of the LLJ at Etosha (key question 3), such as core height and core wind speed (Figures 15 and 16). Given the limited vertical extent of the LLJ, and the fact that jet development is closely tied to the diurnal cycle of heating, this is unsurprising, as the spatial/

21698996, 2021, 14, Downloaded from https://agupubs.onlinelibrary.wiley.com/doi/10.1029/2021JD034746 by Test, Wiley Online Library on [08/03/2023]. See the Terms and Conditions (https://onlinelibrary.wiley.com/terms-and-conditions) on Wiley Online Library for rules of use; OA articles are governed by the applicable Creative Commons License

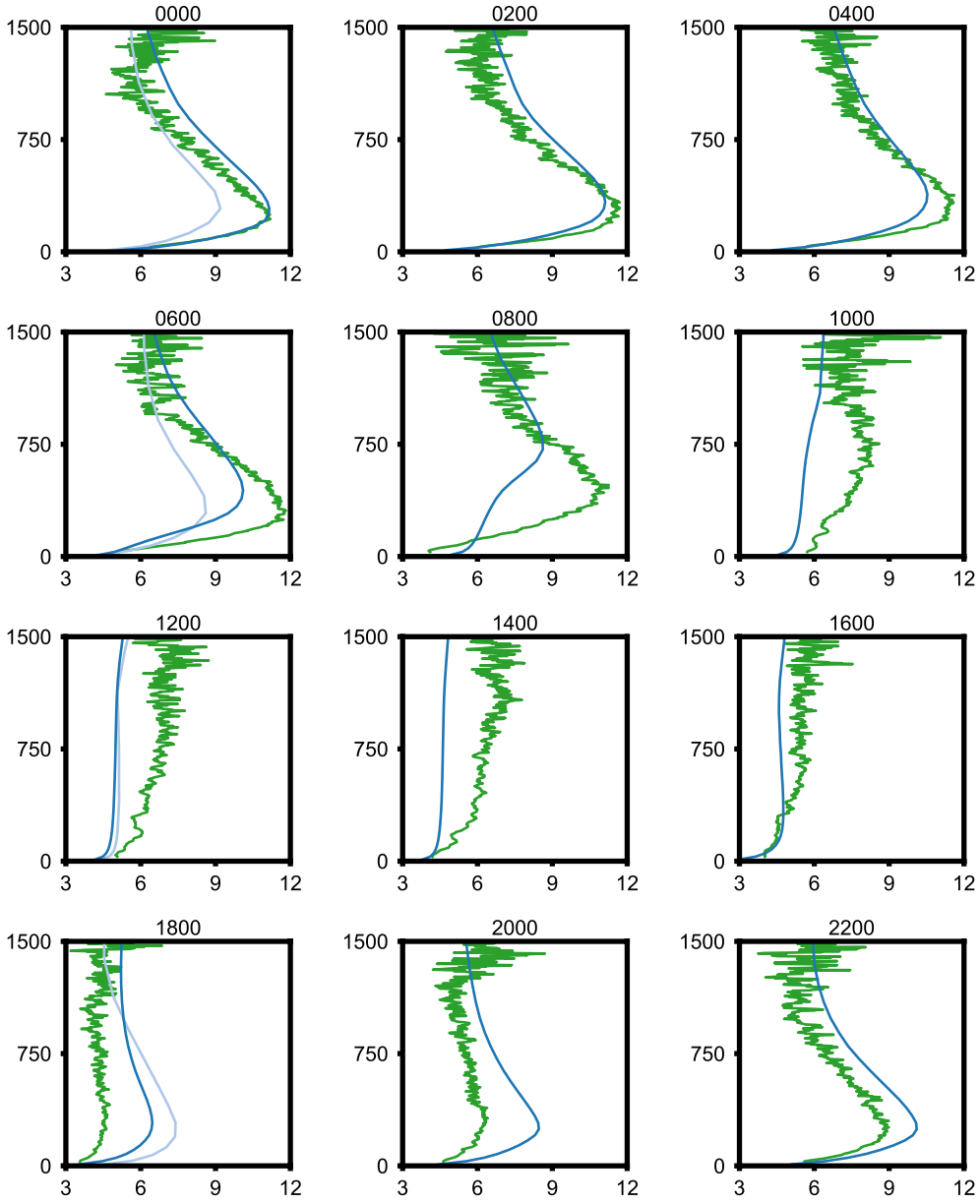


Figure 15. Mean wind speed-height profiles for the 2016 observation period (August 13 to September 25) from the lidar (green), ERA-I (light blue) and ERA5 (dark blue). ERA-I is only available at 00:00, 06:00, 12:00 and 18:00. The 00:00 output from ERA-I and ERA5 is compared with the 00:00–01:00 hourly profile from the lidar.

temporal resolution, and number of model levels is greater in ERA5. Acosta and Huber (2017) demonstrate the importance of grid resolution in simulating the Indo-Gangetic Plains LLJ, with the majority of coarse resolution models from the Coupled Model Intercomparison Project Phase 5 (CMIP5) struggling to resolve the jet. The results presented here agree with the findings of Roberts et al. (2017), who suggest that ERA-I's inability to capture the high wind speed events responsible for emission in the Sahara is due to the difficulties associated with resolving subdaily processes (such as LLJ's). The skill of ERA5 relative to ERA-I emphasizes the importance of using products with high temporal output when studying dust emission.

This paper has described the characteristics of a LLJ at Etosha, and has evaluated its relationship with dust emission from the pan surface. The observations presented are only for one season however, and so more work is required to document the intraannual and interannual variability of the jet, and how this influences dust emissions. The LLJ and its relationship with surface winds has been the primary focus of this work, as

21698996, 2021, 14, Downloaded from https://agupubs.onlinelibrary.wiley.com/doi/10.1029/2021JD034746 by Test, Wiley Online Library on [08/03/2023]. See the Terms and Conditions (https://onlinelibrary.wiley.com/terms-and-conditions) on Wiley Online Library for rules of use; OA articles are governed by the applicable Creative Commons License

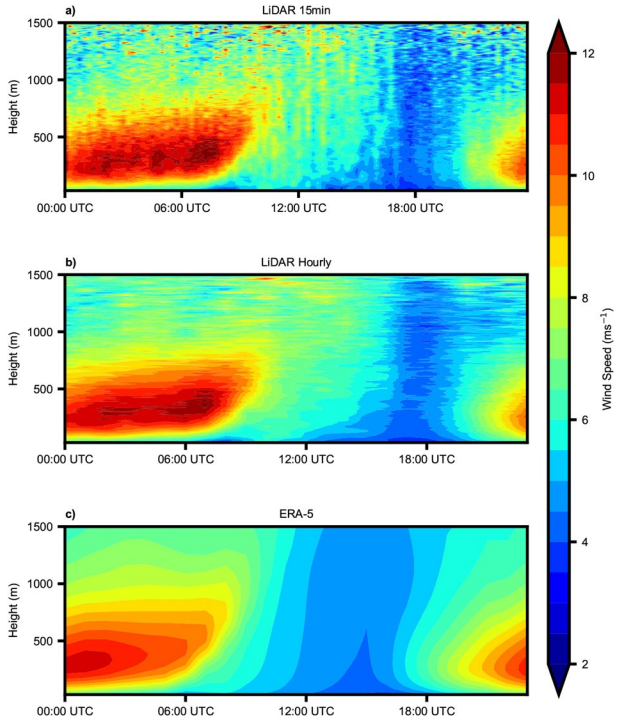


Figure 16. Mean time-height cross sections of wind speed for the 2016 observation period (August 13 to September 25) from (a and b) the lidar and (c) ERA5. The 15 min lidar data in (a) is averaged in (b), so as to give a better comparison with the hourly ERA5 data.

these features of the circulation have been well captured by the available instrumentation (lidar and Davis weather station); this does not however preclude the possibility that other meteorological processes contribute to the uplift of dust at Etosha, and so future work should aim to build on the initial findings presented here. This paper has also evaluated the representation of the LLJ in atmospheric reanalyses, however the observations presented here also offer a constraint on higher resolution models. Recent work suggests that convection-permitting simulations improve the representation of dust-emitting processes across the Sahara (Heinold et al., 2013; Roberts et al., 2018), indicating that the LLJ at Etosha may be better incorporated in similar runs for southern Africa (Stratton et al., 2018).

Data Availability Statement

ERA-I and ERA5 data are maintained by ECMWF. ERA-I data are available online from the ECMWF website (https://www.ecmwf.int/en/forecasts/datasets/reanalysis-datasets/era-interim). ERA5 data are available online from the Copernicus Climate Change Service (https://cds.climate.copernicus.eu/). MSG SEVIRI data are available online from the EUMETSAT Data Center (https://archive.eumetsat.int/usc/). MODIS imagery is available online from EOSDIS Worldview (https://worldview.earthdata.nasa.gov/). Observational data from the CLARIFY-2016 field campaign are available from Richard Washington (richard.washington@ouce.ox.ac.uk).

Acknowledgments
The authors are very grateful to the Ministry of Environment and Tourism for permitting this research (permit 2166/2016) and to Shane Kötting for his superb assistance in the field. Matthew Clements is funded by the NERC doctoral training partnership (NE/L002612/1). The CLARIFY-2016 project was funded by NERC (NE/L01355X/1).

References

Acosta, R. P., & Huber, M. (2017). The neglected Indo-Gangetic plains low-level jet and its importance for moisture transport and precipitation during the peak summer monsoon. *Geophysical Research Letters*, *44*(16), 8601–8610. https://doi.org/10.1002/2017GL074440

Allen, C. J. T., & Washington, R. (2014). The low-level jet dust emission mechanism in the central Sahara: Observations from Bordj-Badji Mokhtar during the June 2011 Fennec Intensive Observation Period. *Journal of Geophysical Research: Atmospheres*, *119*(6), 2990–3015. https://doi.org/10.1002/2013JD020594

Allen, C. J. T., Washington, R., & Engelstaedter, S. (2013). Dust emission and transport mechanisms in the central Sahara: Fennec ground-based observations from Bordj Badji Mokhtar, June 2011. *Journal of Geophysical Research: Atmospheres*, *118*(12), 6212–6232. https://doi.org/10.1002/jgrd.50534

21698996, 2021, 14, Downloaded from https://agupubs.onlinelibrary.wiley.com/doi/10.1029/2021JD034746 by Test, Wiley Online Library on [08/03/2023]. See the Terms and Conditions (https://onlinelibrary.wiley.com/terms-and-conditions) on Wiley Online Library for rules of use; OA articles are governed by the applicable Creative Commons License

Ashpole, I., & Washington, R. (2012). An automated dust detection using SEVIRI: A multiyear climatology of summertime dustiness in the central and western Sahara. *Journal of Geophysical Research: Atmospheres*, *117*(D8), D08202. https://doi.org/10.1029/2011JD016845

Bhattachan, A., D'Odorico, P., & Okin, G. (2015). Biogeochemistry of dust sources in southern Africa. *Journal of Arid Environments*, *117*, 18–27. https://doi.org/10.1016/j.jaridenv.2015.02.013

Blackadar, A. K. (1957). Boundary layer wind maxima and their significance for the growth of nocturnal inversions. *Bulletin of the American Meteorological Society*, *38*(5), 283–290. https://doi.org/10.1175/1520-0477-38.5.283

Boucher, O., Randall, D., Artaxo, P., Bretherton, C., Feingold, G., Forster, P., et al. (2013). Clouds and aerosols, In T. F. Stocker, D. Qin, G.-K. Plattner, M. Tignor, S. K. Allen, J. Boschung, et al. (Eds.), *Climate change 2013: The physical science basis. Contribution of Working Group I to the Fifth Assessment Report of the Intergovernmental Panel on Climate Change* (pp. 571–658). Cambridge University Press. https://doi.org/10.1017/CBO9781107415324.016

Browning, K. A., & Wexler, R. (1982). The determination of kinematic properties of a wind field using doppler radar. *Journal of Applied Meteorology*, *7*(1), 105–113. https://doi.org/10.1175/1520-0450(1968)007<0105:tdokpo>2.0.co;2

Bryant, R. G. (2003). Monitoring hydrological controls on dust emissions: Preliminary observations from Etosha Pan, Namibia. *The Geographical Journal*, *169*(2), 131–141. https://doi.org/10.1111/1475-4959.04977

Caton Harrison, T., Washington, R., & Engelstaedter, S. (2019). A 14-year climatology of Saharan dust emission mechanisms inferred from automatically tracked plumes. *Journal of Geophysical Research: Atmospheres*, *124*(16), 9665–9690. https://doi.org/10.1029/2019JD030291

Dansie, A., Wiggs, G., Thomas, D., & Washington, R. (2017). Measurements of windblown dust characteristics and ocean fertilization potential: The ephemeral river valleys of Namibia. *Aeolian Research*, *29*, 30–41. https://doi.org/10.1016/j.aeolia.2017.08.002

Dee, D. P., Uppala, S. M., Simmons, A. J., Berrisford, P., Poli, P., Kobayashi, S., et al. (2011). The era-interim reanalysis: Configuration and performance of the data assimilation system. *Quarterly Journal of the Royal Meteorological Society*, *137*(656), 553–597. https://doi.org/10.1002/qj.828

Evan, A. T. (2018). Surface winds and dust biases in climate models. *Geophysical Research Letters*, *45*(2), 1079–1085. https://doi.org/10.1002/2017GL076353

Evan, A. T., Flamant, C., Fiedler, S., & Doherty, O. (2014). An analysis of aeolian dust in climate models. *Geophysical Research Letters*, *41*(16), 5996–6001. https://doi.org/10.1002/2014GL060545

Fernald, F. G., Herman, B. M., & Reagan, J. A. (1972). Determination of aerosol height distributions by lidar. *Journal of Applied Meteorology and Climatology*, *11*(3), 482–489. https://doi.org/10.1175/1520-0450(1972)011<0482:DOAHDB>2.0.CO;2

Fiedler, S., Schepanski, K., Heinold, B., Knippertz, P., & Tegen, I. (2013). Climatology of nocturnal low-level jets over North Africa and implications for modeling mineral dust emission. *Journal of Geophysical Research: Atmospheres*, *118*(12), 6100–6121. https://doi.org/10.1002/jgrd.50394

Formenti, P., D'Anna, B., Flamant, C., Mallet, M., Piketh, S. J., Schepanski, K., et al. (2019). The aerosols, radiation and clouds in southern Africa field campaign in Namibia: Overview, illustrative observations, and way forward. *Bulletin of the American Meteorological Society*, *100*(7), 1277–1298. https://doi.org/10.1175/BAMS-D-17-0278.1

Garcia-Carreras, L., Parker, D. J., Marsham, J. H., Rosenberg, P. D., Brooks, I. M., Lock, A. P., et al. (2015). The turbulent structure and diurnal growth of the Saharan atmospheric boundary layer. *Journal of the Atmospheric Sciences*, *72*(2), 693–713. https://doi.org/10.1175/JAS-D-13-0384.1

Garstang, M., Tyson, P. D., Swap, R., Edwards, M., Kllberg, P., & Lindesay, J. A. (1996). Horizontal and vertical transport of air over southern Africa. *Journal of Geophysical Research: Atmospheres*, *101*(D19), 23721–23736. https://doi.org/10.1029/95JD00844

Ginoux, P., Prospero, J. M., Gill, T. E., Hsu, N. C., & Zhao, M. (2012). Global-scale attribution of anthropogenic and natural dust sources and their emission rates based on MODIS deep blue aerosol products. *Reviews of Geophysics*, *50*(3), RG3005. https://doi.org/10.1029/2012RG000388

Haywood, J., & Boucher, O. (2000). Estimates of the direct and indirect radiative forcing due to tropospheric aerosols: A review. *Reviews of Geophysics*, *38*(4), 513–543. https://doi.org/10.1029/1999RG000078

Heinold, B., Knippertz, P., & Beare, R. J. (2015). Idealized large-eddy simulations of nocturnal low-level jets over subtropical desert regions and implications for dust-generating winds. *Quarterly Journal of the Royal Meteorological Society*, *141*(690), 1740–1752. https://doi.org/10.1002/qj.2475

Heinold, B., Knippertz, P., Marsham, J. H., Fiedler, S., Dixon, N. S., Schepanski, K., et al. (2013). The role of deep convection and nocturnal low-level jets for dust emission in summertime west Africa: Estimates from convection-permitting simulations. *Journal of Geophysical Research: Atmospheres*, *118*(10), 4385–4400. https://doi.org/10.1002/jgrd.50402

Hersbach, H., Bell, B., Berrisford, P., Hirahara, S., Horányi, A., Muñoz-Sabater, J., et al. (2020). The ERA5 global reanalysis. *Quarterly Journal of the Royal Meteorological Society*, *146*(730), 1999–2049. https://doi.org/10.1002/qj.3803

Howard, E., & Washington, R. (2018). Characterizing the synoptic expression of the Angola low. *Journal of Climate*, *31*(17), 7147–7165. https://doi.org/10.1175/JCLI-D-18-0017.1

Jemmett-Smith, B. C., Marsham, J. H., Knippertz, P., & Gilkeson, C. A. (2015). Quantifying global dust devil occurrence from meteorological analyses. *Geophysical Research Letters*, *42*(4), 1275–1282. https://doi.org/10.1002/2015GL063078

Jickells, T. D., An, Z. S., Andersen, K. K., Baker, A. R., Bergametti, G., Brooks, N., et al. (2005). Global iron connections between desert dust, ocean biogeochemistry, and climate. *Science*, *308*(5718), 67–71. https://doi.org/10.1126/science.1105959

Knippertz, P., & Todd, M. C. (2012). Mineral dust aerosols over the Sahara: Meteorological controls on emission and transport and implications for modeling. *Reviews of Geophysics*, *50*(1). https://doi.org/10.1029/2011RG000362

Kok, J. F., Parteli, E. J. R., Michaels, T. I., & Karam, D. B. (2012). The physics of wind-blown sand and dust. *Reports on Progress in Physics*, *75*(10), 106901. https://doi.org/10.1088/0034-4885/75/10/106901

Koren, I., Kaufman, Y. J., Washington, R., Todd, M. C., Rudich, Y., Martins, J. V., & Rosenfeld, D. (2006). The Bodélé depression: A single spot in the Sahara that provides most of the mineral dust to the Amazon forest. *Environmental Research Letters*, *1*(1), 014005. https://doi.org/10.1088/1748-9326/1/1/014005

Landman, W. A., & Mason, S. J. (1999). Change in the association between Indian Ocean sea-surface temperatures and summer rainfall over South Africa and Namibia. *International Journal of Climatology*, *19*(13), 1477–1492. https://doi.org/10.1002/(SICI)1097-0088(19991115)19:13<1477::AID-JOC432>3.0.CO;2-W

Larom, D., Garstang, M., Lindeque, M., Raspet, R., Zunckel, M., Hong, Y., et al. (1997). Meteorology and elephant infrasound at Etosha National Park, Namibia. *Journal of the Acoustical Society of America*, *101*(3), 1710–1717. https://doi.org/10.1121/1.418180

Mahowald, N. M., Baker, A. R., Bergametti, G., Brooks, N., Duce, R. A., Jickells, T. D., et al. (2005). Atmospheric global dust cycle and iron inputs to the ocean. *Global Biogeochemical Cycles*, *19*(4), RG3005. https://doi.org/10.1029/2004GB002402

21698996, 2021, 14, Downloaded from https://agupubs.onlinelibrary.wiley.com/doi/10.1029/2021JD034746 by Test, Wiley Online Library on [08/03/2023]. See the Terms and Conditions (https://onlinelibrary.wiley.com/terms-and-conditions) on Wiley Online Library for rules of use; OA articles are governed by the applicable Creative Commons License

Mahowald, N. M., Bryant, R. G., del Corral, J., & Steinberger, L. (2003). Ephemeral lakes and desert dust sources. *Geophysical Research Letters*, *30*(2), 1074–1078. https://doi.org/10.1029/2002GL016041

Mahowald, N. M., & Kiehl, L. M. (2003). Mineral aerosol and cloud interactions. *Geophysical Research Letters*, *30*(9). https://doi.org/10.1029/2002GL016762

Marsham, J. H., Hobby, M., Allen, C. J. T., Banks, J. R., Bart, M., Brooks, B. J., et al. (2013). Meteorology and dust in the central Sahara: Observations from Fennec supersite-1 during the June 2011 intensive observation period. *Journal of Geophysical Research: Atmospheres*, *118*(10), 4069–4089. https://doi.org/10.1002/jgrd.50211

Marsham, J. H., Knippertz, P., Dixon, N. S., Parker, D. J., & Lister, G. M. S. (2011). The importance of the representation of deep convection for modeled dust-generating winds over West Africa during summer. *Geophysical Research Letters*, *38*(16), L16803. https://doi.org/10.1029/2011GL048368

Marsham, J. H., Parker, D. J., Grams, C. M., Taylor, C. M., & Haywood, J. M. (2008). Uplift of Saharan dust south of the intertropical discontinuity. *Journal of Geophysical Research: Atmospheres*, *113*(D21), D21102. https://doi.org/10.1029/2008JD009844

Marticorena, B., & Bergametti, G. (1995). Modeling the atmospheric dust cycle: 1. Design of a soil-derived dust emission scheme. *Journal of Geophysical Research: Atmospheres*, *100*(D8), 16415–16430. https://doi.org/10.1029/95JD00690

Munday, C., & Washington, R. (2017). Circulation controls on southern African precipitation in coupled models: The role of the Angola low. *Journal of Geophysical Research: Atmospheres*, *122*(2), 861–877. https://doi.org/10.1002/2016JD025736

Murray, J. E., Brindley, H. E., Bryant, R. G., Russell, J. E., Jenkins, K. F., & Washington, R. (2016). Enhancing weak transient signals in SEVIRI false color imagery: Application to dust source detection in southern Africa. *Journal of Geophysical Research: Atmospheres*, *121*(17), 199–210. https://doi.org/10.1002/2016JD025221

Nield, J. M., Wiggs, G. F. S., King, J., Bryant, R. G., Eckardt, F. D., Thomas, D. S. G., & Washington, R. (2016). Climate–surface–pore-water interactions on a salt crusted playa: Implications for crust pattern and surface roughness development measured using terrestrial laser scanning. *Earth Surface Processes and Landforms*, *41*(6), 738–753. https://doi.org/10.1002/esp.3860

Park, S., Kim, S.-W., Park, M.-S., & Song, C.-K. (2018). Measurement of planetary boundary layer winds with scanning doppler lidar. *Remote Sensing*, *10*(8), 1261. https://doi.org/10.3390/rs10081261

Preston-Whyte, R. A., Diab, R. D., & Sokolic, F. (1994). Thermo-topographically induced winds in the boundary layer over the etosha pan. *South African Geographical Journal*, *76*(2), 59–62. https://doi.org/10.1080/03736245.1994.9713576

Prospero, J. M., Ginoux, P., Torres, O., Nicholson, S. E., & Gill, T. E. (2002). Environmental characterization of global sources of atmospheric soil dust identified with the NIMBUS 7 total ozone mapping spectrometer (TOMS) absorbing aerosol product. *Reviews of Geophysics*, *40*(1), 2–1. https://doi.org/10.1029/2000RG000095

Reason, C. (2017). *Climate of Southern Africa*. Oxford University Press. https://doi.org/10.1093/acrefore/9780190228620.013.513

Reason, C., & Smart, S. (2015). Tropical south east Atlantic warm events and associated rainfall anomalies over southern Africa. *Frontiers in Environmental Science*, *3*, 24. https://doi.org/10.3389/fenvs.2015.00024

Rife, D. L., Pinto, J. O., Monaghan, A. J., Davis, C. A., & Hannan, J. R. (2010). Global distribution and characteristics of diurnally varying low-level jets. *Journal of Climate*, *23*(19), 5041–5064. https://doi.org/10.1175/2010JCLI3514.1

Roberts, A. J., Marsham, J. H., Knippertz, P., Parker, D. J., Bart, M., Garcia-Carreras, L., et al. (2017). New Saharan wind observations reveal substantial biases in analyzed dust-generating winds. *Atmospheric Science Letters*, *18*(9), 366–372. https://doi.org/10.1002/asl.765

Roberts, A. J., Woodage, M. J., Marsham, J. H., Highwood, E. J., Ryder, C. L., McGinty, W., et al. (2018). Can explicit convection improve modeled dust in summertime west Africa? *Atmospheric Chemistry and Physics*, *18*(12), 9025–9048. https://doi.org/10.5194/acp-18-9025-2018

Schepanski, K., Tegen, I., Laurent, B., Heinold, B., & Macke, A. (2007). A new Saharan dust source activation frequency map derived from MSG-SEVIRI IR-channels. *Geophysical Research Letters*, *34*(18), L18803. https://doi.org/10.1029/2007GL030168

Schepanski, K., Tegen, I., Todd, M. C., Heinold, B., Bönisch, G., Laurent, B., & Macke, A. (2009). Meteorological processes forcing Saharan dust emission inferred from MSG-SEVIRI observations of subdaily dust source activation and numerical models. *Journal of Geophysical Research: Atmospheres*, *114*(D10), D10201. https://doi.org/10.1029/2008JD010325

Shapiro, A., & Fedorovich, E. (2010). Analytical description of a nocturnal low-level jet. *Quarterly Journal of the Royal Meteorological Society*, *136*(650), 1255–1262. https://doi.org/10.1002/qj.628

Sroga, J. T., Eloranta, E. W., & Barber, T. (1980). Lidar measurement of wind velocity profiles in the boundary layer. *Journal of Applied Meteorology and Climatology*, *19*(5), 598–605. https://doi.org/10.1175/1520-0450(1980)019<0598:LMOWVP>2.0.CO;2

Stratton, R. A., Senior, C. A., Vosper, S. B., Folwell, S. S., Boutle, I. A., Earnshaw, P. D., et al. (2018). A pan-African convection-permitting regional climate simulation with the Met Office Unified Model: CP4-Africa. *Journal of Climate*, *31*(9), 3485–3508. https://doi.org/10.1175/JCLI-D-17-0503.1

Swap, R., Garstang, M., Macko, S. A., Tyson, P. D., Maenhaut, W., Artaxo, P., et al. (1996). The long-range transport of southern African aerosols to the tropical south Atlantic. *Journal of Geophysical Research: Atmospheres*, *101*(D19), 23777–23791. https://doi.org/10.1029/95JD01049

Tegen, I., Harrison, S. P., Kohfeld, K., Prentice, I. C., Coe, M., & Heimann, M. (2002). Impact of vegetation and preferential source areas on global dust aerosol: Results from a model study. *Journal of Geophysical Research: Atmospheres*, *107*(D21), AAC 14-1–AAC 14-27. https://doi.org/10.1029/2001JD000963

Todd, M. C., Washington, R., Raghavan, S., Lizcano, G., & Knippertz, P. (2008). Regional model simulations of the Bodélé low-level jet of northern Chad during the Bodélé dust experiment (BoDEx 2005). *Journal of Climate*, *21*(5), 995–1012. https://doi.org/10.1175/2007JCLI1766.1

van de Wiel, B. J. H., Moene, A. F., Steeneveld, G. J., Baas, P., Bosveld, F. C., & Holtslag, A. A. M. (2010). A conceptual view on inertial oscillations and nocturnal low-level jets. *Journal of the Atmospheric Sciences*, *67*(8), 2679–2689. https://doi.org/10.1175/2010JAS3289.1

Vickery, K. J., Eckardt, F. D., & Bryant, R. G. (2013). A sub-basin scale dust plume source frequency inventory for southern Africa, 2005–2008. *Geophysical Research Letters*, *40*(19), 5274–5279. https://doi.org/10.1002/grl.50968

Wagener, T., Guieu, C., Losno, R., Bonnet, S., & Mahowald, N. (2008). Revisiting atmospheric dust export to the southern hemisphere ocean: Biogeochemical implications. *Global Biogeochemical Cycles*, *22*(2), GB2006. https://doi.org/10.1029/2007GB002984

Washington, R., Bouet, C., Cautenet, G., Mackenzie, E., Ashpole, I., Engelstaedter, S., et al. (2009). Dust as a tipping element: The Bodélé depression, Chad. *Proceedings of the National Academy of Sciences*, *106*(49), 20564–20571. https://doi.org/10.1073/pnas.0711850106

Washington, R., & Todd, M. C. (2005). Atmospheric controls on mineral dust emission from the Bodélé depression, Chad: The role of the low level jet. *Geophysical Research Letters*, *32*(17), L17701. https://doi.org/10.1029/2005GL023597

21698996, 2021, 14, Downloaded from https://agupubs.onlinelibrary.wiley.com/doi/10.1029/2021JD034746 by Test, Wiley Online Library on [08/03/2023]. See the Terms and Conditions (https://onlinelibrary.wiley.com/terms-and-conditions) on Wiley Online Library for rules of use; OA articles are governed by the applicable Creative Commons License

Washington, R., Todd, M. C., Engelstaedter, S., Mbainayel, S., & Mitchell, F. (2006). Dust and the low-level circulation over the Bodélé Depression, Chad: Observations from BoDEx 2005. *Journal of Geophysical Research: Atmospheres*, *111*(D3), D03201. https://doi.org/10.1029/2005JD006502

Washington, R., Todd, M. C., Middleton, N. J., & Goudie, A. S. (2003). Dust-storm source areas determined by the total ozone monitoring spectrometer and surface observations. *Annals of the Association of American Geographers*, *93*(2), 297–313. https://doi.org/10.1111/1467-8306.9302003

Zunckel, M., Hong, Y., Brassel, K., & O'Beirne, S. (1996). Characteristics of the nocturnal boundary layer: Okaukuejo, Namibia, during SAFARI-92. *Journal of Geophysical Research: Atmospheres*, *101*(D19), 23757–23766. https://doi.org/10.1029/95JD00624

21698996, 2021, 14, Downloaded from https://agupubs.onlinelibrary.wiley.com/doi/10.1029/2021JD034746 by Test, Wiley Online Library on [08/03/2023]. See the Terms and Conditions (https://onlinelibrary.wiley.com/terms-and-conditions) on Wiley Online Library for rules of use; OA articles are governed by the applicable Creative Commons License

Chapter 4: Summer Dust Emissions From the Etosha Pan, Namibia: The Role of the Namib Anabatic-Sea Breeze System

Whilst the results of the first research paper were novel, and contributed to the current state of knowledge regarding dust emission mechanisms, they only considered dust uplift at Etosha during the winter season. The results of the second research paper therefore consider dust emissions at Etosha throughout the year, and are presented in this chapter. Initially, satellite imagery is used to quantify the seasonal cycle and interannual variability in uplift. Then, a reanalysis dataset is used to evaluate whether the NLLJ identified in the first research paper sustains emissions throughout the annual cycle. The analysis conducted as part of this paper is therefore contingent on one of the findings of the first research paper (that the selected reanalysis dataset captured well the NLLJ), and so the sequencing of papers in this order is appropriate. The reanalysis dataset is then used to identify other atmospheric processes that contribute to dust emissions at Etosha, and what controls their variability. The first two research papers therefore provide a comprehensive overview of the meteorological processes driving uplift throughout the year.

Summer Dust Emissions From the Etosha Pan, Namibia: The Role of the Namib Anabatic-Sea Breeze System

Matthew Clements[1], **Richard Washington**[1]

[1]Climate Research Lab, Oxford University Centre for the Environment, Oxford, UK

Key Points:

- An anabatic-sea breeze helps to drive austral summer dust emissions from one of the Southern Hemisphere's most prominent source areas.
- The anabatic-sea breeze is present throughout the year, however is at its strongest, and propagates furthest inland during austral summer.
- Variability in the strength of the system is driven by changes in the pattern of diabatic heating over the interior of southern Africa.

Corresponding author: Matthew Clements, matthew.clements@ouce.ox.ac.uk

Abstract

This paper utilises Aerosol Index (AI) data from the Total Ozone Mapping Spectrometer (TOMS) instrument, along with ERA5 reanalysis data, to identify atmospheric processes contributing to the uplift of dust from the Etosha Pan through the annual cycle. Etosha is one of the most prominent source areas in the Southern Hemisphere, although very little is known about its meteorology outside of the peak dust season (August – October). Emissions in December (AI = 1.6) are shown to be comparable to those in September (AI = 1.7), the dustiest month in the TOMS record. Unlike in September however, when a nocturnal low-level jet (NLLJ) is the primary emission mechanism, uplift in December is associated with an anabatic-sea breeze that develops along the Namib coast, and propagates inland to reach Etosha during the evening. The system is a response to the thermal contrast between the elevated interior plateau and the adjacent waters of the cool Benguela Upwelling System (BUS), and so is at its strongest during austral summer, when the area of maximum diabatic heating shifts south over southern Africa. Topographic channelling of the flow through the east-west orientated Hoanib River valley is shown to facilitate the inland propagation of the anabatic-sea breeze, and explains the persistence of the system at Etosha's latitude. Evening surface winds at Etosha, associated with the anabatic-sea breeze, are significantly stronger in the dustier December months, when diabatic heating over the subcontinent and hence the zonal thermal gradient are enhanced.

Plain Language Summary

This paper uses satellite and meteorological data to identify the features of southern Africa's weather and climate that contribute to dust emission from the Etosha Pan throughout the year. Etosha is an important source of dust in the Southern Hemisphere, however very little work has been conducted there outside of the winter season, when emissions are at their highest. From the satellite data, it is shown that December is just as dusty as some of the winter months, however there is a difference in the low-level winds between the two seasons; in winter, emissions are driven by a morning peak in surface wind speeds, whereas emissions in December are driven by maximum surface winds during the evening. This evening peak in surface winds is shown to coincide with the arrival of a sea breeze at Etosha, with the system a response to the strong heating of the southern African plateau at this time of year. Evening surface winds associated with the sea breeze are stronger during the dustiest December months at Etosha, and are driven by enhanced heating over the subcontinent.

1 Introduction

Mineral aerosol (dust) has the ability to disturb atmospheric radiative transfer (Haywood & Boucher, 2000; Mahowald & Kiehl, 2003), fertilise marine and terrestrial ecosystems (Jickells et al., 2005; Koren et al., 2006; Mahowald et al., 2005; Wagener et al., 2008) and impact upon human health (Goudie, 2014; Middleton, 2017). For these reasons, dust constitutes an important component of the earth system, and so it is essential that it is accurately represented in state-of-the-art climate models (Boucher et al., 2013). In most coarse-resolution models, dust emission is parameterised, and is given as a function of the cube of surface wind speed u above a specified threshold u_t, so that;

$$q = (u - u_t)^3, when u > u_t \tag{1}$$

where q is the vertical sand flux (Knippertz & Todd, 2012; Kok et al., 2012). Realistic simulation of the emission process is therefore dependant on capturing the surface wind speed distribution in dust source areas, however evaluation studies show that models tend to miss the tail of low-frequency, high wind speed events that drive uplift (Evan, 2018; Roberts et al., 2017), an inevitable consequence of their inability to resolve some key atmospheric processes (Allen & Washington, 2014; Garcia-Carreras et al., 2013).

These key processes include the mix-down of momentum from nocturnal low-level jets (NLLJs) (Fiedler et al., 2013; Knippertz & Todd, 2012; Washington & Todd, 2005), downdrafts from convective storms (cold pool outflows) (Caton Harrison et al., 2021; Heinold et al., 2013; Marsham et al., 2013) and microscale dust devils or dry convective plumes (Jemmett-Smith et al., 2015; Knippertz & Todd, 2012). The current state of knowledge regarding these emission mechanisms comes largely from work conducted in a Saharan context, either through intensive observational campaigns (Washington et al., 2006), remote sensing (Schepanski et al., 2007, 2009) or modelling studies (Heinold et al., 2013; Todd et al., 2008). There are however other important dust source areas globally (Prospero et al., 2002; Washington et al., 2003), although very few studies have investigated the atmospheric controls on uplift outside of North Africa. Ge et al. (2016) use reanalysis data to characterise a NLLJ over the Taklimakan Desert, and show that it is the mix-down of momentum from the jet core that produces an enhancement of aerosol optical depth, consistent with work in the Sahara (Allen & Washington, 2014; Knippertz & Todd, 2012). Of the major Southern Hemisphere sources, the Lake Eyre basin in central Australia has received arguably the most attention, with for example Baddock et al. (2015) highlighting the importance of frontal systems in driving emission. Given the inability of models to capture salient features of the Saharan dust climatology (Evan et al., 2014; Roberts et al., 2017), more work is required to investigate dust-emitting mechanisms, and test model fidelity in other geographical regions.

Remote sensing studies have identified a number of dust source areas across southern Africa (Prospero et al., 2002; Vickery et al., 2013), the most prominent of which are the Etosha and Makgadikgadi pans (Washington et al., 2003), located in northern Namibia and northeastern Botswana resepectively. Whilst annual emissions are lower than those from the major North African sources (e.g., the Bodélé Depression), they are amongst the highest in the Southern Hemisphere, with dust loadings at Etosha comparable to those from the Lake Eyre Basin in Australia (Washington et al., 2003). Whilst previous work has detailed some of the hydrological controls on the availability of sediment from both of the pan surfaces (Bryant, 2003; Mahowald et al., 2003), and developed detection algorithms of dust plumes from satellite derived data (Murray et al., 2016), very little attention has been given to the atmospheric processes contributing to the observed dust loadings. Observational data has shown a NLLJ to be a persistent feature of the boundary layer from August – October (Clements & Washington, 2021; Zunckel et al., 1996), with the mix-down of momentum during the morning breakdown of the jet identified as the primary emission mechanism during this season (Clements & Washington, 2021). It

is not yet known however the extent to which the NLLJ sustains dust emissions beyond austral winter, or whether other atmospheric processes drive uplift at other points in the annual cycle.

Given the need to understand the atmospheric controls on dust emission, and subsequently refine the representation of relevant processes in numerical models, this paper aims to investigate the range of dust-emitting mechanisms operating throughout the annual cycle, in a relatively understudied yet regionally significant source area, by addressing the following key questions: (i) What is the annual cycle of dust emissions from the Etosha Pan? (ii) How do the atmospheric processes responsible for driving dust emission from the Etosha Pan vary through the annual cycle? (iii) What are the spatial and temporal characteristics of the dust emission mechanisms operating at the Etosha Pan, and what controls their variability? (iv) How does variability in the processes described help to account for variability in austral summer dust emissions from the Etosha Pan? The remainder of the paper is structured as follows: Section 2 describes the location and climatic setting of the study area and details the data sources and methods employed. Results are presented in Sections 3, 4, 5 and 6, with each of the key questions addressed in turn. The results are discussed in Section 7 and the papers main findings are summarised.

2 Data and Methods

2.1 Physical Setting

The Etosha Pan is a flat salt pan situated in northern Namiba, covering an area of ≈4,800 km^2 (Prospero et al., 2002). It sits in a topographic depression, and drains a network of ephemeral channels (locally known as oshanas), with the catchment stretching north into the southern Angolan highlands (Preston-Whyte et al., 1994). Rainfall in the catchment and hence inundation of the pan is limited to October – April, when the area of tropical convection moves south. Stable, dry conditions preside over the subcontinent during austral winter, resulting from strong subsidence associated with the descending limb of the overturning Hadley circulation (Reason, 2017).

2.2 TOMS AI Data

Aerosol Index (AI) data from the Total Ozone Mapping Spectrometer (TOMS) instrument is used to monitor dust emissions from the Etosha Pan between 1980 – 1992 (key question 1). During this time, the TOMS instrument was onboard the NASA Nimbus 7 polar-orbiting satellite and took measurements in six ultraviolet (UV) wavelengths, with the initial objective to track changes in the Earth's ozone (McPeters et al., 1996). However, given the absorbing properties of dust in UV wavelengths, the TOMS instrument has been used in numerous studies to identify major source areas (Prospero et al., 2002; Washington et al., 2003). The advantage UV remote sensing has over visible and infrared (IR) wavelengths is its low reflectivity over land surfaces (including deserts), making for efficient detection of airborne dust particles (Torres et al., 2002). For a more detailed analysis of the TOMS instrument, see McPeters et al. (1996).

AI data is given in non-dimensional units, with absorbing aerosols returning positive values, and for dust, the magnitude of the AI signal reflects the optical depth of the aerosol (Bryant, 2003; Herman et al., 1997). The temporal frequency of the data is daily, and it has been projected onto a latitude-longitude grid of resolution 1.0° x 1.0°. In order to monitor dust emissions at Etosha, AI data from the central grid point (18.5°S, 15.625°E) of the plume is used. In section 3, dust emissions at Makgadikgadi are also evaluated, with AI data also coming from the central grid point (20.5°S, 25.625°E) of the respective plume.

2.3 Reanalysis and Gridded Precipitation Data

ERA5 reanalysis data from the European Centre for Medium-Range Weather Forecasts (ECMWF) is used to identify the atmospheric processes contributing to dust emission at Etosha (key question 2), and investigate their spatial and temporal characteristics, as well as the controls on their variability (key question 3). ERA5 data covers the period 1950–present, with analysis fields output at hourly intervals, at a spatial resolution of ≈31 km, and 137 model levels in the vertical. Parameters extracted from the ERA5 dataset for analysis include u and v components of wind (10m and model level), temperature (2m, model and pressure level), specific humidity (model level), top net thermal radiation and divergence (model level). Wind speed was calculated as the square root of the sum of the squared u and v components at each grid point (ws= $\sqrt{u^2 + v^2}$), outgoing longwave radiation (OLR) was calculated as the negative of top net thermal radiation, divided by the averaging period (3600s), whilst potential temperature was calculated from the Poisson equation ($\theta = T(P_0/P)^k$), where T is air temperature, P_0 is a reference pressure of 1,000 hPa, P is the atmospheric pressure and k is the Poisson constant. Where atmospheric data is presented for Etosha, the grid point closest to the centre of the pan (18.5°S, 15.625°E) is used.

The ERA5 dataset benefits from over a decade of research and development since the release of the previous ECMWF reanalysis (ERA-Interim), with an increase in hor-

izontal resolution, an improved data assimilation methodology and refined parameterisation schemes (Hersbach et al., 2020). Upgrades to model parameterisations include the adoption of the 'McRad' radiation scheme (Morcrette et al., 2008), improvements to the original precipitation and convective schemes (Bechtold et al., 2014), as well as advances in the treatment of subgrid turbulent mixing and orographic drag effects (Hersbach et al., 2020). ERA5 also features a new land surface scheme (HTESSEL), which, through the adoption of satellite derived vegetation datasets, has improved the representation of variables such as temperature and humidity at the surface (Boussetta et al., 2013; Hersbach et al., 2020). For a detailed discussion of the ERA5 reanalysis, including data assimilation systems, model setup, and an overview of performance, see Hersbach et al. (2020).

In section 3, precipitation data from the Climate Hazards Group InfraRed Precipitation with Station data (CHIRPS) version 2.0 is used to investigate the effect of inundation on dust emissions at Etosha. CHIRPS utilises satellite derived rainfall estimates in conjunction with station gauge data to produce a daily gridded precipitation dataset from 1981 to near-present with a 0.05°, 0.05° horizontal resolution (Funk et al., 2015). In southern Africa, gauge data is provided by the Southern African Science Service Centre for Climate Change and Adaptive Land Management (SASSCAL) (Funk et al., 2015). For a full discussion of the CHIRPS dataset, see Funk et al. (2015).

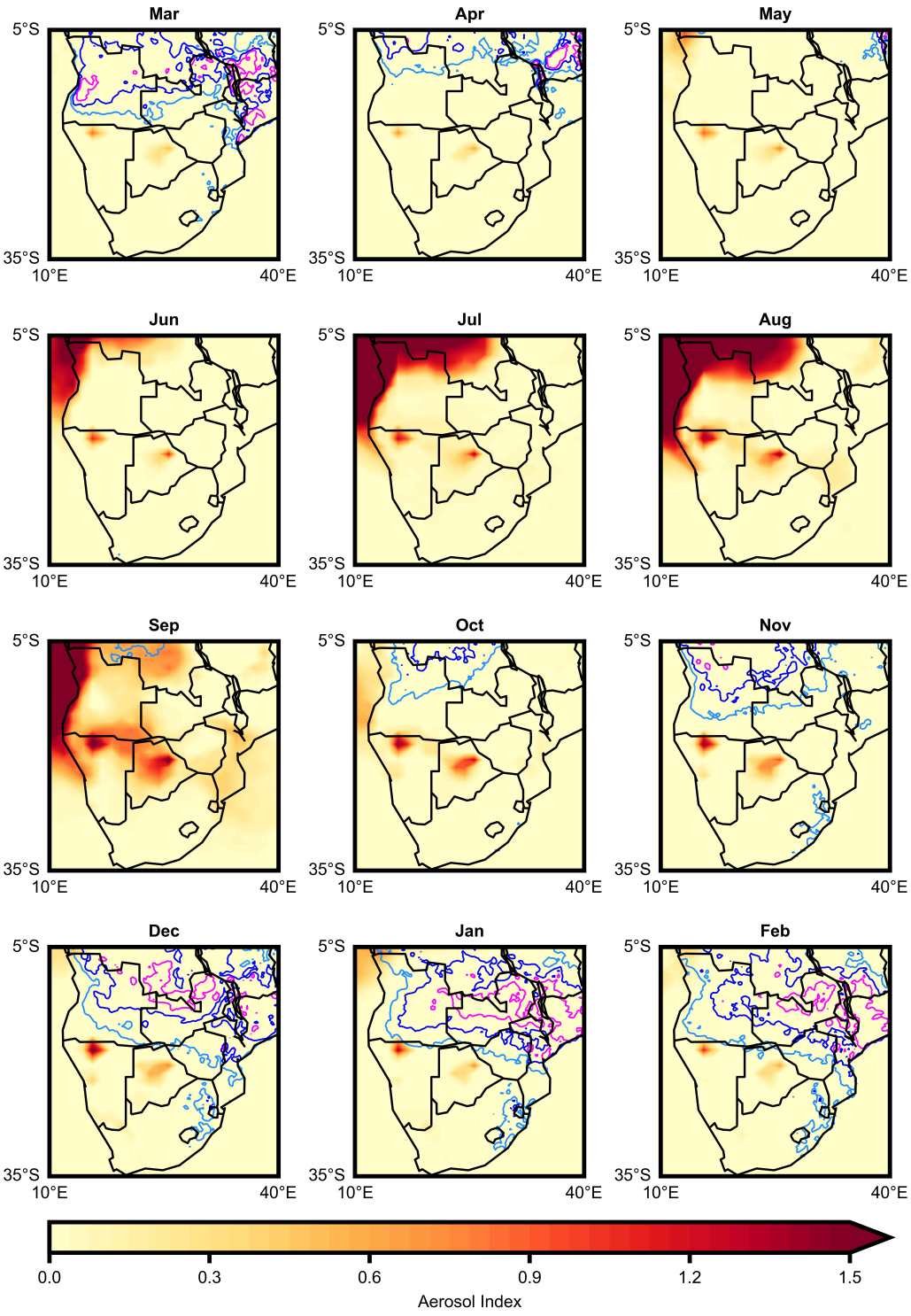


Figure 1. Mean TOMS AI data for 1980-1992. Mean precipitation data for 1981-1992 from the CHIRPS dataset is plotted as 4mmday^{-1} (light blue), 6mmday^{-1} (blue) and 8mmday^{-1} (purple) contours.

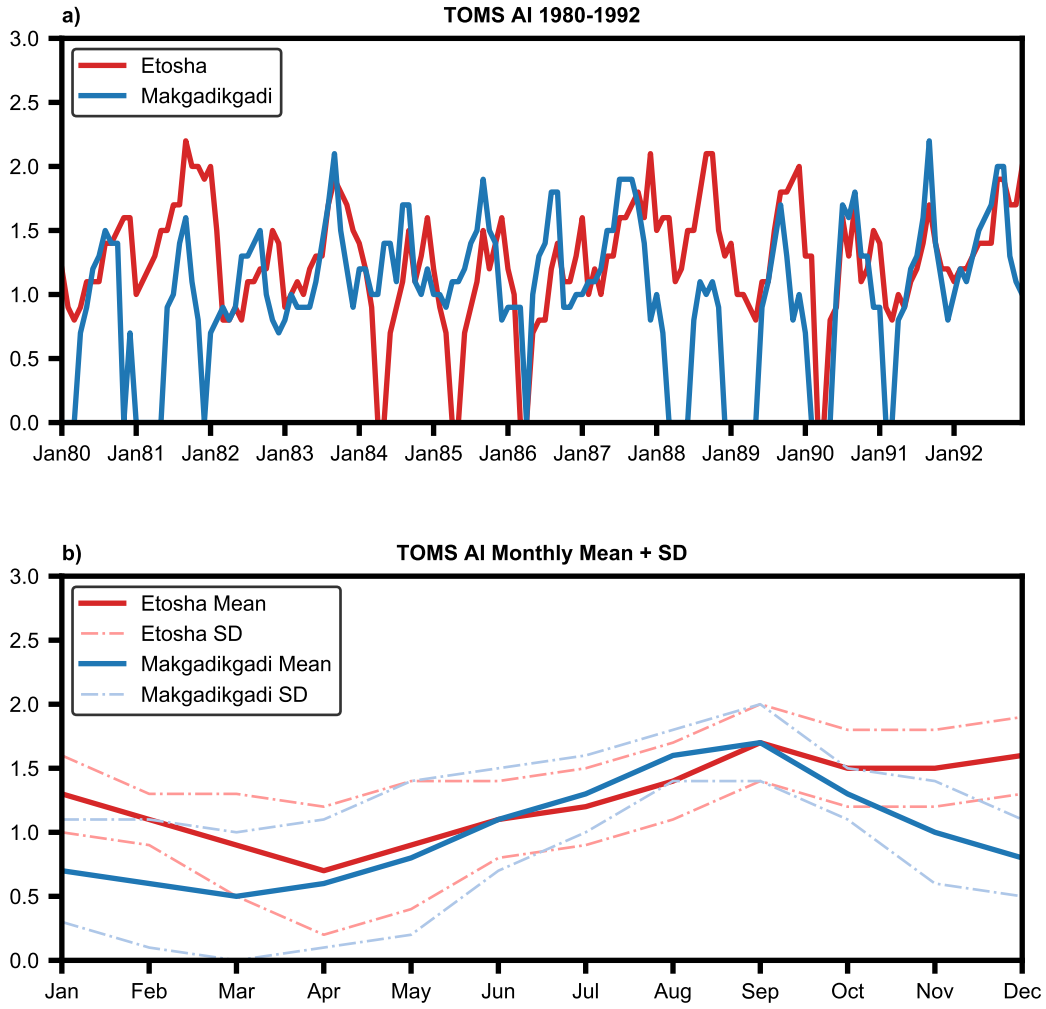


Figure 2. (a) Time series of AI data for the Etosha and Makgadikgadi pans, 1980-1992. (b) Monthly mean and standard deviation of AI for the Etosha and Makgadikgadi pans.

3 Annual Cycle of Dust Emissions at Etosha

The following sections address key question 1: What is the annual cycle of dust emissions from the Etosha Pan?

3.1 Annual Cycle of Dust Emissions

Mean AI data from the TOMS instrument shows two major dust source areas in southern Africa (Figure 1); these are the Etosha and Makgadikgadi Pans, located in northern Namibia (18.75°S, 16.25°E) and north-eastern Botswana (20.75°S, 25.50°E) respectively. Previous studies have utilised TOMS data to demonstrate the predominance of these two source areas in their contribution to total southern African dust emissions (Prospero et al., 2002; Washington et al., 2003), with higher-resolution satellite data exposing more minor contributions from coastal Namib sources and the Kalahari (Murray et al., 2016; Vickery et al., 2013). The high (>1.5) mean AI values observed along the coast of Angola and northern Namibia from June to September (Figure 1) are not indicative of dust aerosol emissions, but are instead the result of savannah fires in the interior of the subcontinent (Herman et al., 1997; Sinha et al., 2003). The biomass burning aerosols are subsequently transported north-westward out over the Atlantic by the tropical easterlies which form part of the inflow towards the convective regions further north (Adebiyi & Zuidema, 2016; Reason, 2017).

Table 1. *TOMS AI Statistics 1980-1992*

	Etosha		Makgadikgadi	
Month	AI Mean	AI SD	AI Mean	AI SD
Jan	1.3	0.3	0.7	0.4
Feb	1.1	0.2	0.6	0.5
Mar	0.9	0.4	0.5	0.5
Apr	0.7	0.5	0.6	0.5
May	0.9	0.5	0.8	0.6
Jun	1.1	0.3	1.1	0.4
Jul	1.2	0.3	1.3	0.3
Aug	1.4	0.3	1.6	0.2
Sep	1.7	0.3	1.7	0.3
Oct	1.5	0.3	1.3	0.2
Nov	1.5	0.3	1.0	0.4
Dec	1.6	0.3	0.8	0.3

Figure 2a shows a time series of AI data for the Etosha Pan between 1980 – 1992, with monthly mean and standard deviation data plotted in Figure 2b and also summarised in Table 1. For reference, AI data for the Makgadikgadi Pan, southern Africa's other major dust source area, is also included. Dust emissions across the subcontinent increase through the winter months (Figure 2b), and peak at the end of the dry season (September), when the highest mean AI values are recorded at both Etosha (AI = 1.7) and Makgadikgadi (AI = 1.7) (Table 1), with a plume also stretching between the two source areas across the northern Kalahari (Figure 1). Mean AI values remain high (>1.5) at Etosha through spring and into summer; indeed, other than September, December (AI = 1.6) is the dustiest month in the TOMS record. This is in contrast to Makgadikgadi, where mean AI values fall to below 1.0 by December, and remain low (<1.0) through the rest of the summer months. Dust emissions across southern Africa reach a minimum from March to May, with mean AI values below 1.0 recorded for both major source areas.

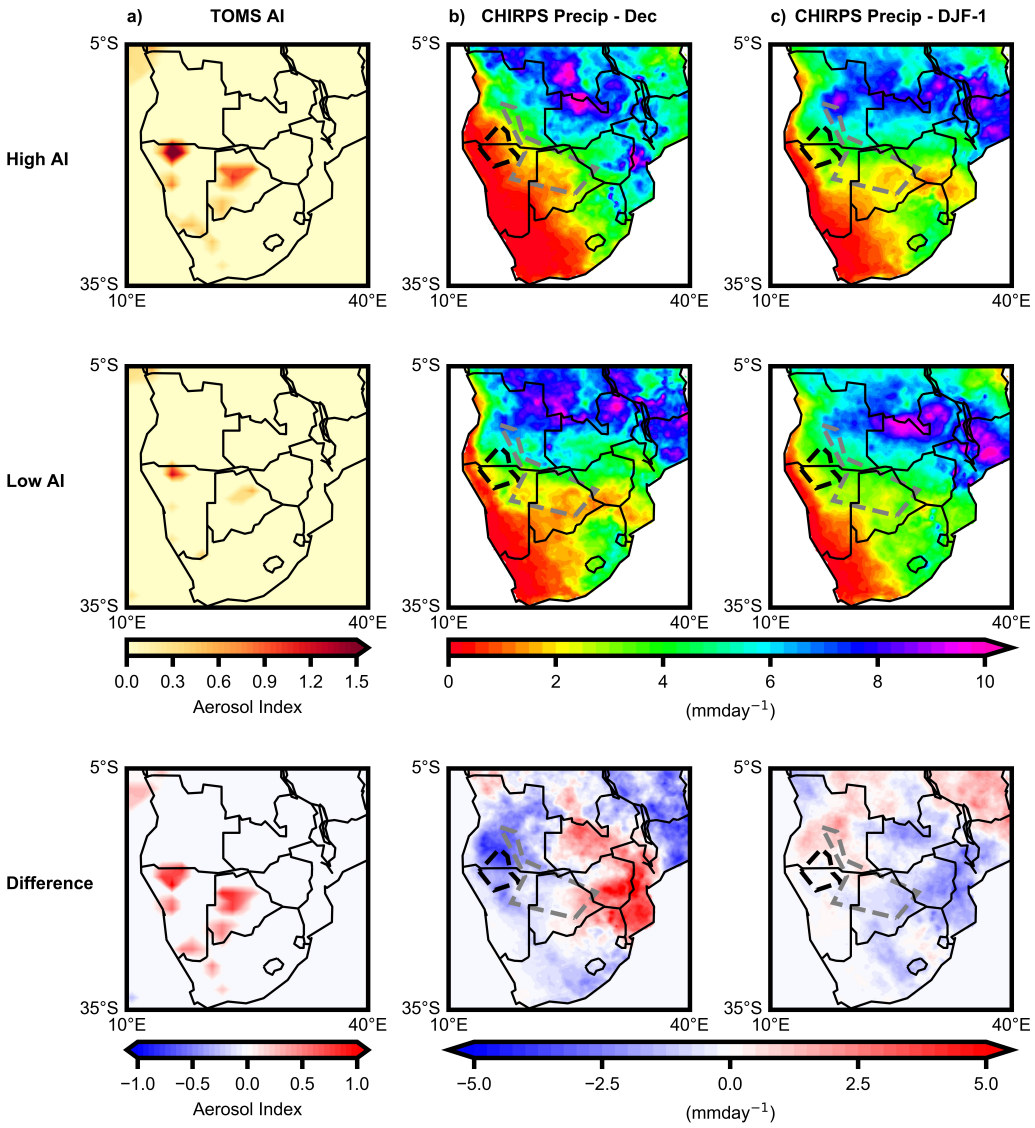


Figure 3. High AI, low AI and difference composites for December months at Etosha of (a) AI, (b) December precipitation and (c) precipitation in the preceding DJF. The difference composites were calculated by subtracting the low AI from the high AI. In (b) and (c), the approximate location of Etosha's catchment is given by the black polygon and Makgadikgadi's by the grey.

3.2 Austral Summer Dust Emissions

The annual cycle of dust emissions at Etosha (and Makgadikgadi) described in section 3.1 is closely linked to the annual cycle of wetting and drying across southern Africa, with fluvial input to the pan regulating the availability of erodible sediment (Bryant, 2003; Murray et al., 2016). Precipitation contours are shown on Figure 1, and reflect the southward migration of the tropical rainbelt during spring and summer, as well as the transition of the Angola Low from a dry to a moist convecting system (Howard & Washington, 2018; Munday & Washington, 2017; Reason, 2017). Shallow inundation events occur at Etosha during the wet season (October – April), and whilst initially suppressing dust emissions, they provide material that is readily deflated once dry (Bryant, 2003; Mahowald & Kiehl, 2003). Previous remote sensing studies have documented the resulting peak in dust emissions towards the end of the dry season (August – October) at Etosha (Prospero et al., 2002; Vickery et al., 2013; Washington et al., 2003), however very little attention has been given to summer dust emissions; this is despite the observation presented in section 3.1 that mean AI values in December are the second highest for any month in the TOMS record.

Table 2. *Etosha TOMS AI Statistics*

	September		December	
Year	AI Mean	Days AI >2	AI Mean	Days AI >2
1980	1.4	2	1.6	7
1981	2.2	19	1.9	14
1982	1.2	0	1.4	4
1983	1.9	12	1.5	8
1984	1.5	2	1.6	10
1985	1.5	0	1.6	9
1986	1.4	2	1.3	4
1987	1.7	10	2.1	16
1988	2.1	19	1.3	3
1989	1.8	6	2.0	15
1990	1.7	2	1.5	6
1991	1.7	7	1.2	0
1992	1.9	13	2.0	18

Table 2 shows mean AI data for each December at Etosha between 1980 – 1992, with the number of individual days where values exceeded 2.0 also reported. The three dustiest December months (1987, 1989, 1992) and the three least dusty (1986, 1988, 1991) were used to construct composites of AI and precipitation (from the CHIRPS dataset) (Figure 3). Precipitation composites for the preceding summer season (DJF-1) are also shown. Difference composites were calculated by subtracting the low AI composite from the high AI composite. As well as a more substantial plume at Etosha, greater AI values are observed across other parts of southern Africa in the high AI composite, with increased dust emissions at Makgadikgadi, across the southern Kalahari and along the Namib coast (Figure 3a). It is also drier in the Etosha catchment during the dusty December months, whereas elevated precipitation totals stretch into northern Namibia and southern Angola in the low AI composite (Figure 3b).

These findings, as well as the fact that the three dustiest December months at Etosha (1987, 1989, 1992) are immediately preceded by the three least dusty (1986, 1988, 1991) (Figure 2a, Table 2), suggest a strong hydrological influence on the availability of sed-

iment during summer. A possible explanation is that increased precipitation in the Etosha catchment in the preceding DJF results in intermittent flow events and fluvial input into the pan. This at first suppresses dust emissions, but replenishes the supply of sediment, which is then deflated in the following year. Due to the increased wetting of the pan surface, the deposited sediment requires a prolonged period of drying before it can be entrained, hence shifting the timing of peak dust emissions from late winter to December. There is however very little difference in the preceding DJF precipitation between the high and low AI composites (Figure 3c), and so a far more likely explanation is that precipitation has an immediate impact in suppressing summer dust emissions, as is the case in the least dusty December months (Figure 3b). This reasoning is also corroborated by the coincidence of the dustiest December month (1987) with strong El Niño conditions; these events are associated with suppressed tropical convection over southern Africa, and hence reduced input to the Etosha pan. The decrease in AI values at Makgadikgadi through the spring and summer months owes to the location of the catchment area (further north and east), which results in earlier inflow to the pan, hence precluding dust emissions.

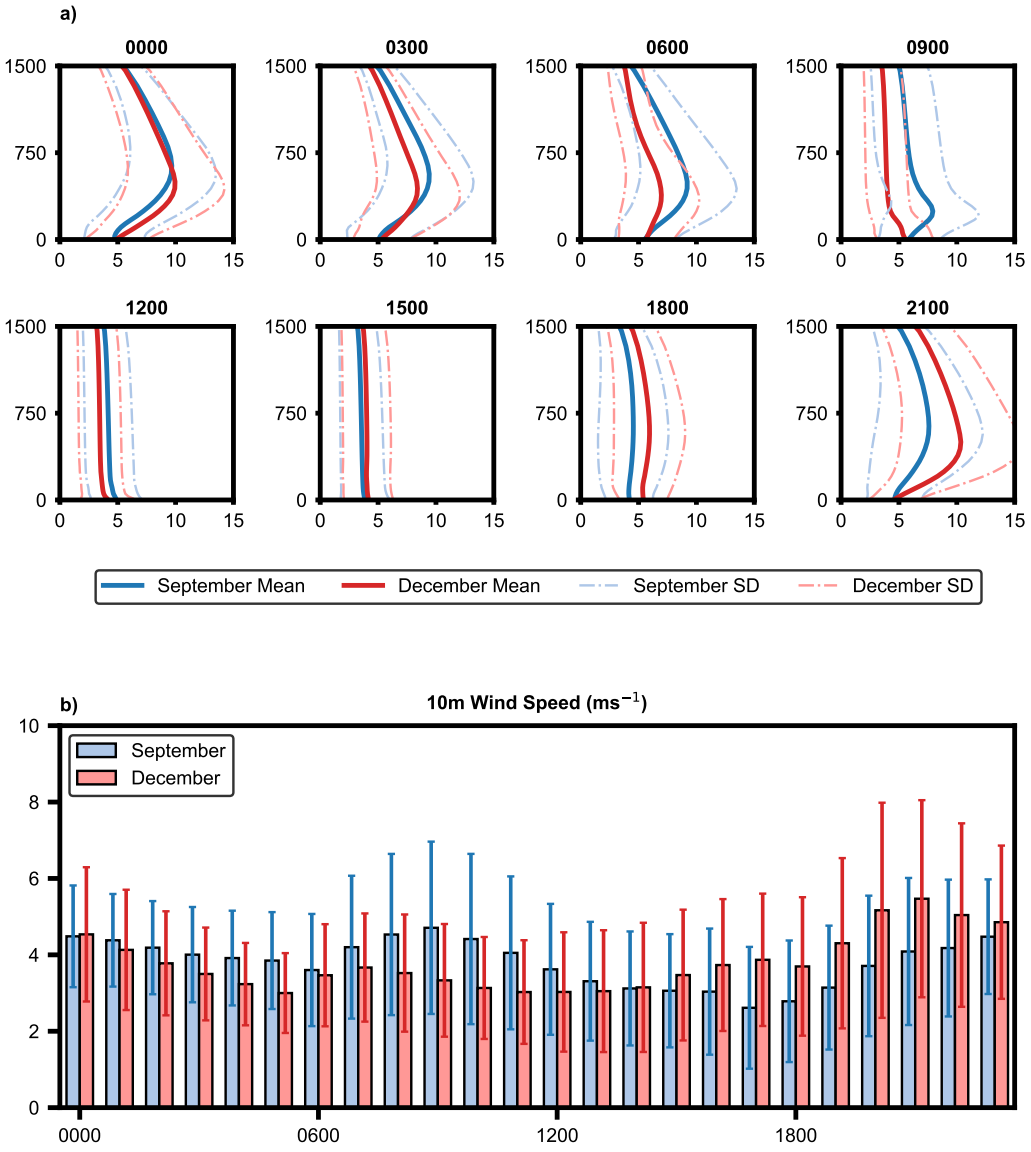


Figure 4. (a) Wind speed-height profiles for high AI September and December composites at Etosha. (b) Diurnal cycle of 10m wind speed for high AI September and December composites at Etosha. All data from ERA5.

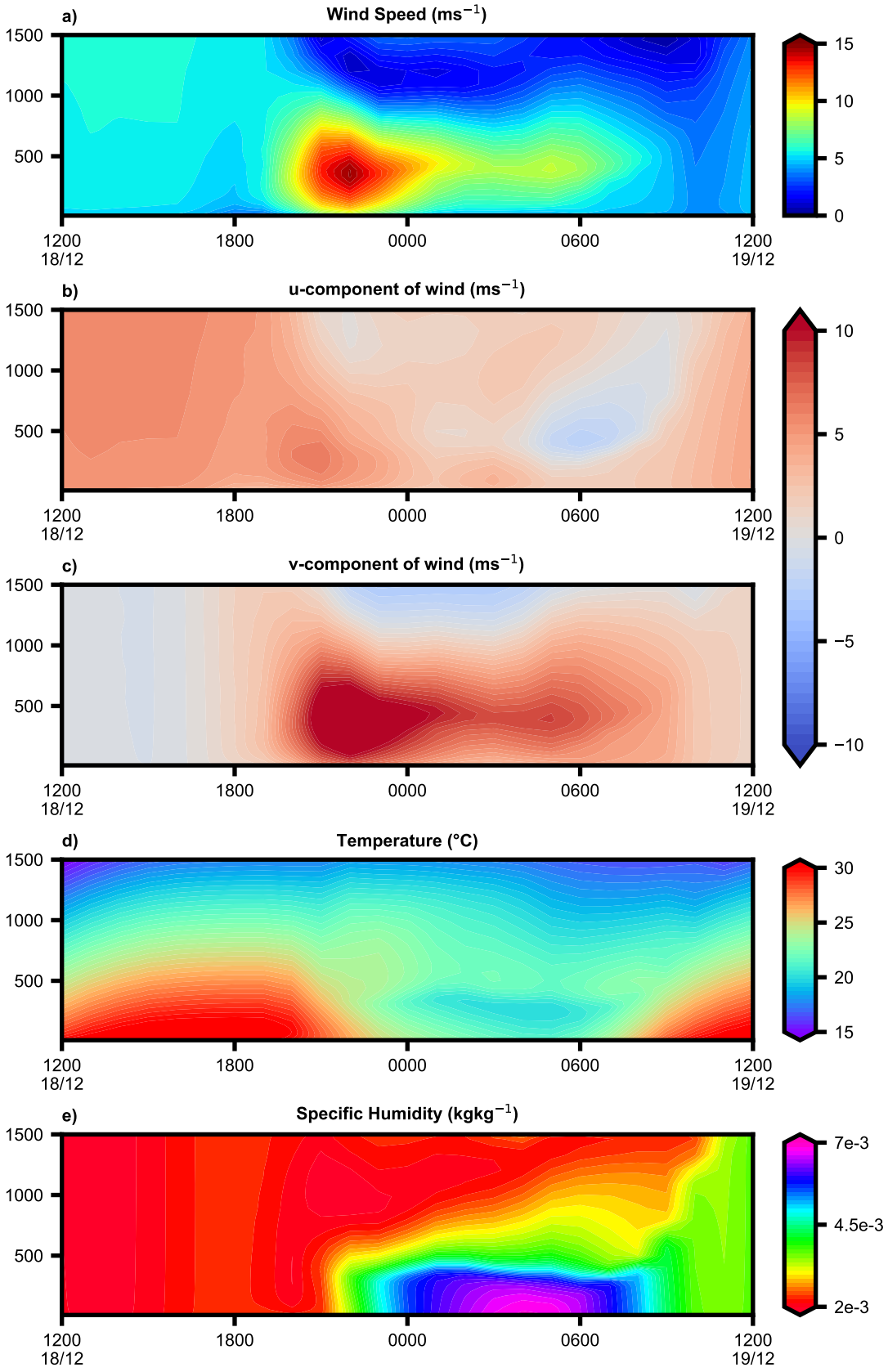


Figure 5. Time-height cross sections of (a) wind speed, (b) u, (c) v, (d) temperature and (e) specific humidity for the period 1200 18 Dec 87 - 1200 19 Dec 87 at Etosha. The 19 Dec is the second dustiest December date in the TOMS record. All data from ERA5.

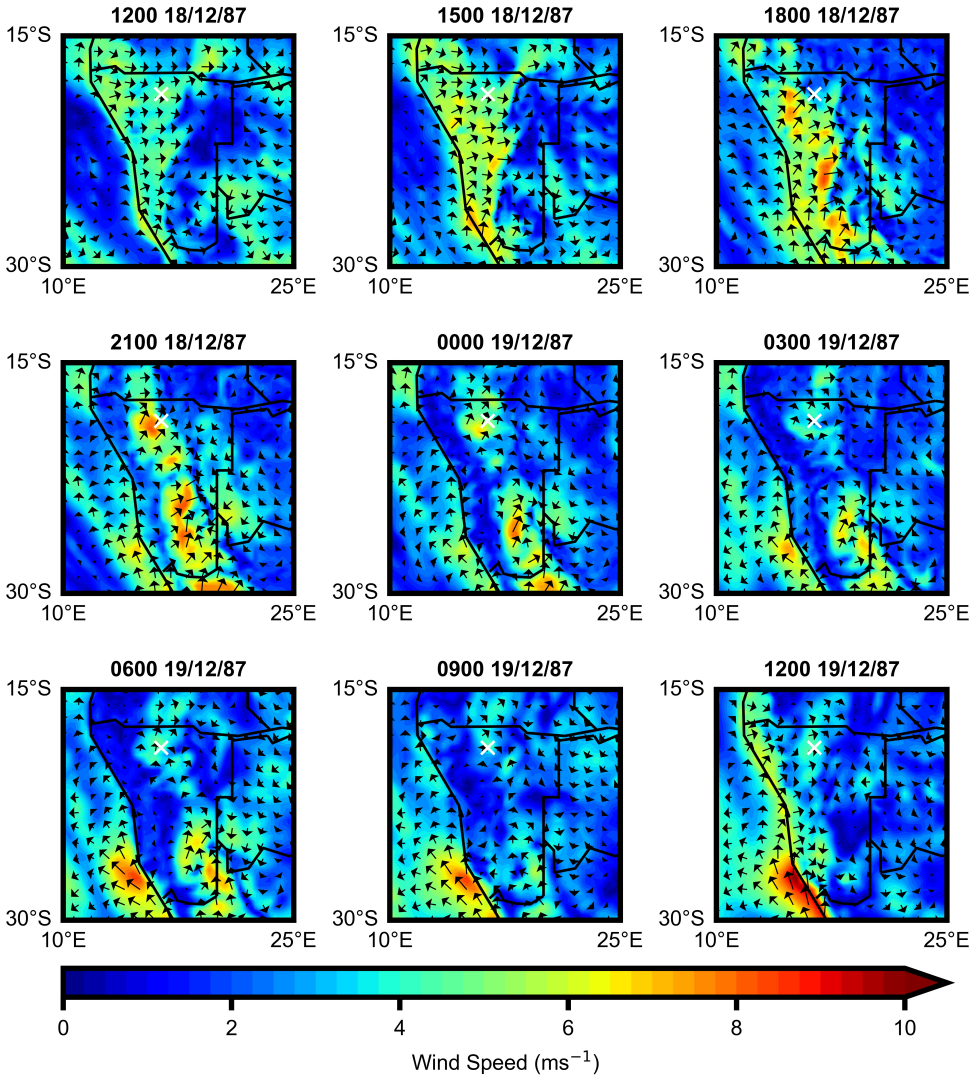


Figure 6. 10m wind speed and vectors for the period 1200 18 Dec 87 - 1200 19 Dec 87. Etosha's location is given by the white cross. The 19 Dec is the second dustiest December date in the TOMS record. All data from ERA5.

4 Atmospheric Controls on Dust Emissions at Etosha

The following sections address key question 2: How do the atmospheric processes responsible for driving dust emission from the Etosha Pan vary through the annual cycle?

4.1 Nocturnal Low-Level Jet

Previous work at Etosha has focused on dust emissions at the end of the dry season, with the mix-down of momentum from a NLLJ identified as the primary emission mechanism (Clements & Washington, 2021). In order to investigate whether the NLLJ is a driver of summer dust emissions, composite wind speed-height profiles have been constructed using ERA5 data for the three dustiest December months in the TOMS record (1987, 1989, 1992) (Figure 4a); for reference, profiles for the three dustiest September months (1981, 1988, 1983) (Table 2) are also shown. September was chosen as it is the dustiest month in the TOMS record, and in-situ observational data has shown the NLLJ to be a persistent feature of the nocturnal boundary layer during the month (Clements & Washington, 2021; Zunckel et al., 1996). Model level data from ERA5 has also been shown to capture well the main features of the NLLJ at Etosha (Clements & Washington, 2021), and so is a pragmatic choice of reanalysis. The diurnal cycle of 10m wind speed for the September and December composites are shown in Figure 4b, also constructed from ERA5 data.

A wind speed-height profile akin to a NLLJ is evident in the December composites (Figure 4a), however the timing of its development and breakdown are not consistent with the theory of frictional decoupling typically associated with jets that form in dryland environments (Blackadar, 1957; Fiedler et al., 2013). A jet profile is first observed at 2100, however this is also the time of peak core wind speeds, with the structure beginning to erode long before sunrise (≈0415) and the onset of surface heating. This is in contrast to the evolution of the NLLJ in September, which strengthens through the nocturnal period, peaks in the hours around sunrise (≈0500) and is subsequently eroded with the increase of eddy viscosity in the daytime boundary layer. These contrasts are reflected in the diurnal cycle of surface winds (Figure 4b); in September, there is a peak between sunrise and midday (≈0900) associated with the mix-down of momentum from the NLLJ as it is eroded, however no such peak is evident in December. Instead, surface wind speeds increase during the evening and peak at 2100, around the time at which the jet profile is also at its strongest (Figure 4a).

4.2 Austral Summer Dust Event Case Study: 19 Dec 1987

The findings presented in section 2.1 suggest that processes other than the mix-down of momentum from a NLLJ are responsible for driving dust emission at Etosha during December. In order to further investigate, Figures 5 and 6 present ERA5 data from midday on 18 December 1987 to midday on 19 December 1987; the 19 December (AI = 3.3) is the second dustiest December date in the TOMS record and the joint second dustiest date for any month. Figure 5 shows time-height cross sections of wind speed, u, v, temperature and specific humidity at Etosha, whilst Figure 6 shows 10m wind speed and vectors for a selected area of southern Africa.

Peak wind speeds (>15ms^{-1}) are recorded at Etosha during the evening of the 18 December in a core ≈300-500m above the surface (Figure 5a). This is consistent with the December composites shown in Figure 4a, which also displayed a core of enhanced wind speeds at ≈500m peaking in the 2100 profile. This flow is associated with an integrated sea breeze-topographic wind (hereinafter referred to as an anabatic-sea breeze) which develops along the Namib coast from 1200 on the 18 December, and propagates inland to reach Etosha by 2100 on the same evening (Figure 6). By the time the sea breeze

front has reached Etosha, the flow has been deflected by Coriolis to give a large southerly component (Figure 5c), and the arrival of air from the Atlantic is accompanied by a drop in temperature (Figure 5d) and sharp increase in the moisture content of the atmosphere (Figure 5e). The inland propagation of the sea-breeze front provides the only intensification of surface wind speeds at Etosha prior to the TOMS signal on the 19 December (Figure 6), and is a plausible atmospheric driver of summer dust emissions.

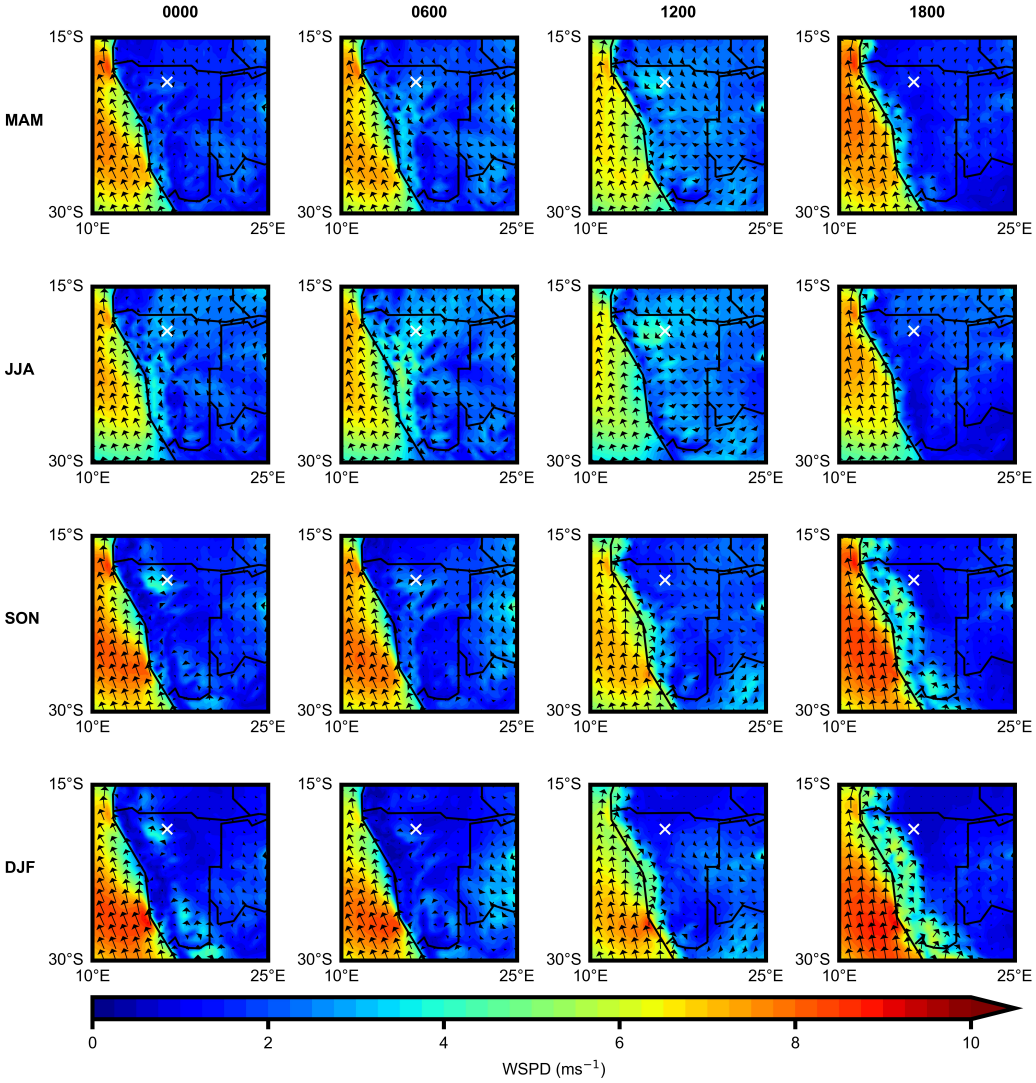


Figure 7. Seasonal climatologies (1981-2010) of 10m wind speed and vectors for 0000, 0600, 1200 and 1800. Etosha's location is given by the white cross. All data from ERA5.

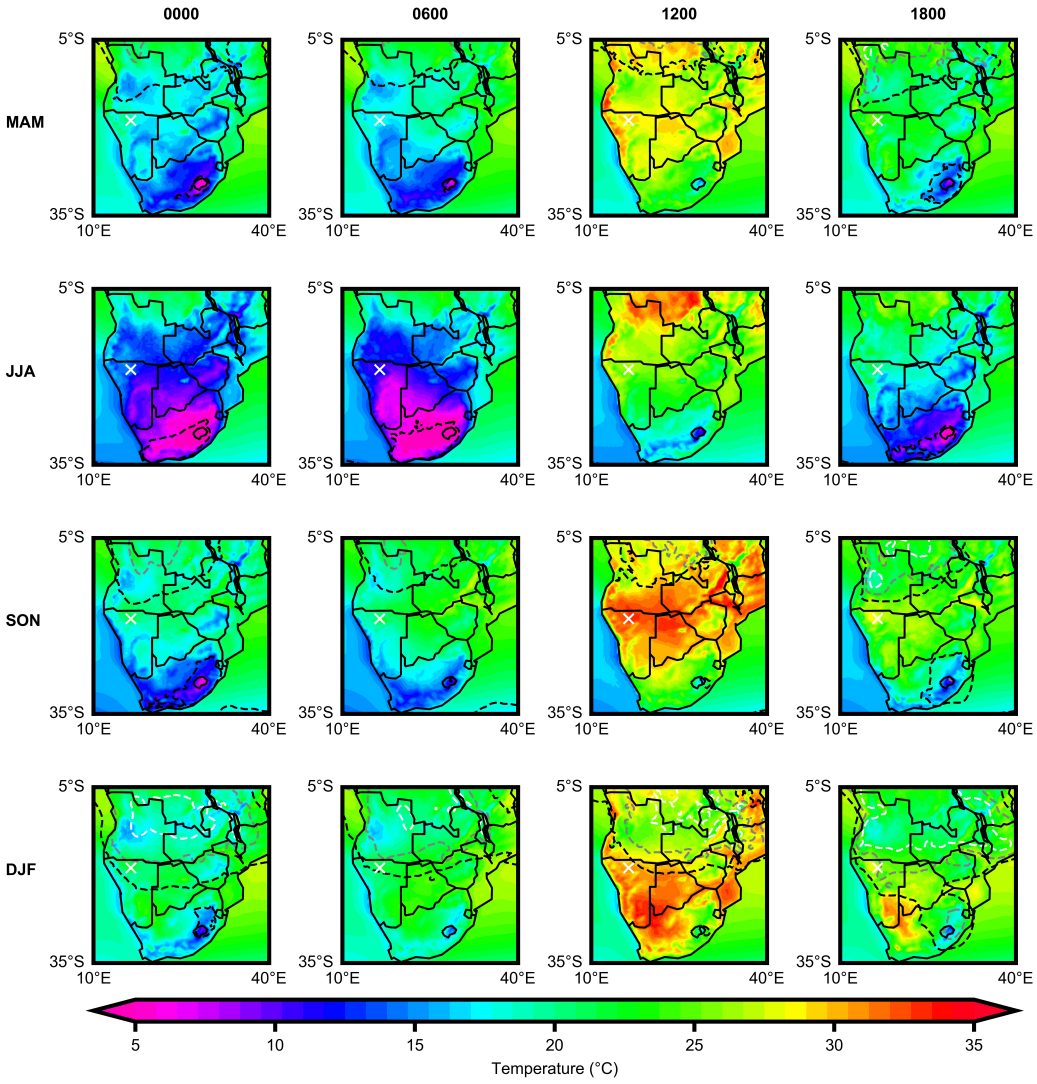


Figure 8. Seasonal climatologies (1981-2010) of 2m temperature and OLR for 0000, 0600, 1200 and 1800. OLR contours are plotted at 200Wm^{-2} (white), 225Wm^{-2} (grey) and 250Wm^{-2} (black). Etosha's location is given by the white cross. All data from ERA5.

5 Climatology of Dust Emission Mechanisms at Etosha

The following sections address key question 3: What are the spatial and temporal characteristics of the dust emission mechanisms operating at the Etosha Pan, and what controls their variability?

5.1 Annual Cycle

Figures 7 and 8 show seasonal climatologies of 10m wind speed and 2m temperature respectively, for selected areas of southern Africa, both constructed from ERA5 data. OLR contours are also included on Figure 8. The mix-down of momentum from a NLLJ is evident at 0600 and 1200 during winter (JJA) and is manifest as a region of enhanced wind speeds across northern Namibia, embedded within the prevailing anticyclonic flow around southern Africa (Figure 7). A detailed analysis of the characteristics of the NLLJ and the controls on its variability has been given by Clements and Washington (2021), and so is not addressed any further in this section.

The anabatic-sea breeze system is present throughout the year, however its strength and the extent of its inland propagation varies considerably by season. In autumn (MAM) and winter, when diabatic heating over the interior of southern Africa is at a minimum (Figure 8), the system is confined to the coastal plains of the Namib below the level of the escarpment, and can be seen as a slight onshore rotation of the trade winds at 1200 and 1800 (Figure 7). Also prominent during winter along the escarpment is an easterly katabatic-land breeze that develops through the nocturnal period (0000) and is at its strongest in the early morning (0600).

As the area of maximum diabatic heating moves south over the central plateau during spring (SON) (Figure 8), the anabatic-sea breeze system strengthens, and subsequently peaks in intensity during summer (DJF) (Figure 7). At this time of year, the area of maximum diabatic heating is over the southern Kalahari and Northern Cape region of South Africa, establishing a strong thermal contrast between the warm, elevated plateau, and the relatively cool waters of the Benguela Upwelling System (BUS). The BUS extends from the southwestern tip of South Africa to the Angola-Benguela Front (ABF) (≈15°S-17°S), with south-easterly wind stress imparted by the trade winds and subsequent offshore Ekman transport driving upwelling of nutrient-dense waters from below the thermocline (Colberg & Reason, 2006; Reason, 2017). The annual cycle of sea surface temperatures (SST's) lags the latitudinal shift in diabatic heating (Figure 8), so that maximum SST's are recorded in the BUS from February – March (when interannual variability in the position of the ABF is also at a maximum (Florenchie et al., 2004)); in the early summer months (e.g. December), conditions are therefore optimal for the development of the anabatic-sea breeze south of the ABF, with intense heating of the interior plateau coupled with relatively cool SST's. After setting in at the coast by midday, the system propagates inland through the afternoon, so that by 1800, a 300km-wide band of south-westerly winds associated with the anabatic-sea breeze stretches from southern Angola to the Karoo Desert. This delayed propagation of the system is consistent with the theoretical work of Rotunno (1983), who states that for locations where the Coriolis parameter is less than the frequency of the oscillatory source of energy (i.e., the diurnal cycle in surface heating), which is true for latitudes less than 30°, the sea-breeze system lags the heating by 180°. Through the evening, the sea breeze front separates from the coast as it continues to move inland, and can be observed in a number of preferential latitudinal bands by 0000.

5.2 Spatial and Temporal Characteristics in Austral Summer

In order to further examine the structure of the anabatic-sea breeze and its diurnal evolution, this section focuses on its characteristics during summer, the season in which

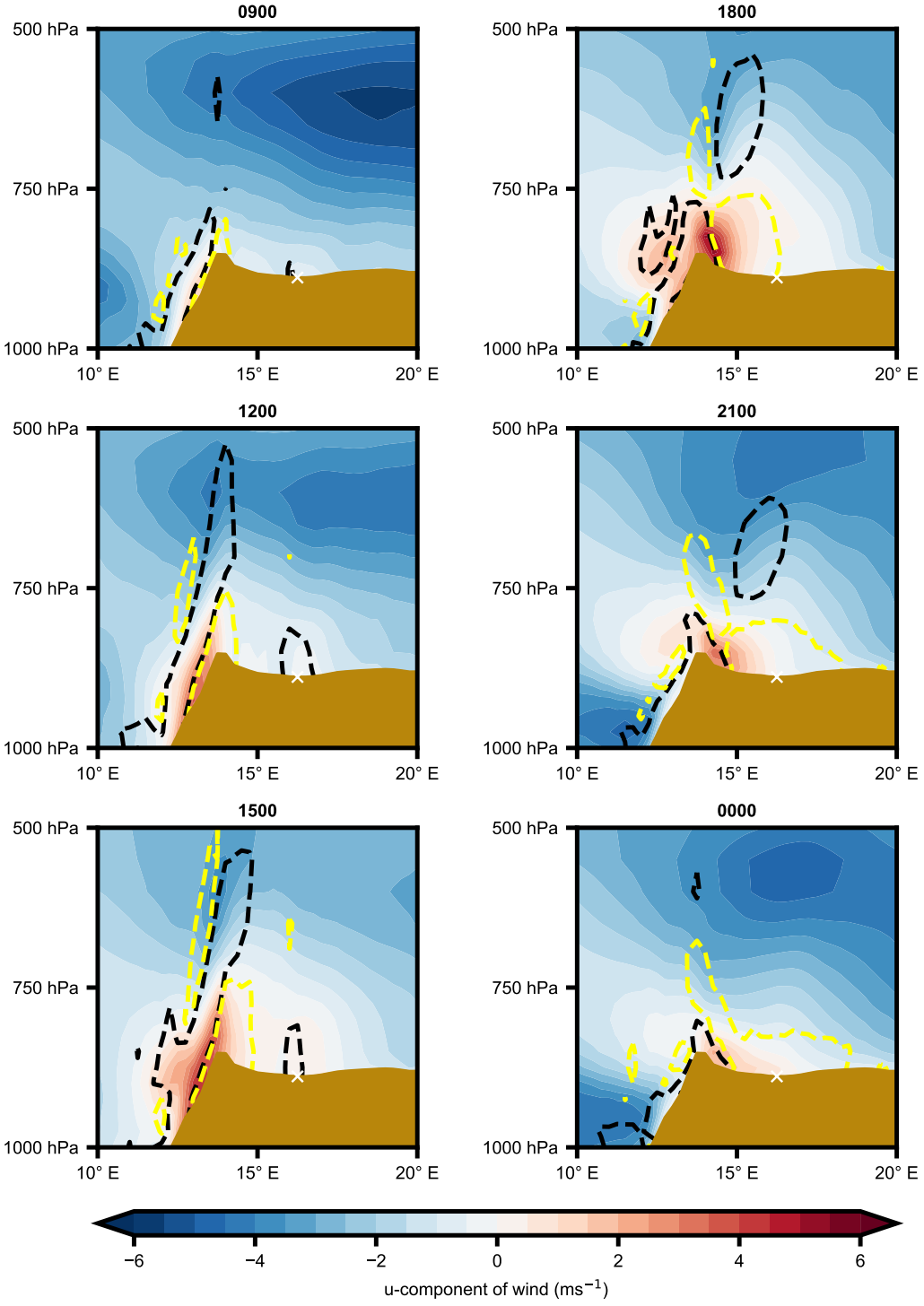


Figure 9. Longitude-height cross section climatology (1981-2010) for DJF of the zonal wind component and divergence (convergence). Areas of divergence (convergence) greater than (less than) 1.0x10^{-5}s^{-1} (-1.0x10^{-5}s^{-1}) are shown by the black (yellow) contours. The cross section is plotted at Etosha's latitude (-18.75), with Etosha's longitude given by the white cross. All data from ERA5.

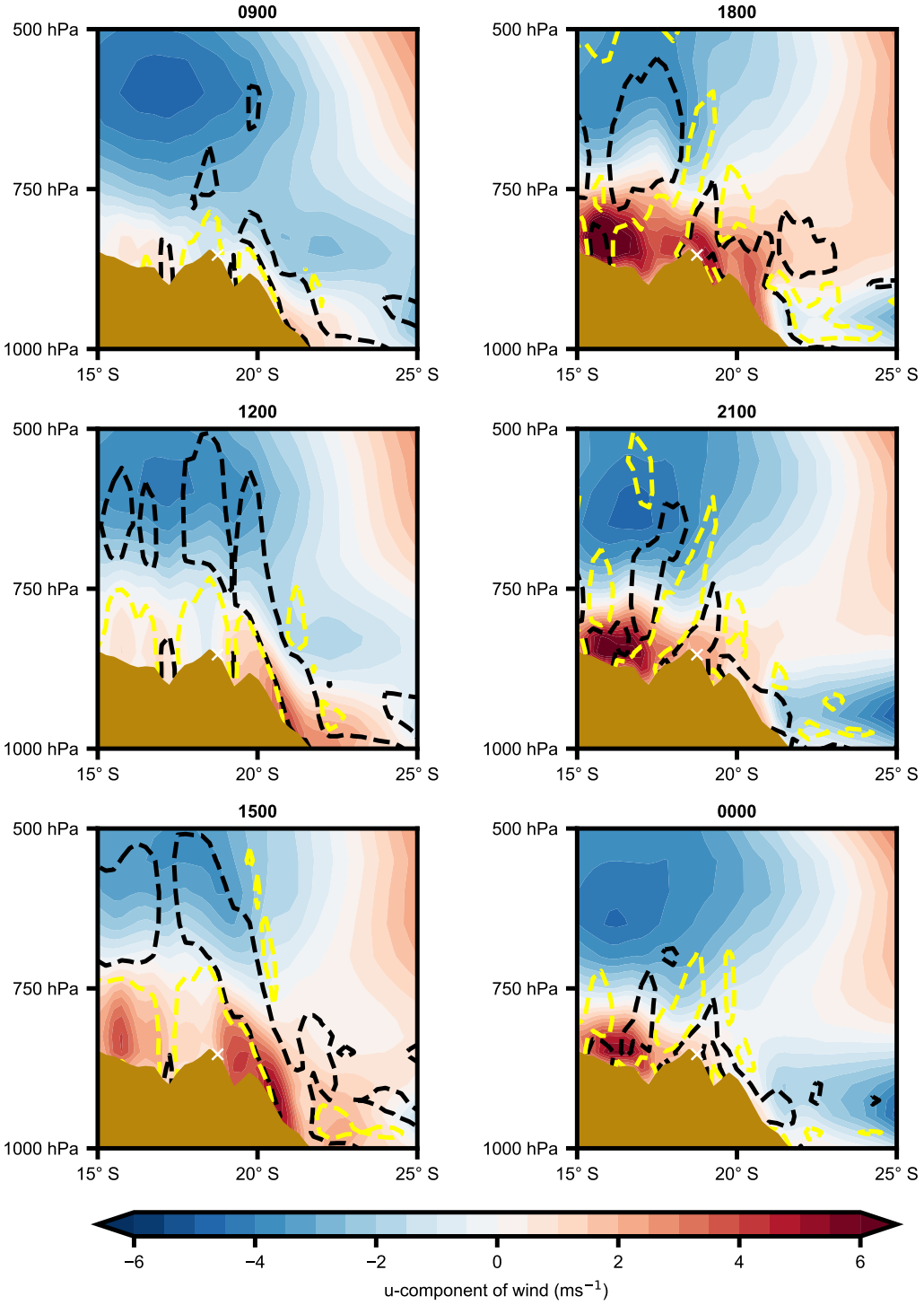


Figure 10. Latitude-height cross section climatology (1981-2010) for DJF of the zonal wind component and divergence (convergence). Areas of divergence (convergence) greater than (less than) 1.0x10^{-5}s^{-1} (-1.0x10^{-5}s^{-1}) are shown by the black (yellow) contours. The cross section is plotted at 14°E, with Etosha's latitude given by the white cross. All data from ERA5.

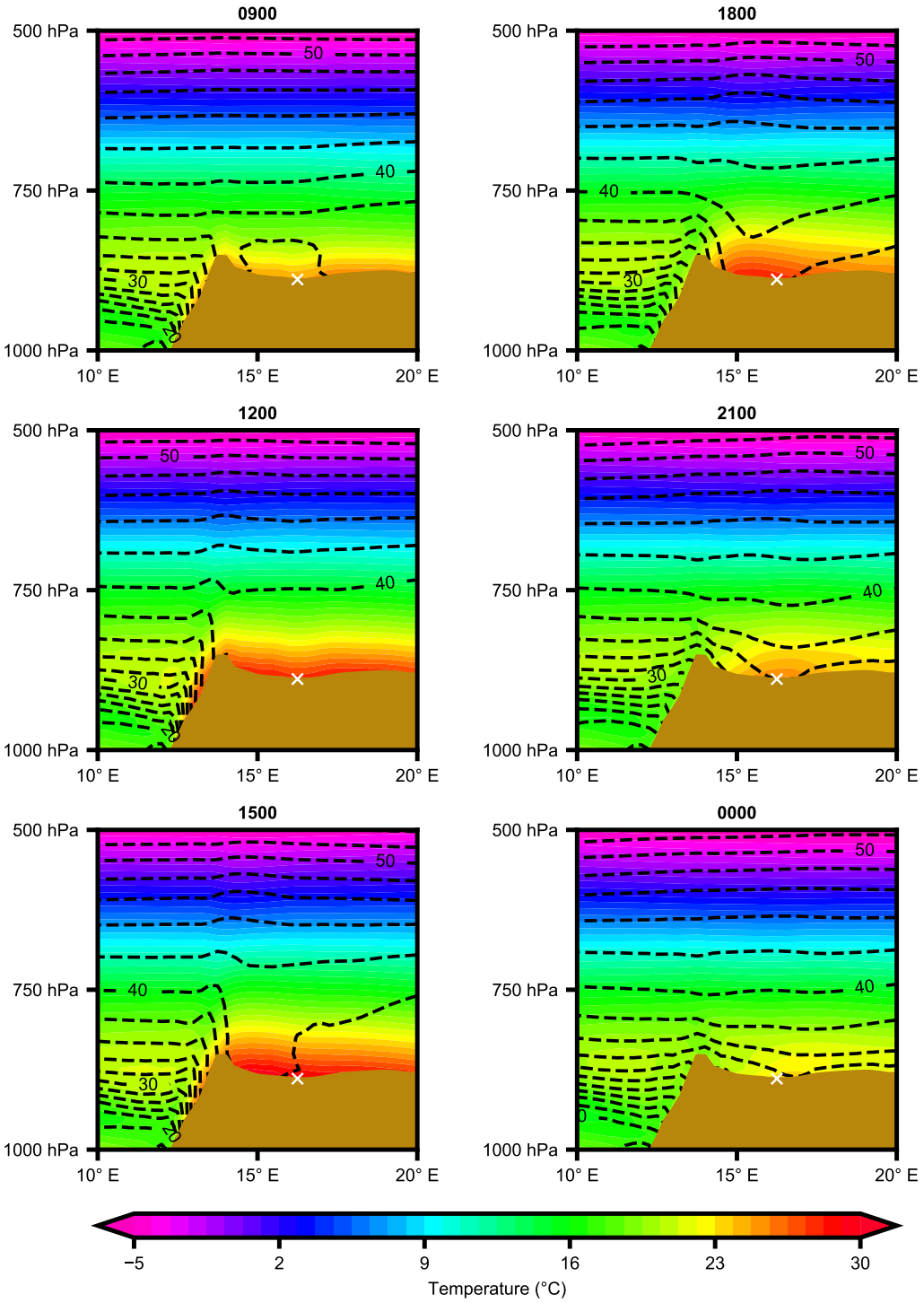


Figure 11. Longitude-height cross section climatology (1981-2010) for DJF of temperature and potential temperature (contours). The cross section is plotted at Etosha's latitude (-18.75), with Etosha's longitude given by the white cross. All data from ERA5.

it is best developed. Figures 9 and 10 show DJF climatologies of zonal wind and divergence/convergence (contours), plotted as latitude-height and longitude-height respectively. In some instances, the meridional component of the flow associated with the anabatic-sea breeze will be greater than the zonal component (e.g. as it propagates inland and is deflected by the Coriolis force), however it is the positive zonal wind that distinguishes the system from the background flow over southern Africa and the trade winds over the south Atlantic, which are both easterly in nature. Hence, for the purposes of identifying the anabatic-sea breeze, the choice of zonal wind in these plots is pragmatic. Figure 11 shows latitude-height DJF climatologies of temperature and potential-temperature (contours).

The anabatic-sea breeze sets in at the coast by 0900 (Figure 9) and strengthens during the morning and early afternoon, so that by 1500 the system presides through the lowest ≈250hPa of the atmosphere. A plume of divergence is evident up to ≈550hPa as the flow is accelerated up the escarpment (≈1400m at Etosha's latitude), with an area of convergence in its immediate lee as the flow is decelerated by friction with the surface. This pattern of upper divergence/lower convergence is consistent with the definition of a sea breeze given by Miller et al. (2003), who state that the circulation is a vertically rotating cell, with rising air currents inland, and sinking currents several kilometers out to sea. The establishment of the anabatic-sea breeze is a direct response to the uneven diabatic heating of the landmass and the adjacent ocean (Figure 11); at 850hPa (just above the surface) a zonal gradient in temperature exists at 0900, and is at its most pronounced at 1500 (when the anabatic-sea breeze is best developed). The daytime profiles of potential temperature are consistent with the modelling work of Smith and Spengler (2011), with a well-mixed layer over the landmass (potential temperature constant with height), and a strong zonal gradient close to the coast (12°E - 14°E) demarking the position of the sea breeze front.

Through the afternoon, the anabatic-sea breeze and its associated areas of divergence and convergence propagate inland (Figure 9) so that by 1800, the system has deteriorated below the level of the escarpment, and the topographically generated plume of divergence has collapsed. As the anabatic-sea breeze continues to move inland, it is deflected by the Coriolis force, producing a rotation of the wind vectors from westerly to south-westerly (Figure 7), hence diminishing the zonal component of the flow as it propagates eastwards (Figure 9). The varying extent of the systems inland propagation at different latitudes is partly a consequence of the topography of the Namib coastline, which features deeply incised river valleys running from east-west. These act to channel the anabatic-sea breeze and accelerate the flow, an effect that is illustrated by the structure of the zonal wind contours in Figure 10. The sea-breeze front is therefore evident in a select number of latitudinal bands at 0000 (Figure 7); one south of ≈25°S and another at ≈19°S, coincident with the location of the Etosha Pan.

The persistence of the system at Etosha's latitude is due to the Hoanib River valley, and is illustrated by the enhanced zonal wind component in the topographic low to the south of Etosha's location at 1500 and 1800 (Figure 10). Topographic channelling of winds has been observed along other Namib river valleys, with maximum flow enhancement recorded downwind of the valley edge (Vickery & Eckardt, 2013; Wiggs et al., 2002). Local scale, north-westerly valley winds can also develop during the daytime independent of the anabatic-sea breeze system (Lindesay & Tyson, 1990), further aiding the inland propagation of the onshore flow.

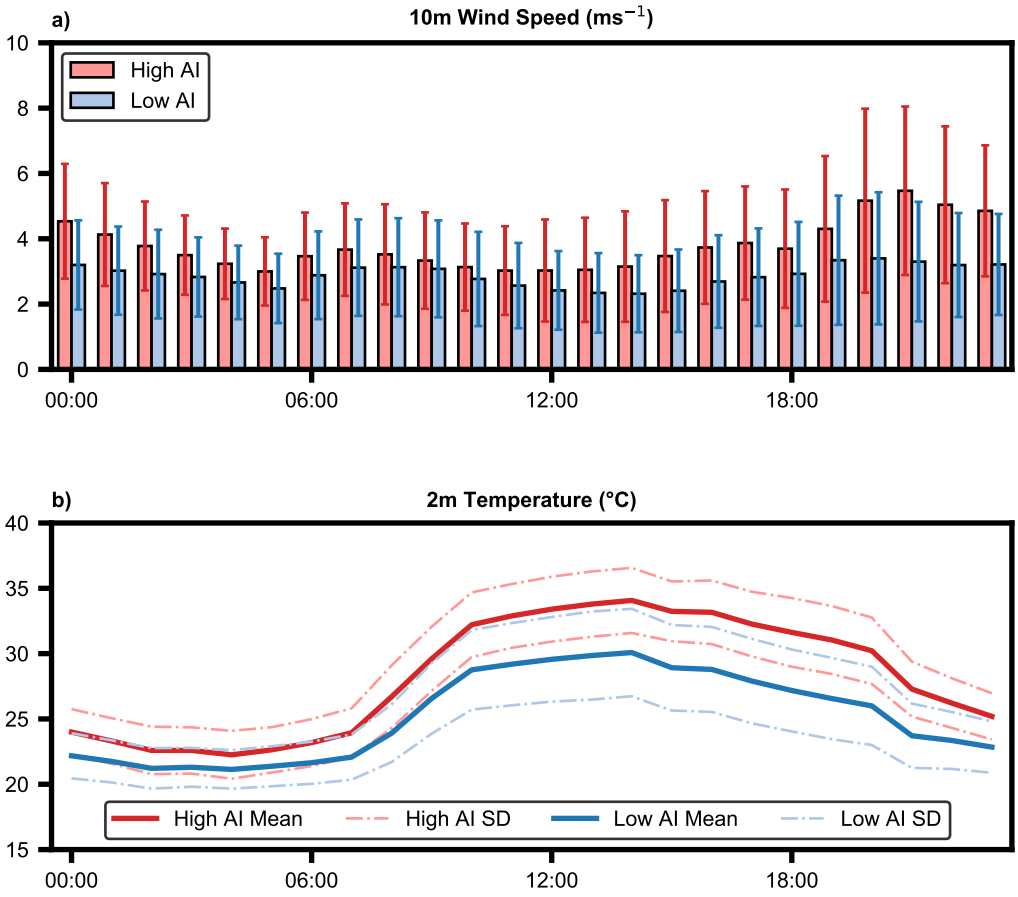


Figure 12. Composite diurnal cycle of (a) 10m wind speed and (b) 2m temperature for high AI and low AI December months at Etosha. All data from ERA5.

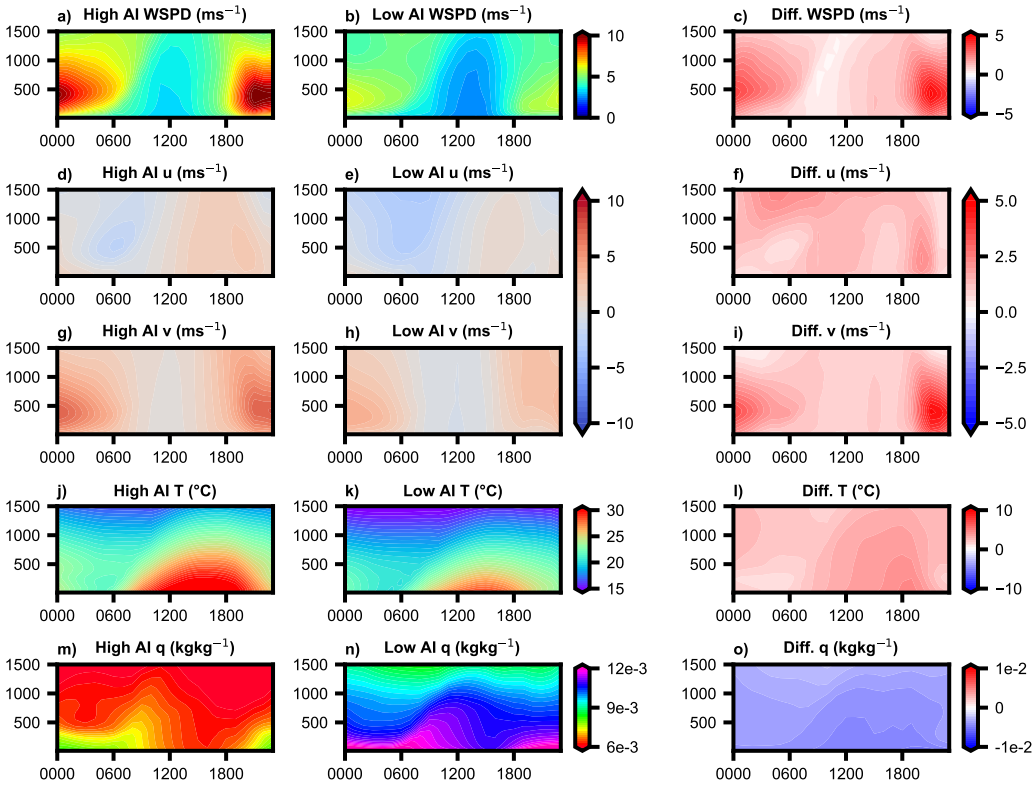


Figure 13. Time-height cross sections of (a-c) wind speed, (d-f) u, (g-i) v, (j-l) temperature and (m-o) specific humidity for December high AI, low AI and difference composites at Etosha. The difference composites were calculated by subtracting the low AI from the high AI. All data from ERA5.

6 Variability in Austral Summer Dust Emissions at Etosha

The following sections address key question 4: How does variability in the processes described in section 5 help to account for variability in austral summer dust emissions from the Etosha Pan?

6.1 Variability in Dust Emission Mechanisms

Figure 12 shows composite diurnal cycles of 10m wind speed and 2m temperature at Etosha for the three dustiest (1987, 1989, 1992) and three least dusty (1986, 1988, 1991) December months (Table 2). Both composites show an increase in surface wind speed from 1800 onwards (Figure 12a), with peak values recorded at 2100 and 2000 in the high and low AI years respectively. Results for unpaired, one-tailed t-tests, testing for difference in the high and low AI mean wind speeds are presented in Table 3. Significant differences were found for all hours at $\alpha = 0.05$, and for all hours from 1200 – 0600 at $\alpha = 0.01$, with a much greater peak in the high AI years ($5.47 \pm 2.58 ms^{-1}$) compared to the low AI (3.40 ± 2.02 ms^{-1}). Time-height cross sections of wind speed, u and v at Etosha for high AI, low AI and difference composites are shown in Figure 13; a stronger flow is recorded through the lowest ≈1km of the atmosphere in the dustiest December months (Figure 13c), with a core of enhanced wind speeds in excess of $10ms^{-1}$ developing at ≈400m from 1800 onwards in the high AI composite (Figure 13a).

Table 3. *Results of T-Test Calculations Performed on High and Low AI December Hourly Composite Surface Wind Speeds*

Time	WS (ms^{-1}) High AI	WS (ms^{-1}) Low AI	t-stat	p-value	t-crit ($\alpha = 0.05$)	t-crit ($\alpha = 0.01$)
0000	4.54	3.20	5.76	$1.84x10^{-8}$	1.65	2.35
0200	3.78	2.92	4.29	$1.45x10^{-5}$	1.65	2.35
0400	3.23	2.66	3.51	$2.81x10^{-4}$	1.65	2.35
0600	3.47	2.88	2.95	$1.78x10^{-3}$	1.65	2.35
0800	3.52	3.13	1.76	$4.03x10^{-2}$	1.65	2.35
1000	3.13	2.77	1.77	$3.91x10^{-2}$	1.65	2.35
1200	3.03	2.42	2.96	$1.73x10^{-3}$	1.65	2.35
1400	3.15	2.32	3.87	$7.93x10^{-5}$	1.65	2.35
1600	3.73	2.69	4.47	$6.91x10^{-6}$	1.65	2.35
1800	3.70	2.93	3.06	$1.26x10^{-3}$	1.65	2.35
2000	5.17	3.40	4.89	$1.19x10^{-6}$	1.65	2.35
2200	5.04	3.20	6.14	$3.09x10^{-9}$	1.65	2.35

The relative strength of the flow at Etosha through the evening hours in the dustiest December months is the result of a better developed anabatic-sea breeze system. Figure 14 shows high AI, low AI and difference composites of 10m wind speed and vectors for a selected area of southern Africa. As the anabatic-sea breeze develops at the coast through the afternoon (1200 and 1500), it is stronger in the high AI years, especially north of ≈23°S, whilst the background easterly flow over the interior of southern Africa is weaker, aiding the subsequent inland propagation of the system. By 1800, the sea breeze front has almost arrived at Etosha in the high AI composite, consistent with the timing of increasing wind speeds presented in Figures 12a and 13a. In the low AI composite, the system begins to dissipate much earlier at Etosha's latitude, with a weak front evident ≈80km west of the pan at 2100.

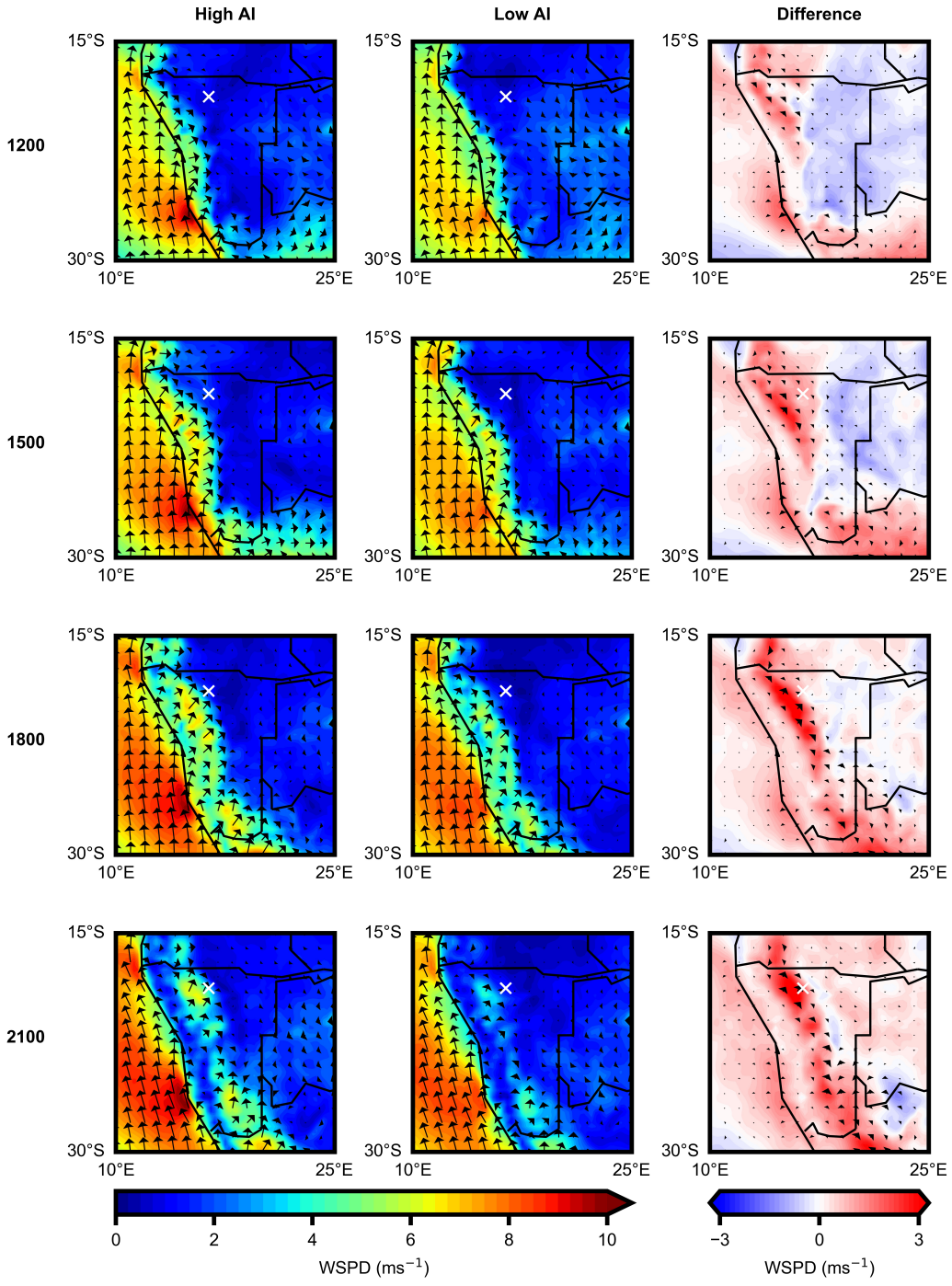


Figure 14. December high AI, low AI and difference composites of 10m wind speed and vectors. Etosha's location is given by the white cross. The difference composites were calculated by subtracting the low AI from the high AI. All data from ERA5.

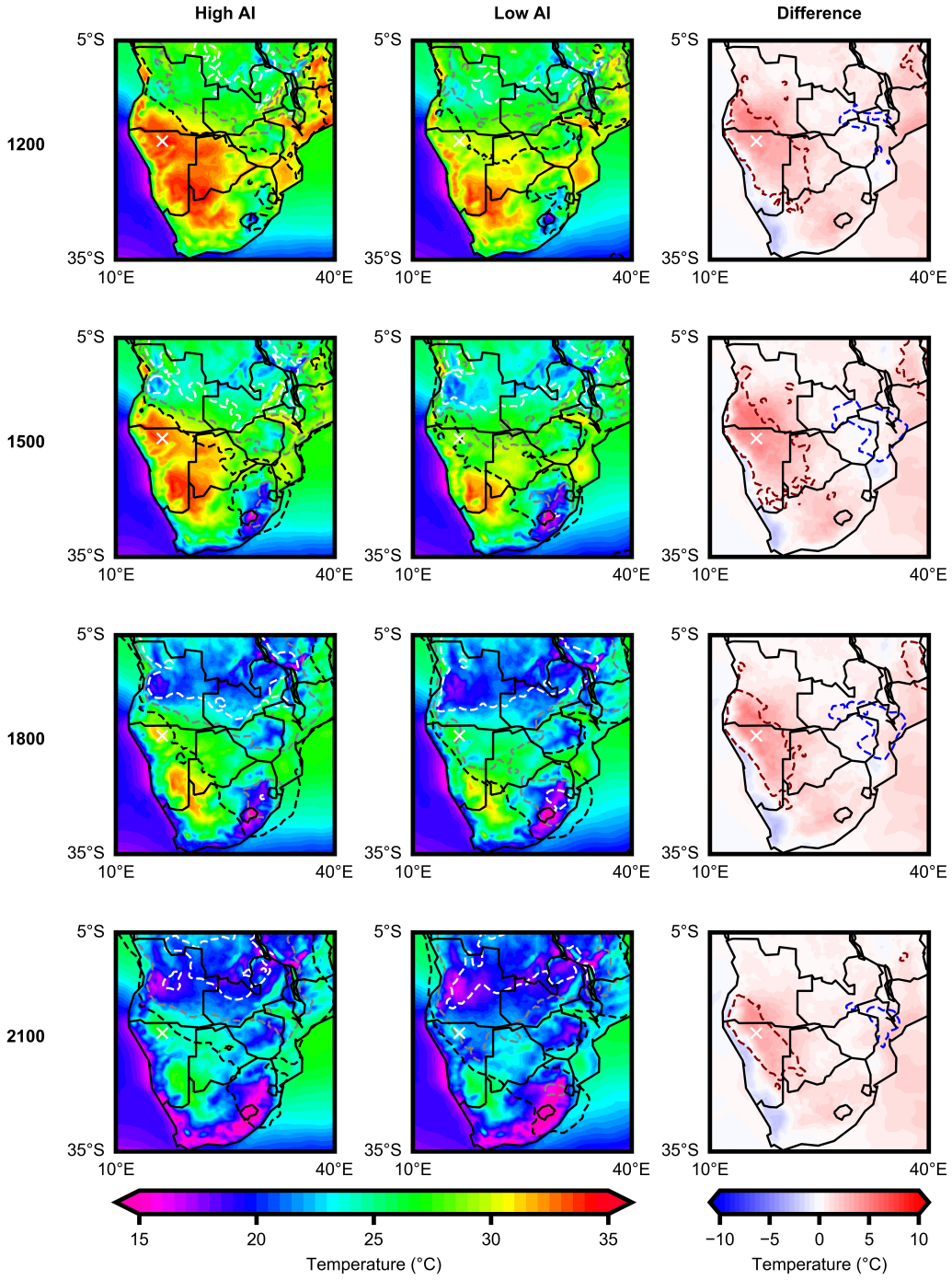


Figure 15. December high AI, low AI and difference composites of 2m temperature and OLR. In the high AI and low AI composites, OLR contours are plotted at 200Wm^{-2} (white), 225Wm^{-2} (grey) and 250Wm^{-2} (black). In the difference composites, the red (blue) contour denotes areas with a +25Wm^{-2} (-25Wm^{-2}) difference. Etosha's location is given by the white cross. The difference composites were calculated by subtracting the low AI from the high AI. All data from ERA5.

6.2 Controls on Variability

The differences in the strength of the anabatic-sea breeze between high and low AI Decembers outlined in section 6.1 can be accounted for by considering the pattern of diabatic heating over the interior of southern Africa, a process that was identified as a key control on the development of the system in section 5. Figure 15 shows high AI, low AI and difference composites of 2m temperature and OLR for a selected area of southern Africa. Diabatic heating is stronger in the high AI composite across the southern Kalahari/Northern Cape region identified in section 5.1 as critical to the development of the anabatic-sea breeze, however there is a more substantial difference in heating between the two composites across northern Namibia and southern Angola (Figure 15). This is also reflected in the diurnal cycle of temperature at Etosha (Figure 12b, Figures 13j-l), with a $\approx 4^{\circ}$C difference in surface temperature between the high and low AI composites at 1400 (Figure 12b).

The contrast in diabatic heating is the result of a south-westward shift in the area of tropical convection during the low AI years, illustrated by the OLR contours in Figure 15, and a moistening of the atmosphere at Etosha (Figures13m-o). This acts to disrupt the pattern of diabatic heating, especially across northern Namibia and southern Angola, and helps to explain the inability of the anabatic-sea breeze to propagate as far inland at Etosha's latitude. Benguela Niños, characterised by positive SST anomalies along the Namib-Angolan coastline (Florenchie et al., 2004; Rouault, 2012), as well as La Niña events, which are associated with a strengthening of the Angola Low (Howard & Washington, 2018), could both drive the observed shift in tropical convection in the low AI composites; indeed, the low AI (1.3) December of 1988 was contemporaneous with a strong La Niña event in the tropical Pacific, for example. The timing of these events does not necessarily coincide with low AI December months however, with for instance the December of 1986 (AI = 1.3) concurrent with negative SST anomalies in the eastern Atlantic (Florenchie et al., 2004).

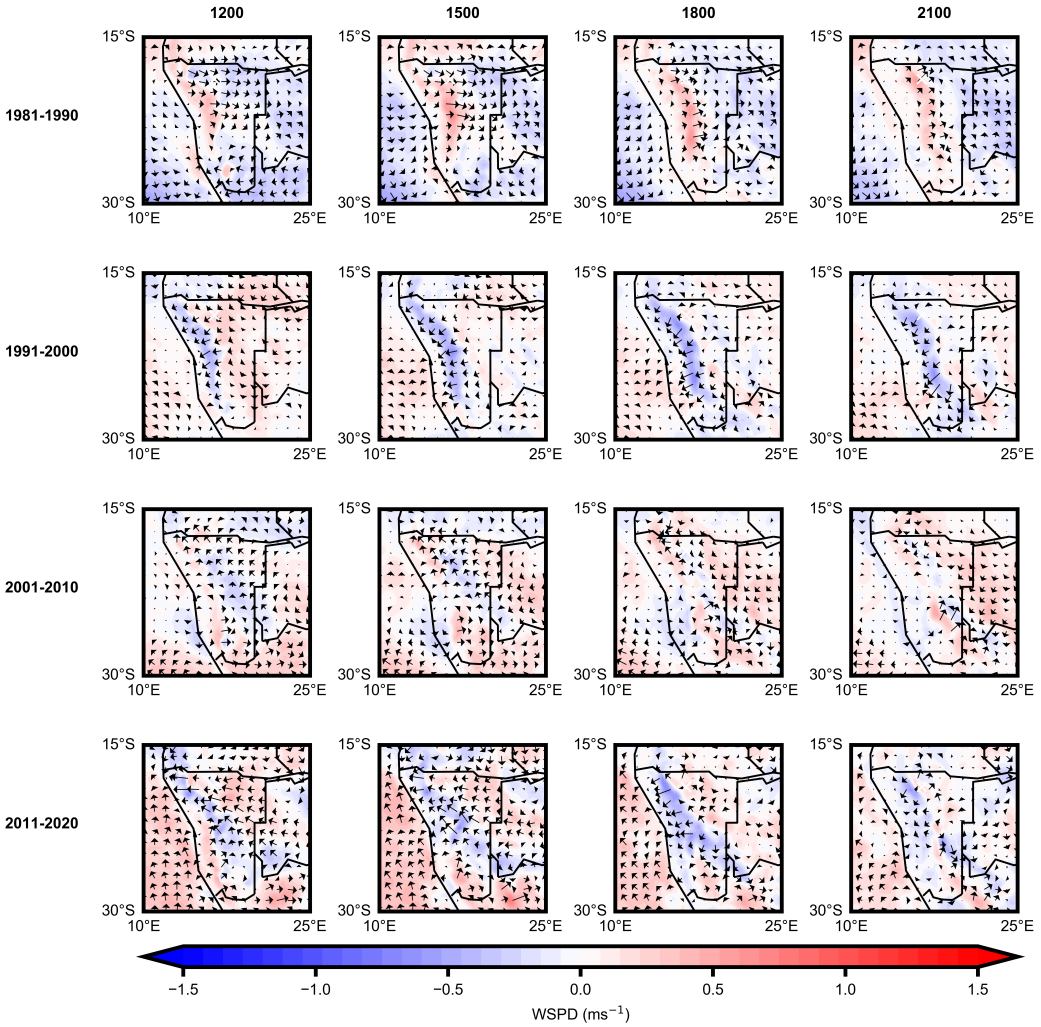


Figure 16. Decadal anomalies of 10m wind speed and vectors for 1200, 1500, 1800 and 2100, for December, with respect to the 1981-2010 climatology. Etosha's location is given by the white cross. All data from ERA5.

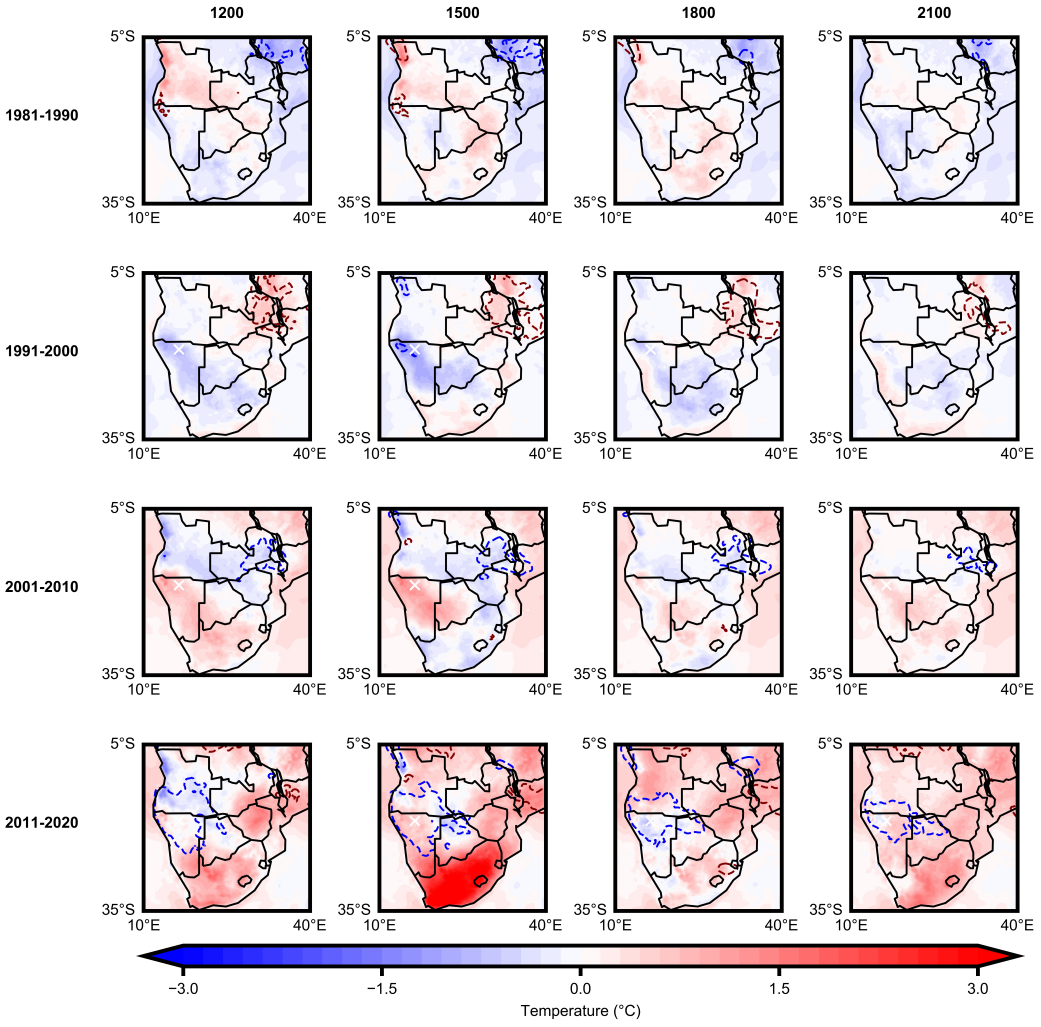


Figure 17. Decadal anomalies of 2m temperature and OLR for 1200, 1500, 1800 and 2100, for December, with respect to the 1981-2010 climatology. The red (blue) contour denotes areas with a $+10\mathrm{Wm}^{-2}$ ($-10\mathrm{Wm}^{-2}$) OLR anomaly. Etosha's location is given by the white cross. All data from ERA5.

7 Discussion and Conclusion

This paper has utilised TOMS AI and ERA5 reanalysis data in order to investigate the atmospheric controls on dust emission from the Etosha Pan throughout the annual cycle. Four key questions were posed in the introduction: (i) What is the annual cycle of dust emissions from the Etosha Pan? (ii) How do the atmospheric processes responsible for driving dust emission from the Etosha Pan vary through the annual cycle? (iii) What are the spatial and temporal characteristics of the dust emission mechanisms operating at the Etosha Pan, and what controls their variability? (iv) How does variability in the processes described help to account for variability in austral summer dust emissions from the Etosha Pan? The results presented in Sections 3, 4, 5 and 6 will now be discussed, and the main findings of the paper summarised, addressing each of the key questions in turn.

Mean AI data for the Etosha Pan shows a peak in dust emissions in September (AI = 1.7) (Figure 1, Table 1), however unlike at Makgadikgadi, southern Africa's other major source area, AI values remain high at Etosha through spring and into summer, with a secondary peak recorded in December (AI = 1.6) (key question 1). The peak in September is consistent with the findings of other remote sensing studies (Prospero et al., 2002; Washington et al., 2003), including those utilising other satellite data (Vickery et al., 2013), however the dust activity observed during summer has received relatively little attention, and hence was the focus of much of this paper. Precipitation composites showed greater rainfall in the Etosha catchment in the low AI December months compared to the high AI months, and very little difference in rainfall in the preceding summer wet season (Figure 3). These results are similar to the findings of Bryant (2003), who showed that inundation events during 1997/98 and 1999/2000 resulted in an immediate reduction of AI values at Etosha.

During the dustiest December months (key question 2), surface wind speeds increase through the evening and peak at 2100, whilst a core of enhanced wind speeds develops at ≈400m and peaks at the same time (Figure 4). This is in contrast to September, with the findings of this study, and previous work utilising in-situ observations at Etosha (Clements & Washington, 2021; Zunckel et al., 1996) showing the typical evolution and breakdown of a NLLJ and associated morning peak in surface winds. These results preclude the possibility of a NLLJ being the primary emission mechanism during summer; indeed, a case study of a dust event (Figures 5 and 6) demonstrates the potential role of an anabatic-sea breeze system that develops along the Namib coast and propagates inland to reach Etosha during the evening, concurrent with the observed peak in surface winds during the dustiest December months.

The anabatic-sea breeze is evident along the Namib coast during all seasons (key question 3), however it is strongest during summer, when it also propagates furthest inland (Figure 7). The system is a response to the thermal contrast between the elevated interior plateau of southern Africa, and the cool waters of the BUS, and hence is best developed when the area of maximum diabatic heating is situated over the southern Kalahari/Northern Cape region, and to the south of the ABF (Figure 8). The west coast of the subcontinent south of ≈15°S therefore provides an ideal physical setting for the development of such a system; whilst the topography of the escarpment is not as extreme in the west as it is along the eastern slopes of Natal, there is a much greater thermal contrast in the west owing to the relatively cool waters of the BUS (December mean SST of ≈17°C at 20°S) compared to the warm Agulhas current of the Indian Ocean (December mean SST of ≈27°C at 25°S)(Lindesay & Tyson, 1990). The position of the South Atlantic Anticyclone (SAA), centred at ≈30°S, 5°W in austral summer, and the anticlockwise rotation of air associated with the high-pressure cell gives south-easterlies along the southwest coast of southern Africa; the stress imparted by these surface winds drives offshore Ekman transport and hence the upwelling of cold water from below the thermocline (Colberg & Reason, 2006; Reason, 2017). The inland propagation of the anabatic-

sea breeze is facilitated at Etosha's latitude by the presence of the Hoanib River valley (Figure 10), with topographic channelling of winds a process that has been observed in some of Namibia's other ephemeral rivers (Vickery & Eckardt, 2013; Wiggs et al., 2002).

Surface wind speeds at Etosha are significantly stronger in the dustiest December months when compared to the least dusty (Figure 12, Table 3) (key question 4), a manifestation of a better developed anabatic-sea breeze (Figure 14). The contrasting strength of the system between the two sets of composites is driven by differences in the pattern of diabatic heating over southern Africa, with a south-westward displacement of the area of tropical convection disturbing the heating over northern Namibia and southern Angola in the low AI years (Figure 15).

Given the predicted future warming across southern Africa (Boucher et al., 2013; Reason, 2017), along with the sensitivity of the anabatic-sea breeze to the degree and location of maximum diabatic heating, there is the potential for longer-term variability in the strength of the system and hence dust emissions at Etosha. In order to explore this possibility, we present 10m wind speed (Figure 16) and 2m temperature (Figure 17) anomalies for December, for the previous four decades, against the 1981-2010 climatology. OLR contours are also included on Figure 17.

The anabatic-sea breeze was best developed during the 1980s (Figure 16), with positive wind speed anomalies and westerly vectors coincident with the position of the sea breeze front as it propagates inland through the evening. Despite the general warming trend observed across southern Africa since 1981 (Figure 17), the strength of the anabatic-sea breeze has not changed appreciably; indeed, the system was relatively weak during the last decade, as shown by the negative wind speed anomalies and easterly vectors coincident with the position of the front. This is partly due to the south-westward shift in the area of tropical convection (indicated by the negative OLR anomaly over northern Namibia/southern Angola) which disturbs the pattern of diabatic heating and modulates the degree of warming across a region of southern Africa shown to be crucial to the development of the anabatic-sea breeze (section 5.1). Another possible explanation for the multi-decadal trends observed in the strength of the system is variability in the position and strength of the SAA, given the role the feature plays in sustaining the BUS and hence the cool SST's off of the coast of subtropical southern Africa. For example, Venegas et al. (1997) show zonal and meridional oscillations in the position of the SAA with periods of 6-7 years and 4 years respectively, whilst Vizy and Cook (2016) report a general poleward shift of the high-pressure cell since the 1980's and a subsequent reduction in upwelling along the Angolan coast.

Another feature of the local circulation that might influence the development of the anabatic-sea breeze system are trapped coastal lows. They are 'trapped' as the marine inversion layer sits beneath the level of the escarpment, and propagate southwards along the Namib coast (Gill, 1977; Reason, 2017). The lows are associated with stratus clouds and also reduce the rate of coastal upwelling (Reason, 2017); these two effects would reduce heating over the southern Kalahari/northern Cape region, whilst also increasing SSTs, hence modulating the zonal thermal contrast critical to the development of the onshore flow.

Whilst the anabatic-sea breeze has been identified in previous work (Howard & Washington, 2018; Lindesay & Tyson, 1990), this is the first time it has been shown to be associated with dust uplift from southern African source areas. Lindesay and Tyson (1990) document the predominance of topographically induced plain-mountain winds, and a thermally induced sea breeze during the daytime in the summer months (both westerly in nature) at a site in the central Namib, with a tendency for these onshore flows to drift inland through the evening. The results presented here suggest that this integrated system is extensive, covering a latitudinal range of up to 15° and propagating up to 5° inland from the coast.

The findings of this study do not preclude other atmospheric processes contributing to summer emissions at Etosha, especially given the importance of convective cold pools in other dust source areas (Allen et al., 2013; Caton Harrison et al., 2019). The inland propagation of the anabatic-sea breeze to Etosha's longitude is contemporaneous with dust uplift from the pan, however it is also plausible that the system plays a key role in triggering convection, which subsequently drives emission from the surface. More work is therefore required, especially across the rest of the summer season, to fully explore the range of atmospheric processes operating at Etosha.

Open Research Section

Data - ERA5 data is maintained by ECMWF and is available online from the Copernicus Climate Change Service (CDS, 2018) (https://doi.org/10.24381/cds.adbb2d47). Translation available via browser plug-in.

Data - TOMS AI data is available online from the IRI data library (IRI, 1996) (https://iridl.ldeo.columbia.edu/SOURCES/.NASA/.GSFC/.TOMS/.NIMBUS7/.monthly/.ai/). Translation available via browser plug-in.

Data - CHIRPS data is maintained by the Climate Hazards Centre and is available online (CHC, 2014) (https://data.chc.ucsb.edu/products/CHIRPS-2.0/). Translation available via browser plug-in.

Acknowledgments

Matthew Clements is funded by the NERC doctoral training partnership (NE/L002612/1).

References

Adebiyi, A. A., & Zuidema, P. (2016). The role of the southern african easterly jet in modifying the southeast atlantic aerosol and cloud environments. *Quarterly Journal of the Royal Meteorological Society*, *142*(697), 1574-1589. doi: https://doi.org/10.1002/qj.2765

Allen, C. J. T., & Washington, R. (2014). The low-level jet dust emission mechanism in the central sahara: Observations from bordj-badji mokhtar during the june 2011 fennec intensive observation period. *Journal of Geophysical Research: Atmospheres*, *119*(6), 2990-3015. doi: https://doi.org/10.1002/2013JD020594

Allen, C. J. T., Washington, R., & Engelstaedter, S. (2013). Dust emission and transport mechanisms in the central sahara: Fennec ground-based observations from bordj badji mokhtar, june 2011. *Journal of Geophysical Research: Atmospheres*, *118*(12), 6212-6232. doi: https://doi.org/10.1002/jgrd.50534

Baddock, M., Parsons, K., Strong, C., Leys, J., & McTainsh, G. (2015). Drivers of australian dust: a case study of frontal winds and dust dynamics in the lower lake eyre basin. *Earth Surface Processes and Landforms*, *40*(14), 1982-1988. doi: https://doi.org/10.1002/esp.3773

Bechtold, P., Semane, N., Lopez, P., Chaboureau, J.-P., Beljaars, A., & Bormann, N. (2014). Representing equilibrium and nonequilibrium convection in large-scale models. *Journal of the Atmospheric Sciences*, *71*(2), 734 - 753. doi: 10.1175/JAS-D-13-0163.1

Blackadar, A. K. (1957). Boundary layer wind maxima and their significance for the growth of nocturnal inversions. *Bulletin of the American Meteorological Society*, *38*(5), 283 - 290. doi: 10.1175/1520-0477-38.5.283

Boucher, O., Randall, D., Artaxo, P., Bretherton, C., Feingold, G., Forster, P., ... Zhang, X. Y. (2013). Clouds and aerosols. In T. F. Stocker et al. (Eds.), *Climate change 2013: The physical science basis. contribution of working group i to the fifth assessment report of the intergovernmental panel on climate change* (pp. 571–657). Cambridge, UK: Cambridge University Press. doi: 10.1017/CBO9781107415324.016

Boussetta, S., Balsamo, G., Beljaars, A., Kral, T., & Jarlan, L. (2013). Impact of a satellite-derived leaf area index monthly climatology in a global numerical weather prediction model. *International Journal of Remote Sensing*, *34*(9-10), 3520-3542. doi: 10.1080/01431161.2012.716543

Bryant, R. G. (2003). Monitoring hydrological controls on dust emissions: preliminary observations from etosha pan, namibia. *The Geographical Journal*,

169(2), 131-141. doi: https://doi.org/10.1111/1475-4959.04977

Caton Harrison, T., Washington, R., & Engelstaedter, S. (2019). A 14-year climatology of saharan dust emission mechanisms inferred from automatically tracked plumes. *Journal of Geophysical Research: Atmospheres*, *124*(16), 9665-9690. doi: https://doi.org/10.1029/2019JD030291

Caton Harrison, T., Washington, R., & Engelstaedter, S. (2021). Satellite-derived characteristics of saharan cold pool outflows during boreal summer. *Journal of Geophysical Research: Atmospheres*, *126*(3), e2020JD033387. doi: https://doi.org/10.1029/2020JD033387

CDS. (2018). Era5 hourly data on single levels from 1959 to present [dataset]. *Copernicus Climate Change Service (C3S) Climate Data Store (CDS)*. doi: https://doi.org/10.24381/cds.adbb2d47

CHC. (2014). Climate hazards group infrared precipitation with station data [dataset]. *Climate Hazards Center Data Store*. Retrieved from `https://data.chc.ucsb.edu/products/CHIRPS-2.0/`

Clements, M., & Washington, R. (2021). Atmospheric controls on mineral dust emission from the etosha pan, namibia: Observations from the clarify-2016 field campaign. *Journal of Geophysical Research: Atmospheres*, *126*(14), e2021JD034746. doi: https://doi.org/10.1029/2021JD034746

Colberg, F., & Reason, C. J. C. (2006). A model study of the angola benguela frontal zone: Sensitivity to atmospheric forcing. *Geophysical Research Letters*, *33*(19). doi: https://doi.org/10.1029/2006GL027463

Evan, A. T. (2018). Surface winds and dust biases in climate models. *Geophysical Research Letters*, *45*(2), 1079-1085. doi: https://doi.org/10.1002/2017GL076353

Evan, A. T., Flamant, C., Fiedler, S., & Doherty, O. (2014). An analysis of aeolian dust in climate models. *Geophysical Research Letters*, *41*(16), 5996-6001. doi: https://doi.org/10.1002/2014GL060545

Fiedler, S., Schepanski, K., Heinold, B., Knippertz, P., & Tegen, I. (2013). Climatology of nocturnal low-level jets over north africa and implications for modeling mineral dust emission. *Journal of Geophysical Research: Atmospheres*, *118*(12), 6100-6121. doi: https://doi.org/10.1002/jgrd.50394

Florenchie, P., Reason, C., Lutjeharms, J., Rouault, M., Roy, C., & Masson, S. (2004, 06). Evolution of interannual warm and cold events in the southeast atlantic ocean. *Journal of Climate - J CLIMATE*, *17*, 2318-2334. doi: 10.1175/1520-0442(2004)017⟨2318:EOIWAC⟩2.0.CO;2

Funk, C., Peterson, P., Landsfeld, M., Pedreros, D., Verdin, J., Shukla, S., ... Michaelsen, J. (2015, 12). The climate hazards infrared precipitation with stations - a new environmental record for monitoring extremes. *Scientific Data*, *2*, 150066. doi: 10.1038/sdata.2015.66

Garcia-Carreras, L., Marsham, J. H., Parker, D. J., Bain, C. L., Milton, S., Saci, A., ... Washington, R. (2013). The impact of convective cold pool outflows on model biases in the sahara. *Geophysical Research Letters*, *40*(8), 1647-1652. doi: https://doi.org/10.1002/grl.50239

Ge, J. M., Liu, H., Huang, J., & Fu, Q. (2016). Taklimakan desert nocturnal low-level jet: climatology and dust activity. *Atmospheric Chemistry and Physics*, *16*(12), 7773–7783. doi: 10.5194/acp-16-7773-2016

Gill, A. E. (1977). Coastally trapped waves in the atmosphere. *Quarterly Journal of the Royal Meteorological Society*, *103*(437), 431-440. doi: https://doi.org/10.1002/qj.49710343704

Goudie, A. S. (2014). Desert dust and human health disorders. *Environment International*, *63*, 101-113. doi: https://doi.org/10.1016/j.envint.2013.10.011

Haywood, J., & Boucher, O. (2000). Estimates of the direct and indirect radiative forcing due to tropospheric aerosols: A review. *Reviews of Geophysics*, *38*(4), 513-543. doi: https://doi.org/10.1029/1999RG000078

Heinold, B., Knippertz, P., Marsham, J. H., Fiedler, S., Dixon, N. S., Schepanski, K., ... Tegen, I. (2013). The role of deep convection and nocturnal low-level jets for dust emission in summertime west africa: Estimates from convection-permitting simulations. *Journal of Geophysical Research: Atmospheres*, *118*(10), 4385-4400. doi: https://doi.org/10.1002/jgrd.50402

Herman, J. R., Bhartia, P. K., Torres, O., Hsu, C., Seftor, C., & Celarier, E. (1997). Global distribution of uv-absorbing aerosols from nimbus 7/toms data. *Journal of Geophysical Research: Atmospheres*, *102*(D14), 16911-16922. doi: https://doi.org/10.1029/96JD03680

Hersbach, H., Bell, B., Berrisford, P., Hirahara, S., Horányi, A., Muñoz-Sabater, J., ... Thépaut, J.-N. (2020). The era5 global reanalysis. *Quarterly Journal of the Royal Meteorological Society*, *146*(730), 1999-2049. doi: https://doi.org/10.1002/qj.3803

Howard, E., & Washington, R. (2018). Characterizing the synoptic expression of the angola low. *Journal of Climate*, *31*(17), 7147 - 7165. doi: 10.1175/JCLI-D-18-0017.1

IRI. (1996). Nasa gsfc toms: Total ozone mapping spectrometer [dataset]. *IRI/LDEO Data Library*. Retrieved from `https://iridl.ldeo.columbia.edu/SOURCES/.NASA/.GSFC/.TOMS/.NIMBUS7/.monthly/.ai/`

Jemmett-Smith, B. C., Marsham, J. H., Knippertz, P., & Gilkeson, C. A. (2015). Quantifying global dust devil occurrence from meteorological analyses. *Geophysical Research Letters*, *42*(4), 1275-1282. doi: https://doi.org/10.1002/2015GL063078

Jickells, T. D., An, Z. S., Andersen, K. K., Baker, A. R., Bergametti, G., Brooks, N., ... Torres, R. (2005). Global iron connections between desert dust, ocean biogeochemistry, and climate. *Science*, *308*(5718), 67–71. doi: 10.1126/science.1105959

Knippertz, P., & Todd, M. C. (2012). Mineral dust aerosols over the sahara: Meteorological controls on emission and transport and implications for modeling. *Reviews of Geophysics*, *50*(1). doi: https://doi.org/10.1029/2011RG000362

Kok, J. F., Parteli, E. J. R., Michaels, T. I., & Karam, D. B. (2012). The physics of wind-blown sand and dust. *Reports on Progress in Physics*, *75*(10), 106901. doi: 10.1088/0034-4885/75/10/106901

Koren, I., Kaufman, Y. J., Washington, R., Todd, M. C., Rudich, Y., Martins, J. V., & Rosenfeld, D. (2006). The bodélé depression: a single spot in the sahara that provides most of the mineral dust to the amazon forest. *Environmental Research Letters*, *1*(1), 014005. doi: 10.1088/1748-9326/1/1/014005

Lindesay, J. A., & Tyson, P. D. (1990). Thermo-topographically induced boundary layer oscillations over the central namib, southern africa. *International Journal of Climatology*, *10*(1), 63-77. doi: https://doi.org/10.1002/joc.3370100108

Mahowald, N. M., Baker, A. R., Bergametti, G., Brooks, N., Duce, R. A., Jickells, T. D., ... Tegen, I. (2005). Atmospheric global dust cycle and iron inputs to the ocean. *Global Biogeochemical Cycles*, *19*(4). doi: https://doi.org/10.1029/2004GB002402

Mahowald, N. M., Bryant, R. G., del Corral, J., & Steinberger, L. (2003). Ephemeral lakes and desert dust sources. *Geophysical Research Letters*, *30*(2). doi: https://doi.org/10.1029/2002GL016041

Mahowald, N. M., & Kiehl, L. M. (2003). Mineral aerosol and cloud interactions. *Geophysical Research Letters*, *30*(9). doi: https://doi.org/10.1029/2002GL016762

Marsham, J. H., Hobby, M., Allen, C. J. T., Banks, J. R., Bart, M., Brooks, B. J., ... Washington, R. (2013). Meteorology and dust in the central sahara: Observations from fennec supersite-1 during the june 2011 intensive observation period. *Journal of Geophysical Research: Atmospheres*, *118*(10), 4069-4089. doi: https://doi.org/10.1002/jgrd.50211

McPeters, R. D., Bhartia, P. K., Krueger, A. J., Herman, J. R., Schlesinger, B. M., Wellemeyer, C. G., ... Cebula, R. P. (1996). Nimbus–7 total ozone mapping spectrometer (toms) data products user's guide. *NASA Reference Publication*.

Middleton, N. (2017). Desert dust hazards: A global review. *Aeolian Research*, *24*, 53-63. doi: https://doi.org/10.1016/j.aeolia.2016.12.001

Miller, S. T. K., Keim, B. D., Talbot, R. W., & Mao, H. (2003). Sea breeze: Structure, forecasting, and impacts. *Reviews of Geophysics*, *41*(3). doi: https://doi.org/10.1029/2003RG000124

Morcrette, J.-J., Barker, H. W., Cole, J. N. S., Iacono, M. J., & Pincus, R. (2008). Impact of a new radiation package, mcrad, in the ecmwf integrated forecasting system. *Monthly Weather Review*, *136*(12), 4773 - 4798. doi: 10.1175/2008MWR2363.1

Munday, C., & Washington, R. (2017). Circulation controls on southern african precipitation in coupled models: The role of the angola low. *Journal of Geophysical Research: Atmospheres*, *122*(2), 861-877. doi: https://doi.org/10.1002/2016JD025736

Murray, J. E., Brindley, H. E., Bryant, R. G., Russell, J. E., Jenkins, K. F., & Washington, R. (2016). Enhancing weak transient signals in seviri false color imagery: Application to dust source detection in southern africa. *Journal of Geophysical Research: Atmospheres*, *121*(17), 10,199-10,219. doi: https://doi.org/10.1002/2016JD025221

Preston-Whyte, R. A., Diab, R. D., & Sokolic, F. (1994). Thermo-topographically induced winds in the boundary layer over the etosha pan. *South African Geographical Journal*, *76*(2), 59-62. doi: 10.1080/03736245.1994.9713576

Prospero, J. M., Ginoux, P., Torres, O., Nicholson, S. E., & Gill, T. E. (2002). Environmental characterization of global sources of atmospheric soil dust identified with the nimbus 7 total ozone mapping spectrometer (toms) absorbing aerosol product. *Reviews of Geophysics*, *40*(1), 2-1-2-31. doi: https://doi.org/10.1029/2000RG000095

Reason, C. (2017). *Climate of southern africa.* Oxford University Press. doi: 10.1093/acrefore/9780190228620.013.513

Roberts, A. J., Marsham, J. H., Knippertz, P., Parker, D. J., Bart, M., Garcia-Carreras, L., ... Walker, D. (2017). New saharan wind observations reveal substantial biases in analysed dust-generating winds. *Atmospheric Science Letters*, *18*(9), 366-372. doi: https://doi.org/10.1002/asl.765

Rotunno, R. (1983). On the linear theory of the land and sea breeze. *Journal of Atmospheric Sciences*, *40*(8), 1999 - 2009. doi: https://doi.org/10.1175/1520-0469(1983)040⟨1999:OTLTOT⟩2.0.CO;2

Rouault, M. (2012). Bi-annual intrusion of tropical water in the northern benguela upwelling. *Geophysical Research Letters*, *39*(12). doi: https://doi.org/10.1029/2012GL052099

Schepanski, K., Tegen, I., Laurent, B., Heinold, B., & Macke, A. (2007). A new saharan dust source activation frequency map derived from msg-seviri ir-channels. *Geophysical Research Letters*, *34*(18). doi: https://doi.org/10.1029/2007GL030168

Schepanski, K., Tegen, I., Todd, M. C., Heinold, B., Bönisch, G., Laurent, B., & Macke, A. (2009). Meteorological processes forcing saharan dust emission inferred from msg-seviri observations of subdaily dust source activation and numerical models. *Journal of Geophysical Research: Atmospheres*, *114*(D10). doi: https://doi.org/10.1029/2008JD010325

Sinha, P., Hobbs, P. V., Yokelson, R. J., Bertschi, I. T., Blake, D. R., Simpson, I. J., ... Novakov, T. (2003). Emissions of trace gases and particles from savanna fires in southern africa. *JOURNAL OF GEOPHYSICAL RESEARCH*, *108*(D13). doi: 10.1029/2002JD002325

Todd, M. C., Washington, R., Raghavan, S., Lizcano, G., & Knippertz, P. (2008).

Regional model simulations of the bodélé low-level jet of northern chad during the bodélé dust experiment (bodex 2005). *Journal of Climate*, *21*(5), 995 - 1012. doi: 10.1175/2007JCLI1766.1

Torres, O., Bhartia, P. K., Herman, J. R., Sinyuk, A., Ginoux, P., & Holben, B. (2002). A long-term record of aerosol optical depth from toms observations and comparison to aeronet measurements. *Journal of the Atmospheric Sciences*, *59*(3), 398 - 413. doi: 10.1175/1520-0469(2002)059⟨0398:ALTROA⟩2.0.CO;2

Venegas, S. A., Mysak, L. A., & Straub, D. N. (1997). Atmosphere–ocean coupled variability in the south atlantic. *Journal of Climate*, *10*(11), 2904 - 2920. doi: 10.1175/1520-0442(1997)010⟨2904:AOCVIT⟩2.0.CO;2

Vickery, K. J., & Eckardt, F. D. (2013). Dust emission controls on the lower kuiseb river valley, central namib. *Aeolian Research*, *10*, 125-133. doi: https://doi.org/10.1016/j.aeolia.2013.02.006

Vickery, K. J., Eckardt, F. D., & Bryant, R. G. (2013). A sub-basin scale dust plume source frequency inventory for southern africa, 2005–2008. *Geophysical Research Letters*, *40*(19), 5274-5279. doi: https://doi.org/10.1002/grl.50968

Vizy, E. K., & Cook, K. H. (2016). Understanding long-term (1982-2013) multi-decadal change in the equatorial and subtropical South Atlantic climate. *Climate Dynamics*, *46*(7-8), 2087-2113. doi: 10.1007/s00382-015-2691-1

Wagener, T., Guieu, C., Losno, R., Bonnet, S., & Mahowald, N. (2008). Revisiting atmospheric dust export to the southern hemisphere ocean: Biogeochemical implications. *Global Biogeochemical Cycles*, *22*(2). doi: https://doi.org/10.1029/2007GB002984

Washington, R., Todd, M., Middleton, N. J., & Goudie, A. S. (2003). Dust-storm source areas determined by the total ozone monitoring spectrometer and surface observations. *Annals of the Association of American Geographers*, *93*(2), 297-313. doi: 10.1111/1467-8306.9302003

Washington, R., & Todd, M. C. (2005). Atmospheric controls on mineral dust emission from the bodélé depression, chad: The role of the low level jet. *Geophysical Research Letters*, *32*(17). doi: https://doi.org/10.1029/2005GL023597

Washington, R., Todd, M. C., Engelstaedter, S., Mbainayel, S., & Mitchell, F. (2006). Dust and the low-level circulation over the bodélé depression, chad: Observations from bodex 2005. *Journal of Geophysical Research: Atmospheres*, *111*(D3). doi: https://doi.org/10.1029/2005JD006502

Wiggs, G. F. S., Bullard, J. E., Garvey, B., & Castro, I. (2002). Interactions between airflow and valley topography with implications for aeolian sediment transport. *Physical Geography*, *23*(5), 366-380. doi: 10.2747/0272-3646.23.5.366

Zunckel, M., Hong, Y., Brassel, K., & O'Beirne, S. (1996). Characteristics of the nocturnal boundary layer: Okaukuejo, namibia, during safari-92. *Journal of Geophysical Research: Atmospheres*, *101*(D19), 23757-23766. doi: https://doi.org/10.1029/95JD00624

Chapter 5: An Analysis of Dust Emission Mechanisms in CMIP6 Models and Their Influence on Simulated Uplift Across Southern Africa

The first two research papers have contributed to the current state of knowledge regarding dust emission mechanisms in an understudied, yet important source area. All three aims stated in Chapter 1 involved evaluating the representation of certain parameters in numerical models, and that is the major contribution of the third research paper, the results of which are presented in this chapter. The models selected are from the latest round of the CMIP experiments as they are the main tools at our disposal for projecting future changes in climate. Initially, the spatial and temporal variability in dust emissions across southern Africa (as documented in the second research paper) is evaluated in the models. Two primary emission mechanisms have been identified in the first two research papers; namely, a NLLJ in winter, and an anabatic-sea breeze in summer, and the representation of these processes is also evaluated in the models. In so doing, this paper contributes to the growing literature on dust-relevant processes in climate models, and is the first attempt to evaluate model skill in a southern African context.

An Analysis of Dust Emission Mechanisms in CMIP6 Models and Their Influence on Simulated Uplift Across Southern Africa

Matthew Clements[1], **Richard Washington**[1]

[1]Climate Research Lab, Oxford University Centre for the Environment, Oxford, UK

Key Points:

- CMIP6 models fail to capture the observed maximum in dust emissions across southern Africa in September and December.
- The models underestimate the strength of a nocturnal low-level jet responsible for driving uplift from a prominent dust source area.
- The models capture well an onshore flow in December that drives simulated emissions along the west coast of southern Africa.

Corresponding author: Matthew Clements, matthew.clements@ouce.ox.ac.uk

Abstract

This paper evaluates the representation of a number of dust-relevant processes across southern Africa in some of the models participating in the 6th phase of the Coupled Model Intercomparison Project (CMIP6). A nocturnal low-level jet (NLLJ) has been shown to drive austral winter dust emissions at Etosha, southern Africa's most prominent source area, however the multi-model mean underestimates observed core wind speeds by $>3 \mathrm{ms}^{-1}$ at 0600, and subsequently fails to capture the peak in morning surface winds associated with jet breakdown. The models capture better an integrated anabatic-sea breeze along the west coast of southern Africa, which has been shown to contribute to uplift at Etosha during austral summer as it propagates inland through the evening. The models tend to miss the observed maximum in uplift over the interior of southern Africa during September, with a concentration of dust source areas along the coast in both seasons. This discrepancy can be partly accounted for by the better representation of the sea breeze system, which is more effective in activating the adjacent coastal sources, however a bias in the location of the background northeasterlies in some of the models helps to sustain these sources during September. The treatment of land surface properties, especially the spatial distribution of soil moisture in the models, also influences where across southern Africa uplift is simulated.

1 Introduction

Mineral aerosol (dust) is a critical component of the earth system, affecting atmospheric radiative transfer (Haywood & Boucher, 2000; Miller & Tegen, 1998; Tegen et al., 1996), cloud microphysical properties (Andreae & Rosenfeld, 2008; Mahowald & Kiehl, 2003), terrestrial and marine biogeochemistry (Dansie et al., 2017; Jickells et al., 2005; Koren et al., 2006), and human health (Goudie, 2014). For these reasons, it is essential that the dust cycle is accurately represented in numerical models, so as to reduce uncertainties in the simulation of current and future climate (Boucher et al., 2013). Evaluation of models that took place in the 5th phase of the Coupled Model Intercomparison Project (CMIP5) show biases in simulated dust emissions and optical depth (DOD); potential sources of this bias include the treatment of land surface properties in the models, the choice of emission parameterisation scheme, the dust size distribution, and the representation of surface wind speeds (Evan, 2018; Evan et al., 2014; Fiedler et al., 2016; Pu & Ginoux, 2018; Wu et al., 2020). Models participating in the latest phase of the project (CMIP6) benefit from advances in resolution and physical parameterisations, however initial analysis of the dust cycle in these simulations still shows large inter-model differences in emissions and DOD (Zhao et al., 2022).

Dust emission is a function of both the capacity of the atmosphere to entrain sediment (erosivity) and the properties of the land surface (erodibility), and as such is sensitive to factors such as grain size, vegetation cover, soil moisture and slope angle (Kok et al., 2012; Wiggs, 2011). Of the CMIP6 models that include dust as a prognostic variable, the majority calculate emissions online through parameterisation schemes of varying sophistication (Marticorena & Bergametti, 1995; Tegen et al., 2002), with surface features described by a threshold friction velocity above which uplift takes place. Accurate representation of the surface wind speed distribution in source areas is therefore critical to realistic simulation of the emission process, however previous studies have shown that models tend to miss the low-frequency, high wind speed events that drive uplift (Evan, 2018; Roberts et al., 2017). This is likely due to the inability of models to adequately capture mesoscale atmospheric processes that generate dust-emitting surface winds (Evan, 2018; Garcia-Carreras et al., 2013; Marsham et al., 2011), for example nocturnal low-level jets (NLLJ's) and cold pool outflows (CPO's) (Allen et al., 2013; Fiedler et al., 2013; Marsham et al., 2013). Evaluating the representation of such processes in the latest phase of the CMIP experiments is therefore an important research task.

Whilst total annual emissions from southern Africa (2,300 Mg) are substantially lower than those from the Sahara (Ginoux et al., 2012), the subcontinent has nonetheless been identified as an important region for dust emissions, with several major source areas located in the arid southwest of the subcontinent (Prospero et al., 2002; Vickery et al., 2013; Washington et al., 2003). Indeed, the Etosha Pan, an ephemeral lake bed located in northern Namibia, is one of the most prominent dust sources in the Southern Hemisphere (Washington et al., 2003), and has been the focus of recent work investigating the meteorological controls on uplift (Clements & Washington, 2021, 2022; Wiggs et al., 2022). In austral winter, when dust emissions peak at Etosha, the breakdown of a persistent NLLJ is the primary driver of emissions, with momentum mixed-down from the jet core enhancing surface winds after sunrise (Clements & Washington, 2021; Wiggs et al., 2022). Clements and Washington (2021) showed that NLLJ core wind speeds were underestimated in ERA-Interim (ERA-I) data, however the skill of coupled models was not evaluated. Contrary to the findings of earlier remote sensing studies, Etosha has also been shown to be emissive during austral summer (Clements & Washington, 2021; Wiggs et al., 2022), with the inland propagation of an integrated anabatic-sea breeze driving uplift during the evening (Clements & Washington, 2022). The representation of this system in coupled models is also yet to be evaluated.

Given the need to refine the simulation of the dust cycle in numerical models, and the lack of previous work assessing dust processes outside of Saharan source areas, this

paper aims to evaluate the representation of dust emissions across southern Africa, as well as the atmospheric processes that drive uplift in CMIP6 models. This will be achieved by addressing the following key questions: (i) What is the spatial distribution of simulated dust emissions in the CMIP6 models and how do they represent the observed climatology in uplift across southern Africa? (ii) How do the CMIP6 models represent the atmospheric processes that drive observed dust emissions at Etosha? (iii) What atmospheric processes are responsible for driving dust emissions simulated in the CMIP6 models, and how do they relate to the spatial distribution of dust emissions identified in key question 1? The remainder of the paper is structured as follows: Section 2 describes the CMIP6 model output evaluated in the paper, as well as the observational, reanalysis and satellite data used for comparison. Results are presented in sections 3, 4, and 5, with each of the key questions addressed in turn. The results are discussed in section 6 and a summary of the papers main findings are given.

2 Data and Methods

2.1 CMIP6 Models

Table 1. *Summary of CMIP6 Models*

Model	Variant-ID	Lon/Lat Grid	Levels in <1500m	Reference
HadGEM3-GC31-MM	r1i1p1f3	432 x 324	14	Ridley et al. (2019)
HadGEM3-GC31-LL	r1i1p1f3	192 x 144	14	Ridley et al. (2019)
MPI-ESM-1-2-HAM	r1i1p1f1	192 x 96	6	Neubauer et al. (2019)
MIROC-ES2L	r1i1p1f2	128 x 64	10	Hajima et al. (2019)
MIROC6	r1i1p1f1	256 x 128	11	Tatebe et al. (2018)
CanESM5	r1i1p2f1	128 x 64	12	Swart et al. (2019)
MRI-ESM2-0	r1i1p1f1	320 x 160	12	Yukimoto et al. (2019)
CNRM-ESM2-1	r1i1p1f2	256 x 128	15	Seferian et al. (2018)

In sections 3 and 4, model output from the CMIP6 historical simulations (1850 – 2014) is evaluated against observational, reanalysis and satellite data, whilst in section 5, the processes controlling dust emissions in the models are analysed. Initial conditions for the historical simulations are obtained from pre-industrial control runs, and they are subsequently forced with time-varying parameters such as greenhouse gas concentrations, aerosol concentrations, solar output, and land use (Andrews et al., 2020; Eyring et al., 2016). Given the aims of the paper are to evaluate the representation of dust emissions and dust-emitting mechanisms (e.g., NLLJ's) in CMIP6 models, the criteria for model selection were as follows:

1. Monthly dust emission data available at the time of writing.
2. 6-hourly u, v, and temperature model level data available at the time of writing.
3. 3-hourly u, v, and temperature surface data available at the time of writing.

The models that met these criteria are detailed in Table 1, along with the ensemble variant-id, the spatial resolution and number of model levels for each of the simulations. All of the models considered in this paper calculate emissions online, whilst half (HadGEM3-GC31-MM, HadGEM3-GC31-LL, MPI-ESM-1-2-HAM, CNRM-ESM2-1) simulate dynamic vegetation.

Variables extracted from the models for analysis include u and v components of wind (surface, model level), temperature (surface, model level), total column soil moisture and geopotential height (850hPa). Wind speed was calculated as the square root of the sum of the squared u and v components at each grid point (ws= $\sqrt{u^2 + v^2}$). For the model levels, which are given as hybrid height coordinates (terrain following in the lower troposphere), data was converted to pressure levels following the equation;

$$p = a * p0 + b * ps \tag{1}$$

where a and b are vertical coordinate formula terms, p0 is a reference pressure level (typically 1000hPa or 1013hPa), and ps is the surface pressure. Pressure level data was then converted to geometric altitude using the hypsometric equation. Where atmospheric data is presented for Etosha, the grid point closest to the centre of the pan in each of the models is used.

2.2 In Situ Observational Data

In section 4, model output is evaluated against in situ observational data from the Etosha Pan. The data was collected at the Okaukuejo field site (19.18°S, 15.92°E), situated on the southwestern perimeter of the pan, as part of the CLoud-Aerosol-Radiation Interactions and Forcing: Year 2016 (CLARIFY-2016) ground-based deployment. The field site was instrumented with a HALO Photonics Doppler lidar and a Davis automatic weather station (AWS), and the data used for evaluating the models was collected in September 2016. The readings taken by the lidar presented in this paper are for horizontal wind speed, with wind components retrieved from a radial velocity distribution using a velocity-azimuth display (VAD) technique (Browning & Wexler, 1968; Park et al., 2018). The vertical resolution of the lidar is 3 m, with the lowest measurement taken at 30 m above the instrument, and the height of the highest measurement variable (between 1 and 2 km), depending on attenuation of the beam signal. The error in the wind speed measurements is <0.2 ms^{-1} and VAD scans were taken every 15 minutes. The AWS was mounted at a height of 3m with wind speed and temperature readings taken every 10 minutes. For a full description of the field site at Etosha and the instrumentation deployed, see Clements and Washington (2021).

2.3 Satellite Imagery

In section 3, dust emission data from the model output is evaluated against Aerosol Index (AI) data from the Total Ozone Mapping Spectrometer (TOMS) (the reasoning behind this approach is discussed in section 3.2). The TOMS instrument was on board the NASA Nimbus 7 polar-orbiting satellite and took measurements in six ultraviolet (UV) wavelengths, and has been used to infer the presence of UV absorbing aerosols (such as dust) in the atmosphere (Prospero et al., 2002; Washington et al., 2003). AI data is given in non-dimensional units with absorbing aerosols returning positive values, and for dust, the magnitude of the AI signal reflects the optical depth of the aerosol (Bryant, 2003; Herman et al., 1997). The frequency of the TOMS output is daily, and is projected onto a latitude-longitude grid of resolution 1.0° x 1.25°. For a full description of the TOMS instrumentation and a discussion of the strengths and limitations of dust detection in the UV wavelengths, see Herman et al. (1997) and Torres et al. (2002).

2.4 Reanalysis Data

In sections 3 and 4, model output is evaluated against ERA5 reanalysis data from the European Centre for Medium-Range Weather Forecasts (ECMWF). ERA5 data covers the period 1950–present, with analysis fields output at hourly intervals, at a spatial resolution of ≈31 km, and 137 model levels in the vertical. Variables extracted from the ERA5 dataset for analysis include u and v components of wind (10m), temperature (2m) and volumetric soil water. Wind speed was calculated as the square root of the sum of the squared u and v components at each grid point (ws= $\sqrt{u^2 + v^2}$). Where atmospheric data is presented for Etosha, the grid point closest to the centre of the pan (18.75°S, 16.25°E) is used. In section 4, monthly mean 850hPa geopotential data for September 2016 is used to select the September month from each model simulation for evaluation (a full description of the method employed is given in section 4.1). This pressure level was selected as it is close to the surface over the elevated interior plateau of southern Africa. The data was converted to geopotential height by dividing by g (9.81ms^{-2}). For a detailed discussion of the ERA5 reanalysis, including data assimilation systems, model setup, and an overview of performance, see (Hersbach et al., 2020).

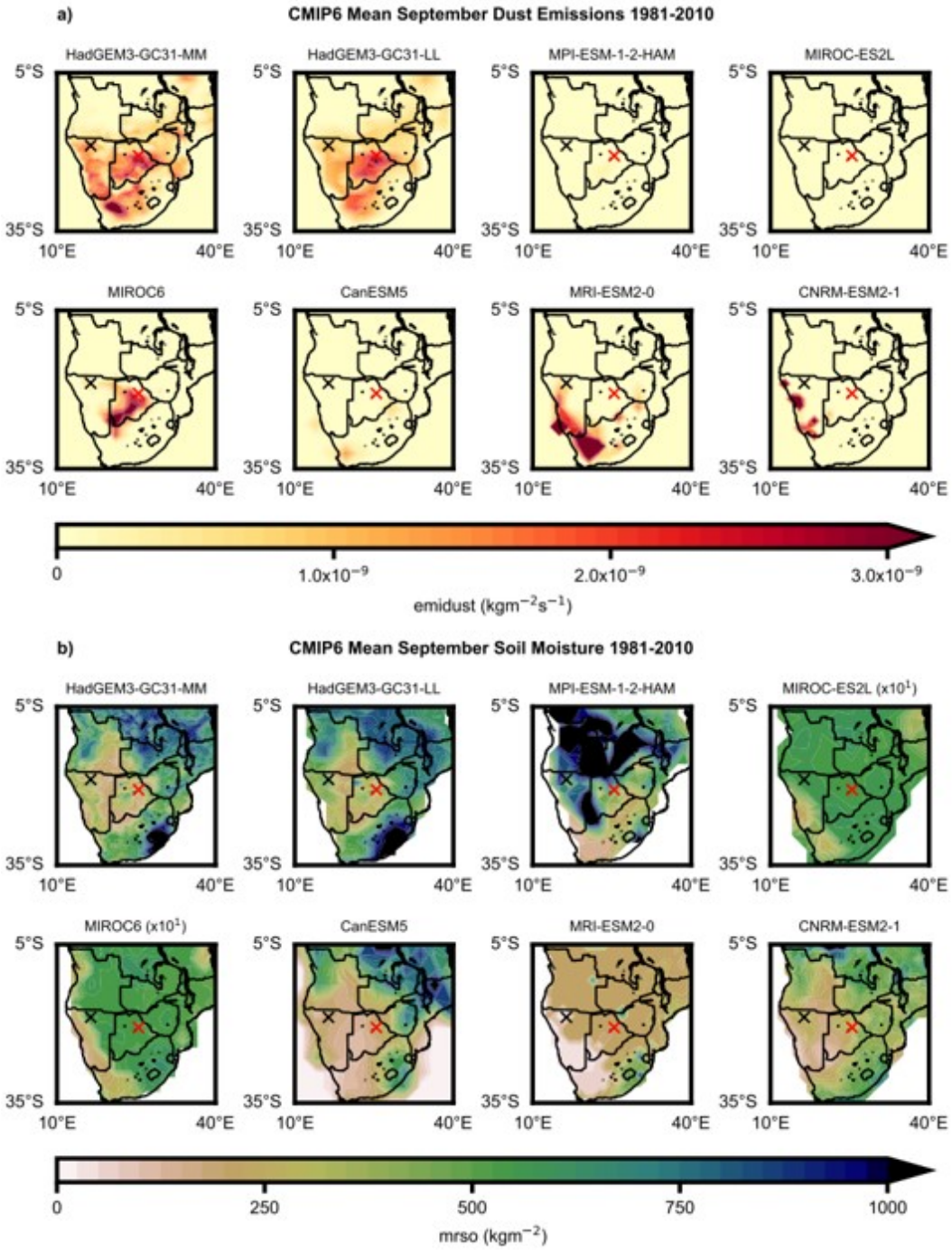


Figure 1. Mean September total emission rate of dust (a) and total column soil moisture (b) in each of the CMIP6 models for the period 1981-2010. The location of the Etosha Pan is given by the black cross and the location of the Makgadikgadi Pan is given by the red cross.

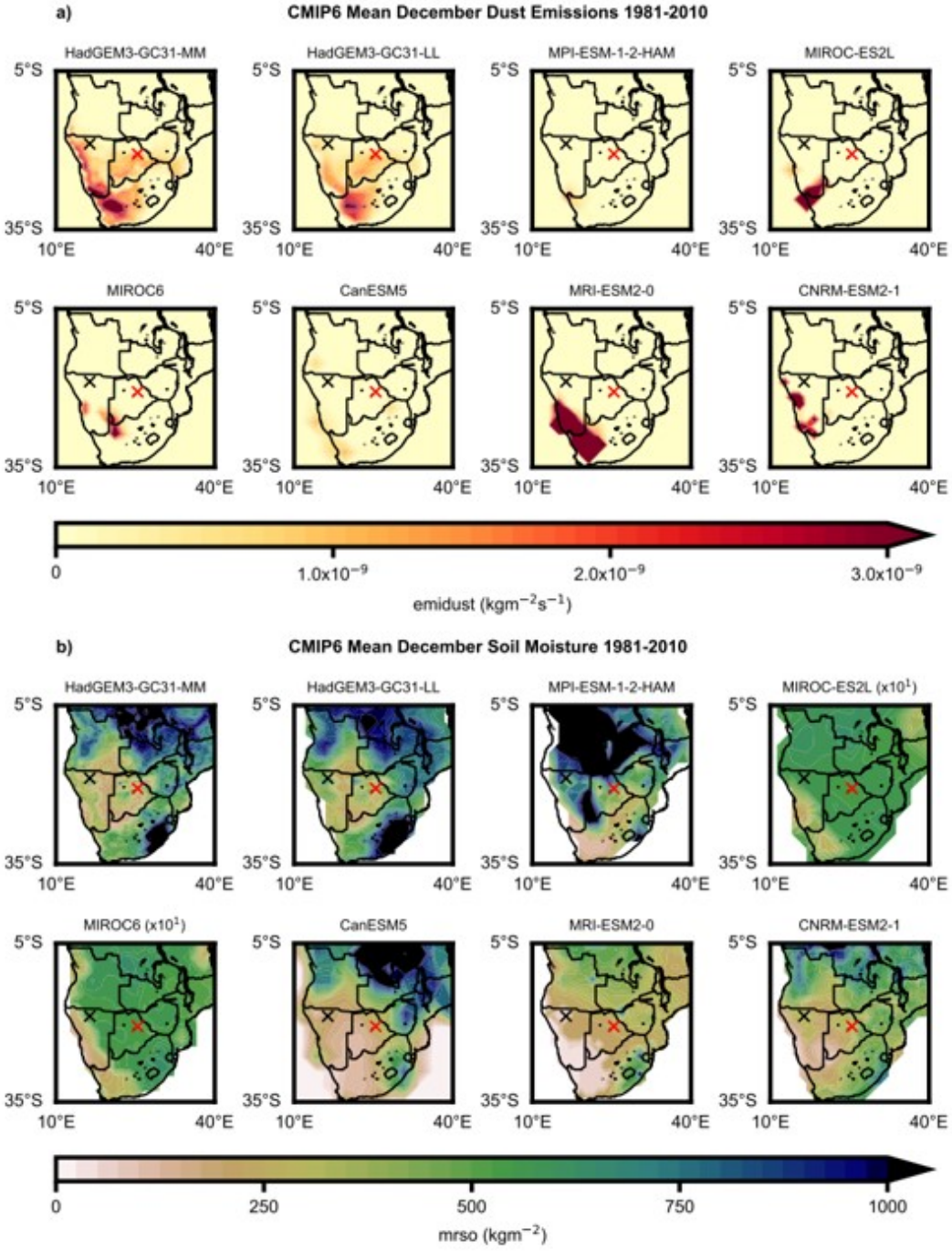


Figure 2. Mean December total emission rate of dust (a) and total column soil moisture (b) in each of the CMIP6 models for the period 1981-2010. The location of the Etosha Pan is given by the black cross and the location of the Makgadikgadi Pan is given by the red cross.

3 Southern African Dust Emissions in CMIP6 Models

The following sections address key question 1: What is the spatial distribution of simulated dust emissions in the CMIP6 models and how do they represent the observed climatology in uplift across southern Africa?

3.1 Spatial Distribution of Emissions in CMIP6 Models

Table 2. *TOMS AI Statistics 1980-1992*

	Etosha		Makgadikgadi	
Month	AI Mean	AI SD	AI Mean	AI SD
Jan	1.3	0.3	0.7	0.4
Feb	1.1	0.2	0.6	0.5
Mar	0.9	0.4	0.5	0.5
Apr	0.7	0.5	0.6	0.5
May	0.9	0.5	0.8	0.6
Jun	1.1	0.3	1.1	0.4
Jul	1.2	0.3	1.3	0.3
Aug	1.4	0.3	1.6	0.2
Sep	1.7	0.3	1.7	0.3
Oct	1.5	0.3	1.3	0.2
Nov	1.5	0.3	1.0	0.4
Dec	1.6	0.3	0.8	0.3

Figures 1 and 2 show the mean spatial distribution of total emission rate of dust (a) and total column soil moisture (b) as simulated by each of the models for the period 1981-2010, for the months of September and December respectively. September was selected for analysis as it is the dustiest month in the TOMS record at the Etosha and Makgadikgadi pans (Table 2), southern Africa's most prominent source areas (Prospero et al., 2002; Washington et al., 2003), whilst December was selected as it is the dustiest month at Etosha during austral summer, outside of the traditional dust season (Clements & Washington, 2022). Work characterising the meteorology of the subcontinent's dust sources has also been conducted during these months (Clements & Washington, 2021, 2022; Wiggs et al., 2022), and hence they form the basis for evaluating the representation of dust-emitting processes in the models in section 4. For reference, the location of the Etosha (black cross) and Makgadikgadi (red cross) pans are shown on Figures 1 and 2.

When evaluating the spatial distribution of dust emissions, the models can be classified into four groups, namely those that simulate uplift; (1) over the interior of southern Africa during September and along the west coast during December (HadGEM3-GC31-MM, HadGEM3-GC31-LL, MIROC6), (2) along the west coast in September and December (MRI-ESM2-0, CNRM-ESM2-1), (3) along the west coast in December but minimal uplift in September (MIROC-ES2L), and (4) minimal uplift in September and December (MPI-ESM-1-2-HAM, CanESM5) (Figures 1a and 2a). The spatial distribution in dust emissions is closely related to the spatial distribution in soil moisture, with seven of the eight models displaying a general northeast – southwest drying trend (Figures 1b and 2b), and hence a concentration of dust emissions in the south and west of southern Africa (Figures 1a and 2a). The exception is the MPI-ESM-1-2-HAM model, which simulates an anomalous region of high (>1000 kgm^{-2}) soil moisture values in the southern Kalahari/Northern Cape region (Figures 1b and 2b); this helps to account for the low

total emissions in this run, which are an order of magnitude below the other models in both September (Figure 1a) and December (Figure 2a).

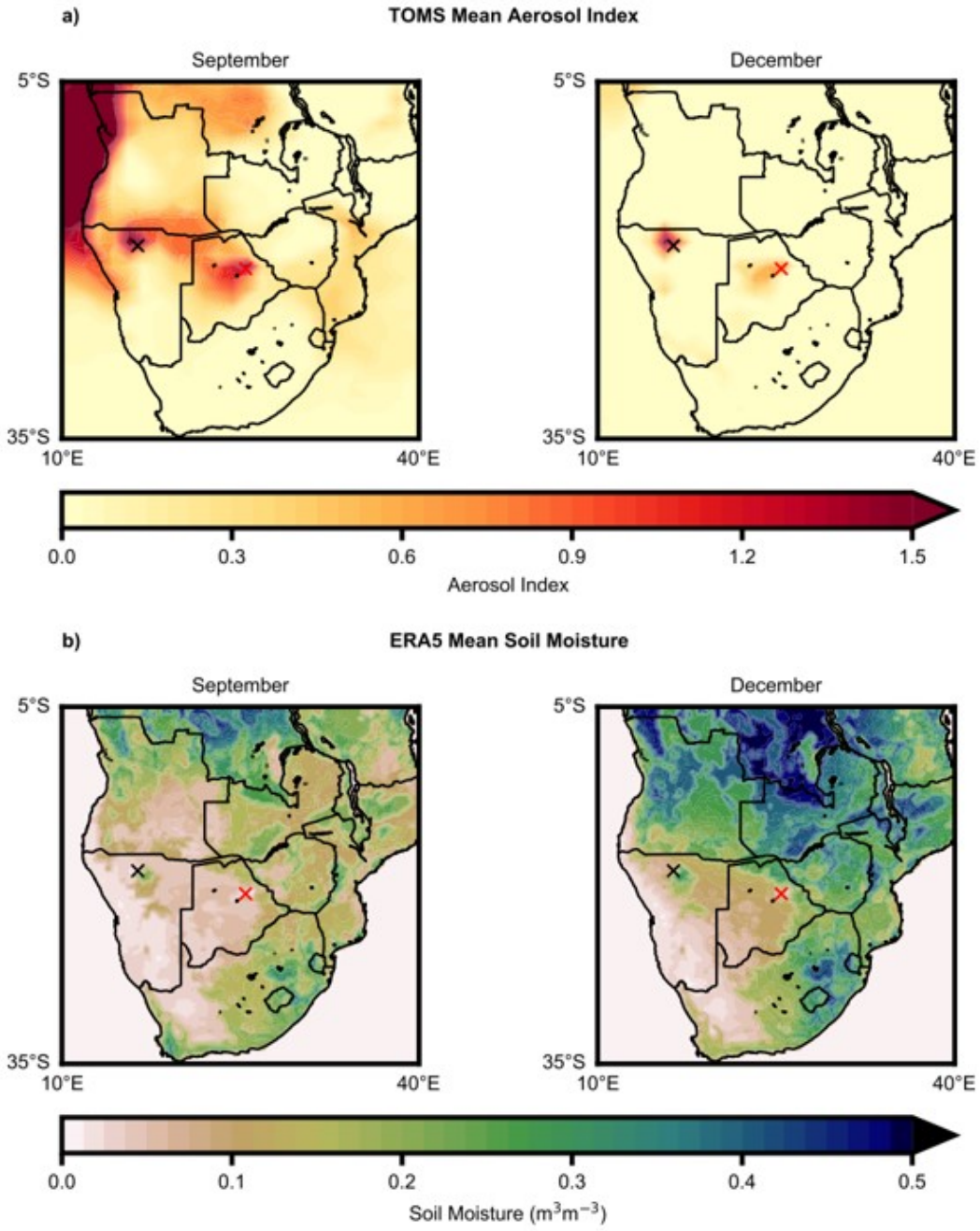


Figure 3. Mean TOMS AI data (a) and ERA5 soil moisture (b) for September and December. The location of the Etosha Pan is given by the black cross and the location of the Makgadikgadi Pan is given by the red cross.

3.2 Comparison with Observed Dust Emissions

In situ observations of dust emission from across southern Africa are sparse, and where available, are either limited in their temporal extent (Haustein et al., 2015) or cover only one of the subcontinent's source areas (Wiggs et al., 2022), and so a direct evaluation of the emission data from the models is implausible. The observed spatial distribution in uplift has however been inferred from remotely sensed dust concentration data (Prospero et al., 2002; Washington et al., 2003), with advances in satellite technology and dust detection techniques corroborating the timing and location of emission events across southern Africa (Murray et al., 2016; Vickery et al., 2013). Figure 3 shows the mean spatial distribution of TOMS AI data (a) and ERA5 soil moisture (b), for the months of September and December. For reference, the location of the Etosha (black cross) and Makgadikgadi (red cross) pans are shown.

In September, maximum dust activity is observed at Etosha and Makgadikgadi and in a belt that stretches between the two pans across the Kalahari (Figure 3a); side from the three models that simulate emissions over the interior of southern Africa (HadGEM3-GC31-MM, HadGEM3-GC31-LL, MIROC6) (Figure 1a), the representation of uplift in the models is poor, with the other runs simulating either uplift along the west coast (MRI-ESM2-0, CNRM-ESM2-1) or very little at all (MPI-ESM-1-2-HAM, CanESM5). In December, the major dust source area is Etosha (Figure 3a), however all of the models that are active at this time of year simulate maximum emissions along the west coast of southern Africa (Figure 2a). Minor dust activity has been observed along the Namib coast in austral summer (Vickery et al., 2013), however it is not the most prominent dust source area in this season. The low bias in simulated emissions at Etosha could be due to the treatment of the land surface in the models, although the majority capture well the general northeast – southwest drying trend observed across the subcontinent (Figures 1b, 2b and 3b). Some of the models (HadGEM3-GC31-MM, HadGEM3-GC31-LL, CanESM5 and CNRM-ESM2-1) are too wet over southern Angola however, which coincides with the Etosha catchment area, whilst the MPI-ESM-1-2-HAM simulation is too wet over the interior of southern Africa. Indeed, Munday and Washington (2018) report systematic wet biases across southern Africa in the CMIP5 models, with Karypidou et al. (2022) confirming that these biases persist in the CMIP6 simulations; given the influence of soil moisture on the threshold friction velocity in emission parameterisation schemes (Pu & Ginoux, 2018; Zhao et al., 2022), this is a possible explanation for the low bias in dust emissions at Etosha. An alternative explanation is that the models do not capture the atmospheric processes responsible for driving dust uplift, an assertion that is investigated in sections 4 and 5.

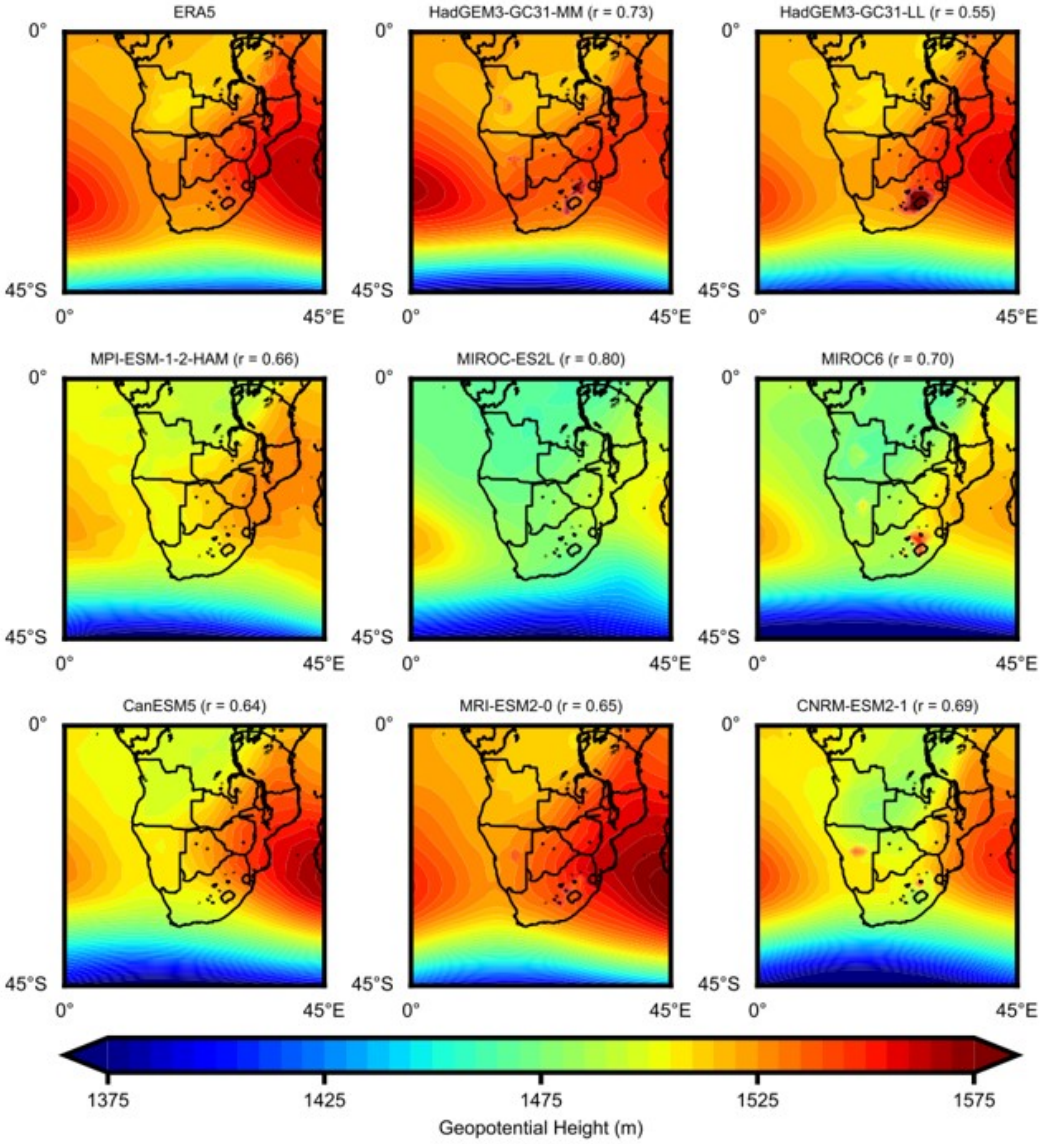


Figure 4. Mean 850hPa geopotential height for the September month selected in each of the CMIP6 models for comparison with the observations.

4 Dust Emission Mechanisms in CMIP6 Models

The following sections address key question 2: How do the CMIP6 models represent the atmospheric processes that drive observed dust emissions at Etosha?

4.1 Nocturnal Low-Level Jets

Nocturnal low-level jets (NLLJ's) have been shown to be a consistent feature of the boundary layer at Etosha during austral winter, and are the primary driver of dust uplift from the pan surface during this season (Clements & Washington, 2021; Zunckel et al., 1996). In this section, the representation of the Etosha NLLJ and associated surface winds are evaluated in the models for one September in each of the simulations. Whilst it would have been possible to construct climatologies for the models, for the purpose of comparison with observations, which are only available for 2016, any results presented represent one month of simulations. September was chosen as it is the dustiest month at Etosha in the TOMS record (Table 2) (Clements & Washington, 2022; Prospero et al., 2002; Washington et al., 2003), and one for which data is available from the lidar and AWS at the pan.

Given that NLLJ strength is sensitive to changes in the background pressure gradient (Shapiro & Fedorovich, 2010; van de Wiel et al., 2010), an attempt has been made to control for this when selecting the September month for each of the models. For each simulation (1981-2010), monthly mean plots of 850hPa geopotential height were created for the area 0° - 45°E, 0° - 45°S and compared against the observed mean for September 2016 (from ERA5 data). The months with the highest correlation coefficient in each simulation were selected for comparison with observations and are detailed in Table 3. Plots of 850hPa geopotential height for each of the selected months are shown in Figure 4.

Table 3. *CMIP6 September Months*

Model	Year	Correlation Coefficient
HadGEM3-GC31-MM	1985	0.73
HadGEM3-GC31-LL	1991	0.55
MPI-ESM-1-2-HAM	1985	0.66
MIROC-ES2L	1987	0.80
MIROC6	1997	0.70
CanESM5	1993	0.64
MRI-ESM2-0	2004	0.65
CNRM-ESM2-1	1987	0.69

Figure 5 shows mean wind speed-height profiles at 0000, 0600, 1200 and 1800 for the models and lidar at Etosha, whilst Figure 6 shows mean wind speed-height and temperature-height profiles at the same times for the models. All of the models broadly simulate the observed diurnal cycle in low-level winds, with a jet-like structure developing in the evening (evident in the 0000 profiles), which is subsequently eroded through the morning (no jet structure in the 1200 profiles) (Figures 5 and 6). Given that the evolution of the NLLJ at Etosha is closely tied to the diurnal cycle in surface heating and the growth of an inversion layer during the nocturnal period (Clements & Washington, 2021; Zunckel et al., 1996) this is unsurprising, as the timing of onset and cessation of surface heating is consistent between the simulations and observations (Figure 7a), and a temperature inversion is evident in seven of the eight model runs by 0000 (Figure 6) (there is no inversion

in the MRI-ESM2-0 simulation, however there is a reduction in the temperature lapse rate from 1800 to 0000).

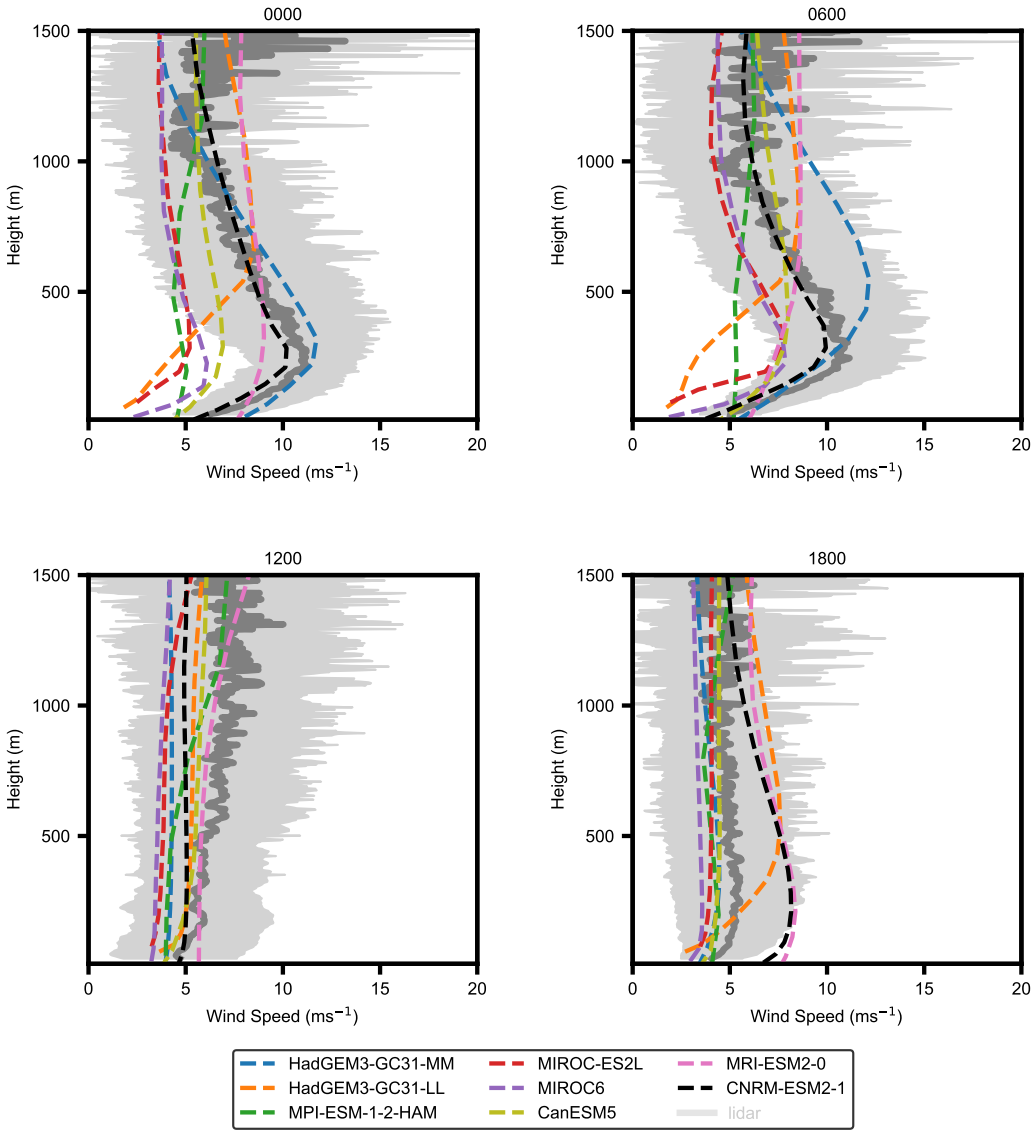


Figure 5. Mean September wind speed-height profiles at 0000, 0600, 1200 and 1800 for the CMIP6 models and lidar at Etosha. The shaded grey area denotes one standard deviation away from the lidar mean.

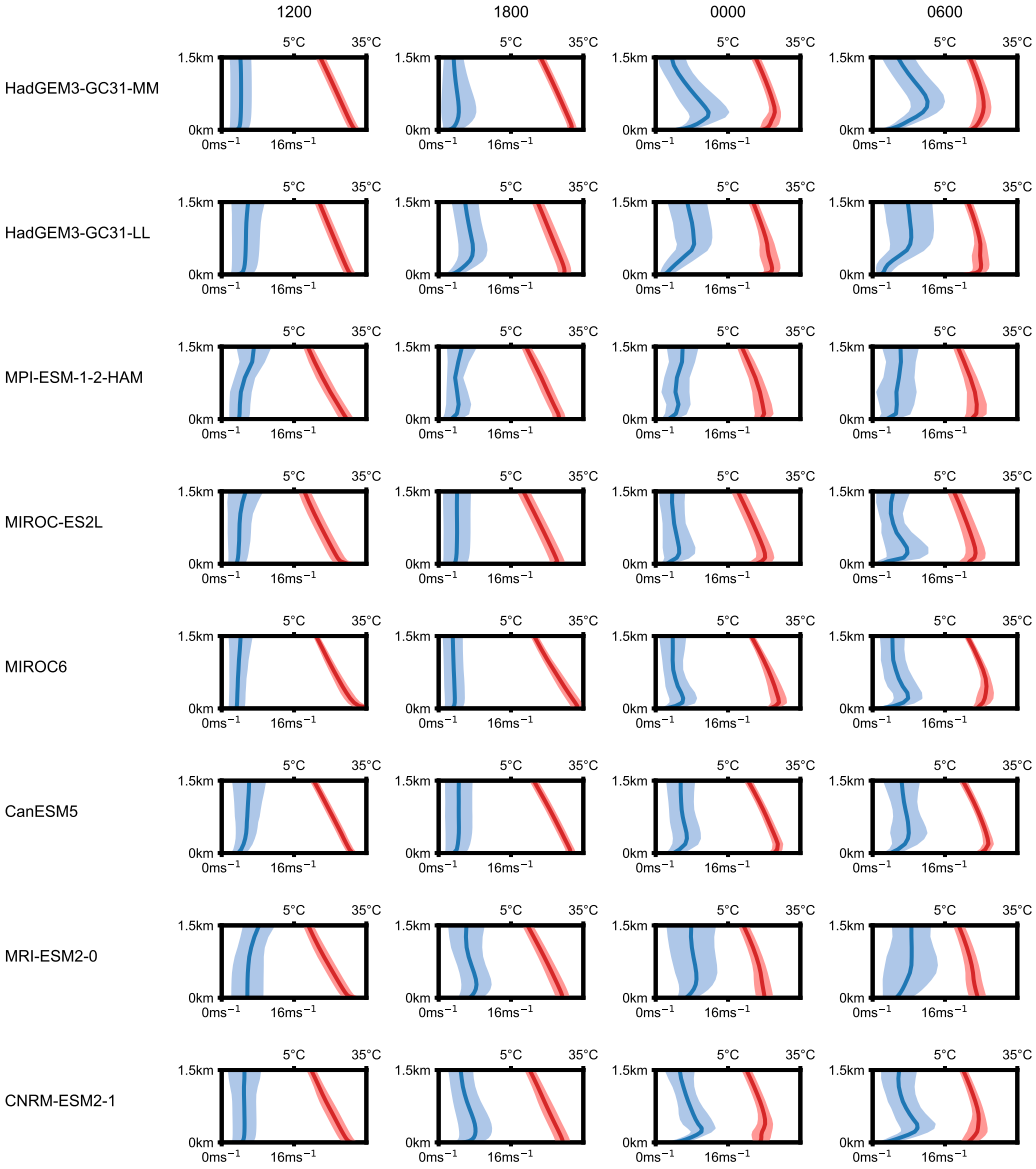


Figure 6. Mean wind speed-height (blue) and temperature-height (red) profiles at 0000, 0600, 1200 and 1800 at Etosha for the selected September month in each model. The shaded areas denote one standard deviation away from the mean profiles.

Table 4. *Results of T-Test Calculations Performed on lidar and CMIP6 model 0600 core wind speeds*

Model	WS (ms^{-1})	p-value	sig ($\alpha = 0.05$)
HadGEM3-GC31-MM	12.15	0.12	n
HadGEM3-GC31-LL	8.54	0.01	y
MPI-ESM-1-2-HAM	5.34	$1.30x10^{-9}$	y
MIROC-ES2L	7.70	$3.24x10^{-4}$	y
MIROC6	7.85	$1.12x10^{-5}$	y
CanESM5	8.00	$3.01x10^{-4}$	y
MRI-ESM2-0	8.64	0.01	y
CNRM-ESM2-1	9.94	0.07	n

Whilst the models generally do well in representing the temporal evolution of the NLLJ, there is considerable variability in simulated jet strength and core height. Table 4 shows the results of unpaired, one-tailed t-tests conducted to test for difference between the lidar and modelled jet core wind speeds at 0600. This time was chosen as it is close to the observed peak in NLLJ strength at Etosha (Clements & Washington, 2021), and also close to the breakdown of the structure, an important process with regards to dust emission. The models tend to underestimate jet core wind speeds at 0000 (multi-model mean of 7.93ms^{-1} compared to lidar mean of 11.20ms^{-1}) and 0600 (multi-model mean of 8.64ms^{-1} compared to lidar mean of 11.82ms^{-1}), with significant differences ($\alpha = 0.05$) in 0600 core wind speeds between the observations and all but two of the models (Table 4). The exceptions are the HadGEM3-GC31-MM and CNRM-ESM2-1 runs, which have the most vertical levels in the lower troposphere (Table 1), and also simulate the deepest inversion layers (≈400m by 0000) (Figure 6). Conversely, there is a group of models (MIROC-ES2L, MIROC6, CanESM5) that underestimate the observed core wind speeds at 0000 by over one standard deviation (Figure 5) and only simulate very shallow inversion layers (<100m) (Figure 6). The relationship between the depth of the inversion layer and the height of the jet core is well demonstrated by the HadGEM3-GC31 models, which both simulate temperature inversions (an isothermal layer in the case of HadGEM3-GC31-LL) to heights of ≈600m at 0600 (Figure 6), and as such generate a jet core that is too deep (in excess of 500m compared to the lidar core of 306m) (Figure 5).

Table 5. *September 0900 Wind Speed Statistics*

Model	WS (ms^{-1})	% Increase from 0600 WS
AWS	5.84	101
HadGEM3-GC31-MM	4.38	29
HadGEM3-GC31-LL	3.17	65
MPI-ESM-1-2-HAM	2.67	45
MIROC-ES2L	2.76	17
MIROC6	3.04	66
CanESM5	3.34	126
MRI-ESM2-0	5.38	8
CNRM-ESM2-1	4.48	68

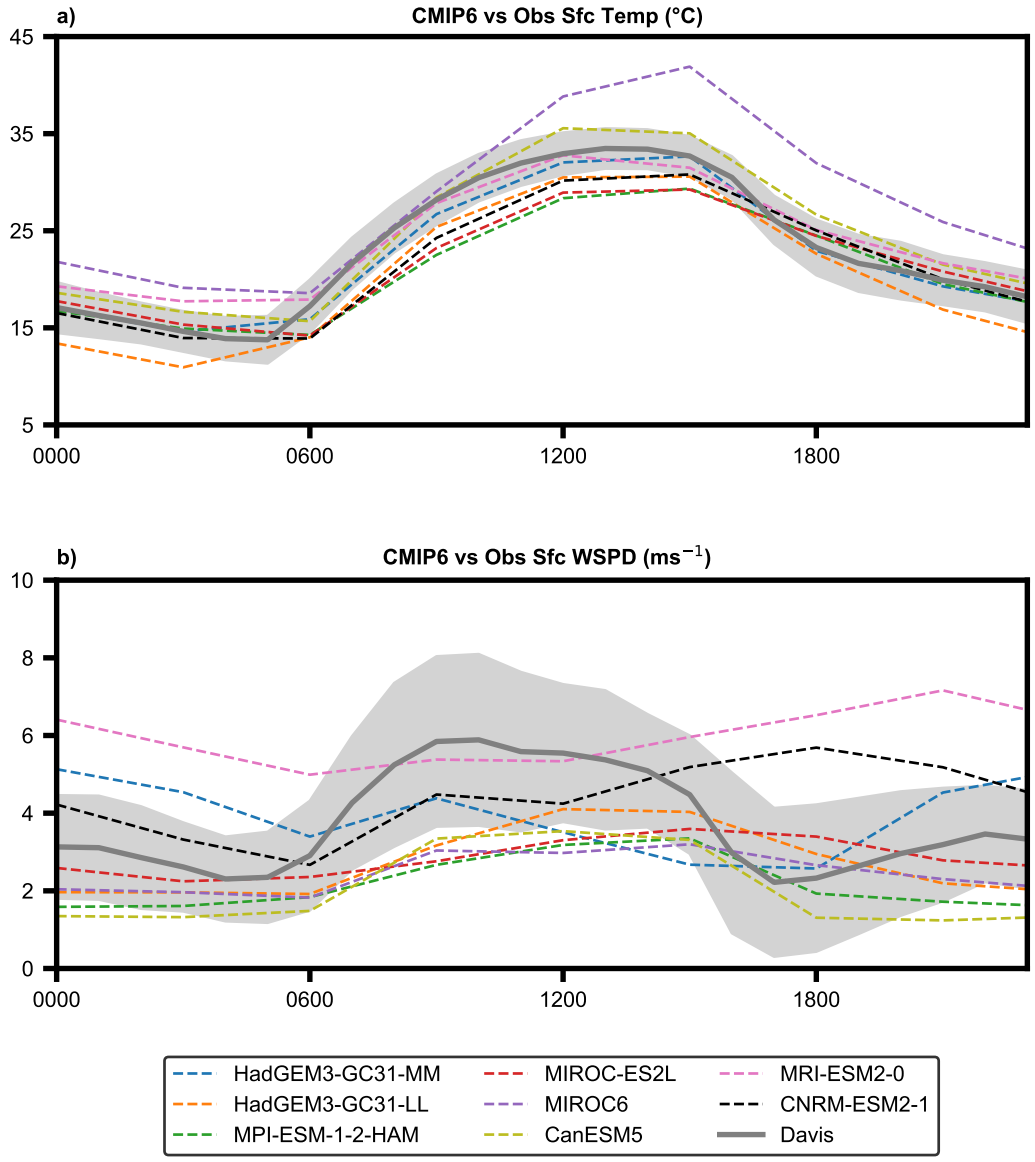


Figure 7. Mean September diurnal cycle of surface temperature (a) and wind speed (b) for the CMIP6 models and AWS at Etosha. The shaded grey areas denotes one standard deviation away from the AWS mean.

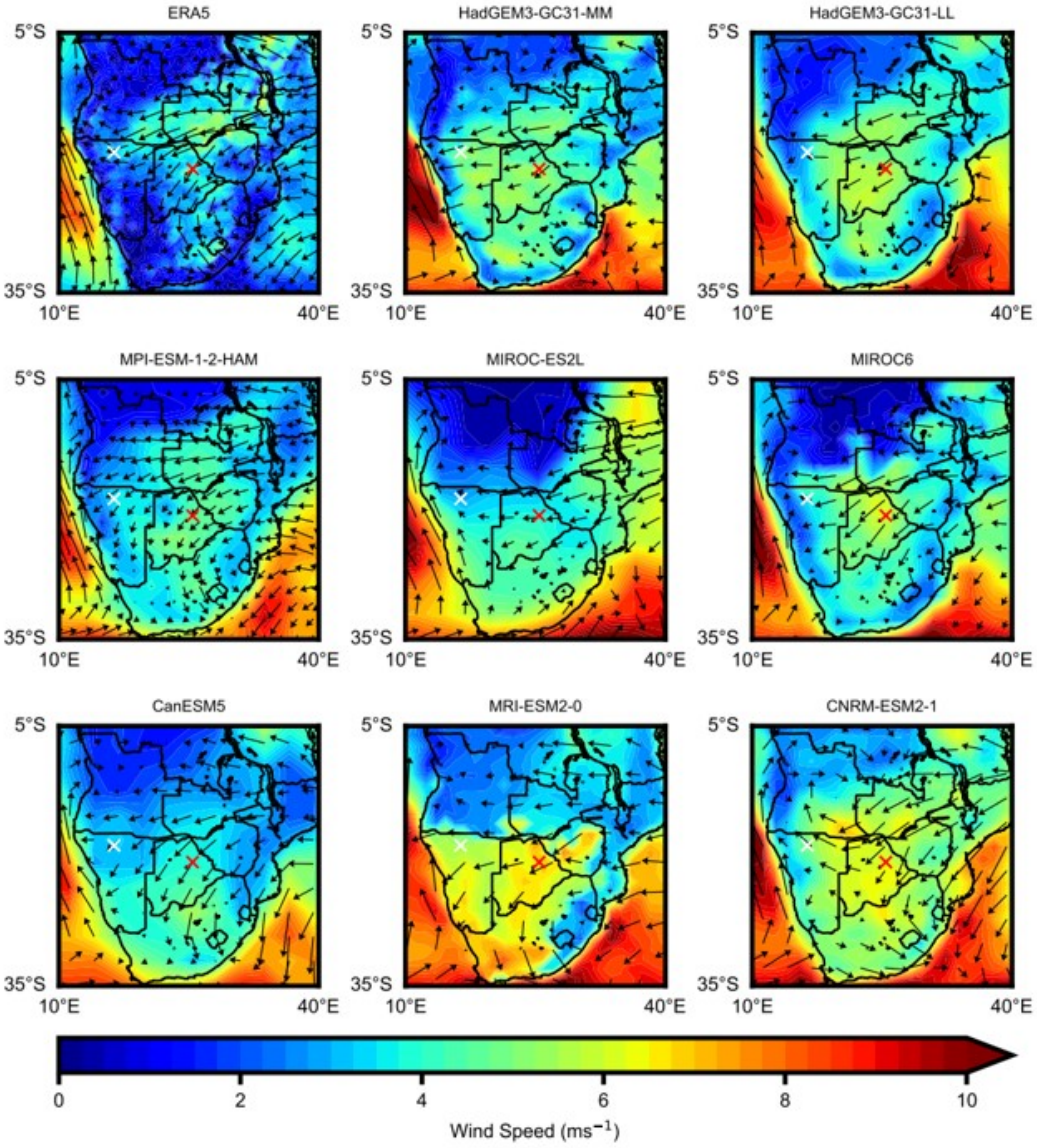


Figure 8. Mean September 0900 surface wind speed and vectors from ERA5 and for the CMIP6 models. The location of the Etosha Pan is given by the white cross and the location of the Makgadikgadi Pan is given by the red cross.

Dust emission is driven by the breakdown of the NLLJ structure after sunrise, and the mixing-down of momentum from the jet core to the surface (Allen & Washington, 2014; Clements & Washington, 2021; Knippertz & Todd, 2012), and so it is essential that the models capture this process and the associated increase in surface wind speeds. Figure 7b shows the mean diurnal cycle of surface wind speed for the models and AWS at Etosha, whilst Table 5 shows 0900 surface wind speed statistics. 0900 was selected as it is the time of peak surface wind speeds at Etosha in austral winter, and coincident with the timing of uplift from the pan (Clements & Washington, 2021; Vickery et al., 2013). In general, the models tend to underestimate the surface wind speeds at the critical time of 0900 (multi-model mean of 3.65ms^{-1} compared to AWS mean of 5.84ms^{-1}) (Table 5), and also underestimate the relative increase in surface wind speed from 0600 to 0900 (multi-model mean of 43% compared to AWS mean of 101%). Only the CNRM-ESM2-1 model captures well the surface wind speed at 0900 (4.48ms^{-1}), and the relative increase from 0600 to 0900 (68%); this model also simulated the most accurate NLLJ profile at 0600 (Figure 5).

The momentum mixed-down from the NLLJ core enhances north-easterly surface winds at Etosha that are embedded in the anticyclonic rotation of air associated with the large-scale subsidence over southern Africa during austral winter (Clements & Washington, 2021; Reason, 2017). Figure 8 shows mean 0900 wind speed and vectors across southern Africa for the models and ERA5, with Etosha sitting at the terminus of a region of strong northeasterlies in the reanalysis data. The treatment of this background flow varies substantially between models, and helps to account for some of the differences in the simulated morning wind speeds at Etosha (Figure 7b). For instance, outside of the period associated with the NLLJ breakdown (0900-1200), surface winds in the MRI-ESM2-0 run are over one standard deviation above the observations (Figure 7b), with this model simulating an area of easterlies/northeasterlies that are displaced too far south and west (Figure 8), hence generating a stronger background flow at Etosha when compared to the ERA5 data. This is in contrast to the CanESM5 model, which captures well the relative increase in surface winds from 0600 to 0900 associated with the NLLJ breakdown (125%) (Figure 7b, Table 5), however the area of strong northeasterlies doesn't get to Etosha's longitude (Figure 8) and so the 0900 surface winds at Etosha are one standard deviation below the observations, despite the NLLJ enhancement.

4.2 Anabatic-Sea Breeze

Given the unique topography and oceanography of the west coast of southern Africa, it is unsurprising that regional topographic and thermal airflows develop in all seasons (Lindesay & Tyson, 1990). An integrated anabatic-sea breeze system has been identified along the Namib coast during austral summer (Howard & Washington, 2018), and its inland propagation has been shown to drive dust-emitting surface winds at Etosha (Clements & Washington, 2022). In this section, the representation of the anabatic-sea breeze and associated surface winds are evaluated in the models for the month of December. ERA5 data has been used to characterise the anabatic-sea breeze, and so climatologies (1981-2010) have been constructed for each of the models. December was chosen as it is the second dustiest month at Etosha (Table 2) and the dustiest month during austral summer when the anabatic-sea breeze is well developed (Clements & Washington, 2022).

Figure 9 shows mean wind speed and vectors along the Namib coast at 0900, 1200, 1500, 1800, 2100 and 0000 for the models and ERA5, whilst Figure 10 shows mean surface temperature for the same times. In general, the models capture well the diurnal cycle of surface winds along the coast, with all eight simulating an onshore flow that develops by 1200, peaks in intensity at 1500 and then dissipates through the evening, consistent with the ERA5 data (Figure 9). Given that the timing of development of the anabatic-sea breeze is driven by the diurnal cycle in diabatic heating over the interior of south-

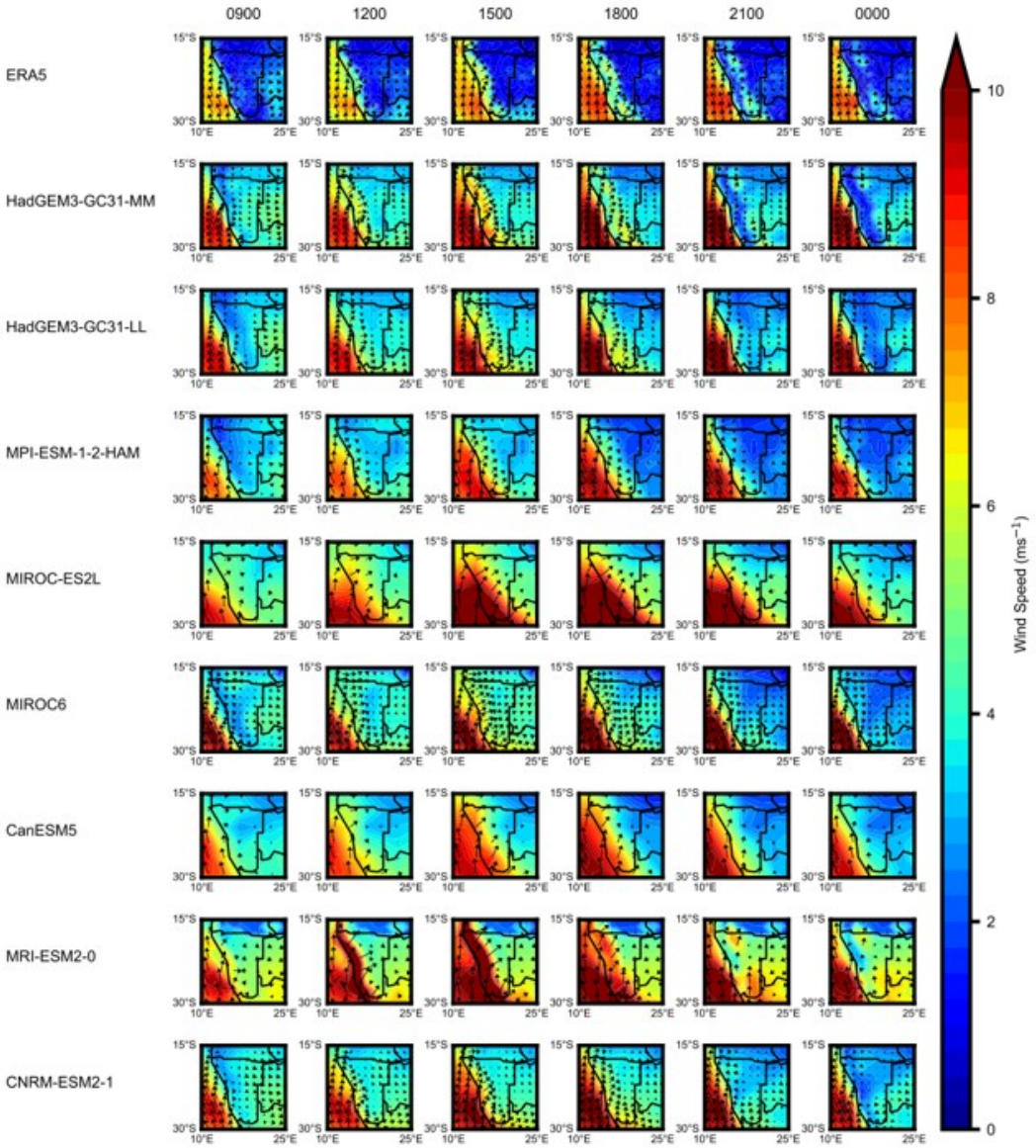


Figure 9. Mean December surface wind speed and vectors at 0900, 1200, 1500, 1800, 2100 and 0000 for the CMIP6 models and ERA5.

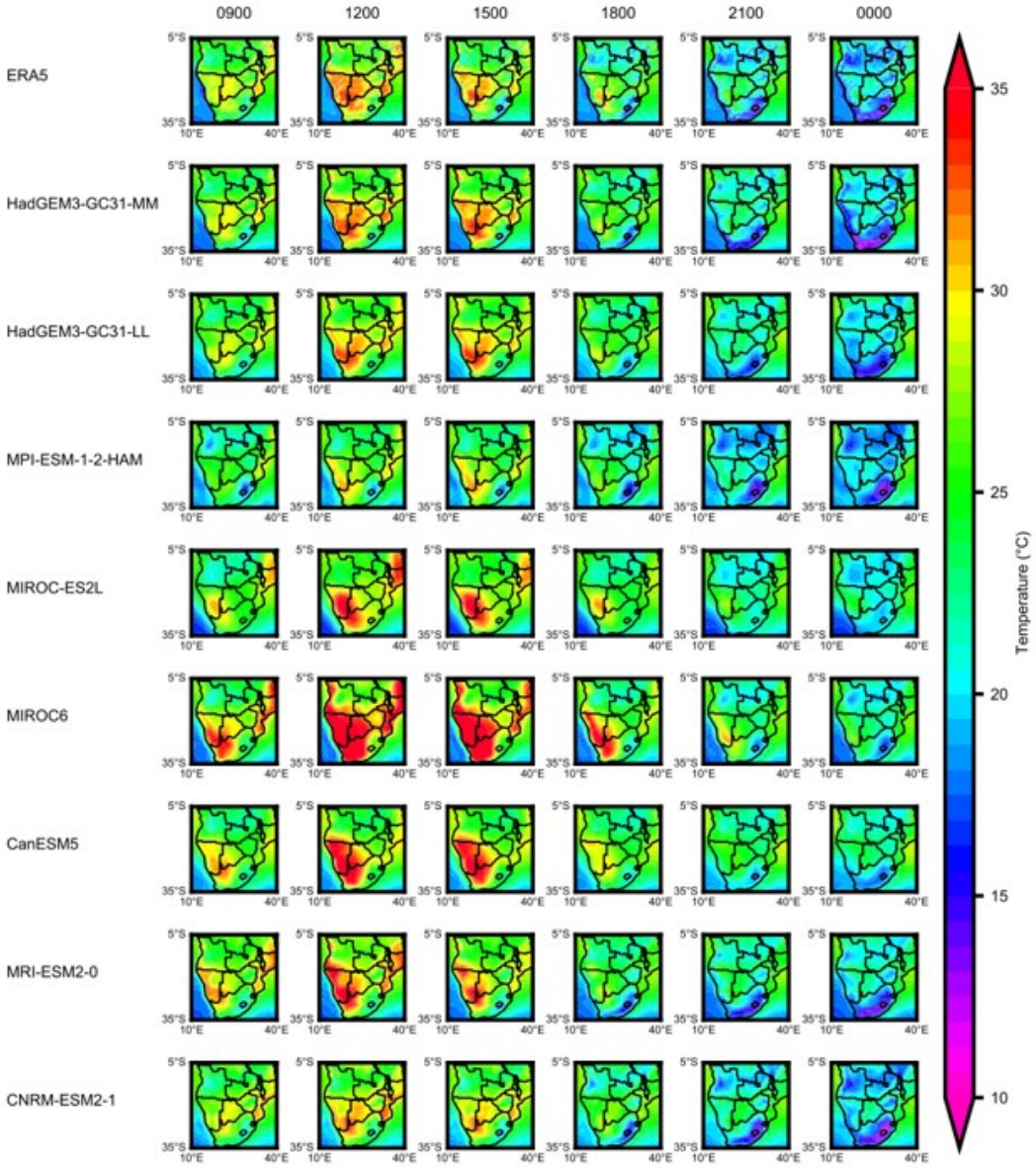


Figure 10. Mean December surface temperature at 0900, 1200, 1500, 1800, 2100 and 0000 for the CMIP6 models and ERA5.

ern Africa (Clements & Washington, 2022), this is unsurprising, as the models are also in agreement with ERA5 in the timing of maximum surface temperatures across the subcontinent (1200-1500) (Figure 10). Whilst the degree of heating in three of the models (MIROC-ES2L, MIROC6, CanESM5) is too strong, the location of the maximum surface temperatures (southern Kalahari/Northern Cape region) is consistent with the ERA5 data. The bias in surface temperatures in the two MIROC runs could be due to the low soil moisture values simulated by both of the models (Figures 1b and 2b), with reduced evaporative cooling resulting in temperatures that are too high (Figure 10), a feedback that was reported in the CMIP5 experiments by Mueller and Seneviratne (2014).

Where the models differ in their simulation of the anabatic-sea breeze is the strength of the system, the degree of inland propagation, and the latitudinal bands in which the system persists through the evening. At 2100, two of the models (HadGEM3-GC31-MM and MRI-ESM2-0) simulate an anabatic-sea breeze front, an area of onshore flow that has become detached from the coast as the system propagates inland, whilst four of the models (HadGEM3-GC31-MM, MIROC6, MRI-ESM2-0 and CNRM-ESM2-1) simulate an onshore flow in two preferential latitudinal bands (≈16°S - 19°S and ≈25°S - 30°S) (Figure 9). The latter of these processes is a consequence of the topography of the Namib coastline; east-west orientated river valleys channel the onshore flow and aid its inland propagation (Clements & Washington, 2022; Vickery & Eckardt, 2013), with the four models that resolve this phenomenon running at the highest spatial resolution (Table 1).

Figure 11b shows the mean diurnal cycle in surface winds for the models and ERA5 at Etosha, whilst Table 5 shows 2100 surface wind speed statistics. 2100 was selected as it is the time of peak surface wind speeds at Etosha in December (Clements & Washington, 2022). The inland propagation of the anabatic-sea breeze to Etosha's longitude during the evening is reflected by the increase in surface winds in the ERA5 data from 1800 onwards (Figure 11b). Only two of the models (HadGEM3-GC31-MM and MRI-ESM2-0) show an increase in wind speed from 1800 to 2100 (Table 5); these are also the only two models that simulate a sea-breeze front that reaches Etosha at 2100 (Figure 9). Of the other six models which show no increase in surface wind speed from 1800 to 2100, the anabatic-sea breeze is either too weak at 2100 (HadGEM3-GC31-LL, MPI-ESM-1-2-HAM, MIROC6, CNRM-ESM2-1), or is simulated too far south (MIROC-ES2L, CanESM5).

Table 6. *December 2100 Wind Speed Statistics*

Model	WS (ms^{-1})	% Increase from 1800 WS
AWS	1.68	52
HadGEM3-GC31-MM	4.88	1
HadGEM3-GC31-LL	2.29	-29
MPI-ESM-1-2-HAM	3.46	-26
MIROC-ES2L	3.38	-19
MIROC6	3.37	-24
CanESM5	2.90	-21
MRI-ESM2-0	7.40	13
CNRM-ESM2-1	4.04	-6

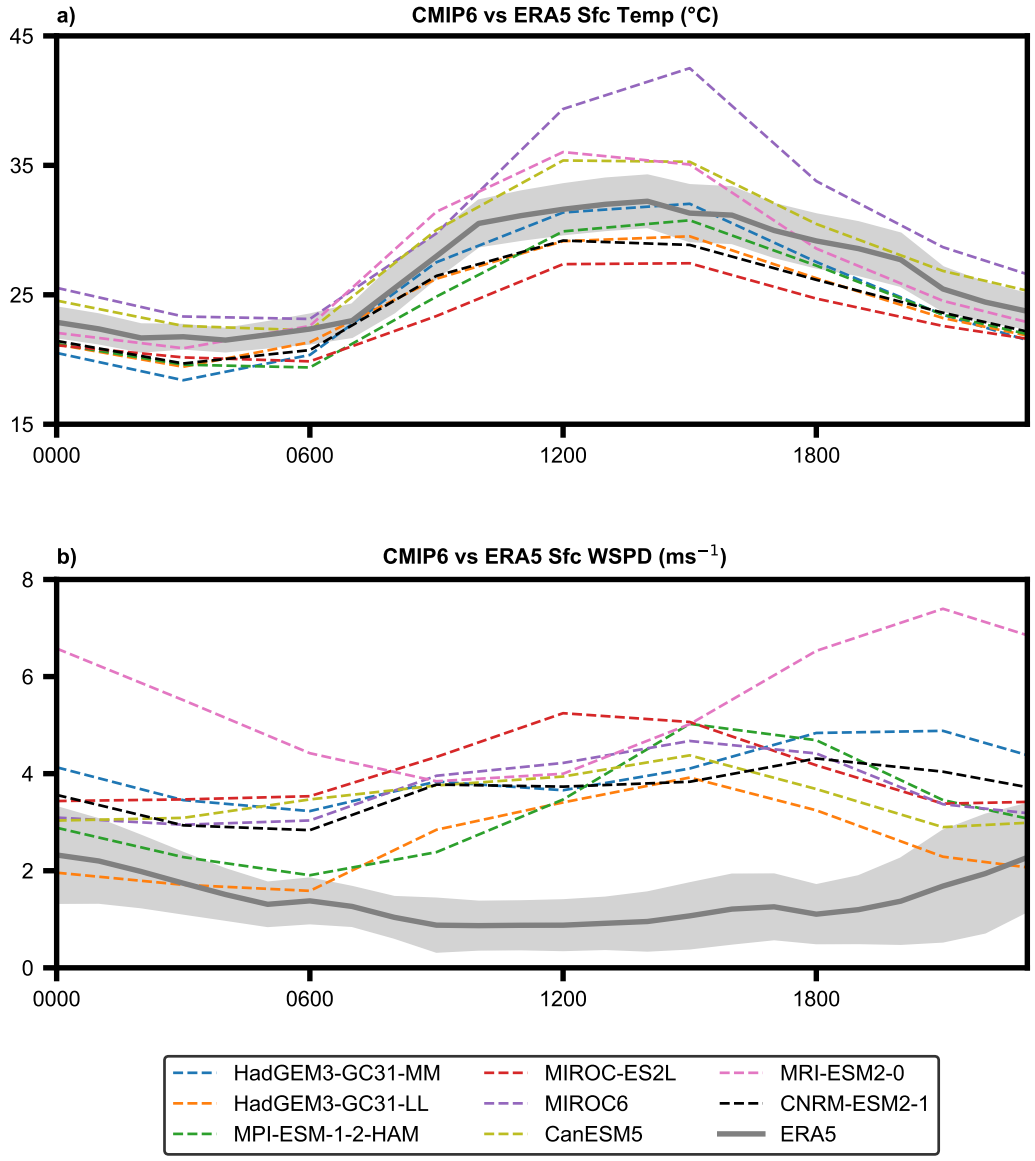


Figure 11. Mean December diurnal cycle of surface temperature (a) and wind speed (b) for the models and AWS at Etosha. The shaded grey areas denotes one standard deviation away from the AWS mean.

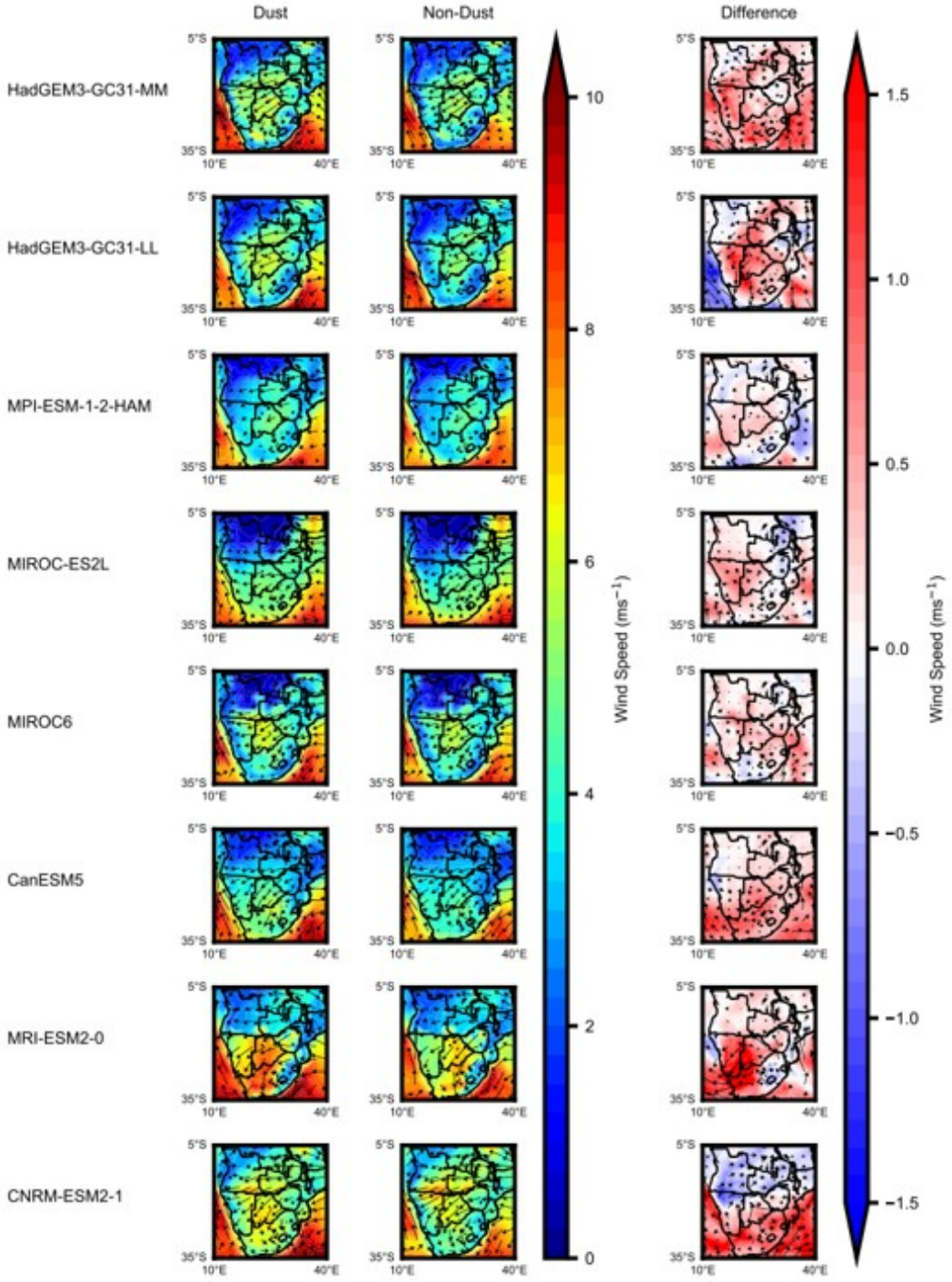


Figure 12. September dust, non-dust and difference composites of 0900 surface wind speed and vectors for the CMIP6 models. The difference composites were calculated by subtracting the non-dust composite from the dust composite.

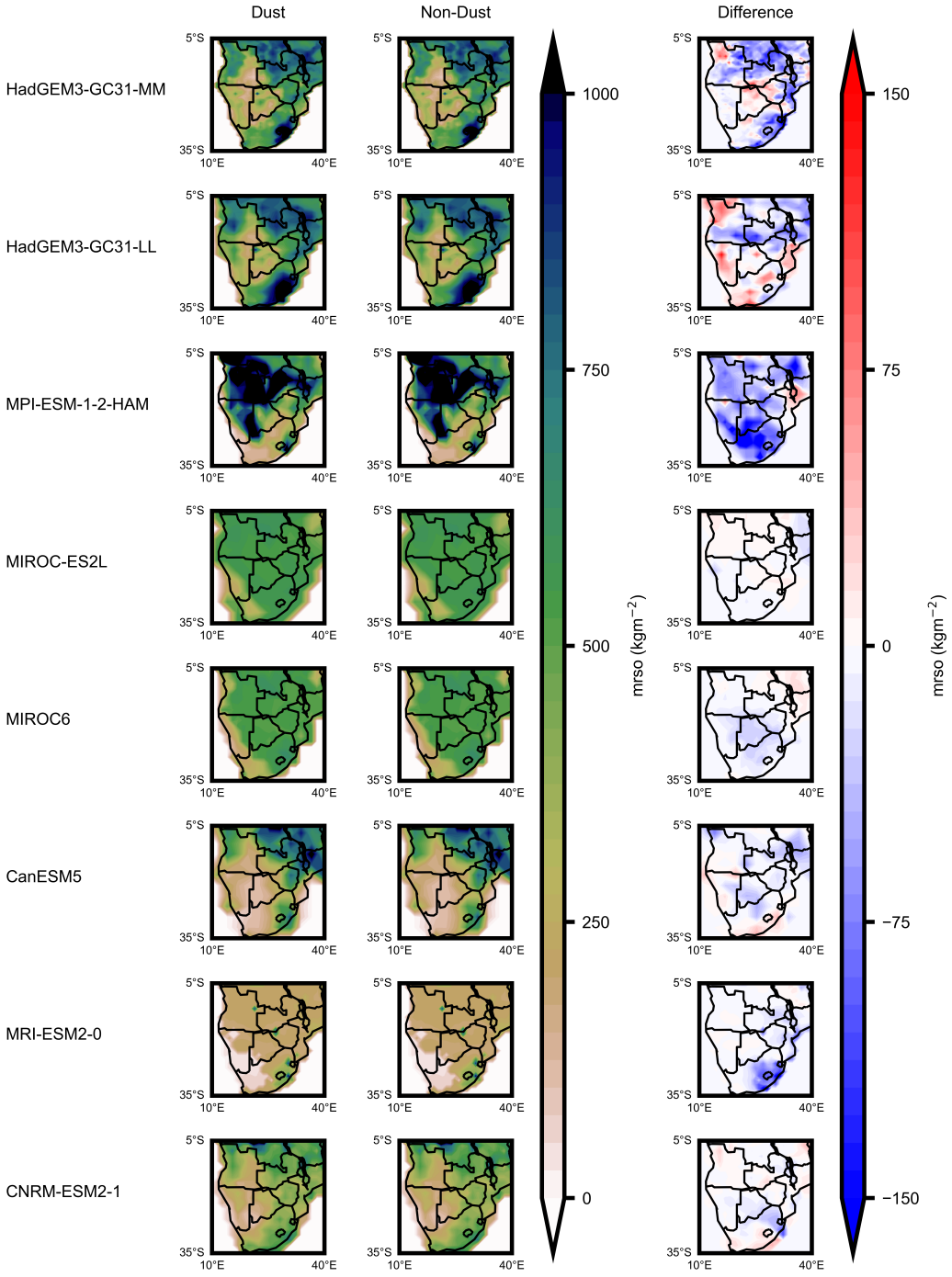


Figure 13. September dust, non-dust and difference composites of soil moisture for the CMIP6 models. The difference composites were calculated by subtracting the non-dust composite from the dust composite.

5 Atmospheric Drivers of Dust Emission in CMIP6 Models

The following sections address key question 3: What atmospheric processes are responsible for driving dust emissions simulated in the CMIP6 models, and how do they relate to the spatial distribution of dust emissions identified in key question 1?

5.1 September Dust Emissions

Figure 12 shows dust, non-dust and difference composites for September 0900 surface wind speed and vectors across southern Africa for each of the models, whilst Figure 13 shows dust, non-dust and difference composites for September soil moisture across southern Africa for each of the models. The composites were calculated by ranking the 30 September months (1981-2010) according to the total emission rate of dust, integrated across the land area that covers 11°E - 27°E and 17°S - 33°S (i.e., the arid southwest of southern Africa), with the dust composite the mean of the top ten percentile and the non-dust the mean of the bottom ten percentile. The difference composite was calculated by subtracting the non-dust composite from the dust composite.

In general, the models simulate a stronger north-easterly flow over the interior of southern Africa in the dust composites (Figure 12); this is especially prominent in the HadGEM3-GC31 models, which are two of the three models that simulate dust emission over the interior of the subcontinent during September (Figure 1a). In the MRI-ESM2-0 model, which was shown to simulate an area of northeasterlies that is displaced too far south and west (Figure 8), the enhanced wind speeds in the dust composite extend into Namibia and cross the Atlantic coast; this is consistent with the location of dust emissions in the model, concentrated along the west coast of southern Africa (Figure 1a). Aside from the MPI-ESM-1-2-HAM model, which simulates minimal dust emissions in both seasons (Figures 1a and 2a), there is very little difference in soil moisture between the dust and non-dust composites (Figure 13), indicating that it is surface wind speed driving variability in emissions during September.

5.2 December Dust Emissions

Figure 14 shows dust, non-dust and difference composites for December 1800 surface wind speed and vectors along the Namib coast for each of the models, whilst Figure 15 shows dust, non-dust and difference composites for December soil moisture across southern Africa for each of the models. The composites were calculated by ranking the 30 December months (1981-2010) according to the total emission rate of dust, integrated across the land area that covers 11°E - 27°E and 17°S - 33°S, with the dust composite the mean of the top ten percentile and the non-dust the mean of the bottom ten percentile. The difference composite was calculated by subtracting the non-dust composite from the dust composite.

With the exception of the MRI-ESM2-0 model, all of the CMIP6 models simulate a stronger onshore flow along the Namib coast in the dust composite (Figure 14). This is consistent with the location of dust emissions in the models, which are concentrated along the west coast of southern Africa in December (Figure 2a). In the MRI-ESM2-0 run, the onshore flow is weaker in the dust composite north of ≈23°S (Figure 14), however south of this latitude the onshore flow is stronger, again consistent with the more southerly location of the dust emissions in this model (Figure 2a).

Unlike in September, soil moisture is an important control on emissions during December, with five of the models (HadGEM3-GC31-MM, HadGEM3-GC31-LL, MPI-ESM-1-2-HAM, CanESM5, CNRM-ESM2-1) simulating a moister surface in the non-dust composite (Figure 15). Precipitation, which is one of the main determinants of soil moisture in the models (Aryal & Evans, 2021; Zhao et al., 2022), has been observed to affect uplift in two ways across southern Africa; delivery of sediment to the pan complexes (which

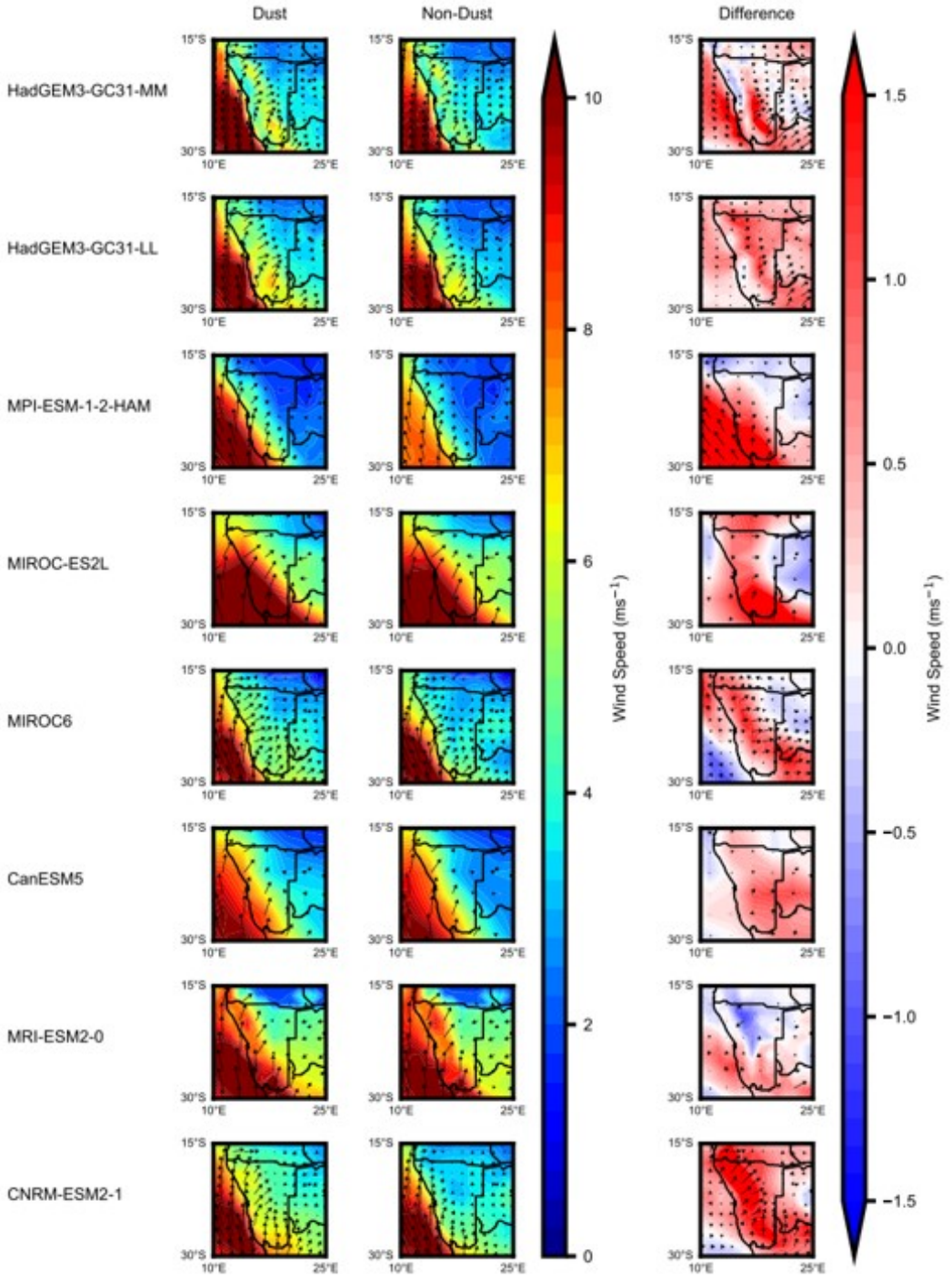


Figure 14. December dust, non-dust and difference composites of 1800 surface wind speed and vectors for the CMIP6 models. The difference composites were calculated by subtracting the non-dust composite from the dust composite.

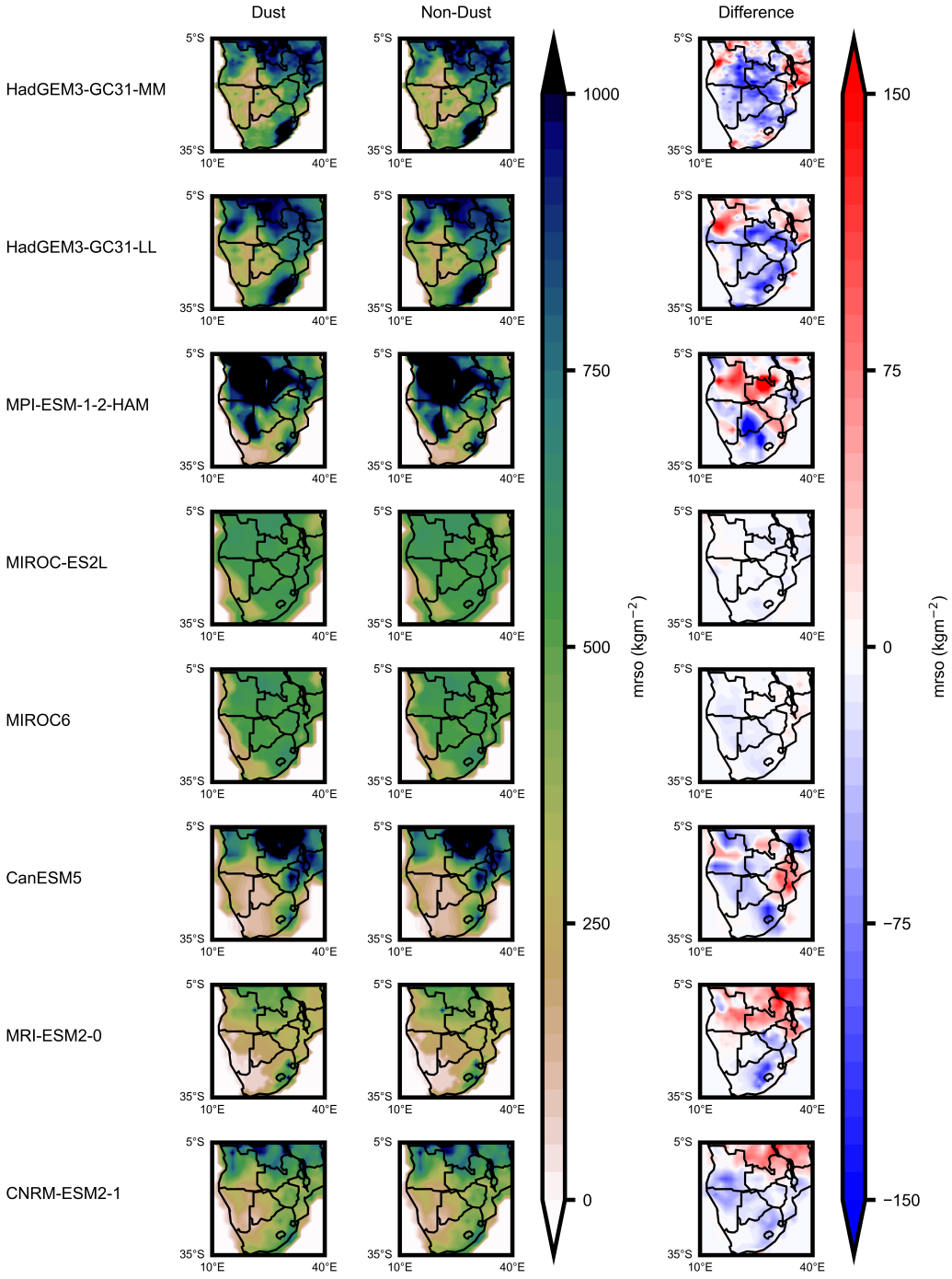


Figure 15. December dust, non-dust and difference composites of soil moisture for the CMIP6 models. The difference composites were calculated by subtracting the non-dust composite from the dust composite.

are the two major dust source areas) that is readily deflated when dry (not represented in the models), and immediate suppression of emissions by raising the threshold friction velocity (parameterised in models) (Bryant, 2003; Mahowald et al., 2003). Given that the wet season across southern Africa runs from October – March (Reason, 2017), this would help to account for the contrast in the soil moisture composites between the two months (Figures 13 and 15), as the immediate suppression of emissions, which is parameterised in the models, occurs in December but not in September.

5.3 Influence on Annual Cycle of Dust Emissions

The composites presented in sections 5.1 and 5.2 help to account for the simulated spatial distribution in emissions, and the contrasts between September and December (Figures 1a and 2a). Properties of the land surface (e.g., soil moisture) influence the location of simulated emissions, so that three models (HadGEM3-GC31-MM, HadGEM3-GC31-LL, MIROC6) are emissive over the interior of southern Africa and along the west coast, and three models (MIROC-ES2L, MRI-ESM2-0, CNRM-ESM2-1) are emissive only along the west coast (the MPI-ESM-1-2-HAM and CanESM5 models are excluded from this part of the analysis as they simulate very little dust in both seasons). The three models that simulate dust over the interior (Figure 1a) get closest to capturing the observed September maximum in dust emissions across the subcontinent (Figure 3a), when the north-easterly flow that predominates at this time of year activates these modelled source areas (Figure 12) (this circulation also activates the coastal sources in the MRI-ESM2-0 dust composites owing to the southwest bias in its location). This is in contrast to the three models that are emissive only along the west coast of southern Africa which are dustier in December (Figure 2a), when the predominance and proximity of the anabatic-sea breeze activates the modelled source areas (Figure 14).

6 Discussion and Conclusions

This paper has utilised in situ meteorological observations, reanalysis data and satellite imagery to evaluate the representation of dust emissions across southern Africa, as well as the atmospheric processes that drive uplift in CMIP6 models. Three key questions were posed in the introduction: (i) What is the spatial distribution of simulated dust emissions in the CMIP6 models and how do they represent the observed climatology in uplift across southern Africa? (ii) How do the CMIP6 models represent the atmospheric processes that drive observed dust emissions at Etosha? (iii) What atmospheric processes are responsible for driving dust emissions simulated in the CMIP6 models, and how do they relate to the spatial distribution of dust emissions identified in key question 1? The results presented in sections 3,4 and 5 will now be discussed, and the main findings of the paper summarised, addressing each of the key questions in turn.

In general, the representation of the spatial distribution of dust emissions across southern Africa in the CMIP6 models is poor (key question 1); only three of the models simulate uplift over the interior of the subcontinent during September (Figure 1a), failing to capture the dust belt that stretches between the Etosha and Makgadikgadi pans at this time of year (Figure 3a), whilst all of the modelled emissions during December are concentrated along the Atlantic coast (Figure 2a), missing the most prominent source area (Etosha) in this month (Figure 3a). Evaluation of the dust cycle across southern Africa in coupled models has been limited, however Pu and Ginoux (2018) show that the CMIP5 simulations fail to capture the observed maximum in dust optical depth (DOD) during late winter/spring (i.e., September), whilst Zhao et al. (2022) find large inter-model differences in simulated DOD in the CMIP6 models; the results presented here suggest that this issue may be a product of the misrepresentation of emissions over the interior of the subcontinent, consistent with the results of Zhao et al. (2022), who also find large inter-model differences in simulated emissions over southern Africa.

The spatial distribution of dust emissions across southern Africa in the CMIP6 models can be partly accounted for by the northeast – southwest gradient in soil moisture (Figures 1b and 2b), with a resulting concentration of simulated emissions in the far southwest of the subcontinent (Figures 1a and 2a). This is with the exception of the MPI-ESM-1-2-HAM model, which simulates an area of high soil moisture values in the southern Kalahari/Northern Cape region in both seasons (Figures 1b and 2b), and hence is one of two models to simulate very little dust emission over southern Africa (Figures 1a and 2a). These results are consistent with the findings of other studies, which have shown soil moisture to suppress emissions in coupled models across other dust source areas by increasing the threshold friction velocity in the emission parameterisation scheme (Pu & Ginoux, 2018; Zhao et al., 2022). The coupling of the dust emission scheme to dynamic vegetation in the HadGEM3-GC31 models (Table 1) might help to explain the seasonal variation in the spatial distribution of emissions (Figure 1a and 2a).

The NLLJ has been shown to be the primary driver of dust uplift at Etosha during austral winter (Clements & Washington, 2021; Wiggs et al., 2022), however there are large inter-model differences in the representation of the mechanism in the CMIP6 simulations, as well the surface winds associated with its breakdown (key question 2). In general, the models with the highest vertical resolution in the lower troposphere capture best the strength of the NLLJ (Figure 5); given that the system is limited in vertical extent to ≈400m at Etosha (Clements & Washington, 2021; Zunckel et al., 1996), this is unsurprising, and also supports previous work which has shown that simulations with higher vertical resolutions better resolve jet features (Acosta & Huber, 2017; Clements & Washington, 2021; Todd et al., 2008). Differences in the parameterisation schemes and treatment of boundary layer turbulence is also likely to influence model skill (Fiedler et al., 2016), evidenced by the inability of the MRI-ESM2-0 run to simulate an inversion layer during the nocturnal period (Figure 6).

The models also underestimate the morning surface wind speeds associated with the breakdown of the NLLJ structure at Etosha (Figure 7); whilst all of the models show a decay of the jet structure between 0600 and 1200 (Figure 5), it is likely that the underestimation of NLLJ strength at 0600 results in insufficient momentum mixed-down to the surface. This low bias in surface winds may help to account for the lack of dust uplift simulated at Etosha during September in the models (Figure 1a). These results are consistent with the findings of previous studies that have shown biases in the representation of surface winds in dust source areas in CMIP5 models (Evan, 2018; Fiedler et al., 2016) and reanalysis data (Roberts et al., 2017).

In December, an integrated anabatic-sea breeze system is present along the west coast of southern Africa (Howard & Washington, 2018; Lindesay & Tyson, 1990), and its inland propagation has been shown to contribute to observed dust emissions at Etosha (Clements & Washington, 2022). In general, the CMIP6 models capture the anabatic-sea breeze better than the NLLJ, with the system present in all eight simulations (Figure 9), which also represent well the spatial distribution of diabatic heating across the subcontinent (Figure 10). The models with the highest spatial resolution are also capable of resolving the channelling of the onshore flow into preferential latitudinal bands (Figure 9), a process which has been shown to be critical to the inland propagation of the system at Etosha's latitude (Clements & Washington, 2022). Despite the skill of the models in representing the anabatic-sea breeze, all eight simulate surface winds that are too strong at Etosha (Figure 11), with only two capturing the observed increase in wind speed from 1800 to 2100, a consequence of the greater inland propagation of the onshore flow in these models (Figure 9).

In general, modelled dust emissions across southern Africa are sensitive to changes in the seasonal features of the circulation (key question 3), with a stronger easterly/north-easterly circulation and anabatic-sea breeze simulated in the dusty September and December months respectively (Figure 12 and 14). In September, this is especially true of the models that simulate dust emissions over the interior of the subcontinent, but is also the case in the MRI-ESM2-0 and CNRM-ESM2-1 runs, where the southwest bias in the location of the easterlies/north-easterlies (Figure 8) activates the modelled source areas along the Atlantic coast. The effect of soil moisture on emissions is more pronounced during December (Figure 15), when immediate wetting of the surface inhibits uplift, a process that is incorporated in models through the dust emission parametrization scheme.

Evaluation of coupled models participating in the previous phases of CMIP has shown biases in the representation of all stages of the dust cycle (Evan, 2018; Evan et al., 2014; Fiedler et al., 2016), with an analysis of dust processes across southern Africa, an important source region, yet to be undertaken for the CMIP6 experiments. This paper has shown that models fail to capture the salient features of the dust emission climatology across the subcontinent, especially the prominence of the Etosha Pan. Mesoscale atmospheric processes that contribute to the uplift of dust (e.g., NLLJ's) and their associated surface winds were problematic for CMIP5 models (Evan, 2018; Fiedler et al., 2016); whilst the jet is well captured by some of the CMIP6 models, surface wind speeds are still underestimated, and likely account for the lack of simulated emissions at Etosha in September. The focus of this paper is on coupled models, as they are the primary tool used for climate prediction (Boucher et al., 2013), however future work should evaluate the representation of southern African dust processes in regional and convection-permitting simulations, which have been shown to improve the agreement between observations and model output across North Africa (Heinold et al., 2015; Roberts et al., 2018).

Open Research Section

Data - Data from the HadGEM3-GC31-MM historical simulation is available from the CEDA archive (Ridley et al., 2019b) (https://10.22033/ESGF/CMIP6.6112). Translation available via browser plug-in.

Data - Data from the HadGEM3-GC31-LL historical simulation is available from the CEDA archive (Ridley et al., 2019a) (https://doi.org/10.22033/ESGF/CMIP6.6109). Translation available via browser plug-in.

Data - Data from the MPI-ESM-1-2-HAM historical simulation is available from the CEDA archive (Neubauer et al., 2019) (https://doi.org/10.22033/ESGF/CMIP6.5016). Translation available via browser plug-in.

Data - Data from the MIROC-ES2L historical simulation is available from the CEDA archive (Hajima et al., 2019) (https://doi.org/10.22033/ESGF/CMIP6.5602). Translation available via browser plug-in.

Data - Data from the MIROC6 historical simulation is available from the CEDA archive (Tatebe & Watanabe, 2018) (https://doi.org/10.22033/ESGF/CMIP6.5603). Translation available via browser plug-in.

Data - Data from the CanESM5 historical simulation is available from the CEDA archive (Swart et al., 2019) (https://doi.org/10.22033/ESGF/CMIP6.3610). Translation available via browser plug-in.

Data - Data from the MRI-ESM2-0 historical simulation is available from the CEDA archive (Yukimoto et al., 2019) (https://doi.org/10.22033/ESGF/CMIP6.6842). Translation available via browser plug-in.

Data - Data from the CNRM-ESM2-1 historical simulation is available from the CEDA archive (Seferian, 2018) (https://doi.org/10.22033/ESGF/CMIP6.4068). Translation available via browser plug-in.

Data - ERA5 data is maintained by ECMWF and is available online from the Copernicus Climate Change Service (CDS, 2018) (https://doi.org/10.24381/cds.adbb2d47). Translation available via browser plug-in.

Data - TOMS AI data is available online from the IRI data library (IRI, 1996) (https://iridl.ldeo.columbia.edu/SOURCES/.NASA/.GSFC/.TOMS/.NIMBUS7/.monthly/.ai/). Translation available via browser plug-in.

Acknowledgments

Matthew Clements is funded by the NERC doctoral training partnership (NE/L002612/1).

References

Acosta, R. P., & Huber, M. (2017). The neglected indo-gangetic plains low-level jet and its importance for moisture transport and precipitation during the peak summer monsoon. *Geophysical Research Letters*, *44*(16), 8601-8610. doi: https://doi.org/10.1002/2017GL074440

Allen, C. J. T., & Washington, R. (2014). The low-level jet dust emission mechanism in the central sahara: Observations from bordj-badji mokhtar during the june 2011 fennec intensive observation period. *Journal of Geophysical Research: Atmospheres*, *119*(6), 2990-3015. doi: https://doi.org/10.1002/2013JD020594

Allen, C. J. T., Washington, R., & Engelstaedter, S. (2013). Dust emission and transport mechanisms in the central sahara: Fennec ground-based observa-

tions from bordj badji mokhtar, june 2011. *Journal of Geophysical Research: Atmospheres*, *118*(12), 6212-6232. doi: https://doi.org/10.1002/jgrd.50534

Andreae, M., & Rosenfeld, D. (2008). Aerosol–cloud–precipitation interactions. part 1. the nature and sources of cloud-active aerosols. *Earth-Science Reviews*, *89*(1), 13-41. doi: https://doi.org/10.1016/j.earscirev.2008.03.001

Andrews, M. B., Ridley, J. K., Wood, R. A., Andrews, T., Blockley, E. W., Booth, B., ... Sutton, R. T. (2020). Historical simulations with hadgem3-gc3.1 for cmip6. *Journal of Advances in Modeling Earth Systems*, *12*(6), e2019MS001995. doi: https://doi.org/10.1029/2019MS001995

Aryal, Y. N., & Evans, S. (2021). Global dust variability explained by drought sensitivity in cmip6 models. *Journal of Geophysical Research: Earth Surface*, *126*(6), e2021JF006073. doi: https://doi.org/10.1029/2021JF006073

Boucher, O., Randall, D., Artaxo, P., Bretherton, C., Feingold, G., Forster, P., ... Zhang, X. Y. (2013). Clouds and aerosols. In T. F. Stocker et al. (Eds.), *Climate change 2013: The physical science basis. contribution of working group i to the fifth assessment report of the intergovernmental panel on climate change* (pp. 571–657). Cambridge, UK: Cambridge University Press. doi: 10.1017/CBO9781107415324.016

Browning, K. A., & Wexler, R. (1968). The determination of kinematic properties of a wind field using doppler radar. *Journal of Applied Meteorology (1962-1982)*, *7*(1), 105–113.

Bryant, R. G. (2003). Monitoring hydrological controls on dust emissions: preliminary observations from etosha pan, namibia. *The Geographical Journal*, *169*(2), 131-141. doi: https://doi.org/10.1111/1475-4959.04977

CDS. (2018). Era5 hourly data on single levels from 1959 to present [dataset]. *Copernicus Climate Change Service (C3S) Climate Data Store (CDS)*. doi: https://doi.org/10.24381/cds.adbb2d47

Clements, M., & Washington, R. (2021). Atmospheric controls on mineral dust emission from the etosha pan, namibia: Observations from the clarify-2016 field campaign. *Journal of Geophysical Research: Atmospheres*, *126*(14), e2021JD034746. doi: https://doi.org/10.1029/2021JD034746

Clements, M., & Washington, R. (2022). Summer dust emissions from the etosha pan, namibia: The role of the namib anabatic-sea breeze system[unpublished manuscript]. *Journal of Geophysical Research: Atmospheres*.

Dansie, A., Wiggs, G., Thomas, D., & Washington, R. (2017). Measurements of windblown dust characteristics and ocean fertilization potential: The ephemeral river valleys of namibia. *Aeolian Research*, *29*, 30 - 41. doi: https://doi.org/10.1016/j.aeolia.2017.08.002

Evan, A. T. (2018). Surface winds and dust biases in climate models. *Geophysical Research Letters*, *45*(2), 1079-1085. doi: https://doi.org/10.1002/2017GL076353

Evan, A. T., Flamant, C., Fiedler, S., & Doherty, O. (2014). An analysis of aeolian dust in climate models. *Geophysical Research Letters*, *41*(16), 5996-6001. doi: https://doi.org/10.1002/2014GL060545

Eyring, V., Bony, S., Meehl, G. A., Senior, C. A., Stevens, B., Stouffer, R. J., & Taylor, K. E. (2016). Overview of the coupled model intercomparison project phase 6 (cmip6) experimental design and organization. *Geoscientific Model Development*, *9*(5), 1937–1958. doi: 10.5194/gmd-9-1937-2016

Fiedler, S., Knippertz, P., & Woodward, S. (2016). A process-based evaluation of dust-emitting winds in the cmip5 simulation of hadgem2-es. *Climate Dynamics*, *46*, 1107–1130. doi: https://doi.org/10.1007/s00382-015-2635-9

Fiedler, S., Schepanski, K., Heinold, B., Knippertz, P., & Tegen, I. (2013). Climatology of nocturnal low-level jets over north africa and implications for modeling mineral dust emission. *Journal of Geophysical Research: Atmospheres*, *118*(12), 6100-6121. doi: https://doi.org/10.1002/jgrd.50394

Garcia-Carreras, L., Marsham, J. H., Parker, D. J., Bain, C. L., Milton, S., Saci, A., ... Washington, R. (2013). The impact of convective cold pool outflows on model biases in the sahara. *Geophysical Research Letters*, *40*(8), 1647-1652. doi: https://doi.org/10.1002/grl.50239

Ginoux, P., Prospero, J. M., Gill, T. E., Hsu, N. C., & Zhao, M. (2012). Global-scale attribution of anthropogenic and natural dust sources and their emission rates based on modis deep blue aerosol products. *Reviews of Geophysics*, *50*(3). doi: https://doi.org/10.1029/2012RG000388

Goudie, A. S. (2014). Desert dust and human health disorders. *Environment International*, *63*, 101-113. doi: https://doi.org/10.1016/j.envint.2013.10.011

Hajima, T., Abe, M., Arakawa, O., Suzuki, T., Komuro, Y., Ogura, T., ... Tachiiri, K. (2019). *Miroc miroc-es2l model output prepared for cmip6 cmip historical [dataset].* Earth System Grid Federation. doi: https://doi.org/10.22033/ESGF/CMIP6.5602

Haustein, K., Washington, R., King, J., Wiggs, G., Thomas, D. S. G., Eckardt, F. D., ... Menut, L. (2015). Testing the performance of state-of-the-art dust emission schemes using do4models field data. *Geoscientific Model Development*, *8*(2), 341–362. doi: 10.5194/gmd-8-341-2015

Haywood, J., & Boucher, O. (2000). Estimates of the direct and indirect radiative forcing due to tropospheric aerosols: A review. *Reviews of Geophysics*, *38*(4), 513-543. doi: https://doi.org/10.1029/1999RG000078

Heinold, B., Knippertz, P., & Beare, R. J. (2015). Idealized large-eddy simulations of nocturnal low-level jets over subtropical desert regions and implications for dust-generating winds. *Quarterly Journal of the Royal Meteorological Society*, *141*(690), 1740-1752. doi: https://doi.org/10.1002/qj.2475

Herman, J. R., Bhartia, P. K., Torres, O., Hsu, C., Seftor, C., & Celarier, E. (1997). Global distribution of uv-absorbing aerosols from nimbus 7/toms data. *Journal of Geophysical Research: Atmospheres*, *102*(D14), 16911-16922. doi: https://doi.org/10.1029/96JD03680

Hersbach, H., Bell, B., Berrisford, P., Hirahara, S., Horányi, A., Muñoz-Sabater, J., ... Thépaut, J.-N. (2020). The era5 global reanalysis. *Quarterly Journal of the Royal Meteorological Society*, *146*(730), 1999-2049. doi: https://doi.org/10.1002/qj.3803

Howard, E., & Washington, R. (2018). Characterizing the synoptic expression of the angola low. *Journal of Climate*, *31*(17), 7147 - 7165. doi: 10.1175/JCLI-D-18-0017.1

IRI. (1996). Nasa gsfc toms: Total ozone mapping spectrometer [dataset]. *IRI/LDEO Data Library*. Retrieved from `https://iridl.ldeo.columbia.edu/SOURCES/.NASA/.GSFC/.TOMS/.NIMBUS7/.monthly/.ai/`

Jickells, T. D., An, Z. S., Andersen, K. K., Baker, A. R., Bergametti, G., Brooks, N., ... Torres, R. (2005). Global iron connections between desert dust, ocean biogeochemistry, and climate. *Science*, *308*(5718), 67–71. doi: 10.1126/science.1105959

Karypidou, M. C., Katragkou, E., & Sobolowski, S. P. (2022). Precipitation over southern africa: is there consensus among global climate models (gcms), regional climate models (rcms) and observational data? *Geoscientific Model Development*, *15*(8), 3387–3404. Retrieved from `https://gmd.copernicus.org/articles/15/3387/2022/`

Knippertz, P., & Todd, M. C. (2012). Mineral dust aerosols over the sahara: Meteorological controls on emission and transport and implications for modeling. *Reviews of Geophysics*, *50*(1). doi: https://doi.org/10.1029/2011RG000362

Kok, J. F., Parteli, E. J. R., Michaels, T. I., & Karam, D. B. (2012). The physics of wind-blown sand and dust. *Reports on Progress in Physics*, *75*(10), 106901. doi: 10.1088/0034-4885/75/10/106901

Koren, I., Kaufman, Y. J., Washington, R., Todd, M. C., Rudich, Y., Martins, J. V.,

& Rosenfeld, D. (2006). The bodélé depression: a single spot in the sahara that provides most of the mineral dust to the amazon forest. *Environmental Research Letters*, *1*(1), 014005. doi: 10.1088/1748-9326/1/1/014005

Lindesay, J. A., & Tyson, P. D. (1990). Thermo-topographically induced boundary layer oscillations over the central namib, southern africa. *International Journal of Climatology*, *10*(1), 63-77. doi: https://doi.org/10.1002/joc.3370100108

Mahowald, N. M., Bryant, R. G., del Corral, J., & Steinberger, L. (2003). Ephemeral lakes and desert dust sources. *Geophysical Research Letters*, *30*(2). doi: https://doi.org/10.1029/2002GL016041

Mahowald, N. M., & Kiehl, L. M. (2003). Mineral aerosol and cloud interactions. *Geophysical Research Letters*, *30*(9). doi: https://doi.org/10.1029/2002GL016762

Marsham, J. H., Hobby, M., Allen, C. J. T., Banks, J. R., Bart, M., Brooks, B. J., ... Washington, R. (2013). Meteorology and dust in the central sahara: Observations from fennec supersite-1 during the june 2011 intensive observation period. *Journal of Geophysical Research: Atmospheres*, *118*(10), 4069-4089. doi: https://doi.org/10.1002/jgrd.50211

Marsham, J. H., Knippertz, P., Dixon, N. S., Parker, D. J., & Lister, G. M. S. (2011). The importance of the representation of deep convection for modeled dust-generating winds over west africa during summer. *Geophysical Research Letters*, *38*(16). doi: https://doi.org/10.1029/2011GL048368

Marticorena, B., & Bergametti, G. (1995). Modeling the atmospheric dust cycle: 1. design of a soil-derived dust emission scheme. *Journal of Geophysical Research: Atmospheres*, *100*(D8), 16415-16430. doi: https://doi.org/10.1029/95JD00690

Miller, R. L., & Tegen, I. (1998). Climate response to soil dust aerosols. *J. Climate*, *11*, 3247–3267. doi: 10.1175/1520-0442(1998)011

Mueller, B., & Seneviratne, S. I. (2014). Systematic land climate and evapotranspiration biases in cmip5 simulations. *Geophysical Research Letters*, *41*(1), 128-134. doi: https://doi.org/10.1002/2013GL058055

Munday, C., & Washington, R. (2018). Systematic climate model rainfall biases over southern africa: Links to moisture circulation and topography. *Journal of Climate*, *31*(18), 7533 - 7548. doi: https://doi.org/10.1175/JCLI-D-18-0008.1

Murray, J. E., Brindley, H. E., Bryant, R. G., Russell, J. E., Jenkins, K. F., & Washington, R. (2016). Enhancing weak transient signals in seviri false color imagery: Application to dust source detection in southern africa. *Journal of Geophysical Research: Atmospheres*, *121*(17), 10,199-10,219. doi: https://doi.org/10.1002/2016JD025221

Park, S., Kim, S.-W., Park, M.-S., & Song, C.-K. (2018). Measurement of planetary boundary layer winds with scanning doppler lidar. *Remote Sensing*, *10*(8), 1261. doi: 10.3390/rs10081261

Prospero, J. M., Ginoux, P., Torres, O., Nicholson, S. E., & Gill, T. E. (2002). Environmental characterization of global sources of atmospheric soil dust identified with the nimbus 7 total ozone mapping spectrometer (toms) absorbing aerosol product. *Reviews of Geophysics*, *40*(1), 2-1-2-31. doi: https://doi.org/10.1029/2000RG000095

Pu, B., & Ginoux, P. (2018). How reliable are cmip5 models in simulating dust optical depth? *Atmospheric Chemistry and Physics*, *18*(16), 12491–12510. doi: 10.5194/acp-18-12491-2018

Reason, C. (2017). *Climate of southern africa.* Oxford University Press. doi: 10.1093/acrefore/9780190228620.013.513

Ridley, J., Menary, M., Kuhlbrodt, T., Andrews, M., & Andrews, T. (2019a). *Mohc hadgem3-gc31-ll model output prepared for cmip6 cmip historical [dataset].* Earth System Grid Federation. doi: https://doi.org/10.22033/ESGF/CMIP6.6109

Ridley, J., Menary, M., Kuhlbrodt, T., Andrews, M., & Andrews, T. (2019b).

Mohc hadgem3-gc31-mm model output prepared for cmip6 cmip historical [dataset]. Earth System Grid Federation. doi: https://doi.org/10.22033/ESGF/CMIP6.6112

Roberts, A. J., Marsham, J. H., Knippertz, P., Parker, D. J., Bart, M., Garcia-Carreras, L., ... Walker, D. (2017). New saharan wind observations reveal substantial biases in analysed dust-generating winds. *Atmospheric Science Letters*, *18*(9), 366-372. doi: https://doi.org/10.1002/asl.765

Roberts, A. J., Woodage, M. J., Marsham, J. H., Highwood, E. J., Ryder, C. L., McGinty, W., ... Crook, J. (2018). Can explicit convection improve modelled dust in summertime west africa? *Atmospheric Chemistry and Physics*, *18*(12), 9025–9048. doi: 10.5194/acp-18-9025-2018

Shapiro, A., & Fedorovich, E. (2010). Analytical description of a nocturnal low-level jet. *Quarterly Journal of the Royal Meteorological Society*, *136*(650), 1255-1262. doi: https://doi.org/10.1002/qj.628

Swart, N. C., Cole, J. N., Kharin, V. V., Lazare, M., Scinocca, J. F., Gillett, N. P., ... Sigmond, M. (2019). *Cccma canesm5 model output prepared for cmip6 cmip historical [dataset].* Earth System Grid Federation. doi: https://doi.org/10.22033/ESGF/CMIP6.3610

Tatebe, H., & Watanabe, M. (2018). *Miroc miroc6 model output prepared for cmip6 cmip historical [dataset].* Earth System Grid Federation. doi: https://doi.org/10.22033/ESGF/CMIP6.5603

Tegen, I., Harrison, S. P., Kohfeld, K., Prentice, I. C., Coe, M., & Heimann, M. (2002). Impact of vegetation and preferential source areas on global dust aerosol: Results from a model study. *Journal of Geophysical Research: Atmospheres*, *107*(D21), AAC 14-1-AAC 14-27. doi: https://doi.org/10.1029/2001JD000963

Tegen, I., Lacis, A. A., & Fung, I. (1996). The influence of mineral aerosols from disturbed soils on the global radiation budget. *Nature*, *380*, 419–422. doi: 10.1038/380419a0

Todd, M. C., Washington, R., Raghavan, S., Lizcano, G., & Knippertz, P. (2008). Regional model simulations of the bodélé low-level jet of northern chad during the bodélé dust experiment (bodex 2005). *Journal of Climate*, *21*(5), 995 - 1012. doi: 10.1175/2007JCLI1766.1

Torres, O., Bhartia, P. K., Herman, J. R., Sinyuk, A., Ginoux, P., & Holben, B. (2002). A long-term record of aerosol optical depth from toms observations and comparison to aeronet measurements. *Journal of the Atmospheric Sciences*, *59*(3), 398 - 413. doi: 10.1175/1520-0469(2002)059⟨0398:ALTROA⟩2.0.CO;2

van de Wiel, B. J. H., Moene, A. F., Steeneveld, G. J., Baas, P., Bosveld, F. C., & Holtslag, A. A. M. (2010). A conceptual view on inertial oscillations and nocturnal low-level jets. *Journal of the Atmospheric Sciences*, *67*(8), 2679 - 2689. doi: 10.1175/2010JAS3289.1

Vickery, K. J., & Eckardt, F. D. (2013). Dust emission controls on the lower kuiseb river valley, central namib. *Aeolian Research*, *10*, 125-133. doi: https://doi.org/10.1016/j.aeolia.2013.02.006

Vickery, K. J., Eckardt, F. D., & Bryant, R. G. (2013). A sub-basin scale dust plume source frequency inventory for southern africa, 2005–2008. *Geophysical Research Letters*, *40*(19), 5274-5279. doi: https://doi.org/10.1002/grl.50968

Washington, R., Todd, M., Middleton, N. J., & Goudie, A. S. (2003). Dust-storm source areas determined by the total ozone monitoring spectrometer and surface observations. *Annals of the Association of American Geographers*, *93*(2), 297-313. doi: 10.1111/1467-8306.9302003

Wiggs, G. F. S. (2011). Sediment mobilisation by the wind. In *Arid zone geomorphology* (p. 455-486). John Wiley and Sons, Ltd. doi: https://doi.org/10.1002/9780470710777.ch18

Wiggs, G. F. S., Baddock, M. C., Thomas, D. S. G., Washington, R., Nield, J. M., Engelstaedter, S., ... Kötting, S. (2022). Quantifying mechanisms of aeolian dust emission: Field measurements at etosha pan, namibia. *Journal of Geophysical Research: Earth Surface*, *127*(8), e2022JF006675. doi: https://doi.org/10.1029/2022JF006675

Wu, C., Lin, Z., & Liu, X. (2020). The global dust cycle and uncertainty in cmip5 (coupled model intercomparison project phase 5) models. *Atmospheric Chemistry and Physics*, *20*(17), 10401–10425. doi: 10.5194/acp-20-10401-2020

Yukimoto, S., Koshiro, T., Kawai, H., Oshima, N., Yoshida, K., Urakawa, S., ... Adachi, Y. (2019). *Mri mri-esm2.0 model output prepared for cmip6 cmip historical [dataset].* Earth System Grid Federation. doi: https://doi.org/10.22033/ESGF/CMIP6.6842

Zhao, A., Ryder, C. L., & Wilcox, L. J. (2022). How well do the cmip6 models simulate dust aerosols? *Atmospheric Chemistry and Physics*, *22*(3), 2095–2119. doi: 10.5194/acp-22-2095-2022

Zunckel, M., Hong, Y., Brassel, K., & O'Beirne, S. (1996). Characteristics of the nocturnal boundary layer: Okaukuejo, namibia, during safari-92. *Journal of Geophysical Research: Atmospheres*, *101*(D19), 23757-23766. doi: https://doi.org/10.1029/95JD00624

Chapter 6: Discussion & Conclusions

6.1) Discussion of Results

In the following sections, the results of the three papers presented in chapters 3, 4 and 5 are discussed within the context of previous research on dust emissions and southern African climate. The discussion is structured around the key questions and research objectives outlined in chapter 1.

6.1.1 Spatial Distribution and Temporal Variability in Dust Emissions

The following sections address key question 1: What are the spatial and temporal characteristics of dust emissions across southern Africa, and how are they represented in numerical models?

6.1.1.1 Spatial Distribution

Of the previous work to have been conducted on dust emissions from southern Africa, the majority has focused on identifying the major source areas across the subcontinent using remote sensing techniques (Prospero et al., 2002; Vickery et al., 2013; Washington et al., 2003), and so the spatial distribution of emissions is perhaps the most certain area of the science. The Etosha and Makgadikgadi pans have been previously identified as the two major dust sources in southern Africa, a finding that has been corroborated by the analysis of TOMS data in paper 2, with Etosha the most prominent in the annual mean, consistent with the results of Washington et al., (2003). The representation of these spatial patterns in coupled models was evaluated in paper 3, and it was found that over half the models miss the observed maximum in uplift in September (the two pans and the dust belt that extends between them across the Kalahari), with a tendency for simulated emissions to be concentrated along

the west coast of southern Africa. Whilst Zhao et al. (2022) found that simulated dust emissions and optical depth (DOD) in CMIP6 models compared well with reanalysis data when integrated across the entire subcontinent, no evaluation of the spatial distribution of these two variables was made, with the results presented in paper 3 suggesting more work is required to constrain the location of uplift in the models.

6.1.1.2 Temporal Variability

As with the spatial distribution of emissions, it has been possible to quantify the annual cycle in dust emissions across southern Africa given the longevity of the satellite products that have been used (Prospero et al., 2002; Vickery et al., 2013; Washington et al., 2003). In paper 2, it was shown that September was the dustiest month across the subcontinent, with the two pan surfaces at their most emissive, consistent with the results of all previous remote sensing studies. A key finding of paper 2 however was that Etosha is an active source area outside of this peak dust season; this is inconsistent with the results of Vickery et al. (2013), who identified no dust plumes at Etosha during December, although this could be a consequence of the difficulties associated with dust detection in the infrared wavelengths in the presence of cloud and water vapour (Ashpole & Washington, 2012; Brindley et al., 2012). Indeed, Bryant (2003) also found dust activity at Etosha through the austral summer months in the TOMS record and critically, Wiggs et al. (2022) have presented in situ observational evidence of uplift from the pan surface during December. Whilst emissions across southern Africa show a clear peak in September, the annual cycle in emissions at Etosha is bimodal, with peaks in September and December.

Dust emissions at Etosha also show a clear diurnal cycle during austral winter, a key finding of paper 1, with uplift triggered exclusively in the hours following sunrise (0900 – 1000 UTC). This is consistent with the results of Vickery et al. (2013) who identify the majority of dust plumes across southern Africa from austral winter – spring; 90% of events are detected in the morning overpass MODIS imagery, whilst 82% of events are detected between 0900 – 1200 in SEVIRI imagery. This finding is also consistent with results from other dust source areas, with a clear diurnal cycle in emissions reflective of the atmospheric processes driving uplift (Marsham et al., 2013; Schepanski et al., 2009; Todd et al., 2008). The identification of dust events in paper 2 was achieved using the TOMS record, and given the temporal frequency of this data (daily), it is not possible to directly quantify the diurnal cycle of emissions during December. Considering the dependence of uplift on surface wind speed, which was shown to peak from 2000 – 2200 UTC at Etosha in December, it is likely that dust events were triggered during the evening hours, an assertion validated by the in-situ observations of Wiggs et al. (2022).

Dust emissions across southern Africa also show variability on longer timescales, with the results of paper 2 showing interannual fluctuations in uplift from the Etosha and Makgadikgadi pans. This interannual variability can be partly accounted for by variability in the strength of the atmospheric processes responsible for driving dust emissions (discussed in chapter 6.1.2), but also by year-to-year changes in the wetting of the pan surfaces, especially at Etosha in the summer season. Below average rainfall in the Etosha catchment during early summer (i.e., December), as was observed during the El Nino event of 1987, essentially results in a protracted dry season, with emissions continuing

outside of the traditional dusty months. This link between hydrology and dust emissions at Etosha has also been noted by Bryant (2003) and Mahowald et al. (2003), who show that inundation of the pan surface leads to immediate suppression of uplift, but may promote greater dust activity in the subsequent dry season through delivery of sediment. This effect is captured by the CMIP6 models evaluated in paper 3, with higher soil moisture values over the southwest of southern Africa in the December non-dust composites suppressing uplift by raising the threshold friction velocity in the dust emission parameterization scheme (Fecan et al., 1999).

6.1.2) Meteorology of Southern African Dust Source Areas

The following sections address key question 2: What are the characteristic features of the meteorology of southern African dust source areas, and how are they represented in numerical models?

6.1.2.1) Mesoscale Atmospheric Processes

In the results of papers 1 and 2, two mesoscale atmospheric processes were shown to be of importance to the meteorology of the Etosha pan; namely, a NLLJ in austral winter and an integrated anabatic-sea breeze in austral summer. A key finding of paper 1 was corroborating the presence of a NLLJ at Etosha during austral winter, as was first reported by Zunckel et al. (1996). The jet is a persistent feature of the nocturnal boundary layer (observed on >90% of mornings during the observation period), with peak core wind speeds >12ms^{-1} recorded between 0600 – 0800. The results of paper 1 build on the initial findings of Zunckel et al. (1996) by utilising more advanced instrumentation, allowing the full depth of the NLLJ to be captured and its diurnal cycle resolved.

Indeed, Zunckel et al. (1996) report core heights of only 125m and wind speeds of 9.4ms^{-1} at 0600, in contrast to the 306m and 11.82ms^{-1} presented in paper 1. The NLLJ at Etosha is comparable to jets observed in other dust source areas, with for example mean wind speeds of 11.3ms^{-1} recorded in the core of the jet at Bordj-Badji Mokhtar in the central Sahara (Allen & Washington, 2014). The skill of reanalyses (paper 1) and coupled models (paper 3) in capturing the key features of the NLLJ at Etosha including core height and wind speed is mixed; all of the simulations show a jet-like feature at 0000, however core wind speeds are underestimated by ERA-I and all but two of the CMIP6 models. The higher vertical resolution of the ERA5, HadGEM3-GC31-MM and CNRM-ESM2-1 output is a likely source of the additional skill of these models, in terms of their ability to accurately resolve the height of the NLLJ core, whilst the two aforementioned CMIP6 models also simulate a well-developed inversion layer, a critical process with regards to the formation of the NLLJ.

Thermally and topographically induced airflows have been reported along the Namib coastline in previous studies (Lindesay & Tyson, 1990), however the inland propagation of these systems, and their subsequent influence on the meteorology of locations to the east of the escarpment has not been investigated. A key finding of paper 2 was the persistence of an integrated onshore anabatic-sea breeze during austral summer; the system sets in at the coast at midday, and is advected inland through the evening so that on some days, the sea-breeze front reaches Etosha's longitude. This is manifest as an increase in the surface wind speed at Etosha from 1800 onwards, although the standard deviation in wind speeds through the evening hours is high, indicative of the irregularity with which the anabatic-sea breeze propagates sufficiently far

inland. This integrated system has been identified in previous work by Howard & Washington (2018), with the overturning circulation associated with the anabatic-sea breeze (eastward ascending branch/westward descending branch) inhibiting the westward movement of tropical lows across the Atlantic coast, helping to maintain the climatological position of the Angola Low. In general, the CMIP6 models evaluated in paper 3 simulate well the anabatic-sea breeze, however only two (HadGEM3-GC31-MM and MRI-ESM2-0) capture the extent of the inland propagation at Etosha's longitude, and hence the evening rise in surface wind speed.

6.1.2.2) Forcing Mechanisms

Both of the mesoscale atmospheric processes described above are a response to the diurnal cycle in diabetic heating, with the evolution of the NLLJ at Etosha following the classic model of frictional decoupling outlined by Blackadar (1957). The results in paper 1 show a clear anticlockwise inertial oscillation of the wind vector at the top of an inversion layer, consistent with conceptual (Shapiro & Fedorovich, 2010; Van de Wiel et al., 2010) and modelling work (Heinold et al., 2015), as well as observations of NLLJ's in other dryland environments (Allen & Washington, 2014; Fiedler et al., 2013). In paper 3, the strength and depth of the simulated inversion layers accounted for some of the inter-model variability in NLLJ strength, with the two models (HadGEM3-GC31-MM, CNRM-ESM2-1) simulating well developed stable layers also generating the strongest jet profiles at 0000 and 0600. Another key finding of paper 1 was the influence of synoptics on NLLJ strength, with ridging of the South Atlantic Anticyclone enhancing the pressure gradient across southern Africa and driving a stronger jet. Again, these results are consistent with conceptual work, which

shows background pressure gradient to be a first order control on NLLJ strength (Shapiro & Fedorovich, 2010; Van de Wiel et al., 2010). The effect of synoptics on jet strength in the CMIP6 models was not evaluated in paper 3, as this was controlled for to ensure a fair comparison with the one season of observational data at Etosha.

The anabatic-sea breeze identified in paper 2 is a direct response to the thermal contrast between the cool water of the BUS, and the warm interior plateau of southern Africa. Whilst heating of the interior is pronounced in austral spring (SON), the strength of the system is sensitive to the location of maximum diabatic heating, and hence is best developed in austral summer (DJF), when the area of maximum heating moves south of a critical latitude, and is centred over the southern Kalahari/Northern Cape Region. This critical latitude is tied to the position of the Angola-Benguela Front (ABF), which separates the warm Agulhas current from the BUS, and is usually sits at ≈15°S - 17°S (Colberg & Reason, 2006; Reason, 2017). The evolution of the anabatic-sea breeze along the Namib coast is consistent with the modelling work of Smith and Spengler (2011) and Racz and Smith (1999), with a well-mixed layer over the interior during the daytime and a sharp gradient in potential temperature at the coast. Whilst there is variability in the degree of diabatic heating over the subcontinent simulated by the models evaluated in paper 3, they all capture well the location of the maximum. The channelling of the onshore flow into preferential latitudinal bands is a consequence of the topography of the Namib coastline (Vickery & Eckardt, 2013), and hence is only captured by the four models (HadGEM3-GC31-MM, MIROC6, MRI-ESM2-0 and CNRM-ESM2-1) with the highest spatial resolution.

6.1.3) Atmospheric Controls on Dust Emission

The following sections address key question 3: What features of the meteorology identified in key question 2 are responsible for driving dust emissions from southern African source areas, and how are these processes represented in coupled models?

6.1.3.1) Surface Winds

Dust uplift occurs when the surface wind speed exceeds a threshold friction velocity (this is also true of simulated emissions in models), and so it is the surface wind speed distribution in dust source areas that is of critical importance to the emission process. One of the key findings of paper 1 was the clear diurnal cycle in surface winds at Etosha during austral winter, with the timing of peak winds (0900 - 1000) coincident with the timing of dust activation described in chapter 6.1.1.2. The surface winds during these hours were also significantly stronger on days when dust plumes were detected compared to when there was no dust activity at Etosha. This is consistent with the results of paper 2, which showed a clear peak in surface wind speeds in the dustiest September months at 0900. Similar diurnal cycles of surface winds have been observed in North African dust source areas (Allen & Washington, 2014; Fiedler et al., 2013; Knippertz & Todd, 2012), and are linked to the breakdown of the NLLJ structure (discussed in chapter 6.3.2). In general, the CMIP6 models evaluated in paper 3 do not capture well the magnitude of the surface winds through the morning hours, a likely consequence of their underestimation of NLLJ strength.

The diurnal cycle of surface winds at Etosha in December, as reported in paper 2, shows a peak in the evening hours (2000 - 2200), and as was the case in

austral winter, the wind speeds during this period are significantly stronger in the dustiest December months. Again, this intensification of the surface circulation is invariably linked to the mesoscale processes operating at this time of year (discussed in chapter 6.3.2), however there are other plausible mechanisms other than the anabatic-sea breeze capable of generating stronger evening surface winds. For example, CPO's have been identified as an important uplift mechanism in the central and western Sahara during summer (Caton Harrison et al., 2021; Knippertz & Todd, 2012; Marsham et al., 2013), and given the tendency of their parent storms to form during the late afternoon/evening, are associated with uplift later in the diurnal cycle. The CMIP6 models evaluated in paper 3 do not capture well the surface wind speed distribution at Etosha during December, with only two models (HadGEM3-GC31-MM and MRI-ESM2-0) simulating an increase in wind speed through the evening hours.

6.1.3.2) Mesoscale Atmospheric Processes

A key finding of paper 1 was the relationship between the boundary layer and surface winds at Etosha during austral winter, with the breakdown of the NLLJ structure after sunrise generating the midmorning peak in surface winds described in chapter 6.1.3.1. There are two critical features of the jet when considering its influence on dust emissions; one is the strength of the structure (i.e., the magnitude of the core wind speeds), and the other is the timing of peak core wind speeds. With regards to the former, core wind speeds were significantly stronger on days where dust plumes were detected, with greater momentum mixed-down to the surface upon NLLJ breakdown. With regards to the latter, Etosha is shown to sit at a favourable latitude, as the pace of the

inertial oscillation produces peak jet intensity at around sunrise, allowing for a more abrupt breakdown of the structure. This is consistent with work conducted at Bordj-Badji Mohktar (21°N), which sits at a similar latitude to Etosha (19°S) in the Northern Hemisphere, and would help to explain the efficacy of the jets observed in these two locations in driving dust emissions (Allen & Washington, 2014), and also the modelling work conducted by Heinold et al. (2015), who showed that the optimal latitude for an abrupt NLLJ breakdown was ≈20°. Whilst NLLJ's have been identified in other dust source areas (Allen et al., 2013; Todd et al., 2008; Washington & Todd, 2005), and a jet has previously been observed at Etosha (Zunckel et al., 1996), this is the first time that uplift from the pan surface has been directly attributed to the mechanism.

An equivalent result in paper 2 was the finding that the anabatic-sea breeze was better developed in the dustiest December months, and propagated further inland at Etosha's latitude through the evening hours. Thermal and topographic airflows have been identified across different geographic regions, and as was described in chapter 6.1.2.1, have also been observed along the Namib coastline (Lindesay & Tyson, 1990), however this is the first time that dust activity in the Southern Hemisphere has been attributed to such a process. Wiggs et al. (2022) suggest that uplift at Etosha during austral summer is driven by CPO's, with abrupt changes in temperature and relative humidity cited as characteristic signatures of outflow events; the results of paper 2 show that the arrival of the anabatic-sea breeze at Etosha would induce similar changes in these variables however. Given the southward migration of the area of tropical convection during austral summer, and the fact that CPOs have been identified as a key uplift mechanism in other dust source areas (Knippertz & Todd, 2012;

Marsham et al., 2008, 2013), outflow events are not precluded as a driver of emissions at Etosha. It is plausible that both processes are involved, with the arrival of the sea breeze front and its associated areas of convergence/divergence triggering convective activity in the vicinity of the pan. To the authors knowledge, this is the first time a sea-breeze system has been implicated in the dust emission process, and so is a key finding of the thesis. The closest analogue in North Africa would be uplift associated with the West African Monsoon (WAM) circulation (i.e., another thermally driven circulation), where monsoon surges trigger convective activity (and hence CPOs) further north across the Sahara (Engelstaedter et al., 2015; Knippertz & Todd, 2012).

6.1.3.3) Synoptic Forcing

The efficacy of the mesoscale atmospheric processes outlined in chapter 6.1.3.2 in driving dust emissions from the Etosha pan have been shown in papers 1 and 2 to be synoptically modulated. Whilst the background pressure gradient is a control on NLLJ core wind speeds, it also influences the strength of the north-easterly flow within which the dust-emitting surface winds at Etosha are embedded (Washington et al., 2003). A key finding of paper 1 was that dust events in austral winter are synonymous with the ridging of the SAA, which produces a stronger jet at Etosha (see chapter 6.1.2.2), but also a stronger background flow. This synoptic modulation of emissions associated with NLLJ's is consistent with observations from other source areas such as the Bodele Depression (Todd et al., 2008; Washington & Todd, 2005) and the western Sahara (Fiedler et al., 2013; Knippertz & Todd, 2012). Changes in the strength of this background flow helps to account for variability in the CMIP6 models evaluated in paper 3, with the runs that generate dust over the interior of

southern Africa (HadGEM3-GC31-MM, HadGEM3-GC31-LL, MIROC6) all simulating a stronger easterly/north-easterly circulation in the dustier September months. The treatment of this flow in some of the models (MRI-ESM2-0, CNRM-ESM2-1) helps to explain the spatial distribution of emissions, as a south-westerly bias in its position activates the simulated source regions along the Atlantic coast.

Synoptics also contribute to the observed variability in the strength of the anabatic-sea breeze (and hence dust emissions) in December, with a key finding of paper 2 the north-eastward (south-westward) displacement of the area of tropical convection in the dusty (non-dusty) months. The effect of this was to disturb the spatial distribution of diabatic heating across the subcontinent so that in the dustiest December months, the area of maximum heating stretched from the southern Kalahari/Northern Cape region up to the Namibia-Angola border, hence driving a stronger onshore flow at Etosha's latitude. Determining the cause of this shift in the area of tropical convection was beyond the scope of paper 2, however it is invariably linked to the dominant modes of climate variability in southern Africa (i.e., ENSO, Benguela Ninos) (Florenchie et al., 2004; Howard & Washington, 2018; Reason, 2017; Rouault, 2012).

6.2) Future Dust Research in Southern Africa

6.2.1 Temporal Extent of Meteorological Observations

6.2.1.1) Interannual Variability in NLLJ

In paper 1, the existence of a strong and persistent NLLJ at Etosha was confirmed, however observations of the jet and associated surface winds covered only one dry season; the findings of this thesis could therefore be expanded on by monitoring the pan across multiple years. Given the remote nature of the source area, and the logistical challenges associated with instrumenting the field site, this could also be achieved using reanalysis data, as the NLLJ was shown to be well represented in ERA5. By extending the analysis of Etosha's meteorology across multiple dry seasons, it would be possible to quantify interannual variability in the strength of the NLLJ and associated surface winds. Work in North Africa has shown that interannual variability in dust emissions from the Bodele Depression is closely related to the strength of the NLLJ (Washington & Todd, 2005), however a preliminary assessment of southern African source areas suggests that they are supply limited, and it is year-to-year variability in the wetting of the pan surfaces (and hence sediment delivery) that controls interannual fluctuations in uplift (Bryant, 2003; Washington et al., 2003). Quantifying year-to-year changes in the strength of the NLLJ (whether through observations or reanalysis) would permit a more detailed analysis of the controls on interannual variability in emissions from Etosha.

6.2.1.2) Relationship Between Anabatic-Sea Breeze and Convection

In paper 2, it was shown that Etosha is emissive during December, outside of the traditional dust season (June – October, as characterised by early remote sensing work (Prospero et al., 2002; Washington et al., 2003)), a finding that has been subsequently corroborated by observations from the pan (Wiggs et al., 2022). Whilst the inland propagation of the anabatic-sea breeze clearly contributes to uplift at Etosha, the role of CPOs in driving emission, as well as the relationship between the sea breeze and convective activity remains unclear. These issues could be clarified by extending the meteorological observations at Etosha into austral summer, as lidar data (used in conjunction with other instrumentation) from North African source areas has been used to detect and attribute dust activity to CPOs (Allen et al., 2013). Caton-Harrison et al. (2021) have developed an automated approach to track dust-emitting CPOs across the Sahara using the SEVIRI RGB composite (utilised in paper 1 to detect dust plumes), and so extending the analysis of that dataset into December would also help in diagnosing convective activity close to Etosha. Fully elucidating the relationship between the anabatic-sea breeze and convection is not only critical to understanding dust emissions at Etosha, but also fundamental to determining the effect of the system on regional circulation features such as the Angola Low (Howard & Washington, 2018).

6.2.1.3) Drivers of Dust Uplift in Austral Spring

The results of the three papers have focused on emissions during austral winter and summer, however dust activity across southern Africa is not exclusive to these seasons. Indeed, analysis of the TOMS data in paper 2 shows that Etosha remains dusty during austral spring (between the AI peaks in September and December), whilst the observations presented by Wiggs et al.

(2022) indicate that although the overall frequency of dust events is lower in this season, the dust flux associated with each event is at its highest in November. Extending the meteorological observations into austral spring would permit an analysis of the atmospheric processes driving uplift during this season, and would show whether the NLLJ and anabatic-sea breeze contribute to emissions outside of austral winter and summer respectively. A hypothesis is that there is a transition during austral spring, when the southward movement of the area of maximum diabatic heating (and associated instability) inhibits the development of the NLLJ, but generates a stronger sea-breeze that propagates further inland. Alternatively, both mechanisms could operate concurrently, as has been observed with NLLJ's and CPOs in some Saharan source areas (Allen et al., 2013; Allen & Washington, 2014).

6.2.2 Spatial Coverage of Meteorological Observations

6.2.2.1) Spatial Extent of NLLJ

The observations presented in paper 1 are for a point on the edge of the Etosha pan, and so whilst they have been useful in quantifying the characteristics of the NLLJ and associated surface winds at that location, the spatial extent of the jet has not been evaluated; the findings of this thesis could therefore be built upon by expanding the coverage of meteorological observations across a broader area. As was discussed in chapter 6.2.1, instrumenting remote source areas is logistically challenging, and so a plausible alternative would be to analyse the spatial extent of the NLLJ using reanalysis data, especially given the skill with which ERA5 represents the jet at Etosha. This is an approach used by Rife et al. (2010), who compile a global climatology of NLLJ's using

reanalysis data from the NCAR Mesoscale Model. Jets have been shown to extend across large parts of North Africa (Fiedler et al., 2013), with for example elevated wind speeds associated with the Bodele NLLJ detected over an area covering 1200km (Todd et al., 2008).

6.2.2.2) Drivers of Dust Uplift from Other Source Areas

Whilst the research conducted as part of the thesis has considered dust emissions and the atmospheric drivers of uplift across southern Africa, a large focus of the work has been on the Etosha Pan. This is partly due to the prominence of the source area, but also the availability of high-quality, in situ data from the pan, which has made it possible to characterise the meteorology at Etosha, and determine the atmospheric controls on dust uplift. Analysis of the TOMS data in paper 2 shows that emissions from Makgadikgadi are comparable to those from Etosha during September, whilst Vickery et al. (2013) detect the highest number of dust plumes from sources along the Namib coastline. A logical progression of the research conducted as part of this thesis is therefore an extension of the meteorological observations to cover the other major southern African source areas, so as to account for the spatial distribution in dust emissions across the subcontinent, and also investigate whether the mesoscale processes identified in papers 1 and 2 contribute to uplift elsewhere (e.g., the anabatic-sea breeze activating the coastal Namib sources).

6.2.3) Modelling Work

6.2.3.1) Convection Permitting Simulations

In paper 3, the representation of dust emissions and dust-emitting processes across southern Africa were evaluated in CMIP6 simulations. Coupled models

were selected for analysis as they are the primary tool for predicting future climate change (Boucher et al., 2013), and so reducing uncertainties associated with the representation of dust in these simulations is an important research task. Recent studies have however shown that regional, high-resolution model runs improve the representation of mesoscale processes such as NLLJ's and CPOs (Garcia-Carreras et al., 2021, Roberts et al., 2018); in the case of CPOs, this is unsurprising, as convection in these simulations is explicitly resolved, whereas the parent storm is missing from coarser resolution model runs with parameterised convection. A convection-permitting, regional climate simulation for Africa (CP4A) has been run using the Met Office Unified Model, and preliminary analysis has shown it to improve the representation of summer rainfall across West Africa (Stratton et al., 2018). A progression of the research conducted as part of this thesis would be to evaluate the Etosha NLLJ and anabatic-sea breeze in CP4A, and assess whether the greater resolution and different physical parameterisations also improve the representation of these processes.

6.2.3.2) Response of Mesoscale Processes to Future Climate Change

Predictions of future climate change in the west of southern Africa show reductions in precipitation and increasing temperatures over the course of the 21st century (see Chapter 1) (Almazroui et al., 2020; Reason et al., 2017), which could lead to changes in the distribution and temporal variability of dust emissions across the subcontinent. Given that the models evaluated in paper 3 fail to capture key aspects of the contemporary dust emission climatology, any future predictions of dust uplift would be fraught with uncertainty, however several of the models capture well the NLLJ and anabatic-sea breeze; a logical

progression of the research conducted as part of this thesis would be to use these models to assess future changes in the strength of these systems under different warming scenarios. Both mechanisms are driven by the diurnal cycle of diabatic heating, and so any future warming, as well as changes to land surface properties (surface roughness is a control on NLLJ evolution (Heinold et al., 2015)), would likely affect the efficacy of the processes in driving dust emissions.

6.3) Summary of Main Findings

The main findings of the research conducted as part of this thesis will now be summarised in the context of the seven research objectives outlined in chapter 1.

1. *What are the spatial and temporal characteristics of dust emissions across southern Africa, and how are they represented in numerical models?*

    a. Characterise the spatial distribution of dust emissions across southern Africa and evaluate their representation in coupled models.

In September, peak dust emissions are recorded from the Etosha and Makgadikgadi Pans, with a belt of dust activity stretching between them across the Kalahari. Less than half of the models evaluated in paper 3 captured this distribution, with emissions showing a tendency to concentrate along the west coast of southern Africa. In December, Etosha is the primary dust source across the subcontinent, however this is not captured in any of the models evaluated in paper 3.

    b. Characterise the variability in southern African dust emissions across a range of different timescales.

There is a clear diurnal cycle in dust emissions from the Etosha Pan during austral summer, with all dust events in paper 1 activated in the hours following sunrise. Whilst it was not possible to characterise the diurnal cycle of emissions at Etosha in austral summer, the peak in surface winds during the evening is consistent with recent observational work conducted at the pan. The seasonal

cycle in emissions from Etosha diverges from the rest of the subcontinent during austral summer, with the pan as emissive in December as it was during the austral winter months. Interannual variability in emissions from the subcontinent is controlled by both the efficacy of the dust-emitting winds and the wetting of the pan surfaces during austral summer.

2. *What are the characteristic features of the meteorology of southern African dust source areas, and how are they represented in numerical models?*

    c. Characterise the key meteorological processes operating across southern Africa's dust source areas and identify the controls on their variability.

The atmospheric processes operating at Etosha vary by season; a persistent NLLJ is observed during austral winter, whereas the inland propagation of an integrated anabatic-sea breeze influence the diurnal cycle of surface winds during austral summer.

    d. Evaluate the representation of the key meteorological processes in reanalyses and coupled models, and assess the influence of resolution and physical parametrisations on model skill.

The representation of the NLLJ in the CMIP6 models is poor, with the multi-model mean underestimating core wind speeds at 0600 by >3ms^{-1}. The two models with the greatest vertical resolution simulate a well-developed inversion layer and the most realistic jet structure. The representation of the anabatic-sea breeze in the models is better, with the greater spatial resolution in some of the runs capturing the channelling of the onshore flow into several latitudinal bands.

3. *What features of the meteorology identified in key question 2 are responsible for driving dust emissions from southern African source areas, and how are these processes represented in coupled models?*

    e. Identify the atmospheric processes from key question 2 that contribute to the uplift of dust from southern African source areas.

With regards to dust emission, it is the breakdown of the NLLJ structure during the morning hours, and the subsequent enhancement of the surface winds that is the critical process, whilst ridging of the SAA drives a stronger NLLJ and background surface flow at Etosha. Etosha's location adjacent to the head of the Hoanib River valley aids the inland propagation of the anabatic-sea breeze, so that on occasion, it reaches the pan and raises the surface wind speed during the evening.

    f. Evaluate the representation of the dust-emitting processes in coupled models, and assess the influence of resolution and physical parametrisations on model skill.

The representation of the surface wind speed distribution at Etosha in both September and December is poor, with the models generally failing to capture the observed peaks in surface winds associated with the two mesoscale processes.

    g. Assess how the representation of the dust-emitting processes helps to account for the spatial distribution of emissions in coupled models described in key question 1.

The spatial distribution of the simulated emissions is both a function of the resolved meteorology, and the characteristics of the land surface, with soil

moisture exerting a strong influence on the locations of the modelled source areas. The better representation of the anabatic-sea breeze might help to account for the tendency of the models to simulate dust emissions along the coast.

This thesis has for the first time considered the atmospheric processes contributing to dust emissions from southern African source areas and their representation in numerical models. Two key emission mechanisms have been identified, a NLLJ and an anabatic-sea breeze system, however the analysis conducted relied on observations that were limited in both their spatial coverage and temporal extent. Field campaigns dedicated to instrumenting the Etosha and Makgadikgadi pans, as well as other global source areas, should be a focus of future research projects, so that the full range of atmospheric processes contributing to dust uplift can be identified. The representation of the two key emission mechanisms in numerical models was shown to be mixed, corroborating earlier modelling work conducted in a Saharan context. The emphasis of this research was on coupled models, as they are our main tools for projecting future climate change, however more work should be directed at evaluating higher resolution regional and convection permitting models, so as to ascertain the additional skill they provide in terms of their representation of the dust cycle.

References

Acosta, R. P., & Huber, M. (2017). The neglected Indo-Gangetic plains low-level jet and its importance for moisture transport and precipitation during the peak summer monsoon. Geophysical Research Letters, 44(16), 8601–8610. https://doi.org/10.1002/2017GL074440

Allen, C. J. T., & Washington, R. (2014). The low-level jet dust emission mechanism in the central Sahara: Observations from Bordj-Badji Mokhtar during the June 2011 Fennec Intensive Observation Period. Journal of Geophysical Research: Atmospheres, 119(6), 2990–3015. https://doi.org/10.1002/2013JD020594

Allen, C. J. T., Washington, R., & Engelstaedter, S. (2013). Dust emission and transport mechanisms in the central Sahara: Fennec ground based observations from Bordj Badji Mokhtar, June 2011. Journal of Geophysical Research: Atmospheres, 118(12), 6212–6232. https:// doi.org/10.1002/jgrd.50534

Almazroui, M., Saeed, F., Saeed, S. et al. Projected Change in Temperature and Precipitation Over Africa from CMIP6. Earth Syst Environ 4, 455–475 (2020). https://doi.org/10.1007/s41748-020-00161-x

Andreae, M., & Rosenfeld, D. (2008). Aerosol–cloud–precipitation interactions. part 1. the nature and sources of cloud-active aerosols. Earth-Science Reviews, 89 (1), 13-41. doi: https://doi.org/10.1016/j.earscirev.2008.03.001

Andrews, M. B., Ridley, J. K., Wood, R. A., Andrews, T., Blockley, E. W., Booth, B., . . . Sutton, R. T. (2020). Historical simulations with hadgem3- gc3.1 for

cmip6. Journal of Advances in Modeling Earth Systems, 12 (6), e2019MS001995. doi: https://doi.org/10.1029/2019MS001995

Aryal, Y. N., & Evans, S. (2021). Global dust variability explained by drought sensitivity in cmip6 models. Journal of Geophysical Research: Earth Surface, 126 (6), e2021JF006073. doi: https://doi.org/10.1029/2021JF006073

Ashpole, I., & Washington, R. (2012). An automated dust detection using SEVIRI: A multiyear climatology of summertime dustiness in the central and western Sahara. Journal of Geophysical Research: Atmospheres, 117(D8), D08202. https://doi.org/10.1029/2011JD016845

R. M. Banta and R. K. Newsom and J. K. Lundquist and Y. L. Pichugina and R. L. Coulter and L. Mahrt (2002). Nocturnal Low-Level Jet Characteristics Over Kansas During Cases-99. Boundary-Layer Meteorology, 105, 221–252.

B.O. Bauer, R.G.D. Davidson-Arnott, P.A. Hesp, S.L. Namikas, J. Ollerhead, I.J. Walker, (2009) Aeolian sediment transport on a beach: Surface moisture, wind fetch, and mean transport, Geomorphology, Volume 105, Issues 1–2. Pages 106-116.

Bechtold, P., Semane, N., Lopez, P., Chaboureau, J.-P., Beljaars, A., & Bormann, N. (2014). Representing equilibrium and nonequilibrium convection in large scale models. Journal of the Atmospheric Sciences, 71 (2), 734 - 753. doi: 10.1175/JAS-D-13-0163.1

Bhattachan, A., D'Odorico, P., & Okin, G. (2015). Biogeochemistry of dust sources in southern Africa. Journal of Arid Environments, 117, 18–27. https://doi.org/10.1016/j.jaridenv.2015.02.013

Blackadar, A. K. (1957). Boundary layer wind maxima and their significance for the growth of nocturnal inversions. Bulletin of the American Meteorological Society, 38(5), 283–290. https://doi.org/10.1175/1520-0477-38.5.283

BONNER, W. D. (1968). CLIMATOLOGY OF THE LOW LEVEL JET, Monthly Weather Review, 96(12), 833-850.

Boucher, O., Randall, D., Artaxo, P., Bretherton, C., Feingold, G., Forster, P., et al. (2013). Clouds and aerosols, In T. F. Stocker, D. Qin, G.-K. Plattner, M. Tignor, S. K. Allen, J. Boschung, et al. (Eds.), Climate change 2013: The physical science basis. Contribution of Working Group I to the Fifth Assessment Report of the Intergovernmental Panel on Climate Change (pp. 571–658). Cambridge University Press. https:// doi.org/10.1017/CBO9781107415324.016

Boussetta, S., Balsamo, G., Beljaars, A., Kral, T., & Jarlan, L. (2013). Impact of a satellite-derived leaf area index monthly climatology in a global numerical weather prediction model. International Journal of Remote Sensing, 34 (9-10), 3520-3542. doi: 10.1080/01431161.2012.716543

Brindley, H., Knippertz, P., Ryder, C., and Ashpole, I. (2012), A critical evaluation of the ability of the Spinning Enhanced Visible and Infrared Imager (SEVIRI) thermal infrared red-green-blue rendering to identify dust events: Theoretical analysis, J. Geophys. Res., 117, D07201, doi:10.1029/2011JD017326.

Browning, K. A., & Wexler, R. (1982). The determination of kinematic properties of a wind field using doppler radar. Journal of Applied Meteorology, 7(1), 105–113. https://doi.org/10.1175/1520-0450(1968)0072.0.co;2

Bryant, R. G. (2003). Monitoring hydrological controls on dust emissions: Preliminary observations from Etosha Pan, Namibia. The Geographical Journal, 169(2), 131–141. https://doi.org/10.1111/1475-4959.04977

Caton Harrison, T., Washington, R., & Engelstaedter, S. (2019). A 14-year climatology of Saharan dust emission mechanisms inferred from automatically tracked plumes. Journal of Geophysical Research: Atmospheres, 124(16), 9665–9690. https://doi.org/10.1029/2019JD030291

Caton Harrison, T., Washington, R., & Engelstaedter, S. (2021). Satellite-derived characteristics of saharan cold pool outflows during boreal summer. Journal of Geophysical Research: Atmospheres, 126 (3), e2020JD033387. doi: https://doi.org/10.1029/2020JD033387

Clements, M., & Washington, R. (2021). Atmospheric controls on mineral dust emission from the etosha pan, namibia: Observations from the clarify-2016 field campaign. Journal of Geophysical Research: Atmospheres, 126 (14), e2021JD034746. doi: https://doi.org/10.1029/2021JD034746

Clements, M., & Washington, R. (2022). Summer dust emissions from the etosha pan, namibia: The role of the namib anabatic-sea breeze system[unpublished manuscript]. Journal of Geophysical Research: Atmospheres.

Colberg, F., & Reason, C. J. C. (2006). A model study of the angola benguela frontal zone: Sensitivity to atmospheric forcing. Geophysical Research Letters, 33 (19). doi: https://doi.org/10.1029/2006GL027463

Dansie, A., Wiggs, G., Thomas, D., & Washington, R. (2017). Measurements of windblown dust characteristics and ocean fertilization potential: The

ephemeral river valleys of Namibia. Aeolian Research, 29, 30–41. https://doi.org/10.1016/j.aeolia.2017.08.002

Dee, D. P., Uppala, S. M., Simmons, A. J., Berrisford, P., Poli, P., Kobayashi, S., et al. (2011). The era-interim reanalysis: Configuration and performance of the data assimilation system. Quarterly Journal of the Royal Meteorological Society, 137(656), 553–597. https://doi. org/10.1002/qj.828

Dubovik, O., Holben, B., Eck, T. F., Smirnov, A., Kaufman, Y. J., King, M. D., Tanré, D., & Slutsker, I. (2002). Variability of Absorption and Optical Properties of Key Aerosol Types Observed in Worldwide Locations, Journal of the Atmospheric Sciences, 59(3), 590-608.

F. D. Eckardt & N. Kuring (2005). SeaWiFS identifies dust sources in the Namib Desert. International Journal of Remote Sensing, 26(19), 4159-4167.

Eckardt, Robert G. Bryant, Graham McCulloch, Baruch Spiro, Warren W. Wood (2008) The hydrochemistry of a semi-arid pan basin case study: Sua Pan, Makgadikgadi, Botswana, Applied Geochemistry, Volume 23, Issue 6, Pages 1563-1580.

Emmel, C., Knippertz, P., and Schulz, O. (2010). Climatology of convective density currents in the southern foothills of the Atlas Mountains. Journal of Geophysical Research, 115, D11115.

Engelstaedter, S., and Washington, R. (2007). Temporal controls on global dust emissions: The role of surface gustiness. Geophysical Research Letters, 34, L15805.

Evan, A. T. (2018). Surface winds and dust biases in climate models. Geophysical Research Letters, 45(2), 1079–1085. https://doi. org/10.1002/2017GL076353

Evan, A. T., Flamant, C., Fiedler, S., & Doherty, O. (2014). An analysis of aeolian dust in climate models. Geophysical Research Letters, 41(16), 5996–6001. https://doi.org/10.1002/2014GL060545

Eyring, V., Bony, S., Meehl, G. A., Senior, C. A., Stevens, B., Stouffer, R. J., & Taylor, K. E. (2016). Overview of the coupled model intercomparison project phase 6 (cmip6) experimental design and organization. Geoscientific Model Development, 9 (5), 1937–1958. doi: 10.5194/gmd-9-1937-2016

Fecan, F., Marticorena, B., and Bergametti, G.: (1999). Parametrization of the increase of the aeolian erosion threshold wind friction velocity due to soil moisture for arid and semi-arid areas, Ann. Geophys.-Atmos. Hydr., 17, 149–157.

Fernald, F. G., Herman, B. M., & Reagan, J. A. (1972). Determination of aerosol height distributions by lidar. Journal of Applied Meteorology and Climatology, 11(3), 482–489. https://doi.org/10.1175/1520-0450(1972)0112.0.CO;2

Fiedler, S., Schepanski, K., Heinold, B., Knippertz, P., & Tegen, I. (2013). Climatology of nocturnal low-level jets over North Africa and implications for modeling mineral dust emission. Journal of Geophysical Research: Atmospheres, 118(12), 6100–6121. https://doi. org/10.1002/jgrd.50394

Fiedler, S., Knippertz, P., & Woodward, S. (2016). A process-based evaluation of dust-emitting winds in the cmip5 simulation of hadgem2-es. Climate Dynamics, 46 , 1107–1130. doi: https://doi.org/10.1007/s00382-015-2635-9

Florenchie, P., Reason, C., Lutjeharms, J., Rouault, M., Roy, C., & Masson, S. (2004, 06). Evolution of interannual warm and cold events in the southeast atlantic ocean. Journal of Climate - J CLIMATE, 17 , 2318-2334. doi: 10.1175/1520-0442(2004)017h2318:EOIWACi2.0.CO;2

Formenti, P., D'Anna, B., Flamant, C., Mallet, M., Piketh, S. J., Schepanski, K., et al. (2019). The aerosols, radiation and clouds in southern Africa field campaign in Namibia: Overview, illustrative observations, and way forward. Bulletin of the American Meteorological Society, 100(7), 1277–1298. https://doi.org/10.1175/BAMS-D-17-0278.1

Funk, C., Peterson, P., Landsfeld, M., Pedreros, D., Verdin, J., Shukla, S., . . . Michaelsen, J. (2015, 12). The climate hazards infrared precipitation with stations - a new environmental record for monitoring extremes. Scientific Data, 2, 150066. doi: 10.1038/sdata.2015.66

Garcia-Carreras, L., Parker, D. J., Marsham, J. H., Rosenberg, P. D., Brooks, I. M., Lock, A. P., et al. (2015). The turbulent structure and diurnal growth of the Saharan atmospheric boundary layer. Journal of the Atmospheric Sciences, 72(2), 693–713. https://doi.org/10.1175/ JAS-D-13-0384.1

Garstang, M., Tyson, P. D., Swap, R., Edwards, M., Kllberg, P., & Lindesay, J. A. (1996). Horizontal and vertical transport of air over southern Africa. Journal of Geophysical Research: Atmospheres, 101(D19), 23721–23736. https://doi.org/10.1029/95JD00844

Ge, J. M. and Liu, H. and Huang, J. and Fu, Q (2016). Taklimakan Desert nocturnal low-level jet: climatology and dust activity. Atmospheric Chemistry and Physics, 16, 7773-7783

Ginoux, P., Prospero, J. M., Gill, T. E., Hsu, N. C., & Zhao, M. (2012). Global-scale attribution of anthropogenic and natural dust sources and their emission rates based on MODIS deep blue aerosol products. Reviews of Geophysics, 50(3), RG3005. https://doi. org/10.1029/2012RG000388

Goldreich, Y. and Tyson, P. D. 1988. 'Diurnal and inter-diurnal variations in large-scale atmospheric turbulence over southern Africa, S. Afi. Geogr. J., 70, 48-56.

Goudie, A. S. (2014). Desert dust and human health disorders. Environment International, 63 , 101-113. doi: https://doi.org/10.1016/j.envint.2013.10.011

Hardisty, J., Whitehouse, R. Evidence for a new sand transport process from experiments on Saharan dunes . Nature 332, 532–534 (1988).

Haustein, K., Washington, R., King, J., Wiggs, G., Thomas, D. S. G., Eckardt, F. D., . . . Menut, L. (2015). Testing the performance of state-of-the-art dust emission schemes using do4models field data. Geoscientific Model Development, 8 (2), 341–362. doi: 10.5194/gmd-8-341-201

Haywood, J., & Boucher, O. (2000). Estimates of the direct and indirect radiative forcing due to tropospheric aerosols: A review. Reviews of Geophysics, 38(4), 513–543. https://doi.org/10.1029/1999RG000078

Heinold, B., Knippertz, P., & Beare, R. J. (2015). Idealized large-eddy simulations of nocturnal low-level jets over subtropical desert regions and implications for dust-generating winds. Quarterly Journal of the Royal Meteorological Society, 141(690), 1740–1752. https://doi. org/10.1002/qj.2475

Heinold, B., Knippertz, P., Marsham, J. H., Fiedler, S., Dixon, N. S., Schepanski, K., et al. (2013). The role of deep convection and nocturnal low-level jets for dust emission in summertime west Africa: Estimates from convection-permitting simulations. Journal of Geophysical Research: Atmospheres, 118(10), 4385–4400. https://doi.org/10.1002/jgrd.50402

Hennen, M., Chappell, A., Webb, N., Schepanski, K., Baddock, M., Eckardt, F., Kandakji, T., Lee, J., Nobakht, M., and von Holdt, J.: Evaluating dust emission model performance using dichotomous satellite observations of dust emission, Geosci. Model Dev.

Herman, J. R., Bhartia, P. K., Torres, O., Hsu, C., Seftor, C., & Celarier, E. (1997). Global distribution of uv-absorbing aerosols from nimbus 7/toms data. Journal of Geophysical Research: Atmospheres, 102 (D14), 16911-16922. doi: https:// doi.org/10.1029/96JD03680

Hersbach, H., Bell, B., Berrisford, P., Hirahara, S., Horányi, A., Muñoz-Sabater, J., et al. (2020). The ERA5 global reanalysis. Quarterly Journal of the Royal Meteorological Society, 146(730), 1999–2049. https://doi.org/10.1002/qj.3803

M.H.T. Hipondoka, H. Jousse, J. Kempf, D. Busche

Fossil evidence for perennial lake conditions during the Holocene at Etosha Pan, Namibia: news and views. South Afr. J. Sci., 102 (2006), pp. 93-95,

Howard, E., & Washington, R. (2018). Characterizing the synoptic expression of the Angola low. Journal of Climate, 31(17), 7147–7165. https://doi.org/10.1175/JCLI-D-18-0017.1

Jemmett-Smith, B. C., Marsham, J. H., Knippertz, P., & Gilkeson, C. A. (2015). Quantifying global dust devil occurrence from meteorological analyses. Geophysical Research Letters, 42(4), 1275–1282. https://doi.org/10.1002/2015GL063078

Jickells, T. D., An, Z. S., Andersen, K. K., Baker, A. R., Bergametti, G., Brooks, N., et al. (2005). Global iron connections between desert dust, ocean biogeochemistry, and climate. Science, 308(5718), 67–71. https://doi.org/10.1126/science.1105959

Kaufman, Y., Tanré, D. & Boucher, O. (2002). A satellite view of aerosols in the climate system. Nature, 419, 215–223

Knippertz, P., Deutscher, C., Kandler, K., Müller, T., Schulz, O., and Schütz, L. (2007), Dust mobilization due to density currents in the Atlas region: Observations from the Saharan Mineral Dust Experiment 2006 field campaign, J. Geophys. Res., 112, D21109, doi:10.1029/2007JD008774.

Knippertz, P., and Todd, M. C. (2010). The central west Saharan dust hot spot and its relation to African easterly waves and extratropical disturbances. Journal of Geophysical Research, 115, D12117.

Knippertz, P., & Todd, M. C. (2012). Mineral dust aerosols over the Sahara: Meteorological controls on emission and transport and implications for modeling. Reviews of Geophysics, 50(1). https://doi.org/10.1029/2011RG000362

Kok, J. F., Parteli, E. J. R., Michaels, T. I., & Karam, D. B. (2012). The physics of wind-blown sand and dust. Reports on Progress in Physics, 75(10), 106901. https://doi.org/10.1088/0034-4885/75/10/106901

Koren, I., Kaufman, Y. J., Washington, R., Todd, M. C., Rudich, Y., Martins, J. V., & Rosenfeld, D. (2006). The Bodélé depression: A single spot in the Sahara that provides most of the mineral dust to the Amazon forest. Environmental Research Letters, 1(1), 014005. https:// doi.org/10.1088/1748-9326/1/1/014005

Landman, W. A., & Mason, S. J. (1999). Change in the association between Indian Ocean sea-surface temperatures and summer rainfall over South Africa and Namibia. International Journal of Climatology, 19(13), 1477–1492. https://doi.org/10.1002/ (SICI)1097-0088(19991115)19:133.0.CO;2-W

Larom, D., Garstang, M., Lindeque, M., Raspet, R., Zunckel, M., Hong, Y., et al. (1997). Meteorology and elephant infrasound at Etosha National Park, Namibia. Journal of the Acoustical Society of America, 101(3), 1710–1717. https://doi.org/10.1121/1.418180

Liao, H., and Seinfeld, J. H. (1998). Radiative forcing by mineral dust aerosols: Sensitivity to key variables. Journal of Geophysical Research, 103(D24), 31637–31645.

Lindesay, J. A., & Tyson, P. D. (1990). Thermo-topographically induced boundary layer oscillations over the central namib, southern africa. International Journal of Climatology, 10 (1), 63-77. doi: https://doi.org/10.1002/joc.3370100108

Lyon, B., & Mason, S. J. (2007). The 1997–98 Summer Rainfall Season in Southern Africa. Part I: Observations, Journal of Climate, 20(20), 5134-5148.

Mahowald, N. M., Baker, A. R., Bergametti, G., Brooks, N., Duce, R. A., Jickells, T. D., et al. (2005). Atmospheric global dust cycle and iron inputs to the ocean.

Global Biogeochemical Cycles, 19(4), RG3005. https://doi.org/10.1029/2004GB002402

Mahowald, N. M., Bryant, R. G., del Corral, J., & Steinberger, L. (2003). Ephemeral lakes and desert dust sources. Geophysical Research Letters, 30(2), 1074–1078. https://doi.org/10.1029/2002GL016041

Mahowald, N. M., & Kiehl, L. M. (2003). Mineral aerosol and cloud interactions. Geophysical Research Letters, 30(9). https://doi. org/10.1029/2002GL016762

Mahowald, N. M. and Kloster, S. and Engelstaedter, S. and Moore, J. K. and Mukhopadhyay, S. and McConnell, J. R. and Albani, S. and Doney, S. C. and Bhattacharya, A. and Curran, M. A. J. and Flanner, M. G. and Hoffman, F. M. and Lawrence, D. M. and Lindsay, K. and Mayewski, P. A. and Neff, J. and Rothenberg, D. and Thomas, E. and Thornton, P. E. and Zender, C. S. (2010). Observed 20th century desert dust variability: impact on climate and biogeochemistry. Atmospheric Chemistry and Physics, 10(22), 10875-10893

Mahrt, L.: 1999, 'Stratified Atmospheric Boundary Layers', Boundary-Layer Meteorol. 90, 375-396

Mann, G. W. and Carslaw, K. S. and Spracklen, D. V. and Ridley, D. A. and Manktelow, P. T. and Chipperfield, M. P. and Pickering, S. J. and Johnson, C. E. (2010). Description and evaluation of GLOMAP-mode: a modal global aerosol microphysics model for the UKCA composition-climate model. Geoscientific Model Development, 3(2), 519-551.

Marsham, J. H., Hobby, M., Allen, C. J. T., Banks, J. R., Bart, M., Brooks, B. J., et al. (2013). Meteorology and dust in the central Sahara: Observations from Fennec supersite-1 during the June 2011 intensive observation period. Journal

of Geophysical Research: Atmospheres, 118(10), 4069–4089. https://doi.org/10.1002/jgrd.50211

Marsham, J. H., Knippertz, P., Dixon, N. S., Parker, D. J., & Lister, G. M. S. (2011). The importance of the representation of deep convection for modeled dust-generating winds over West Africa during summer. Geophysical Research Letters, 38(16), L16803. https://doi. org/10.1029/2011GL048368

Marsham, J. H., Parker, D. J., Grams, C. M., Taylor, C. M., & Haywood, J. M. (2008). Uplift of Saharan dust south of the intertropical discontinuity. Journal of Geophysical Research: Atmospheres, 113(D21), D21102. https://doi.org/10.1029/2008JD009844

Marticorena, B., & Bergametti, G. (1995). Modeling the atmospheric dust cycle: 1. Design of a soil-derived dust emission scheme. Journal of Geophysical Research: Atmospheres, 100(D8), 16415–16430. https://doi.org/10.1029/95JD00690

Martin, J. H. (1990). Glacial-interglacial CO2 change: The Iron Hypothesis. Paleoceanography, 5(1), 1– 13.

McPeters, R. D., Bhartia, P. K., Krueger, A. J., Herman, J. R., Schlesinger, B. M., Wellemeyer, C. G., . . . Cebula, R. P. (1996). Nimbus–7 total ozone mapping spectrometer (toms) data products user's guide. NASA Reference Publication

Middleton, N. (2017). Desert dust hazards: A global review. Aeolian Research, 24 , 53-63. doi: https://doi.org/10.1016/j.aeolia.2016.12.001

Miller, R. L., & Tegen, I. (1998). Climate response to soil dust aerosols. J. Climate, 11 , 3247–3267. doi: 10.1175/1520-0442(1998)011

Miller, R.L., P. Knippertz, C. Pérez García-Pando, J.P. Perlwitz, and I. Tegen (2014). Impact of dust radiative forcing upon climate. In Mineral Dust: A Key Player in the Earth System. P. Knippertz and J.- B.W. Stuut, Eds. Springer, 327-357.

Morcrette, J.-J., Barker, H. W., Cole, J. N. S., Iacono, M. J., & Pincus, R. (2008). Impact of a new radiation package, mcrad, in the ecmwf integrated forecasting system. Monthly Weather Review, 136 (12), 4773 - 4798. doi: 10.1175/2008MWR2363.1

Munday, C., & Washington, R. (2017). Circulation controls on southern African precipitation in coupled models: The role of the Angola low. Journal of Geophysical Research: Atmospheres, 122(2), 861–877. https://doi.org/10.1002/2016JD025736

Murray, J. E., Brindley, H. E., Bryant, R. G., Russell, J. E., Jenkins, K. F., & Washington, R. (2016). Enhancing weak transient signals in SEVIRI false color imagery: Application to dust source detection in southern Africa. Journal of Geophysical Research: Atmospheres, 121(17), 199–210. https://doi.org/10.1002/2016JD025221

Nicholson, S. E., & Grist, J. P. (2003). The Seasonal Evolution of the Atmospheric Circulation over West Africa and Equatorial Africa, Journal of Climate, 16(7), 1013-1030.

Nield, J. M., Wiggs, G. F. S., King, J., Bryant, R. G., Eckardt, F. D., Thomas, D. S. G., & Washington, R. (2016). Climate–surface–pore-water interactions on a salt crusted playa: Implications for crust pattern and surface roughness

development measured using terrestrial laser scanning. Earth Surface Processes and Landforms, 41(6), 738–753. https://doi.org/10.1002/esp.3860

Park, S., Kim, S.-W., Park, M.-S., & Song, C.-K. (2018). Measurement of planetary boundary layer winds with scanning doppler lidar. Remote Sensing, 10(8), 1261. https://doi.org/10.3390/rs10081261

Preston-Whyte, R. A., Diab, R. D., & Sokolic, F. (1994). Thermo-topographically induced winds in the boundary layer over the etosha pan. South African Geographical Journal, 76(2), 59–62. https://doi.org/10.1080/03736245.1994.9713576

Prospero J.M. (1996). Saharan Dust Transport Over the North Atlantic Ocean and Mediterranean: An Overview. In: Guerzoni S., Chester R. (eds) The Impact of Desert Dust Across the Mediterranean. Environmental Science and Technology Library, vol 11. Springer, Dordrecht.

Prospero, J. M., Ginoux, P., Torres, O., Nicholson, S. E., & Gill, T. E. (2002). Environmental characterization of global sources of atmospheric soil dust identified with the NIMBUS 7 total ozone mapping spectrometer (TOMS) absorbing aerosol product. Reviews of Geophysics, 40(1), 2–1. https://doi.org/10.1029/2000RG000095

Pu, B., & Ginoux, P. (2018). How reliable are cmip5 models in simulating dust optical depth? Atmospheric Chemistry and Physics, 18 (16), 12491–12510. doi: 10.5194/acp-18-12491-2018

Rácz, Z. and Smith, R.K. (1999), The dynamics of heat lows. Q.J.R. Meteorol. Soc., 125: 225-252. https://doi.org/10.1002/qj.49712555313

Reason, C. (2017). Climate of Southern Africa. Oxford University Press. https://doi.org/10.1093/acrefore/9780190228620.013.513

Reason, C., & Smart, S. (2015). Tropical south east Atlantic warm events and associated rainfall anomalies over southern Africa. Frontiers in Environmental Science, 3, 24. https://doi.org/10.3389/fenvs.2015.00024

Rife, D. L., Pinto, J. O., Monaghan, A. J., Davis, C. A., & Hannan, J. R. (2010). Global distribution and characteristics of diurnally varying low-level jets. Journal of Climate, 23(19), 5041–5064. https://doi.org/10.1175/2010JCLI3514.1

Roberts, A. J., Marsham, J. H., Knippertz, P., Parker, D. J., Bart, M., Garcia-Carreras, L., et al. (2017). New Saharan wind observations reveal substantial biases in analyzed dust-generating winds. Atmospheric Science Letters, 18(9), 366–372. https://doi.org/10.1002/asl.765

Roberts, A. J., Woodage, M. J., Marsham, J. H., Highwood, E. J., Ryder, C. L., McGinty, W., et al. (2018). Can explicit convection improve modeled dust in summertime west Africa? Atmospheric Chemistry and Physics, 18(12), 9025–9048. https://doi.org/10.5194/ acp-18-9025-2018

Rouault, M. (2012). Bi-annual intrusion of tropical water in the northern benguela upwelling. Geophysical Research Letters, 39 (12). doi: https://doi.org/10.1029/ 2012GL052099

Rosenfeld, Daniel and Rudich, Yinon and Lahav, Ronen (2001). Desert dust suppressing precipitation: A possible desertification feedback loop. National Academy of Sciences, 98(11), 5975-5980.

Schepanski, K., Tegen, I., Laurent, B., Heinold, B., & Macke, A. (2007). A new Saharan dust source activation frequency map derived from MSG-SEVIRI IR-channels. Geophysical Research Letters, 34(18), L18803. https://doi.org/10.1029/2007GL030168

Schepanski, K., Tegen, I., Todd, M. C., Heinold, B., Bönisch, G., Laurent, B., & Macke, A. (2009). Meteorological processes forcing Saharan dust emission inferred from MSG-SEVIRI observations of subdaily dust source activation and numerical models. Journal of Geophysical Research: Atmospheres, 114(D10), D10201. https://doi.org/10.1029/2008JD010325

L. Schütz and M. Sebert (1987). Mineral aerosols and source identification. Journal of Aerosol Science, 18(1), 1-10.

Shapiro, A., & Fedorovich, E. (2010). Analytical description of a nocturnal low-level jet. Quarterly Journal of the Royal Meteorological Society, 136(650), 1255–1262. https://doi.org/10.1002/qj.628

Sinha, P., Hobbs, P. V., Yokelson, R. J., Bertschi, I. T., Blake, D. R., Simpson, I. J., . . . Novakov, T. (2003). Emissions of trace gases and particles from savanna fires in southern africa. JOURNAL OF GEOPHYSICAL RESEARCH , 108 (D13). doi: 10.1029/2002JD002325

Smith, R.K. and Spengler, T. (2011), The dynamics of heat lows over elevated terrain. Q.J.R. Meteorol. Soc., 137: 250-263. https://doi.org/10.1002/qj.737

Spavins-Hicks, Z. D., Washington, R., & Munday, C. (2021). The Limpopo low-level jet: Mean climatology and role in water vapor transport. Journal of Geophysical Research: Atmospheres, 126, e2020JD034364. https://doi.org/10.1029/2020JD034364

Sroga, J. T., Eloranta, E. W., & Barber, T. (1980). Lidar measurement of wind velocity profiles in the boundary layer. Journal of Applied Meteorology and Climatology, 19(5), 598–605. https://doi.org/10.1175/1520-0450(1980)0192.0.CO;2

Stensrud, D. J. (1996). Importance of Low-Level Jets to Climate: A Review, Journal of Climate, 9(8), 1698-1711.

Stratton, R. A., Senior, C. A., Vosper, S. B., Folwell, S. S., Boutle, I. A., Earnshaw, P. D., et al. (2018). A pan-African convection-permitting regional climate simulation with the Met Office Unified Model: CP4-Africa. Journal of Climate, 31(9), 3485–3508. https://doi.org/10.1175/ JCLI-D-17-0503.1

Swap, R., Garstang, M., Macko, S. A., Tyson, P. D., Maenhaut, W., Artaxo, P., et al. (1996). The long-range transport of southern African aerosols to the tropical south Atlantic. Journal of Geophysical Research: Atmospheres, 101(D19), 23777–23791. https://doi. org/10.1029/95JD01049

Tegen, I., Harrison, S. P., Kohfeld, K., Prentice, I. C., Coe, M., & Heimann, M. (2002). Impact of vegetation and preferential source areas on global dust aerosol: Results from a model study. Journal of Geophysical Research: Atmospheres, 107(D21), AAC 14-1–AAC 14-27. https:// doi.org/10.1029/2001JD000963

Tegen, I., Lacis, A. A., & Fung, I. (1996). The influence of mineral aerosols from disturbed soils on the global radiation budget. Nature, 380 , 419–422. doi: 10 .1038/380419a0

Textor, C. and Schulz, M. and Guibert, S. and Kinne, S. and Balkanski, Y. and Bauer, S. and Berntsen, T. and Berglen, T. and Boucher, O. and Chin, M. and

Dentener, F. and Diehl, T. and Easter, R. and Feichter, H. and Fillmore, D. and Ghan, S. and Ginoux, P. and Gong, S. and Grini, A. and Hendricks, J. and Horowitz, L. and Huang, P. and Isaksen, I. and Iversen, I. and Kloster, S. and Koch, D. and Kirkevag, A. and Kristjansson, J. E. and Krol, M. and Lauer, A. and Lamarque, J. F. and Liu, X. and Montanaro, V. and Myhre, G. and Penner, J. and Pitari, G. and Reddy, S. and Seland, O. and Stier, P. and Takemura, T. and Tie, X (2006). Analysis and quantification of the diversities of aerosol life cycles within AeroCom. Atmospheric Chemistry and Physics, 6(7), 1777-1813.

Thorpe, A. J. & Guymer, T. H. (1977). The nocturnal jet. Q. J. R. Meteorol. Soc., 103: 633–653.

Todd, M. C., Washington, R., Raghavan, S., Lizcano, G., & Knippertz, P. (2008). Regional model simulations of the Bodélé low-level jet of northern Chad during the Bodélé dust experiment (BoDEx 2005). Journal of Climate, 21(5), 995–1012. https://doi. org/10.1175/2007JCLI1766.1

Torres, O., Bhartia, P. K., Herman, J. R., Sinyuk, A., Ginoux, P., & Holben, B. (2002). A long-term record of aerosol optical depth from toms observations and comparison to aeronet measurements. Journal of the Atmospheric Sciences, 59 (3), 398 - 413. doi: 10.1175/1520-0469(2002)059h0398: ALTROAi2.0.CO;2

Tyson, P. D. 1967. ‘Some characteristics of the mountain wind over Pietermaritzburg’, Proceedings of the Jubilee Conference uj‘the Sourh African Geographical Society, Durban, pp. 103-128

van de Wiel, B. J. H., Moene, A. F., Steeneveld, G. J., Baas, P., Bosveld, F. C., & Holtslag, A. A. M. (2010). A conceptual view on inertial oscillations and

nocturnal low-level jets. Journal of the Atmospheric Sciences, 67(8), 2679–2689. https://doi.org/10.1175/2010JAS3289.1

Vickery, K. J., & Eckardt, F. D. (2013). Dust emission controls on the lower kuiseb river valley, central namib. Aeolian Research, 10 , 125-133. doi: https://doi .org/10.1016/j.aeolia.2013.02.006

Vickery, K. J., Eckardt, F. D., & Bryant, R. G. (2013). A sub-basin scale dust plume source frequency inventory for southern Africa, 2005– 2008. Geophysical Research Letters, 40(19), 5274–5279. https://doi.org/10.1002/grl.50968

von Holdt, J. R. C., Eckardt, F. D., Baddock, M. C., & Wiggs, G. F. S. (2019). Assessing landscape dust emission potential using combined ground-based measurements and remote sensing data. Journal of Geophysical Research: Earth Surface, 124, 1080– 1098. https://doi.org/10.1029/2018JF004713

Wagener, T., Guieu, C., Losno, R., Bonnet, S., & Mahowald, N. (2008). Revisiting atmospheric dust export to the southern hemisphere ocean: Biogeochemical implications. Global Biogeochemical Cycles, 22(2), GB2006. https://doi.org/10.1029/2007GB002984

Washington, R., Todd, M., Middleton, N. J., & Goudie, A. S. (2003). Dust-storm source areas determined by the total ozone monitoring spectrometer and surface observations. Annals of the Association of American Geographers, 93 (2), 297-313. doi: 10.1111/1467-8306.9302003

Washington, R., Bouet, C., Cautenet, G., Mackenzie, E., Ashpole, I., Engelstaedter, S., et al. (2009). Dust as a tipping element: The Bodélé

depression, Chad. Proceedings of the National Academy of Sciences, 106(49), 20564–20571. https://doi.org/10.1073/pnas.0711850106

Washington, R., & Todd, M. C. (2005). Atmospheric controls on mineral dust emission from the Bodélé depression, Chad: The role of the low level jet. Geophysical Research Letters, 32(17), L17701. https://doi.org/10.1029/2005GL023597

Washington, R., Todd, M. C., Engelstaedter, S., Mbainayel, S., & Mitchell, F. (2006). Dust and the low-level circulation over the bod´el´e depression, chad: Observations from bodex 2005. Journal of Geophysical Research: Atmospheres, 111 (D3). doi: https://doi.org/10.1029/2005JD006502

WEXLER, H. (1961), A Boundary Layer Interpretation of the Low-level Jet. Tellus, 13: 368-378. https://doi.org/10.1111/j.2153-3490.1961.tb00098.x

Wiggs, G. F. S., Bullard, J. E., Garvey, B., & Castro, I. (2002). Interactions between airflow and valley topography with implications for aeolian sediment transport. Physical Geography, 23 (5), 366-380. doi: 10.2747/ 0272-3646.23.5.366

Wiggs, G. F. S. (2011). Sediment mobilisation by the wind. In Arid zone geomorphology (p. 455-486). John Wiley and Sons, Ltd. doi: https://doi.org/10.1002/ 9780470710777.ch18

Wiggs, G. F. S., Baddock, M. C., Thomas, D. S. G., Washington, R., Nield, J. M., Engelstaedter, S., . . . K¨otting, S. (2022). Quantifying mechanisms of aeolian dust emission: Field measurements at etosha pan, namibia. Journal of Geophysical Research: Earth Surface, 127 (8), e2022JF006675. doi: https://doi.org/10.1029/2022JF006675

Wu, C., Lin, Z., & Liu, X. (2020). The global dust cycle and uncertainty in cmip5 (coupled model intercomparison project phase 5) models. Atmospheric Chemistry and Physics, 20 (17), 10401–10425. doi: 10.5194/acp-20-10401-2020

Zhao, A., Ryder, C. L., & Wilcox, L. J. (2022). How well do the cmip6 models simulate dust aerosols? Atmospheric Chemistry and Physics, 22 (3), 2095–2119. doi: 10.5194/acp-22-2095-2022

Zunckel, M., Hong, Y., Brassel, K., & O'Beirne, S. (1996). Characteristics of the nocturnal boundary layer: Okaukuejo, namibia, during safari-92. Journal of Geophysical Research: Atmospheres, 101 (D19), 23757-23766. doi: https://doi.org/10.1029/95JD00624

Data Sources:

Observational Data:

Lidar and weather station data from Etosha were collected as part of the CLARIFY-2016 field campaign and are available from Professor Richard Washington in the School of Geography and the Environment.

Reanalysis Data:

ERA-I data is maintained by ECMWF and is available online from their website (https://www.ecmwf.int/en/forecasts/datasets/reanalysis-datasets/era-interim).

ERA5 data is maintained by ECMWF and is available online from the Copernicus Climate Change Service (https://doi.org/10.24381/cds.adbb2d47).

Satellite and Gridded Precipitation Data:

MSG SEVIRI data is maintained by EUMETSAT and is available online from their Data Center (https://archive.eumetsat.int/usc/).

MODIS imagery is maintained by NASA and is available online from EOSDIS Worldview (https://worldview.earthdata.nasa.gov/).

TOMS AI data is maintained by NASA and is available online from the IRI data library (https://iridl.ldeo.columbia.edu/SOURCES/.NASA/.GSFC/.TOMS/.NIMBUS7/.monthly/.ai/).

CHIRPS data is maintained by the Climate Hazards Centre and is available online from their website (https://data.chc.ucsb.edu/products/CHIRPS-2.0/).

Model Data:

Data from the HadGEM3-GC31-MM historical simulation is available from the CEDA archive (https://10.22033/ESGF/CMIP6.6112).

Data from the HadGEM3-GC31-LL historical simulation is available from the CEDA archive (https://doi.org/10.22033/ESGF/CMIP6.6109).

Data from the MPI-ESM-1-2-HAM historical simulation is available from the CEDA archive (https://doi.org/10.22033/ESGF/CMIP6.5016).

Data from the MIROC-ES2L historical simulation is available from the CEDA archive (https://doi.org/10.22033/ESGF/CMIP6.5602).

Data from the MIROC6 historical simulation is available from the CEDA archive (https://doi.org/10.22033/ESGF/CMIP6.5603).

Data from the CanESM5 historical simulation is available from the CEDA archive (https://doi.org/10.22033/ESGF/CMIP6.3610).

Data from the MRI-ESM2-0 historical simulation is available from the CEDA archive (https://doi.org/10.22033/ESGF/CMIP6.6842).

Data from the CNRM-ESM2-1 historical simulation is available from the CEDA archive (https://doi.org/10.22033/ESGF/CMIP6.4068).

Appendix A: Co-authorship statement

The papers submitted as part of this thesis were co-authored by Matthew Clements and Professor Richard Washington.

In each of the papers, Matthew Clements was responsible for the experimental design, data analysis, plotting of figures and tables, and the writing of the paper. Richard Washington was responsible for the experiment design and assisted in writing the paper.